UNIVERSITÀ DEGLI STUDI DI PARMA

Dottorato di Ricerca in Fisica

Ciclo XXIX

Growth and Investigation of Different Gallium Oxide Polymorphs

Coordinator:
Chiar.mo Prof. Cristiano Viappiani

Supervisor:
Chiar.mo Prof. Roberto Fornari

Candidate: Francesco Boschi

2014-2016

To my family

Table of contents

Most used abbreviations

a.u.	Arbitrary Units
AFM	Atomic Force Microscopy
ALD	Atomic Layer Deposition
ALE	Atomic Layer Epitaxy
APB	Anti-Phase Boundary
BL	Boundary Layer
CL	Cathodoluminescence
CVD	Chemical Vapour Deposition
DFT	Density Functional Theory
DHM	Dynamic Hysteresis Measurement
DSC	Differential Scanning Calorimetry
EFG	Edge-defined Film-fed Growth
FET	Field-Effect Transistor
FFT	Fast Fourier Transform
FWHM	Full-Width at Half-Maximum
GGA	Generalised Gradient Approximation
HRTEM	High-Resolution Transmission Electron Microscopy
HVPE	Halide Vapour Phase Epitaxy
MESFET	Metal-Semiconductor Field-Effect Transistor
MFC	Mass Flow Controller
MOCVD	Metalorganic Chemical Vapour Deposition
MOSFET	Metal-Oxide-Semiconductor Field-Effect Transistor
PCS	Photocurrent Spectroscopy
PID	Proportional-Integral-Derivative (power control system)
PLD	Pulsed Laser Deposition

QM	Horizontal offset of the substrate from the plasma plume in off-axis PLD (1 QM ~ 1.4 mm)
RMS	Root Mean Square (square root of the arithmetic mean of the squares of a set of numbers, here always referring to surface roughness)
RTE	Raman Tensor Element
SAED	Selected Area Diffraction
sccm	Standard Cubic Centimetres per Minute
SEM	Scanning Electron Microscopy
STEM	Scanning Transmission Electron Microscopy
TB	Twin Boundary
TEM	Transmission Electron Microscopy
TMA	Trimethylaluminium
TMG	Trimethylgallium
UV	Ultraviolet
VPE	Vapour Phase Epitaxy
VPSIC	Variational Pseudo Self-Interaction Correction (density functional approach)
XRD	X-Ray Diffraction

Introduction

The popularity of semiconductor oxides dates back several decades. Due to their wide bandgap, chemical and thermal stability, and variety of available growth techniques, they are, together with semiconductor nitrides, the most studied materials for high power electronics and optoelectronic devices operating in the UV and visible spectral range.

Among them, gallium oxide was discovered at the end of 19th century[1], when the new element gallium and its compounds were first described. After an initial period of purely basic research, the interest for this material started to arise as first applications were proven, such as phosphor host material for emissive displays[2,3], catalyst and photocatalyst for a series of chemical reactions[4–6], gas sensors in both oxidising and reducing environments[7–9], transparent conductive electrodes[10,11]. For these conventional applications, however, crystal quality has never been a major concern, and in some cases polycrystalline or even amorphous materials were preferred.

The development of crystal growth technology recently allowed to obtain high quality bulk Ga_2O_3 single crystals[12,13], as well as homo- and hetero-epitaxial layers[14–17]. This technological progress, combined with the possibility of controlled *n*-type doping in a wide range[18–21], paved the way to the field of semiconductor industry, with some applications already proven: substrates for GaN heteroepitaxy[22,23], UV optoelectronic devices[24,25] and power transistors[16,26].

What makes Ga_2O_3 of great interest is in fact its extremely high critical breakdown field, whose value is strictly related to the material bandgap[27] and estimated to be about 8 MV/cm[28]. Critical field in turn determines a Baliga Figure of Merit (BFOM)[29] at least four times larger than that calculated for the main competitors SiC an GaN, thus making gallium oxide one of the most promising materials for high power electronics. Transferring electric power with low losses is one of today's major challenges in research; it is hence not surprising that the number of publications on gallium oxide exponentially increased during the last decade, closely following the advancements of the related technology.

However, Ga_2O_3 as a crystalline material is still quite new. Further research is required both to improve the growth process and to clarify some ambiguous or even contradictory results about fundamental properties that can currently be found in literature. It is the case, for instance, of the wide spread of the reported bandgap values, especially when they are measured by optical absorption (4.5-4.9 eV[10,11,13,18,30]), as well as of some ambiguities in the discussion of Raman spectra, or the lack of lattice expansion data at high temperature. Furthermore, technological issues such as domain growth during heteroepitaxy and difficulties in contact formation call for a solution, as they limit the final film and device quality. Although these issues were partially solved utilising complicated preparation steps, it is definitely necessary to better understand and optimise the relevant technology. As a last point, it

must be mentioned that the actual structure of the metastable Ga_2O_3 polymorphs is still matter of debate, while most of their properties remain unknown.

So far, research activity was almost exclusively focused on the thermodynamically stable β phase, neglecting that gallium oxide can form five other polymorphs. Among them, ε-Ga_2O_3 is the most stable[31] and recently proved to grow at lower temperatures than β-Ga_2O_3[32], displaying at the same time good matching with commercial high symmetry substrates. Moreover, being the bandgap value close to the one of the β phase, it should in principle maintain a comparable BFOM, thus remaining extremely promising for the development of power electronics devices. As it will be shown in the following, it is also easier to obtain symmetric/Ohmic contacts on its surface with respect to β-Ga_2O_3, which requires more complicated surface treatments[28] or even implantation[33]. In addition to this, unfortunately, the few available reports show evident contradictions between calculated[31,34] and experimental[35] crystal structures, thus making the study of this phase challenging, but very interesting, from a fundamental point of view.

This scenario provided the main motivations for the present work: first, to develop a reproducible and reliable deposition technology for high quality gallium oxide thin films at low temperature; second, to highlight unclear or unknown fundamental properties of both films and bulk material. Most of the work described in this thesis was carried out between the Physics Department of Parma University and IMEM-CNR Institute, and expanded through the three years with internal and external collaborations.

The employed growth techniques were Metalorganic Chemical Vapour Deposition (MOCVD) and Atomic Layer Deposition (ALD). The advantages of vapour phase growth are well known: it is fast and versatile, thus widely applied by the industry; it allows for growth at relatively low temperatures, as well as freedom in the choice of reagents and precise control over doping. In addition, the ALD variant provides extremely high conformal deposition and thickness control, while crystallinity can be achieved at even lower temperatures and the process is suitable for industrial scaling and mass production. Finally, as it will become evident in the course of this thesis, chemical methods are convenient for the deposition of ε-Ga_2O_3, as they allow obtaining metastable phases at relatively low temperature and with no need for additional doping.

The Ph.D. period also included a three-months research stay at the University of Leipzig, hosted by the Semiconductors Physics Group. The aim was to get acquaintance with a new deposition technique for Ga_2O_3, namely Pulsed Laser Deposition (PLD), understanding process-related parameters and conceptual issues. This visit also represented an important chance for acquiring expertise in the fields of film characterisation and realisation of metal contacts for basic test devices. A basic know-how about photolithography and fabrication/characterisation of field-effect transistors (FETs) based on the deposited layers was also developed.

In chapter 1 the properties of the different Ga_2O_3 polymorphs are discussed, starting with a focused description of the stable β phase and its actual applications. The main features and available information background of other polymorphs, especially ε-Ga_2O_3, are also summarised in this chapter.

Chapter 2 includes an overview of the deposition techniques employed for this thesis, namely MOCVD, ALD and PLD, describing their main characteristics, the involved physical and chemical mechanisms, as well as the related technological aspects. In the second part of this chapter, the actual experimental growth setups are presented, including a collection of the most representative deposition parameters.

Chapter 3 deals with the characterisation of the deposited Ga_2O_3 layers. In the first part, the core activity of this Ph.D. work is covered: the investigation of the relationship between growth parameters and final quality of ε-Ga_2O_3 CVD layers, together with the assessment of some unexplored properties of this polymorph. The real structure of the ε phase is unambiguously determined by electron microscopy and X-Ray diffraction. It is found that this structure presents a spontaneous polarisation and that it is ferroelectric in nature. After discussing other physical properties of the deposited films, leading to the fabrication of a functioning UV-detector, the section dedicated to ε-Ga_2O_3 concludes with the description of some recent improvements to the reactor and with the presentation of the first results obtained by ALD. In the final part of chapter 3, the main outcomes of the research period in Leipzig are discussed. It is shown how a variant of the PLD technique, the so-called "off-axis" configuration, can be employed to limit film damage during the deposition process, thus increasing the final β-Ga_2O_3 surface quality and allowing for ring FETs successful fabrication.

In chapter 4, a study on the anisotropy of some physical properties in bulk β-Ga_2O_3 is reported. In particular, the results of polarised Raman spectroscopy measurements are compared with existing literature, solving some of the ambiguities related to sample orientation. A comparison between different procedures for obtaining Raman tensor elements from angular fitting of A_g modes intensities is proposed, as well. Furthermore, it is shown how the bandgap edge, measured by optical absorption with polarised light, changes with crystal orientation, backing-up the experimental results with *ab-initio* calculations. The chapter ends with a study on the thermal expansion of bulk β-Ga_2O_3, which leads to the determination of the lattice expansion coefficients in the temperature range 300–600 K by powder diffraction.

Finally, chapters 5 collects the conclusive remarks of this work, and provides an outlook on the future activity.

CHAPTER 1 - Gallium oxide

Gallium oxide is a wide-bandgap semiconductor belonging to the more general family of sesquioxides. It is in fact an ionic compound consisting of three oxygen anions for each two gallium cations, which leads to the general chemical formula Ga_2O_3.

Six different polymorphic forms of gallium oxides have been reported until now (see Table 1.1), each one having similar close-packing of oxygen layers, with different filling of tetrahedral and octahedral gallium site, as displayed schematically in Figure 1.1.

Table 1.1: Gallium oxide polymorphs.

Phase	Symmetry	Space group	Lattice constants	Data type
α	rhombohedral	$R\bar{3}c$	a = 4.9825 Å c = 13.433 Å	Experimental[36]
			a = 5.059 Å c = 13.618 Å	Calculated[34]
β	monoclinic	$C2/m$	a = 12.214 Å b = 3.0371 Å c = 5.7981 Å β = 103.83°	Experimental[37]
			a = 12.27 Å b = 3.04 Å c = 5.80 Å β = 103.7°	Calculated[38]
γ	cubic (spinel)	$Fd\bar{3}m$	a = 8.23760 Å	Experimental[35]
δ	cubic (bixbyite)	$Ia\bar{3}$	a = 10.00 Å	Experimental[39]
			a = 9.401 Å	Calculated[34]
ε	hexagonal	$P6_3mc$	a = 2.9036 Å c = 9.2554 Å	Experimental[35]
	orthorhombic	$Pna2_1$	a = 5.120 Å b = 8.792 Å c = 9.410 Å	Calculated[34]
(κ)	orthorhombic (transient)	$Pna2_1$	a = 5.0557 Å b = 8.68842 Å c = 9.27585 Å	Experimental[35]

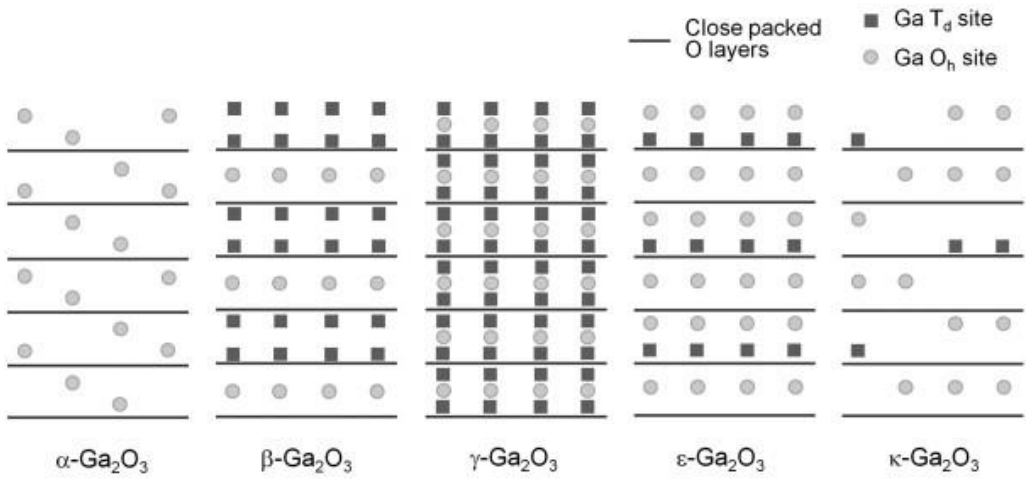

Figure 1.1: Simplified stacking sequence of different Ga_2O_3 polymorphs (from Playford *et al.*[35]). The polymorphs β and γ are based on a face-centred cubic oxygen lattice, while the others are based on a hexagonal close-packed oxygen lattice. Note that oxygen layers may actually be distorted from planarity, and that not all Ga sites are fully occupied.

Even if the polymorphic nature of Ga_2O_3 is well known, however, the vast majority of literature and research work has up to now focused mainly on the monoclinic β phase. The latter has been recognised as the only form which remains stable up to the melting point, while all other polymorphs are metastable (see formation energies in Figure 1.2) and tend to transform to β at sufficiently high temperatures. This fact, together with the difficulties in obtaining high quality single crystals, has so far strongly limited the possibility to characterise these phases. Hence, many fundamental properties are still unknown or matter of debate, and sometimes even the existence of the polymorph itself is criticised.

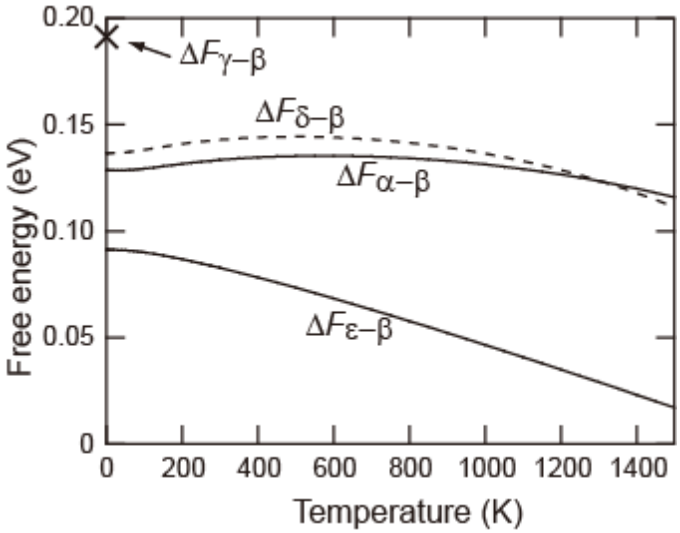

Figure 1.2: Temperature dependence of the difference in Helmholtz free energy between metastable polymorphs and β-Ga_2O_3 (from Yoshioka *et al.*[34]). For most of the temperature range, the formation energies are clearly $\beta < \varepsilon < \alpha < \delta < \gamma$.

1.1 The stable β phase

As anticipated, β-Ga_2O_3 is the most diffused and studied gallium oxide polymorph, as it is the only one to be stable up to the melting point. This high thermal stability allows to produce high quality bulk single crystals and epitaxial films, making this material available for extensive characterisation. A summary of the main physical properties is reported in Table 1.2. Although this phase has been well characterised with respect to the metastable forms, literature data still show some contradictions.

1.1.1 Crystal structure

This monoclinic phase displays $C2/m$ symmetry, with four formula units per crystallographic cell, and it is characterised by four lattice parameters, namely *a*, *b*, *c*, and β. The lattice parameters were first reported by Kohn *et al.*[40], while the structure was solved by Geller[41]. Initial doubts about the effective symmetry being even lower ($P1$ space group[42]) were removed by later studies, with XRD symmetry and systematic extinctions clearly indicating a *C*-centred monoclinic lattice with $C2/m$ space group. In particular, a more recent study by Åhman *et al.*[37] is often referred to by other publications because of its superior precision, 10 times better with respect to previous works.

Figure 1.3 shows the β-Ga_2O_3 lattice unit cell. It is composed by two crystallographically inequivalent gallium sites and three inequivalent oxygen sites, all of them located at $4i(x, 0, z)$ positions and arranged in a distorted cubic closed-packed array. The crystal structure can be described in terms of GaO_6 octahedra and GaO_4 tetrahedra, occupied in equal proportion, in a similar fashion to θ-Al_2O_3. Zigzag double chains of edge-sharing GaO_6 octahedra are linked by single chains of vertex-sharing GaO_4 tetrahedra along the ***b*** axis.

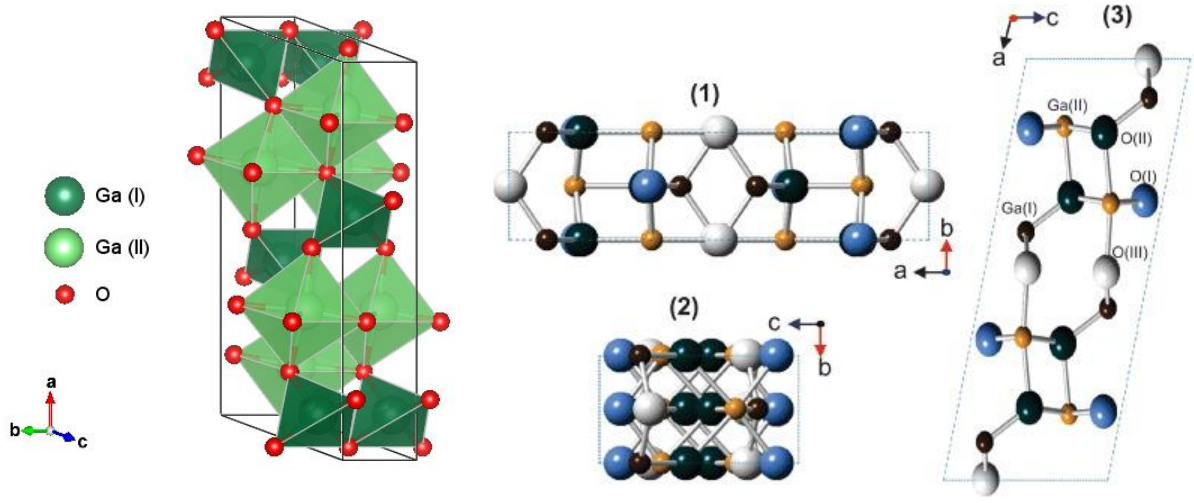

Figure 1.3: Left: Crystallographic unit cell of β-Ga_2O_3 highlighting different gallium coordination. Right (from Janowitz *et al.*[43]): Projection along (1) ***c***- (2) ***a***- and (3) ***b***-axis. Inequivalent gallium and oxygen sites are marked with different colours.

Table 1.2: Some physical properties of β-Ga_2O_3.(Partially taken from Stepanov *et al.*[44])

Property	Value	Reference
Crystal system	Monoclinic	Geller[41], Åhman[37]
Space group	$C2/m$	Geller[41], Åhman[37]
Lattice parameters		
a	12.214(3) Å	Åhman[37]
b	3.0371(9) Å	Åhman[37]
c	5.7981(9) Å	Åhman[37]
β	103.83(2)°	Åhman[37]
Density	5.95 g/cm^3	Tamura Corporation[45]
Dielectric constant	9.9–10.2	Passlack[46]
	13.9	Lee[47]
Bandgap	4.85 ± 0.1 eV	Janowitz[43]
	4.9	Orita[10]
	4.7	Tippins[48]
	4.52 (***E***‖***c***) – 4.79 (***E***‖***b***) eV	Ueda[49]
	4.4	Passlack[46]
Electron effective mass	0.28 m_e	Varley[20], Janowitz[43]
Melting Point	1740 °C	Roy[39]
	1795 °C	Víllora[19]
	1820 ± 20 °C	Galazka[13]
Specific heat	0.56 J/gK	Janowitz[43]
	0.49 J/gK	Tamura Corporation[45]
Thermal conductivity		
[100]	10.9 ± 1.0 W/mK	Guo[50]
	13 W/mK	Víllora[51]
[-201]	13.3 ± 1.0 W/mK	Guo[50]
[001]	14.7 ± 1.5 W/mK	Guo[50]
[110]	27.0 ± 2.0 W/mK	Guo[50]
	21 W/mK	Galazka[52]
Thermal expansion coefficient		
[100]	$1.8 \cdot 10^{-6}$ K^{-1}	Víllora[51]
[010]	$4.2 \cdot 10^{-6}$ K^{-1}	Víllora[51]
[001]	$4.2 \cdot 10^{-6}$ K^{-1}	Víllora[51]
Vickers hardness		
(101)	9.7 GPa	Tamura Corporation[45]
(-201)	12.5 GPa	Tamura Corporation[45]
Young's modulus	230 GPa	Tamura Corporation[45]
Refractive index (at 532 nm)		
‖ [010]	1.9523	Bhaumik[53]
⊥(100)	1.9201	Bhaumik[53]
Electronic mobility	110–130 cm^2/Vs	Janowitz[43]
	300 cm^2/Vs (extrapolated)	Higashiwaki[28]
Critical breakdown field	8 MV/cm	Higashiwaki[28]
BFOM (for DC and low frequency)	3444	Higashiwaki[28]

1.1.2 Electronic structure

Most of the studies about electronic structure of β-Ga_2O_3 have been theoretical. Approaches based on basic Density Functional Theory (DFT) in Local Density Approximation (LDA) provide a good qualitative description, although they tend to underestimate absolute values, especially the bandgap[54,55]. Thanks to hybrid functionals it is possible to get a more accurate picture, with a better agreement between calculations and experimental results[20,38,56].

Conduction band minimum (CBM) in β-Ga_2O_3 is located at the Γ point of the Brillouin Zone (BZ). While authors commonly agree on this result and on the indirect nature of the bandgap, the same does not hold for the position of the valence band maximum (VBM). In fact, the valence band is almost flat and displays very little dispersion, which makes the exact position of its absolute maximum difficult to determine. He *et al.*[38] located the valence band maximum at the M point, though almost degenerate with the one at the Γ point. The calculated bandgap values were 4.66 eV (M–Γ indirect) and 4.69 eV (Γ direct). Similar quasi-degeneracy was obtained also by Varley *et al.*[20], but with larger values of indirect (4.83 eV) and direct (4.87 eV) bandgaps. Here, VBM occurred just off the M point. On the contrary, Peelaers *et al.*[56] identified VBM on the line connecting I and L points, i.e. on the face of the BZ. Bandgap values were however similar to those found by Varley *et al.*[20], namely 4.84 eV and 4.88 eV for indirect and direct transitions, respectively.

The experimental work by Janowitz *et al.*[43] seems to shed some light on the VBM issue. Fundamental gaps and electronic structures were determined along high-symmetry directions of the BZ by Angular Resolved Photoemission Spectroscopy (ARPES). A detailed plot of the experimental band structure is shown in Figure 1.4 and displays nearly perfect agreement with theory. The measured bandgap was again indirect, with a magnitude of 4.85 ± 0.1 eV and with the valence band maximum located in the vicinity of the M point. At the centre of the BZ, a direct gap of 4.9 ± 0.1 eV was observed.

Further analysis of dipole-matrix element revealed that indirect transitions are predicted to be about one order of magnitude weaker than the direct ones[20]. This fact, together with the small energy difference between direct and indirect bandgap, would define β-Ga_2O_3 as an "almost" direct-gap material and was used by Varley *et al.*[20] to account for the sometimes high optical gap (~ 4.9 eV[10]) measured when evaluating absorption onsets. This explanation, however pertinent, does not take into account other effects, for instance absorption anisotropy, as it will be discussed in the section dedicated to the optical properties of β-Ga_2O_3 (1.1.4).

As for other band-related properties, a small and almost isotropic electron effective mass was calculated (0.27–0.28 m_e)[20,56] and confirmed by experimental results[43]. On the contrary, effective hole mass is expected to be highly anisotropic and larger, due to the flatness of the valence band. A large value of 40 m_e was roughly estimated along the Γ–Z direction, while a significantly smaller hole effective mass of 0.40 m_e was obtained along the Γ–A direction[20].

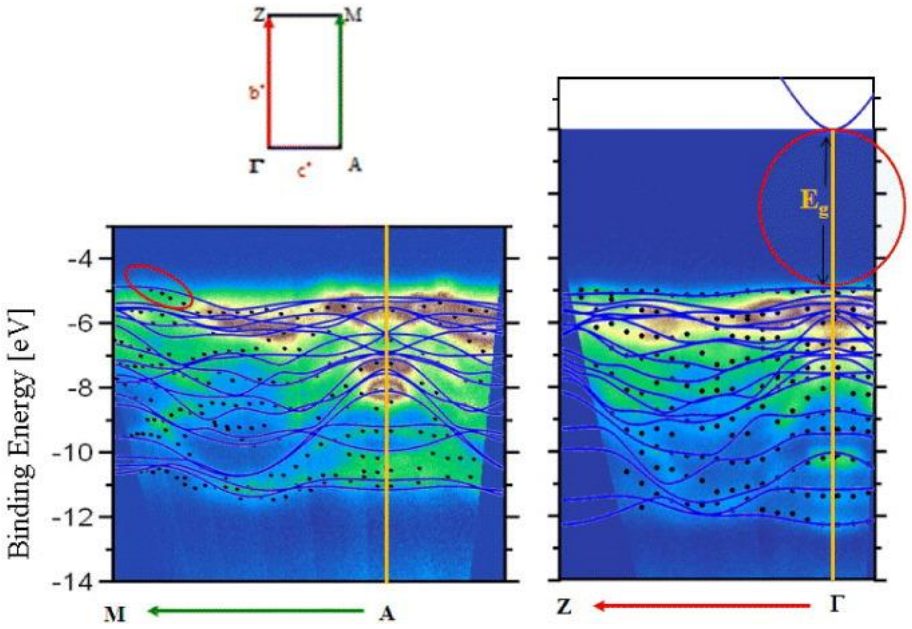

Figure 1.4: Experimental electronic band structure of β-Ga_2O_3, measured by ARPES along the A–M (left) and Γ–Z (right) directions of the BZ. Black dots represent the experimental bands derived from a fitting procedure to the spectra. For the sake of comparison, calculated band structures based on density functional theory are shown as blue lines. The red marked areas highlight the regions of the direct and indirect gaps. Top: sketch of the investigated BZ directions. (From Janowitz *et al.*[43])

1.1.3 Thermal properties

β-Ga_2O_3 has a poor thermal conductivity, half of that of Al_2O_3 and one order of magnitude less than GaN. Due to structural anisotropy, the highest value is observed along the [010], while the lowest is along [100]. Thermal conductivity k was measured by laser-flash methods[51,52] and time domain thermoreflectance[50], which led to slightly different results (see Table 1.2). The behaviour of k as a function of temperature T can be fitted by a simple equation in the form:

$$k(T) = AT^{-m} \tag{1.1}$$

where exponent m is about 3.5 in the range 80–200 K and about 1.2 at 200–495 K. Further, all works concur that at low temperature heat conduction is limited not only by phonon scattering, but also by free electron scattering, thus deviating from the typical $T^{3/2}$ dependence.

Thermal expansion was investigated by Víllora *et al.*[51] (see Figure 1.5), who reported the expansion coefficient of the three lattice constants in the temperature range 5–293 K. As can be evinced from Table 1.2. coefficients of *b* and *c* are practically identical and roughly double that of *a*. The behaviour of expansion coefficients at higher temperatures (300–700 K) was the subject of a recent paper published in the framework of this thesis[57], and will be dealt with in chapter 4. This information, previously missing in literature, is of great technological interest, since it allows to evaluate the thermal mismatch when planning heteroepitaxial growth both of and on β-Ga_2O_3.

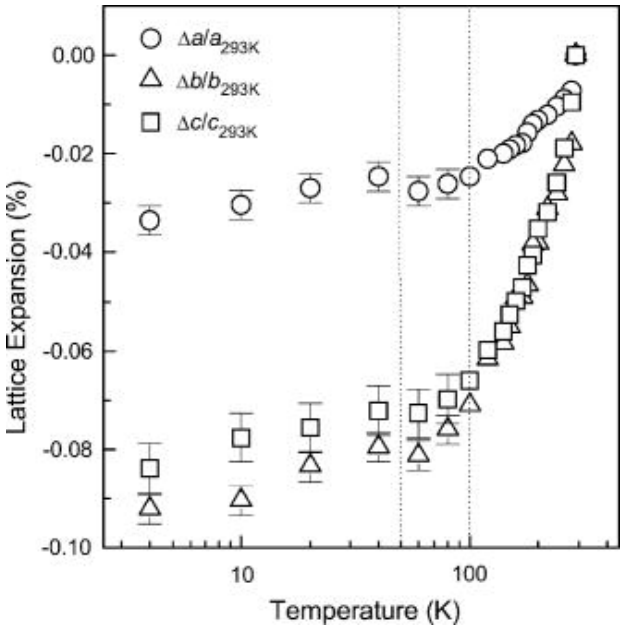

Figure 1.5: Behaviour of β-Ga_2O_3 lattice parameters as a function of temperature. (From Víllora *et al.*[51])

1.1.4 Optical properties

Pure β-Ga_2O_3 crystals, due to their large bandgap, are colourless and show high transparency up to the UV range of electromagnetic radiation. Impurities and defects can determine crystals colouration, which in turn gives a first indication on the material conductivity[13,52]. Figure 1.6 shows transmittance spectra of β-Ga_2O_3 crystals with different carrier concentrations. Insulating β-Ga_2O_3 can be either colourless, due to the steep absorption edge at 255–260 nm, or light-yellowish, associated to minor absorption in the blue region of the visible spectrum. On the other hand, *n*-type semi-conductive crystals usually display a blueish colouration, which can be ascribed to increased free-carrier absorption in red and NIR regions of the spectrum. As a final point, impurities such as carbon cause a greyish colouration.

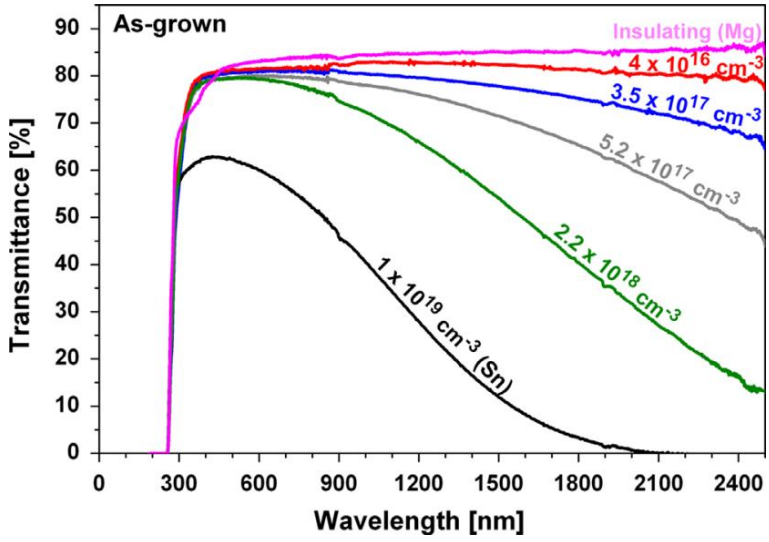

Figure 1.6: Transmittance spectra of as-grown β-Ga_2O_3 single crystals obtained by the Czochralski method with various free electron concentrations. (From Galazka *et al.*[52])

Close to the absorption onset at 260 nm, that can be attributed to intrinsic band-to band transitions, typical spectra also exhibit a shoulder around 270 nm. Víllora *et al.*[58] ascribed this phenomenon to transitions from the valence band perturbed by Ga^{3+} vacancies to the conduction band. The authors also criticised, at least in this regard, a previous interpretation given by Ueda *et al.*[49], which was related to anisotropy, since it was not compatible with emission spectra.

Nevertheless, absorption anisotropy in β-Ga_2O_3 is a recognised experimental fact[30,49], further supported by first principle calculations. This phenomenon was first reported in the pioneering work of Matsumoto *et al.* in 1974[30], followed by a reappraisal by Ueda *et al.* in 1997[49]. Using UV light polarised along the directions ***b*** and ***c*** of (100) Ga_2O_3 platelets, these authors showed that the bandgap values were higher by about 0.15–0.27 eV when ***E*****||*****b***. While the reported values for ***E*****||*****c*** are in good agreement (4.50 and 4.52 eV), for ***E*****||*****b*** the agreement between the two works was somewhat more qualitative (4.65 and 4.79 eV), and the reasons for this discrepancy were not discussed. As shown schematically in Figure 1.7, ***E*****||*****b*** and ***E*****||*****c*** transitions were interpreted as the direct-allowed ones from the valence band with Γ^{2-} symmetry to the bottom of the conduction band with Γ^{1+} and from Γ^{1-} to Γ^{1+}, respectively[49]. In spite of the current knowledge about absorption anisotropy in β-Ga_2O_3, it is surprising that many recent papers reported bandgap values without providing the crucial information about sample orientation and measurement geometry, often resulting in scattered values of the extrapolated bandgap widths. A work published in the framework of this thesis recently shed more light on the optical properties-band structure relationships in bulk β-Ga_2O_3[59], which will be dealt with in chapter 4. Here, the conclusions of the two works mentioned above will be verified also on crystal orientations not investigated so far, while *ab initio* computation will provide further insight on physical phenomenology of optical anisotropy.

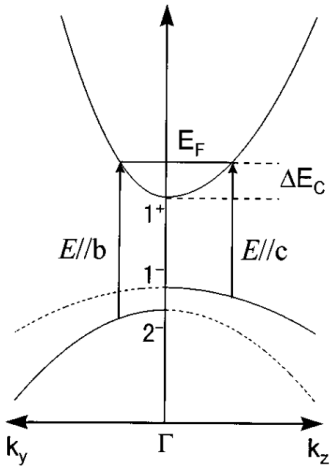

Figure 1.7: Schematic diagram of the allowed band-to-band transitions in β-Ga_2O_3 ***k***-space. (From Ueda *et al.*[49])

An extensive study on the refractive index of β-Ga_2O_3 single crystals as a function of temperature was carried out by Bhaumik *et al.*[53], along both the [010] direction and the direction perpendicular to

(100) plane. Resulting fits with Sellmeier's equation are reported in Figure 1.8. It was further shown that the refractive index linearly increases with temperature, with a thermal coefficient of ~ 10^{-5} °C^{-1}.

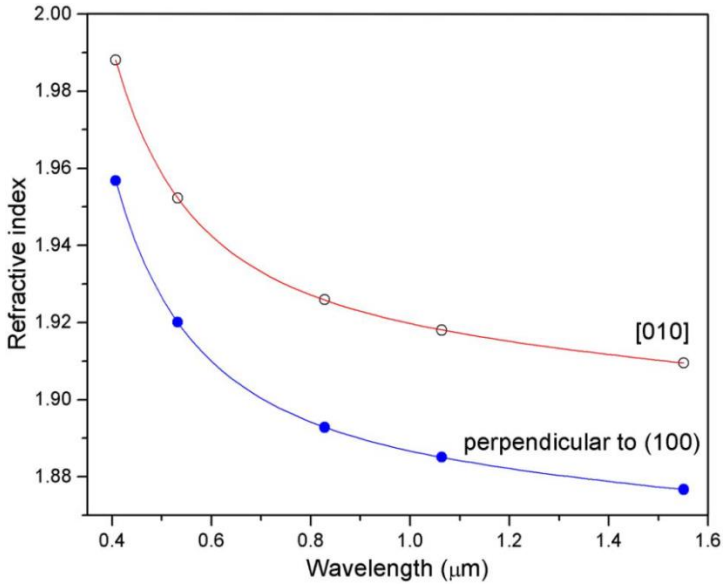

Figure 1.8: Fitting Sellmeier's equation for β-Ga_2O_3 at 30 °C (from Bhaumik *et al.*[53]).

β-Ga_2O_3 crystals typically display at least two emission bands, located in the near-UV (3.2–3.6 eV) and blue (2.8–3.0 eV) regions of the electromagnetic spectrum[60–65]. The mechanisms involved in the two processes are depicted schematically in Figure 1.9. The well-known UV emission is not affected by sample preparation nor by the presence of impurities, and can be ascribed to radiative recombination between free electrons and self-trapped holes[63,65]. In the blue emission process, both donors and acceptors are probably involved[62,65]. A possible mechanism would be a rate-determining transfer by tunnel effect of an electron from a donor cluster to a hole trapped at an acceptor site. Subsequently, a fast electron–hole recombination would occur at the acceptor site with a strong electron-phonon coupling, giving rise to the blue emission[65]. An additional green emission band is observed in doped β-Ga_2O_3 crystals and is probably associated with self-trapped or bound excitons. Typical impurities giving green luminescence are Be, Ge, Sn, and Li, while Fe and Cu act as killers for the blue emission[62].

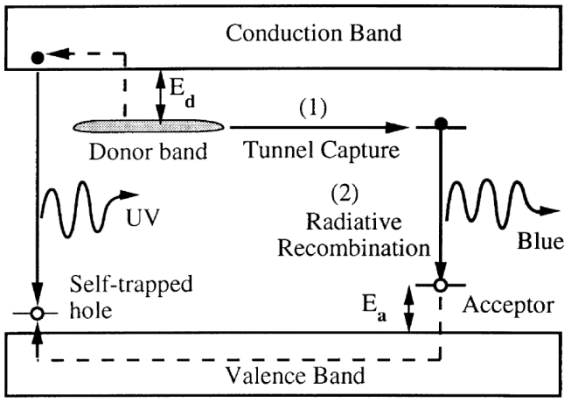

Figure 1.9: Model for UV and blue luminescence in gallium oxide. (From Binet *et al.*[65])

Concerning vibrational properties of β-Ga_2O_3, with space group $C2/m$ and 10 atoms in the unit cell, at $\boldsymbol{k}$ = 0 group theory predicts a total of 30 normal modes:

$$\Gamma_{vib} = 10A_g + 5B_g + 5A_u + 10B_u \quad (1.2)$$

of which $(1A_u + 2B_u)$ are acoustic. This leaves 15 Raman (A_g and B_g) and 12 infrared (A_u and B_u) optically active modes[66–69]. β-Ga_2O_3 vibrational properties were thoroughly investigated by Dohy *et al.*[66], which first reported a complete wavenumber assignment for all modes based on their symmetry (see Table 1.3).

Table 1.3: Optical vibrational modes of β-Ga_2O_3. (From Dohy *et al.*[66])

Raman		Infrared	
Mode	Wavenumber (cm^{-1})	Mode	Wavenumber (cm^{-1})
A_g	763	B_u	760
A_g	657	B_u	720
B_g	651	A_u	668
A_g	628	B_u	640
A_g	475	B_u	525
B_g	475	A_u	455
A_g	415	B_u	375
B_g	353	A_u	n.o. (352 calc.)
A_g	346	B_u	310
A_g	318	B_u	290
A_g	199	A_u	250
A_g	169	B_u	155
B_g	147		
B_g	114		
A_g	111		

In particular, the two types of Raman modes can be selectively observed, depending on the respective polarisation of incident and analysed light, thus further confirming that β-Ga_2O_3 indeed belongs to $C2/m$ space group[66]. The modes below 200 cm^{-1} were attributed to libration and translation of the doubly connected straight chains of GaO_6 edge-shared octahedra running along the ***b***-axis of the crystal. In the range 318–415 cm^{-1}, the modes could be ascribed to the deformation of GaO_6 octahedra. Finally, the last group of Raman modes above 600 cm^{-1} would represent the stretching and bending of GaO_4 tetrahedra.

A reappraisal of Raman characterisation will be presented in chapter 4. Besides a comparison with previously reported data, some light will be shed on some anomaly in the relationship between Raman intensity and crystal orientation, which we noticed in previous works. As a final point, tensor elements of A_g modes will be determined, comparing traditional procedures to those proposed in very recent works by Kranert *et al.*[70,71].

1.1.5 Electrical properties

Conductivity and doping

Intrinsically, gallium oxide is an insulating material, due to its wide bandgap. It is however well-known to display *n*-type conductivity even when it is not intentionally doped.

This *n*-type semiconducting behaviour has for a long time been ascribed to the presence of oxygen vacancies, which could be easily ionised and form active donors. Authors were led to this interpretation by recognising the strong correlation between high conductivity β-Ga_2O_3 and the oxygen partial pressure in the growth environment. For instance, controllable values in the range 10^{-9}–38 $\Omega^{-1}cm^{-1}$ were obtained during floating zone process by decreasing the oxygen content in the growth atmosphere[18]. An analogous trend was observed in Czochralski growth under CO_2 atmosphere, whose partial pressure was used to control the conductivity of the grown material[52]. Once again, the latter decreased when CO_2 partial pressure was increased, while the colour of the ingots deviated from blue, associated with free carrier absorption, to transparent.

However, recent theoretical investigations on different types of impurities in β-Ga_2O_3 indicate that oxygen vacancies should actually have an activation energy which is too high to significantly affect the carrier concentration, thus acting as deep donors and not contributing to electrical conductivity[20,72]. Indeed, some authors ascribe the *n*-type behaviour of unintentionally doped β-Ga_2O_3 to the presence of hydrogen[20]. Moreover, it was recently demonstrated that commercially available Ga_2O_3 powders can be effectively considered as Si-doped[19]. This would be an additional possible cause of the often observed high electrical conductivity, thus further proving that oxygen vacancies would have no sizeable effect on the phenomenon.

As for electron mobility μ_e , it is usually reported to fluctuate around 100 cm^2/Vs at room temperature, with a decreasing trend when free carrier concentration increases. Within $n = 10^{15}$–10^{16} cm^{-3}, which is the typical range used for the drift layer of vertical power devices, a value of $\mu_e \sim 300$ cm^2/Vs was extrapolated[73].

Doping is one of the most effective solutions to control free carrier concentration and electrical conductivity of β-Ga_2O_3 crystals. Group IV elements can act as substitutional dopants for gallium sites, with Si and Ge preferring the tetrahedral coordination of Ga(I) while Sn shows higher affinity for octahedral Ga(II) sites. On the other hand, oxygen can be substituted by group VII elements such as Cl and F, both replacing O(I). Tin doping during melt growth gives low incorporation efficiency

due to evaporation of Sn, however the incorporated impurity atoms still grant highly conductive crystals and provide high concentration ($n \sim 10^{18}$ cm^{-3}) of free electrons[18,74].

The incorporation of Si impurities is more readily achieved when growth is performed from the melt. In fact, despite the accommodation of Ge and Sn in Ga sites being more straightforward with respect to Si, due to the smaller relative difference in ionic radii $\Delta R/R_{Ga}$ (+16% and -14% versus -40%, respectively), silicon tends to remain in the melt during growth. High free electron concentrations can be reached with this type of doping impurity, with n in the range 10^{16}–10^{18} cm^{-3}[19]. At low doping levels, almost all incorporated Si is electrically active. At higher impurity concentrations, the fraction of electrically active silicon may decrease down to 5%. Silicon impurities can be also introduced by ion implantation, allowing for further increase of the free carrier concentration up to 10^{19} cm^{-3}[33].

Semi-insulating crystals can be obtained by magnesium doping, which acts as a very efficient compensating acceptor and allows to achieve resistivities down to $6 \cdot 10^{11}$ Ωcm[64]. In Czochralski growth, Mg was also found to stabilise the process and reduce probability of spiral formation[52], while if added as dopant during β-Ga_2O_3 thin-films deposition it can apparently change the final bandgap[75].

On the other hand, evidence of unambiguous *p*-type conduction in β-Ga_2O_3 has not yet been reported. Based on I-V measurements solely, Liu *et al.*[76] claimed *p*-type conductivity in nitrogen-doped β-Ga_2O_3 nanowires, but no further analysis was performed. In this regard, Zhang *et al.*[55] proposed a theoretical model in which nitrogen was revealed as a shallow acceptor impurity. *P*-type conductivity was again reported by Tomm *et al.*[77], as a result of introduction of low amounts of Ge or Ti dopants during melt growth of β-Ga_2O_3. However, hole concentration was far too low to allow any practical application. Another recent theoretical study by Varley *et al.*[63] seems to discourage the possibility of hole conduction in this material, due to strong self-localisation and, consequently, very low mobility values. Thus, even if holes were introduced in the system, no significant *p*-type conductivity would be observed.

Properties related to power-electronics

Some of β-Ga_2O_3 electrical properties have made it a cutting-edge material for power electronics applications. The critical field necessary to produce avalanche carrier multiplication, hence leading to material breakdown, is usually referred to as E_b and can be directly derived by the bandgap E_g using the empirical relationship[27]

$$E_b = 1.73 \cdot 10^5 \left(E_g\right)^{2.5} \tag{1.3}$$

For β-Ga_2O_3 this value has been estimated to exceed 8 MV/cm, which is about three times larger than those of direct competitors, namely SiC and GaN. The potential of a material to minimise conduction losses in power devices is expressed by its Baliga's Figure of Merit (BFOM), which depends on E_b itself, on the relative dielectric constant ϵ and on the mobility μ:

$$BFOM \propto \epsilon \mu E_b^3 \quad (1.4)$$

β-Ga_2O_3 has a BFOM of 3444, calculated under direct current and low frequency regimes, second only to diamond and at least four time larger than those of SiC and GaN. However, the lower thermal conductivity might be a drawback in terms of power devices applications. This factor is still under investigation. The main power electronics-related properties of β-Ga_2O_3 are summarised in Table 1.4 and compared to those of other common semiconductors and wide bandgap materials.

Table 1.4: Properties of β-Ga_2O_3 compared to common semiconductors and wide-bandgap materials[26].

	Si	GaAs	4H-SiC	GaN	Diamond	β-Ga_2O_3
E_g (eV)	1.1	1.4	3.3	3.4	5.5	4.7–4.9
μ (cm^2/Vs)	1400	8000	1000	1200	2000	300
E_b (MV/cm)	0.3	0.4	2.5	3.3	10	8
ϵ	11.8	12.9	9.7	9.0	5.5	10
BFOM	1	15	340	870	24664	3444
Thermal conductivity (W/cmK)	1.5	0.55	2.7	2.1	10	0.23 [010] 0.13 [100]

Metal contacts to β-Ga_2O_3

Metal contacts are essential both to investigate fundamental properties and to build electronic devices. Even though many methods have been proposed to deposit Ohmic electrodes on β-Ga_2O_3, different outcomes have been achieved and the results were hardly reproducible. This can be most likely ascribed to the strong dependence of contacts quality on surface properties, which are in turn strictly related to how the material surface is processed.

The most common element employed to obtain Ohmic contacts to β-Ga_2O_3 is titanium. Usually, a bilayer structure Au/Ti or Al/Ti is directly deposited on the β-Ga_2O_3 surface, with a thicker layer of a passivating metal to protect the actual contact (~ 50 nm) from oxidation[51,78–82]. Víllora *et al.*[51] further claimed the as-deposited electrodes show good Ohmic behaviour, without any need for thermal treatment and independently of the additional metal deposited on Ti. Annealing of Au/Ti electrodes in O_2 was actually seen to shift the contact behaviour from Ohmic- to Schottky-type in thin films[83]. This could be ascribed to accumulation of negatively charged defects at the surface, either Ga vacancies or interstitial or adsorbed oxygen, causing upward band-bending and failure to make Ohmic contacts[72]. On the contrary, 10 minutes thermal annealing of Al/Ti electrodes in nitrogen atmosphere at 500 °C were reported to be beneficial for obtaining low contact resistance and linear I-V characteristics on PLD thin-films[80,81], as it was also previously suggested by Suzuki *et al.*[82] for single crystal substrates.

Higashiwaki *et al.*[28] reported a significant reduction of Au/Ti contact resistance to β-Ga_2O_3 by a preliminary Reactive Ion Etching (RIE) surface treatment, using a gas mixture of BCl_3 and Ar for 1 min (Figure 1.10a). Sasaki *et al.*[33] were able to achieve a further improvement of this Ohmic behaviour by Si^+ ion implantation. An activation efficiency above 60% was obtained after annealing at 950 °C, which is a much lower temperature than those necessary for the electrical activation of the ion-implanted dopants in SiC (1400–1700 °C) and GaN (1100–1350 °C). Then, Au/Ti electrodes were evaporated and further annealed at 450 °C for 1min in a nitrogen gas atmosphere, leading to the characteristics shown in Figure 1.10b.

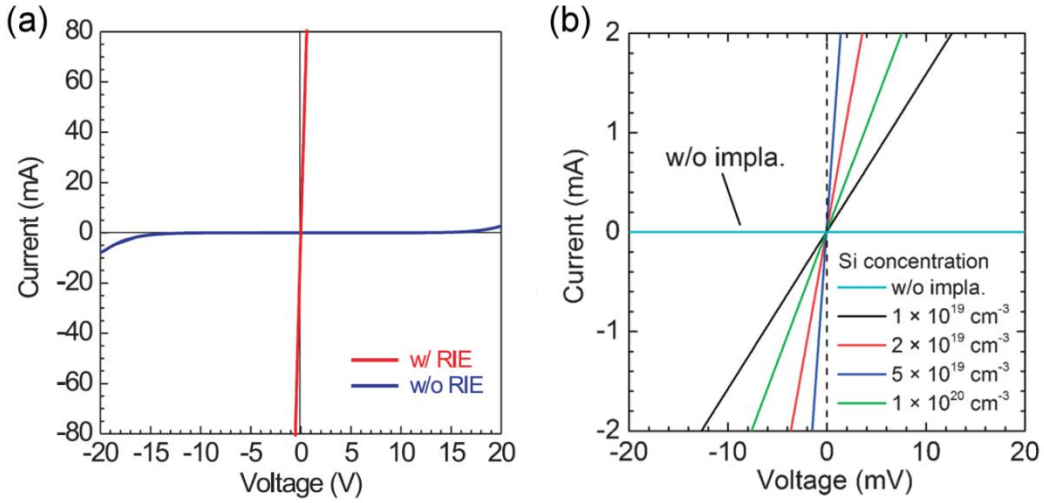

Figure 1.10: (a): Comparison between I-V characteristics of Au/Ti Ohmic contacts to β-Ga_2O_3 with and without RIE treatment[28]. (b): Comparison between IV characteristics of Au/Ti Ohmic contacts before and after Si+ implantation at different concentrations[33].

Despite the latter being the most effective way to obtain Ohmic contacts to β-Ga_2O_3 until now, simpler and less time consuming procedures have also been proposed, such as alloying of metallic indium[84], surface painting with Ga-In eutectic[85], or alloying Sn using a capacitor discharge, which prevents sample heating[21,85].

1.2 Growth of β-Ga_2O_3

1.2.1 Bulk crystals

High quality, bulk β-Ga_2O_3 single crystals can be effectively grown from the melt. Generally speaking, melt growth outperforms other techniques in terms of crystal quality, growth rate and scalability for mass production. However, when applied to gallium oxide there are some critical issues that need to be accounted for. Even if β-Ga_2O_3 has a congruent melting point at 1800 °C, thermal decomposition can occur already above 1200 °C if heating is performed under oxygen-deficient atmosphere[13]. Moreover, evaporation of the melt causes undesired mass transport and can

compromise the growth quality. It is thus crucial to operate in oxidising environment[86]. The choice of a suitable crucible is also a limiting factor, since the latter must withstand high process temperatures, an oxidising ambient and eventually corrosion by metallic gallium. To this purpose, iridium is commonly employed, sapphire crucibles have been reported, as well[87].

One of the first approaches to β-Ga_2O_3 melt growth was the crucible-free Verneuil technique[65,88,89], recently followed by more flexible processes, such as floating zone[18,74,77,90–92], Czochralski[13,21,52,86] and Edge-defined Film-fed Growth (EFG)[12,45,93]. Nowadays, only Czochralski and EFG pulling are actually applied to growth of scientific as well as commercial β-Ga_2O_3 single crystals.

Czochralski process consists in dipping a rotating crystal seed in a melt contained in a crucible. While slowly pulling the seed upwards, crystal growth proceeds at the solid-liquid interface as a cylindrical ingot is formed. High-quality, large diameter single crystals can be obtained with high growth rates using this technique. Ga_2O_3 growth by Czochralski method is typically performed in indium crucibles, under oxidising pressure to avoid decomposition[13,86]. The process remains stable when low free carrier concentrations are maintained in the solid. For $n > 10^{18}$ cm^{-3}, absorption in the near-IR occurs, destabilising radiative heat transfer at the interface, which in turn tends to become concave and induces spiral formation[52]. Advancement in crystal growth technology allowed to increase the size of ingots from 10 mm diameter by 20 mm in 2000[86] to 50 mm diameter by 75 mm in 2014[52].

EFG is a recently developed variant of pulling methods which grants accurate control of the final ingot shape, from ribbon-like wafers to more complex geometries, by means of an appropriate die (see Figure 1.11). This allows to drastically reduce post-growth machining and manufactory costs. For Ga_2O_3, EFG was first demonstrated by Shimamura *et al.* in 2006[93]. In 2008, high quality EFG crystals grown at 10 mm/h were already reported[12], with rocking curves exhibiting 70–160 arcsec FWHM and etch pit density of about 10^5 cm^2. Industrial production of β-Ga_2O_3 wafers was recently started by Tamura Corporation (Japan), with 2 inch diameter substrates already available and 4–6 inch wafers under development[45].

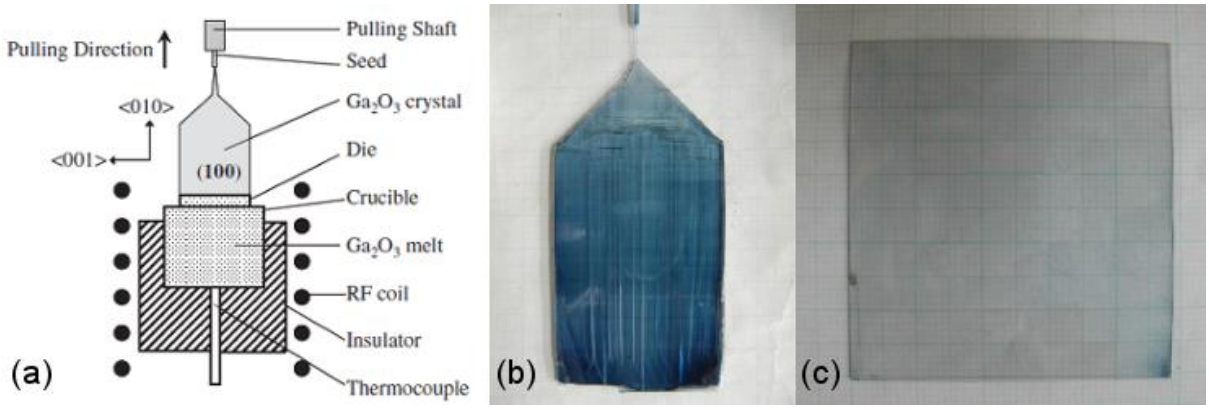

Figure 1.11: EFG of β-Ga_2O_3 as reported by Aida *et al.*[12]; (a): experimental setup, (b): as-grown single-crystalline ribbon (50×70×3 mm^3) and (c): polished wafer (48×50×0.5 mm^3).

1.2.2 Thin films and nanostructured materials

β-Ga_2O_3 films deposition was achieved using a variety of techniques and on different templates. Homoepitaxy provides films with superior quality[14,15,26] but is relatively unexploited, primarily because of the still expensive β-Ga_2O_3 substrates. Therefore, most of the research activities on β-Ga_2O_3 films are still based on heterosubstrates. Among these, α-Al_2O_3 (sapphire) is by far the most common[78,94–97], because of its abundance, high quality, large wafer size, and low cost. Despite its hexagonal crystal structure being substantially different from the monoclinic lattice of β-Ga_2O_3, the latter grows almost heteroepitaxially, by accommodating the (-201) lattice plane onto (0001) oriented sapphire. This stacking can take place in six possible equivalent orientations, giving rise to planar domains rotated by 60°[94,98,99]. The latter are currently the most limiting factor for fabricating high performance thin-film devices. An interesting recent study by Schewski *et al.*[96] further suggested that, independently from the employed technique, (-201) β-Ga_2O_3 grows plastically relaxed on 3 monolayers of pseudomorphic α-Ga_2O_3. This proved to be the case of MOCVD-, PLD- and MBE-grown layers. Aside from sapphire, other explored substrate choices that can be found in literature are SiC[24], GaAs[100], $MgAl_2O_4$[101], MgO[75,102] and yttrium-stabilised zirconia[17].

As for the deposition techniques, basic chemical routes such as spray pyrolysis[103,104] or sol-gel[105–107] have the advantage of requiring simple equipment and low temperature deposition, allowing at the same time for large area coverage and high throughput, but can only produce poly- or nanocrystalline materials.

Physical-chemical vapour transport processes can be developed exploiting the decomposition β-Ga_2O_3 in low-oxygen content or reducing atmosphere: reverse reactions allow to produce gallium oxide crystals. Polycrystalline or amorphous materials were obtained this way, which could be converted to β-Ga_2O_3 only after thermal treatments[108–110]. Sputtering leads to similar results in terms of crystal quality[6,105,111], while layers with higher crystallinity can be deposited by Pulsed Laser Deposition (PLD) of a ceramic target[10,80,112]. In this case, doping can be achieved by adding the desired impurity to the target itself.

Different variants of chemical vapour deposition (CVD) have been widely employed for the growth of high quality β-Ga_2O_3 layers. Halide Vapour Phase Epitaxy (HVPE) is usually based on the reaction between chloride gallium precursors, such as $GaCl_3$[113] or GaCl[97,114,115], and an oxygen. This technique is well-known for the high deposition rates (up to some hundreds μm/h) and for the high quality of the deposited layers. The latter can be usually ascribed to the lack of carbon contamination in the growth chamber, as well as to the high employed growth temperatures (above 1000 °C). In 2015 Oshima *et al.*[97] reported quasi-heteroepitaxial growth of β-Ga_2O_3 on *c*-sapphire by HVPE. This result was achieved thanks to off-angled substrates, which drastically reduced the formation of planar domains.

Lower growth temperatures are normally employed when using Metal Organic Chemical Vapour Deposition (MOCVD). The latter usually makes use of precursors such as trimethylgallium (TMG)[15,116] or triethylgallium (TEG)[100,117], while water, oxygen or N_2O are common oxidising agents. Despite some authors claimed to have obtained β-Ga_2O_3 films below 700°C[101,118], higher temperatures (~ 800 °C) are often reported to produce better quality layers[15,119,120]. In these works, water is also suggested to act as a more effective oxidising agent than elemental oxygen, leading to smooth film surfaces.

Atomic Layer Deposition (ALD) was also explored as a possible technique to deposit gallium oxide layers[121–125]. By the establishment a self-limiting, saturating surface reactions regime, as it will be dealt with more in detail in chapter 2, ALD allows in principle low-temperature growth and extremely precise control over film thickness, conformity and uniformity. Even though this approach often resulted in a smooth, layer-by-layer growth, the obtained films were always reported to be amorphous and could be crystallised to β-Ga_2O_3 after thermal treatments at high temperature[121,122,125].

Molecular Beam Epitaxy (MBE), is known to produce extremely smooth layers of controlled composition, thus enabling the development of high performance devices. For β-Ga_2O_3, conventional Knudsen cells can be employed to supply both gallium and dopants fluxes, while pure oxygen is inefficient and has to be provided by either radio-frequency (RF) plasma[14,126,127] or ozone[16,28,73] sources. Typical process temperatures range between 600 and 900 °C, while growth rates depend on the technique. Ozone MBE has higher growth rate than its RF plasma counterpart, with a maximum reported value of 0.7 μm/h[73] compared to 132 nm/h[127], but precise control of intentional doping can be more difficult due to high background pressure.

1.3 Applications of β-Ga_2O_3 as wide bandgap semiconductor

A comprehensive overview of gallium oxide employed as sensor, catalyst and luminescent phosphorous can be found within a recent review work by Stepanov *et al.*[44], however it is beyond the purpose of this thesis. Here, only applications of β-Ga_2O_3 as a wide bandgap semiconductor will be rapidly reviewed.

Electronic devices built directly on β-Ga_2O_3 single crystals have already been demonstrated. Schottky Barrier Diodes (SBDs) were obtained by Sasaki *et al.*[128] by depositing Au(250 nm)/Ti(5 nm)/Pt(15 nm) circular contacts on unintentionally-doped (010) substrates. The Pt barrier height at the interface was estimated to be about 1.3–1.5 eV, comparable to those exhibited by SiC and GaN, with a good ideality factor of 1.03–1.04 and a 150 V breakdown voltage. It was stressed that breakdown was not related to intrinsic material properties, but to intensification of the electric field to the cathode electrode edge. As an alternative to Pt, high-performance SBDs based on Au/Ni contacts were more recently developed on EFG grown (-201) single crystals, displaying a nearly perfect ideality factor of 1.01[129].

Field effect transistors are one of the most promising applications for gallium oxide in power electronics. Higashiwaki *et al.*[28] described *n*-channel MESFETs based on 300 nm *n*-type Sn-doped β-Ga_2O_3 MBE layers deposited as channel on (010) Mg-doped semi-insulating crystals grown by the floating zone technique. The final device was fabricated exploiting the ring-geometry, with Au/Ti Ohmic contacts deposited after BCl_3 RIE treatment of the surface and the same Au/Ti/Pt Schottky gates described above (see Figure 1.12a). Off-state breakdown voltage at 30 V was as high as 257 V, causing irreversible burning of the electrodes. Off-state leakage current was 3 mA, with a maximum observed on/off ratio of 10000. Authors claimed these characteristics were comparable if not superior to those exhibited by the first GaN devices in the early 1990's. The same group demonstrated the first high-performance depletion-mode MOSFETs based on gallium oxide[130,131]. With respect to the previously described MESFETs, here Si-ion implantation doping was performed to source and drain electrode regions, in order to obtain low-resistance Ohmic contacts to the Sn-doped *n*-Ga_2O_3 channel[130]. The device surface was passivated by means of an Al_2O_3 gate dielectric film formed by ALD and allowed to significantly reduce gate leakage, as shown in Figure 1.12b. Even with this simple structure, effective gate modulation of the drain current was observed, with stable operation sustained up to 250 °C. The device showed extremely low off-state drain leakage of less than a few pA/mm, leading to a high drain current on/off ratio of over ten orders of magnitude. A three-terminal off-state breakdown voltage (V_b) of 370 V was observed. Substantial enhancement in V_b up to 755 V was later achieved with a gate-connected field plate[131]. The device structure, shown in Figure 1.12c, was here more complex. Effective surface passivation and high Ga_2O_3 material quality contributed to the absence of drain current collapse. In addition to the increased V_b, high on/off current ratios up to nine orders of magnitude and normal operation at 300 °C were achieved.

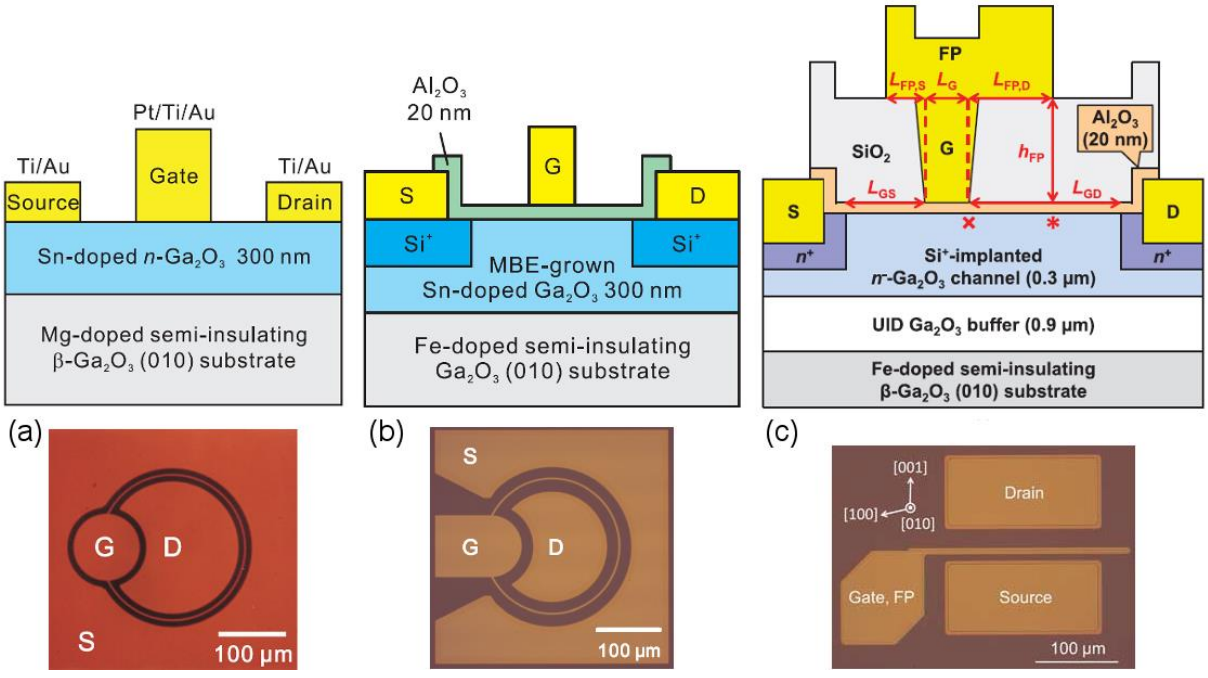

Figure 1.12: Different types of FETs based on β-Ga_2O_3. (a): MESFET[28]; (b): depletion-mode MOSFET[130]; (c): depletion-mode MOSFET with gate-connected field plate[131].

β-Ga_2O_3 can be also conveniently used as substrate for GaN heteroepitaxy and thus for developing GaN-based electronic and optoelectronic devices. Since native GaN substrates remain expensive and difficult to produce, the majority of GaN devices has been so far grown on foreign substrates, with various issues to confront with[44]. Sapphire is the most established, however its insulating nature prevents the fabrication of vertical devices. SiC is conductive, but still rather costly, and it displays high blue optical absorption. Silicon has even more drawbacks, due its opaqueness, large lattice mismatch and chemical reactivity. In this regard, β-Ga_2O_3 is a most suitable candidate, as it combines (semi)conductivity, full optical transparency up to UV and availability of high quality bulk crystals. Growth of GaN epilayers on β-Ga_2O_3 has been demonstrated by MOCVD[22,132], HVPE[133,134] and MBE[23,135,136], resulting in the fabrication of blue[22] and green[132] LEDs with high output intensity. While early works focused on the growth on (100)-oriented substrates, the process was hindered by the cleavage nature of (100) planes, which can cause striping of both substrates and epilayers. As a possible alternative, (-201) substrates were recently tested[137], and the first reported high-brightness InGaN blue LEDs were indeed grown on (-201) β-Ga_2O_3[138].

Deep-UV, solar-blind photodetectors based on β-Ga_2O_3 were demonstrated in different geometries, such as vertical Schottky diodes[79,82], interdigitated metal-semiconductor-metal structures[25] and heterojunctions[24]. These devices displayed a strong sensitivity to the solar-blind region, with response times of the order of milliseconds[24] and high responsivities up to 10^3 A/W[82] in the best cases.

1.4 Metastable phases

The first comprehensive report about reproducible chemical processes to obtain metastable Ga_2O_3 polymorphs was the pioneering work of Roy *et al.* in 1952[39]. Even if α and γ forms were to some extent already known, this was the first time that δ- and ε-Ga_2O_3 could be identified. These chemical routes produced materials with poor crystalline quality, often contaminated by β-Ga_2O_3 and difficult to characterise; however, they represented a landmark for most of the following research.

Recently, Playford *et al.*[35] revisited Roy experiments as well as some intermediate work. They managed to solve for the first time, by Total Neutron Diffraction, all the obtained polymorphs structures, adding κ-Ga_2O_3 to the picture. As it will be shown in the following, however, these results do not always match other experimental findings and they seem to be partially in contrast with first principle calculations.

Only by studying single-phase, highly crystalline materials it will be possible to shed some light on the properties of these polymorphs. This has been happening already during these very last years, with the development of dedicated thin-film deposition techniques.

1.4.1 α-Ga_2O_3

α-Ga_2O_3 was first reported by Zachariasen in 1928[139] and was the first metastable polymorph to be unambiguously characterised from a structural point of view[36]. Its symmetry is rhombohedral, belonging to $R\bar{3}c$ space group, which is the classic corundum structure analogous to α-Al_2O_3. The crystallographic cell consists of six Ga_2O_3 formula units (Figure 1.13a). It has two independent lattice parameters, *a* and *c*, and two internal coordinate variables z_{Ga} and x_O . The structure can be modelled as a hexagonal close-packing of oxygen ions, where the gallium ions occupy two-thirds of the octahedral sites. Each Ga octahedron, moderately distorted, shares one face and three edges with three other octahedra.

This polymorph can be synthesised by heating GaO(OH) in air between 450 °C and 550 °C, while it converts to beta upon annealing at 650 °C, at atmospheric pressure[35,39]. Vice versa, under pressure it is beta that converts to alpha, due to the higher density of the latter (6.273 vs 5.757 g/cm^3)[38]. Raman spectroscopy was recently employed to study the β-to-α transition of crystalline Ga_2O_3 powder under pressure. All seven Raman active modes predicted by group theory ($\Gamma_{Raman} = 2A_{1g} + 5E_g$) were observed (Table 1.5).

Table 1.5: Calculated and experimental wavenumbers (cm^{-1}) of α-Ga_2O_3 Raman modes. (From Machon *et al.*[67])

Mode	Wavenumber (calculated)	Wavenumber (experimental)
A_{1g}	215	217.4
E_g	239	240.8
E_g	281	286.1
E_g	344	328.7
E_g	410	432.2
A_{1g}	551	573
E_g	680	688.1

Theoretical modelling, besides confirming the experimental crystal structure, allowed to investigate some additional physical properties[38]. Regarding the electronic structure, a wide indirect bandgap of 5.03 eV and a relatively low effective mass of 0.276 m_0 were obtained. Moreover, due to the superior symmetry, its electronic band structure displays a high level of VB-degeneracy, as it can be evinced from Figure 1.13b.

As for optical properties, dielectric constant values of 3.07 in the basal plane and of 2.97 along the ***c***-axis were extrapolated from the calculated dielectric function. Despite this anisotropy being even more pronounced than in the case of β-Ga_2O_3, no anisotropy in the optical absorption edge was observed. As a final point, first principle calculations suggest α-Ga_2O_3 to have higher bulk modulus, Debye temperature, refractive index and reflectance with respect to β-Ga_2O_3.

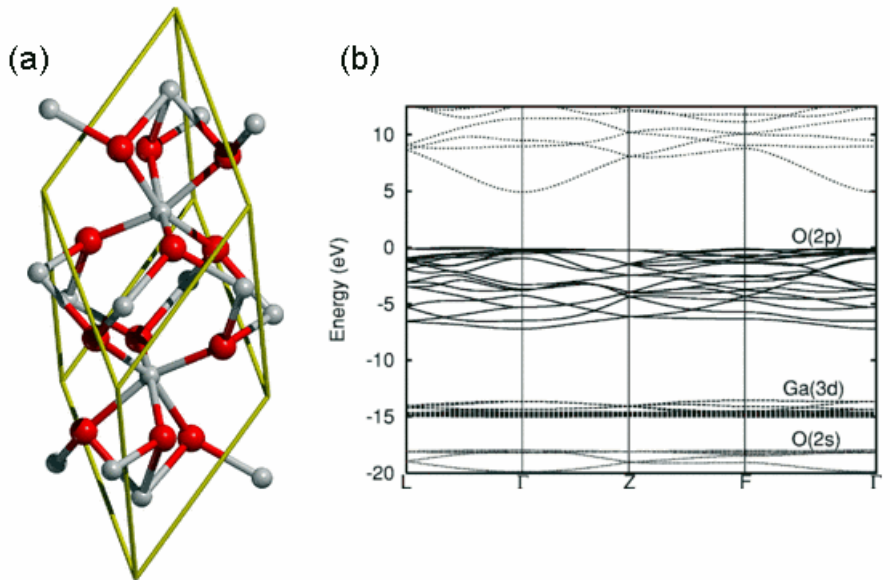

Figure 1.13: Unit cell (a) and calculated band structure (b) of α-Ga_2O_3. The ***k*** points are at Γ= (000), L= (0 ½ 0), Z = (½ ½ ½), F = (½ ½ 0). (From He *et al.*[38])

α-Ga_2O_3 was recently obtained in the form of thin films at relatively low growth temperatures by means of vapour phase techniques. Ultrasonic Mist CVD at 430–470 °C on *c*-oriented sapphire resulted in nearly single-crystalline α phase with an optical bandgap of 5.3 eV. Furthermore, high quality layers were deposited by Halide Vapour Phase Epitaxy (HVPE) at 550 °C, again on (0001) sapphire. Single crystalline, twin-free α-Ga_2O_3 was obtained with this process, while the bandgap value was comparable (5.16 eV).

1.4.2 γ-Ga_2O_3

The only certain cubic phase of gallium oxide, γ-Ga_2O_3, was first reported by Böhm in 1940[140]. The space group has been identified as $Fd\bar{3}m$, with a measured density of 5.7607 g/cm^3, structurally related to defected spinels[35]. Even if cubic symmetry and the space group are well established, the same does not hold for the effective local structure. First principle studies led to 14 inequivalent solutions, with no clear preference for gallium site occupancies, thus suggesting a structure based on a disordered distribution of gallium vacancies[34].

This phase can be synthesised from calcination at 500 °C of the precipitation product of a solution of $Ga(NO_3)_3 \cdot 9H_2O$ (gallium nitrate hydrate) in ethanol. However, Playford *et al.*[35] proved solvothermal reaction of metallic gallium at 240 °C in 2-aminoethanol to be the most effective process to obtain crystalline γ-Ga_2O_3 powders.

Because of their high surface area, mesoporous γ-Ga_2O_3 xerogels are of particular interest for potential applications in heterogeneous catalysis[141]. This is possible thanks to the presence in the structure of tetrahedral Ga sites, which act as Lewis acid sites when exposed at the surface, thus

determining the reactivity of the surface itself[4]. The same holds for β-Ga_2O_3, but not for example in the case of α and δ polymorphs, which only contain octahedral sites.

γ-Ga_2O_3 thin films were obtained by pulsed laser deposition on (0001) sapphire, with a substrate temperature of 500 °C and an oxygen pressure of 0.05 Pa inside the chamber[142]. No secondary phase was observed, and the layers displayed ferromagnetism up to 350 K. The authors found that doping with Mn (up to 7%) was essential to stabilise the γ phase, while undoped films crystallised into β-Ga_2O_3. In a later work, they also recognised the role of Mn doping in improving the crystallinity of the γ phase films when grown on (100) $MgAl_2O_4$ substrates[143]. On the other hand, almost pure, single-crystalline γ-Ga_2O_3 was obtained for the first time with no need of chemical doping by Mist CVD at 390°C on (100) $MgAl_2O_4$. This allowed the authors to investigate some of its intrinsic optical properties. The refractive index in the visible region was estimated to be within 2.0 and 2.1, whereas the optical bandgap was evaluated to be 5.0 eV and 4.4 eV for direct and indirect transitions, respectively.

1.4.3 δ-Ga_2O_3

δ-Ga_2O_3 was one of the two phases discovered by Roy *et al.*[39] and was synthesised by thermal decomposition of $Ga(NO_3)_3 \cdot 9H_2O$. It was assigned to $Ia\bar{3}$ space group, showing a bixbyite structure similar to other sesquioxides, such as Mn_2O_3 and In_2O_3. The structural backbone can be described by hexagonal close-packed oxygen layers, solely filled by octahedral metal sites. First principle calculation were made on this phase and resulted in smaller lattice parameters (see Table 1.1), Roy's data being probably influenced by the presence of residual water molecules[34]. Nevertheless, no full crystallographic model was ever proposed, due to synthesis issues in absence of stabilising elements. Lately, Playford *et al.*[35] reported that this polymorph could be just a nanocrystalline form of ε mixed with β, and ascribed the previous misinterpretation of the structure to incorrect peak indexing in Roy's work.

δ-Ga_2O_3 being an actual self-standing phase is still matter of debate. However, very recent experimental studies about its spectroscopic properties and chemical reactivity actually suggest this "phase" to be just a mixture of ε- and β-Ga_2O_3[144]. In fact, steam reforming experiments do not show high CO_2 selectivity, which is characteristic of bixbyite-type basic oxides like In_2O_3. On the contrary, the catalytic profile is very similar to ε-Ga_2O_3. As a further proof, all Raman modes observed for δ-Ga_2O_3 (broad features at 245, 530, 635, 718, and 808 cm^{-1}),can be also found for ε-Ga_2O_3, as displayed by the inset plot of Figure 1.14.

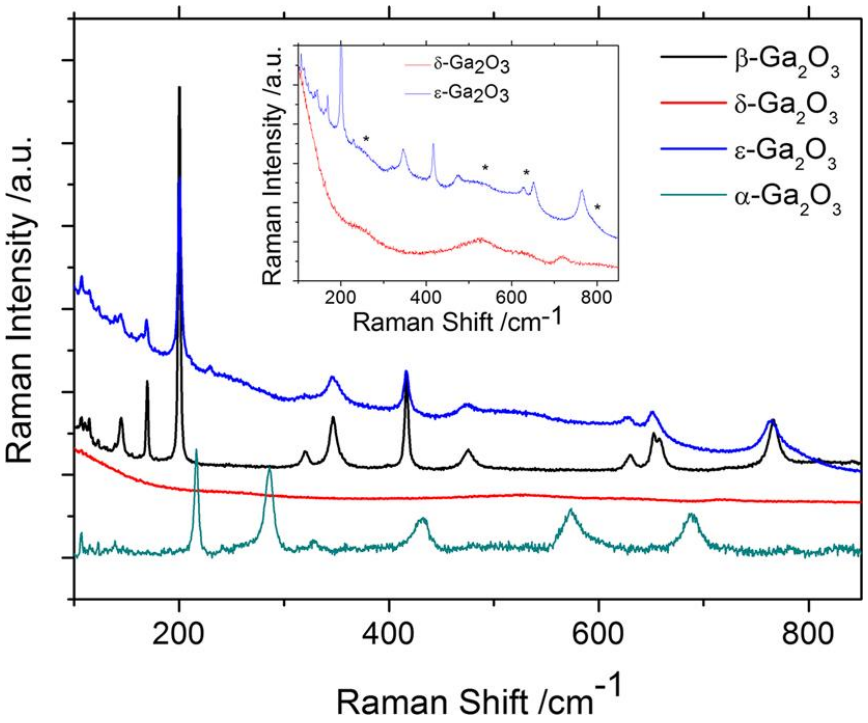

Figure 1.14: Raman spectra of different Ga_2O_3 polymorphs (from Penner *et al.*[144]). A magnified comparison between δ and ε phases is shown in the inset. All the broad bands characterising the alleged "δ-Ga_2O_3" spectra seem to be in common with ε-Ga_2O_3 (see asterisks). The latter additionally shows intense peaks due to β contamination.

1.4.4 ε- and κ-Ga_2O_3

ε-Ga_2O_3 has been recognised as the most stable phase of gallium oxide after β-Ga_2O_3, and maintains this behaviour in a wide temperature range (see Figure 1.2). Even so, its actual structure remains unclear and it is still object of vibrant debate.

It was first synthesised in 1952 by Roy *et al.*[39], by further heating of δ-Ga_2O_3 above 500 °C. Even though the authors managed to identify the new phase, they were not able to solve its crystal structure and they tentatively assigned it to the orthorhombic system. In 2012, revisiting Roy's experience and despite a remarkable β-contamination of their samples, Playford *et al.*[35] first solved the crystal structure of ε-Ga_2O_3 experimentally, within the hexagonal $P6_3mc$ space group. The lattice is made of a hexagonal close-packed array of oxygen ions, with gallium partially occupying both octahedral and tetrahedral sites, analogous to a disordered variant of ε-Fe_2O_3 previously reported by Tronc *et al.*[145]. The measured density for this structure was 6.4299 g/cm^3. According to the authors, structural misinterpretation could be due to similarity between diffraction data of hexagonal ε/β mixed phase and a supposed orthorhombic ε. This similarity would be however only superficial and orthorhombic symmetry would not explain all the observed features.

These results however collide with previous first principle calculations by Yoshioka *et al.*[34] (see Table 1.1). Based on Roy's report, orthorhombic $Pna2_1$ space group was in fact theoretically predicted for the ε phase, similar to κ-Al_2O_3 and with a theoretical density of 5.88 g/cm^3. To further

support their findings, the authors here referred to a recent experimental work[112], in which an unknown polymorph of gallium oxide was grown by PLD on *c*-sapphire at 550 °C and 1 mPa. The latter was assigned to orthorhombic $Pna2_1$ space group by XRD measurements, with lattice parameters a = 5.04, b = 8.73, and c = 9.26 Å. Interestingly, from further XRD analysis it appeared that the unit cell might have higher symmetry than orthorhombic. It is also worth stressing that these high quality PLD films were apparently stabilised by Sn doping, while the supposed "ε phase" was not observed in nominally-undoped Ga_2O_3 films deposited on the same substrates[146]. Nonetheless, the quality of the deposited layers was sufficiently high to allow for fabrication of top gate FETs, using the films as *n*-channel layers. Field-induced current modulation was successfully observed, as shown in Figure 1.15.

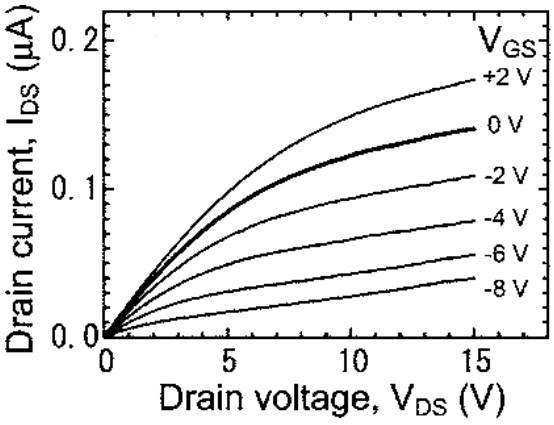

Figure 1.15: Output characteristics of a FET having an epitaxial Sn-doped Ga_2O_3 film as channel layer. Measurements were performed at room temperature. (From Matsuzaki *et al.*[112])

More recent first principle calculations by Maccioni *et al.*[31] also concluded that ε-Ga_2O_3 is orthorhombic and, in addition, that it should present pyroelectric character. A spontaneous polarisation value of 0.23 C/m^2 was estimated, similar to BaTiO, three times larger than AlN and ten times larger than GaN. Piezoelectric coefficients were also sizeable, but one order of magnitude smaller than in standard ferroelectrics like PZT. Moreover, the authors claim that the $P6_3mc$ solution proposed by Playford *et al.*[35] would still exhibit a similar spontaneous polarisation, due to the polar character of that space group. Orthorhombic $Pna2_1$ and hexagonal $P6_3mc$ structures can be actually transformed into one another by local distortions, and thus may be competing energy minima, close to each other. $Pna2_1$ is in fact a subgroup of $P6_3mc$, and a polar-axis view of the Ga sites in the orthorhombic structure clearly shows a distorted hexagonal pattern. In chapter 3 we will propose a solution to these ambiguities in crystal structure determination of ε-Ga_2O_3 and demonstrate that this phase is not only pyroelectric, but ferroelectric.

Practically no physical characterisation has been carried out on ε-Ga_2O_3 before this thesis. Raman spectra were measured on powder-like, β-contaminated samples prepared following a variation of Playford's approach (see once more Figure 1.14), while the study of surface reactivity evidenced the presence of strong acidic surface sites[144]. Furthermore, emission properties were observed by

cathodoluminescence (CL) on crystalline ε-Ga_2O_3 nanorods, obtained after 600°C calcination of α-GaOOH nanorods[147]. Interactions with the electron beam produced broad emission bands ranging from 350 to 780 nm, with the peak maximum at about 520 nm and a shoulder at 460 nm. This CL emission was suggested to originate from the recombination of an electron on a donor formed by oxygen vacancies and a hole on an acceptor formed by gallium vacancies.

During the last few years, the first experimental works on thin-films deposition were reported, paving the way to solid fundamental characterisation, as well as to technological applications. In 2015 Oshima *et al.*[32] obtained the first phase-pure films to be expressly defined as "ε phase". Growth was performed by HVPE at atmospheric pressure and 550 °C, using gallium chloride and ozone as precursors. *c*-AlN and *c*-GaN were successfully employed as substrates, due to the favourable lattice spacing and good matching with the same $P6_3mc$ space group. Very surprisingly, the best results were obtained when growth was performed "heteroepitaxially" on (-201) β-Ga_2O_3. The authors suggested a prominent role of the chosen substrate in order to stabilise the desired phase, followed by the growth temperature. The high quality of the films allowed to determine the optical bandgap of ε-Ga_2O_3 for the first time, which resulted to be 4.9 eV (Figure 1.16), hence comparable to that of β-Ga_2O_3. Films also showed high thermal stability up to around 700 °C.

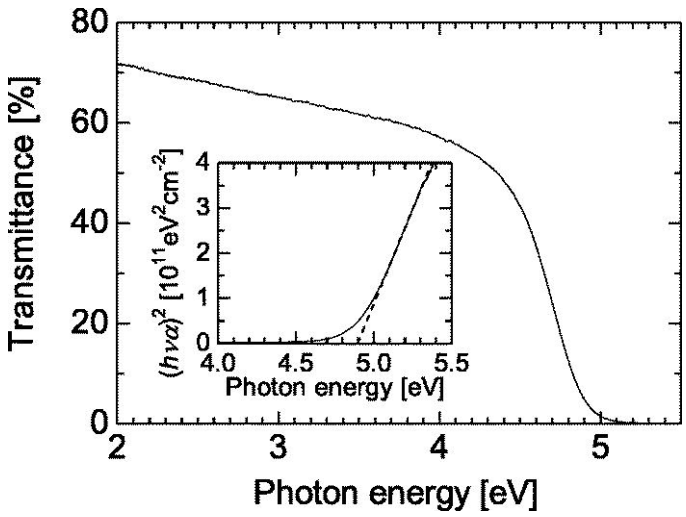

Figure 1.16: Transmittance spectrum of an ε-Ga_2O_3 thin film. Inset: Tauc plot and gap extrapolation. (From Oshima *et al.*[32])

Besides the work of Oshima *et al.*[32], there are only two more papers on deposition of crystalline ε-Ga_2O_3 thin films: one relevant to the MOCVD/ALD growth on *c*-sapphire performed during the framework of this thesis[148], which will be extensively discussed in chapters 2 and 3, and a recent letter dealing with MOCVD on 6H-SiC[149]. In the latter, growth was carried out at 500 °C and 35 mbar, using O_2 and triethylgallium (TEGa) as precursors and Ar as carrier gas. The single-phase, relatively high-quality ε-Ga_2O_3 layers remained stable up to 800 °C. This results, together with the thermal treatments performed by Oshima *et al.*[32], corroborates the theoretical prediction that once epitaxially stabilised this phase does not transform back to beta, due to symmetry reasons[31].

As mentioned in the introductory section of this thesis, the interest for this phase lies not only in its unexplored fundamental properties, but also in the possible technological applications. The measured value of the bandgap, though still not supported by band structure modelling, is comparable to β-Ga_2O_3, hence very promising for the fields of UV optolelectronics and power electronics. In this regard, moreover, the first ε-Ga_2O_3 layers proved to be stable at least up to the usual operating temperature of devices. Another intriguing possibility of application in semiconductor industry is given by the favourable matching with nitrides. For instance, Maccioni *et al.*[31] suggested that ε-Ga_2O_3 could be grown epitaxially on GaN and at the same time form a confined, high-concentration electron gas at the interface with the latter, which could be exploited for fabrication of HEMTs.

κ-Ga_2O_3

Playford *et al.*[35] also reported the existence of an orthorhombic phase of gallium oxide, separated however from ε-Ga_2O_3. It was recognised as a transient polymorph, analogous to κ-Al_2O_3 and thus referred to as κ-Ga_2O_3, which formed during the thermal decomposition process of $Ga_5O_7(OH)$ (gallium oxyhydroxide) to β-Ga_2O_3 and could not be isolated by the authors. Even if they described the two phases separately, they also acknowledged a strict analogy between ε and κ structures, as shown in Figure 1.17. Furthermore, space group and lattice parameters of this so-called κ phase were very close to those found by other authors for orthorhombic ε-Ga_2O_3 (see Table 1.1).

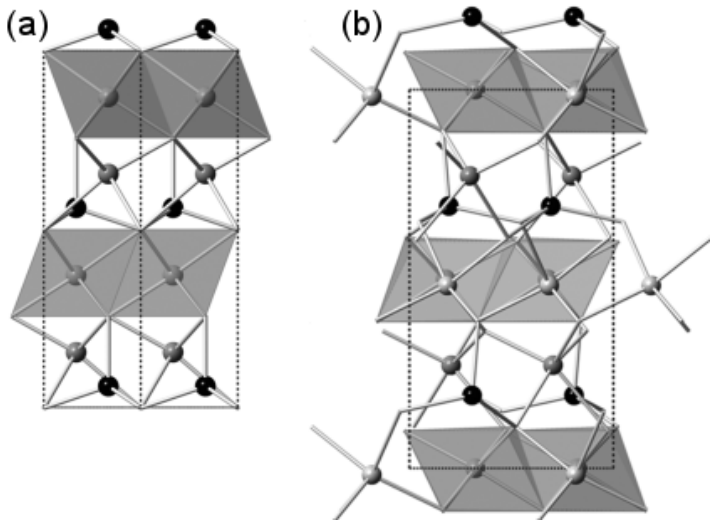

Figure 1.17: Comparison and affinity between the crystal structures of (a): ε-Ga_2O_3 and (b): the supposed transient polymorph κ-Ga_2O_3 (from Playford *et al.*[35]). Note that, in the case of the ε phase, Ga sites are only partially occupied.

The literature state of art hence leaves some crucial questions open. Are ε and κ two different phases, indeed? Is ε-Ga_2O_3 hexagonal or orthorhombic? In the following, we will provide new sound arguments about the actual crystallographic nature of ε-Ga_2O_3 thin films (see chapter 3).

CHAPTER 2 - Deposition of ε- and β-Ga_2O_3 epitaxial layers

In this chapter, the deposition techniques employed in the framework of this thesis will be described. An overview of the three growth methods, namely CVD, ALD and PLD, will be followed by the actual experimental section and by an overview of the deposited layers.

Epitaxial growth of reproducible, high quality ε-Ga_2O_3 thin films by MOCVD and ALD, together with the relative characterisation that will be extensively discussed in the next chapter, represented the core subject of this thesis. Most of the experimental activity was carried out in Parma, both at the Physics Department of the University and at IMEM-CNR Institute, under the supervision of Prof. Roberto Fornari.

PLD β-Ga_2O_3 layers were deposited and studied during the research period at the University of Leipzig. The aim was to increase the conductivity and mobility of heteroepitaxial β-Ga_2O_3 thin-films as a starting point for building *n*-cannel MESFETs. An abrupt increase of the resistivity was in fact observed at very low film thicknesses (< 100 nm), which was ascribed to the high defectivity of the initial layers. A possible way to improve their quality could be through reduction/elimination of the heavier, highly energetic clusters that are ejected from the target, which can in turn damage the film surface and structure. Two variants of the PLD process were studied to this purpose: *eclipse* and *off-axis*. Another explored path towards structural improvement was to use a gallium oxide thin film as seeding layer in standard PLD configuration. The activity was overseen by Prof. Marius Grundmann and Dr. Holger von Wenckstern.

2.1 Fundamentals

2.1.1 Chemical vapour deposition

Chemical vapour deposition (CVD) is a widely interdisciplinary field even in its fundamental principles[150–152], ranging from gas phase reaction chemistry and thermodynamics, to kinetics and fluid-dynamical transport mechanisms, of which only a brief outline will be provided here. It is an extremely versatile process, suitable for the synthesis of coatings, powders and fibres, as well as monolithic components of metals, non-metals and composite materials. It is thus not surprising that typical fields of application encompass semiconductor industry, optical components and protective coatings.

The process involves the deposition of a solid material on the surface of a substrate as the result of a heterogeneous vapour phase chemical reaction, taking place on the surface itself or in its close

vicinity. The resulting material can be obtained in the form of bulk, powder or, in the most common case, thin-film. By varying the experimental conditions (temperature, pressure, composition of the gas phase, etc.) it is possible to finely tune its physical-chemical properties. The involved reactions, which can be activated by heat, plasma or light, represent the step distinguishing CVD from physical vapour approaches.

Several advantages make CVD the most employed vapour phase technique:

- Precise tuning of chemical composition and physical structure, as well as versatility in depositing elementary and compound materials, can be achieved by dynamical control of the gas phase composition.
- Relatively high deposition rates can be achieved, resulting in thick layers and cost-effective processes.
- The not strictly line-of-sight nature of the process produces both uniform deposition and low porosity even on irregular substrates and patterned areas.
- No ultra-high vacuum conditions are usually requested.

However, CVD techniques also exhibit some drawbacks. The high vapour pressure needed for the precursors is often met by hazardous or toxic substances, and shared by many of the by-products. This implies the presence of additional control and waste disposal systems, which further increase the costs of the apparatus. Moreover, most processes require temperatures above 600 °C, which limits the classes of usable substrates. Some common variants, such as Plasma-Enhanced CVD (PECVD) and MOCVD allow to partially overcome this problem, since they can usually operate at lower temperatures either by activating the necessary chemical reaction with a non-thermal source or by employing more reactive precursors, respectively.

Deposition sequence

The elements that will compose the resulting crystalline solid are initially contained in gaseous precursors and supplied to a growth chamber, generally kept at high temperature. The steps determining the deposition sequence can be schematically outlined as follows (Figure 2.1).

- The injection process occurs by means of a carrier gas, which also allows to dilute the reactants to the desired concentration.
- Reactants diffuse through the boundary layer and reach the substrate surface, where they are adsorbed. During this step, homogeneous reactions can take place in the gas phase, through which the elements that form the crystalline solid are made available as pure atomic or molecular species.
- On the surface, the actual deposition reactions take place, mediated by surface diffusion.
- Reaction by-products diffuse back into the gas phase through the boundary layer.

The slowest among these steps is the one determining the overall rate of the process.

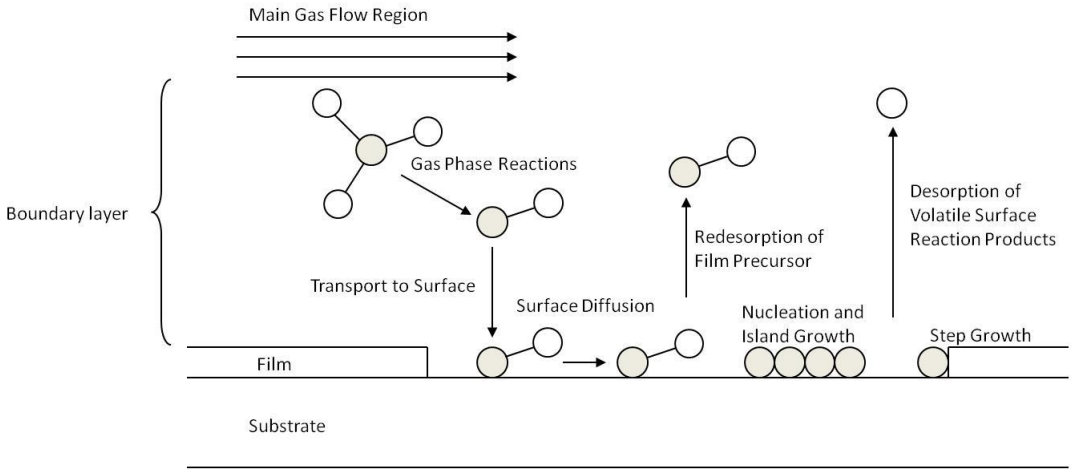

Figure 2.1: Deposition steps determining the CVD process.

Under certain conditions, homogeneous reactions in the gas phase could be also followed by homogeneous nucleation. This outcome is generally undesirable, since the final material quality would be lowered by spurious precipitates or low adherence of the grown layers. Moreover, the high process temperatures could induce solid-state reactions, such as phase transformation, precipitation or recrystallisation. It is important to stress that in most cases the actual reactions taking place inside the growth chamber are not known.

The overall CVD process is controlled by three contributions:

- *Thermodynamics*: it determines the driving force (supersaturation) of the process.
- *Flow dynamics*: it determines the properties of the boundary layer and thus the mass transport associated with the diffusion of species in the gas phase.
- *Kinetics*: it is associated with reaction rates in both gas phase and at gas/solid interface.

Thermodynamics

In order for the desired chemical reactions to take place, it is necessary to fulfil the required thermodynamical conditions. Naming A_i the i-th chemical precursor and B_j the j-th by-product formed during the growth of the material M_{cryst} , the overall fundamental reaction of the CVD process can be expressed as follows[152]:

$$a_1A_1 + a_2A_2 + \cdots + a_nA_n \rightarrow M_{cryst} + b_1B_1 + b_2B_2 + \cdots + b_nB_n \qquad (2.1)$$

where a_i and b_i are the i-th and j-th stoichiometric coefficients of reagents and products, respectively. Even if Eq. 2.1 does not take into account possible intermediate reactions, it can still be used to describe the thermodynamics of the system. In the case of CVD, the process takes place at constant pressure and the equilibrium constant K_P has the well-known form

$$K_P = \frac{\prod_{j=1}^{m}\left(p_{B_j}^{eq}\right)^{b_j}}{\prod_{i=1}^{n}\left(p_{A_i}^{eq}\right)^{a_i}} \qquad (2.2)$$

where $p_{A_i}^{eq}$ and $p_{B_i}^{eq}$ respectively represent the equilibrium partial pressures of reactants and by-products. The equilibrium constant is related to the Gibbs free energy variation for the considered reaction :

$$ln\, K_P = -\frac{\Delta G_r}{RT} \tag{2.3}$$

At constant pressure, the *van't Hoff equation* can be readily derived from the previous one:

$$\left(\frac{\partial\, ln\, K}{\partial T}\right)_P = \frac{\Delta H_r}{RT^2} \tag{2.4}$$

As a first conclusion, it can be observed that here the sign of the reaction enthalpy variation ΔH_r determines the direction of the mass transport. For vapour → solid reactions, the mass transfer takes place from the cooler zone to the hotter one in the case of endothermic reactions ($\Delta H_r > 0$), while the opposite holds for exothermic reactions ($\Delta H_r < 0$). Since the majority of the reactions involved in CVD processes are endothermic, the substrate is generally at higher temperature with respect to the reactor walls, in order to obtain deposition only on the desired zone (*cold-wall* configuration). However, a temperature gradient inside the reaction chamber can cause undesired convection; hence, in some cases it is preferable to heat the whole reactor (*hot-wall* configuration).

A steady crystal growth can be only achieved in non-equilibrium conditions, under the action of a driving force. This can be expressed as difference $\Delta\mu$ between the chemical potential of the nutrient phase (here the vapour) and of the crystal at a given temperature T. For each of the gaseous species the chemical potential $\mu_i(T)$ is given by the expression $\mu_i(T) = \mu_i^0(T) + RT \ln p_i$, where $\mu_i^0(T)$ is the standard value for the pure i-th specie at 1 atm, while the chemical potential of the solid can be approximated to the one at equilibrium:

$$\mu_{vap} = \sum_{i=1}^{n} a_i \mu_i^0 - \sum_{j=1}^{m} b_j \mu_j^0 - RT\, ln\left(\frac{\prod_{j=1}^{m} p_{B_j}^{b_j}}{\prod_{i=1}^{n} p_{A_i}^{a_i}}\right) \tag{2.5}$$

$$\mu_{cryst} = \sum_{i=1}^{n} a_i \mu_i^0 - \sum_{j=1}^{m} b_j \mu_j^0 - RT\, ln\, K_P\,(T) \tag{2.6}$$

from which the expression for the driving force $\Delta\mu = \left(\mu_{vap} - \mu_{cryst}\right)$ of a CVD process is derived:

$$\Delta\mu = RT\, ln\left[\frac{\prod_{i=1}^{n}\left(\frac{p_{A_i}}{p_{A_i}^{eq}}\right)^{a_i}}{\prod_{j=1}^{m}\left(\frac{p_{B_j}}{p_{B_j}^{eq}}\right)^{b_j}}\right] \tag{2.7}$$

For vapour phase processes, $\Delta\mu$ represents the supersaturation, and the condition $\Delta\mu > 0$ ensures a positive growth rate. In order to have a positive supersaturation, the logarithm argument in Eq. 2.7

must be greater than 1. This condition can be fulfilled if the reactants partial pressure is maintained above the equilibrium value by a constant resupply of precursors, while products are continuously removed by the carrier flux. In particular, it can be shown that the growth rate $\Re$ of such a system is given by:

$$\Re = \Re_{max}\left[1 - exp\left(-\frac{\Delta\mu}{RT}\right)\right] \tag{2.8}$$

As it appears from 2.7, the rate of the CVD process is a function of supersaturation and approaches R_{max} with increasing $\Delta\mu$.

Moreover, supersaturation not only drives the growth rate, but also determines which kind of structure will be ultimately grown (Figure 2.2). It is in fact possible to engineer the CVD process so that the growth proceeds epitaxially, mimicking within certain limits the crystallographic parameters of the substrates, which acts as seed for crystallisation. In this case, the technique is called Vapour Phase Epitaxy (VPE). Here, the work conditions are generally closer to the equilibrium, i.e. the required supersaturation is quite low.

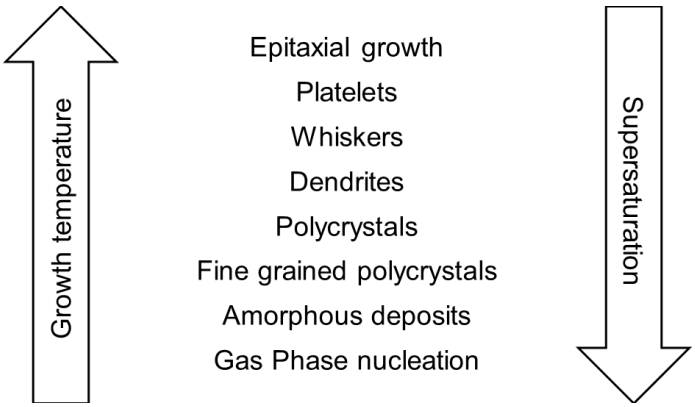

Figure 2.2: Possible structures formed at different growth temperatures and supersaturation levels during a CVD process[151].

Boundary layer and kinetic considerations

As mentioned previously, the deposition is strongly influenced by the dynamics of the gaseous flux. Navier-Stokes equations can solve the flow-dynamic problem, fully describing the fluid field velocity in the reactor chamber. Unfortunately, solutions can be found only numerically; however, an approximated and useful analytical approach can be applied to horizontal reactors, which involves the boundary layer.

For viscous fluids, namely when the mean free path of gas particles is much smaller than the physical dimensions of the system, it is possible to distinguish between laminar and turbulent flow regimes. The latter is undesirable, as the occurrence of convection hinders a precise control over the growth conditions. The discrimination between the two regimes is usually performed on the base of *Reynold's number*:

$$R_e = \frac{\rho v d}{\eta} \tag{2.9}$$

a dimensionless parameter determined by the flow mass density ρ, its velocity v, the viscosity η and the characteristic system size d. For R_e < 1100 the flux is laminar, for R_e > 2100 it is turbulent, while for intermediate values the regime is mixed.

Under laminar-flow conditions, the gas velocity is null in the proximity of the tube or substrate surface and increases gradually while approaching to the bulk of the gas phase. The region involved in this variation is called *boundary layer* and represents a flow portion close to the substrate in which velocity, temperature and chemical composition differ from those characteristic of the main flow. It is thus more appropriate to distinguish between different types of boundary layer, though in most cases they overlap (see Figure 2.3).

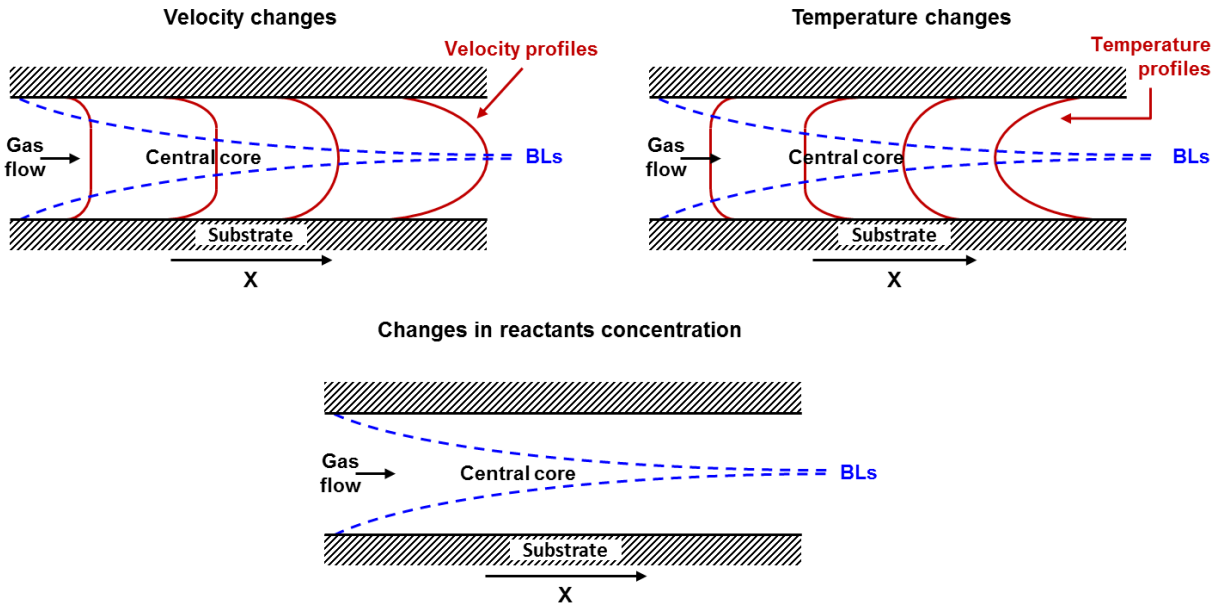

Figure 2.3: Schematic velocity, temperature and concentration boundary layers (BLs) in an horizontal flow tube[150]. Velocity and temperature profiles, ideally recorded at different positions along the tube, are also shown in the respective scheme.

In order to reach the substrate surface, the reactants need to diffuse through the boundary layer, whose thickness at a distance x from the inlet is given by:

$$\delta = \sqrt{\frac{x}{R_e}} \tag{2.10}$$

Hence, δ increases with increasing distance from the inlet and with decreasing flow velocity.

At this point, the possible rate-limiting steps for a CVD process can be defined. These steps involve all growth-related mechanisms, and can be summarised as follows:

- *Thermodynamic control:* valid for very low flow velocities at high temperatures, it implies that deposition rate equals the rate at which mass is introduced in the reactor.
- *Nucleation control:* limiting factor only at low supersaturation levels.
- *Homogeneous reactions control:* due to the formation of key species in the vapour.
- *Surface kinetics control.*
- *Mass transport control.*

For a given growth condition (fixed supersaturation) the net growth rate is usually discussed in terms of the slowest step between surface kinetics and mass transport. The Arrhenius plot in Figure 2.4 can help identifying the limiting factor and thus the growth regime.

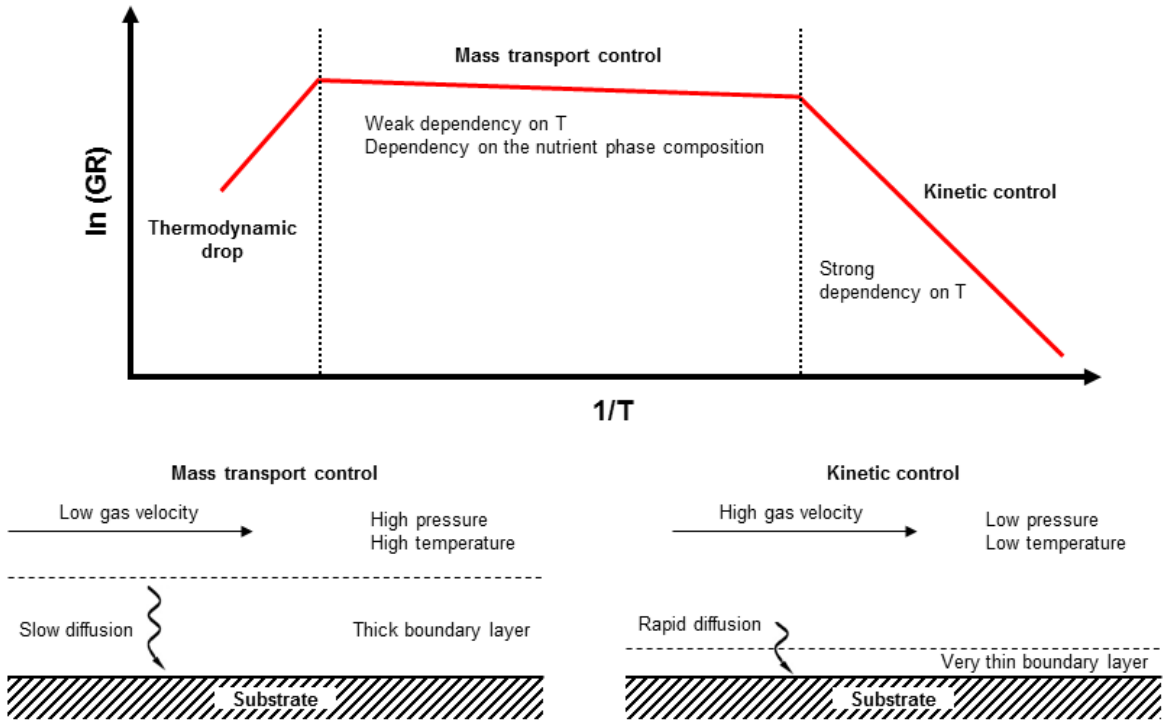

Figure 2.4: Top: Schematic Arrhenius plot of the logarithmic growth rate versus the reciprocal temperature. Bottom: Typical conditions for mass transport and kinetic control mechanisms[150].

The surface kinetics control-regime is strongly dependent on the temperature. It occurs when the deposition rate is lower than both the rate at which the mass is injected inside the chamber and the rate of mass transport (diffusion) within the boundary layer. This is usually the case at high flow velocity, low temperature and low pressure, as these conditions determine a thinning of the boundary layer and an increasing in the diffusion coefficient (see Eq. 2.10), namely the most favourable conditions for the reactant species to reach the substrate.

The mass transport control-regime is established by two factors, which may act simultaneously or separately: first, the low diffusion coefficients through the boundary layer of both reactants towards the substrate and reaction by-products towards the main gas stream; second, low injection rates of precursors into the reactor. Generally, low flow velocity, high temperature and high pressure lead to an increase of the size of the boundary layer and hinder at the same time the diffusion of the various

species within it. High temperatures also allow for the surface reactions to take place faster. The diffusive flux J_D through the boundary layer can be expressed as[151]:

$$J_D = \frac{D}{RT}\frac{P_b - P_s}{\delta} \tag{2.11}$$

where D is the diffusion coefficient, P_b the pressure in the gas flux and P_s the pressure at the surface. A straightforward consequence of Eq. 2.11 is that for a still substrate with its surface parallel to the flow direction, the deposition will take place faster at the inlet side, where the boundary layer is thinner, resulting in an inhomogeneous film thickness. In order to overcome this problem, rotating or inclined substrates are often employed (see Figure 2.5).

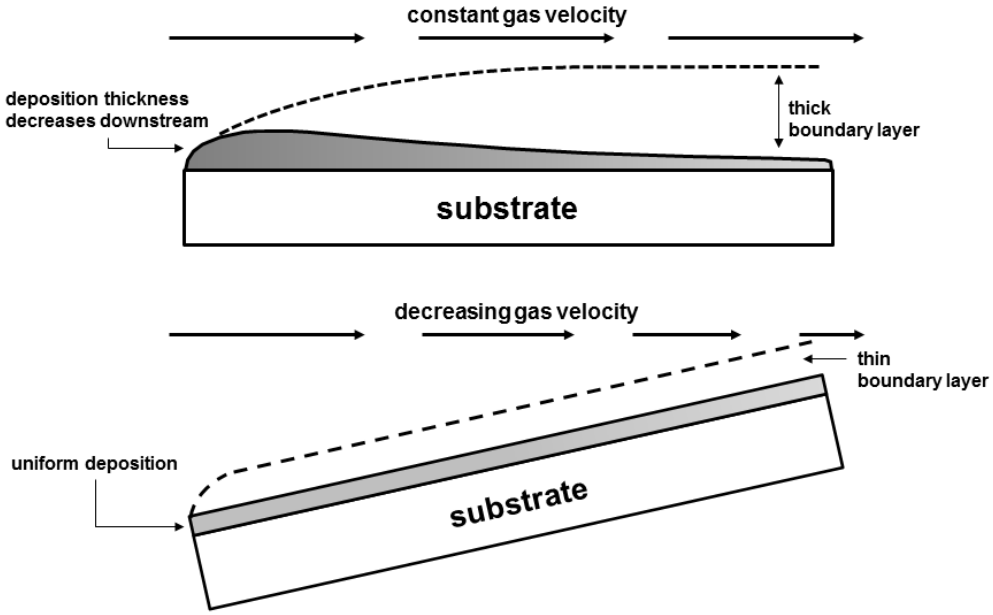

Figure 2.5: Effect of mass transport control regime over the final film thickness when employing a substrate parallel to the gas flow (top) with respect to an inclined configuration (bottom)[150].

Precursors characteristics

Even though there is no perfect CVD precursor, the choice is governed by certain general characteristics which can be summarised as follows:

- Stability at room temperature.
- Sufficient volatility at low temperature, so that it can be easily transported to the reaction zone without condensing inside the lines.
- Sufficiently large temperature window between evaporation and decomposition, in order to provide sufficient thermal stability during evaporation and transport, thus avoiding premature decomposition.
- Clean decomposition pathway with no undesired parasitic reactions.
- Capability of being produced in a very high degree of purity.
- Cost-effectiveness.
- Non-hazardousness.

In particular, MOCVD offers a wide variety of precursors to choose from. These are metal atoms bonded to organic radicals which can be usually found in the form of liquids with high vapour pressure at room temperature, and for this reason they are stored in proper cylinders and immersed in thermostatic baths. The bath temperature allows to precisely control the vapour pressure of the liquid and thus the exact amount of metal-organic delivered to the growth chamber. Most MOCVD reactions occur in the temperature range of 300–800 °C and at pressure varying from less than 1 Torr to atmospheric. The methyl metal-organics start to decompose at 200 °C and the ethyl metal-organics at approximately 110°C[150].

For MOCVD of Ga_2O_3, the gallium-alkyls are among the more frequently used precursors, due to their high volatility and because they ensure a relatively low temperature deposition. The main drawback is their pyrophoric nature, that calls for additional safety systems.

2.1.2 Atomic layer deposition

The origins of atomic layer epitaxy (ALE) date back to the pioneering work of Tuomo Suntola, carried out during the 1970s in Finland[153]. The first processes were applied to the deposition of ZnS and to the development of electroluminescent displays. Later, the technique was more frequently addressed to as atomic layer deposition (ALD), since most films were not epitaxial and amorphous layers were even preferred for applications such as dielectrics and diffusion barriers. With the related technological progress, works and reviews describing ALE and ALD fundamentals and applications started to appear[154–157].

ALD is essentially a surface technique, based on sequentially-controlled, self-limiting, saturating surface reactions. The substrate surface is exposed alternatively to each reactant, so that each step involves a chemical reaction adding a single monoatomic layer of the deposited material (not necessarily a full monolayer, as it will be discussed later). The process is thus chemistry-driven, strongly depending on precursors volatility and reactivity with the surface, and allows to achieve atomic-level control on the growth of ultrathin and conformal films.

ALD is an established technique in constant development, attractive for every application field in which high quality coatings are required. In particular, semiconductor processing was main driving force behind the recent progress in ALD technology. However, a wide variety of materials can be effectively deposited. It is in fact mostly employed for compounds (II-VI and III-V semiconductors, oxides, nitrides, sulphides, phosphides…), but it can be extended to covalent materials, metals, polymers, and it is especially suitable to tailor complex film structures, such as superlattices, doping layers, nanolaminates, alloys and graded films.

Advantages of ALD depend on the deposited material and type of application, however they can be generally summarised into three macro-categories:

- *High quality films*: thickness and composition of the deposited layers can be controlled at the atomic level and depend directly on the number of deposition cycles. Excellent step-coverage and extremely conformal deposition, even on high aspect ratio structures, are a direct consequence of the self-limiting nature of the process. Saturation conditions also favour the formation of continuous, dense, homogeneous and pinhole-free films, which are crucial characteristics required for high quality dielectrics. Layers with excellent adhesion are usually obtained by ALD.
- *Flexibility*: single crystals can be usually obtained at low growth temperatures, as fluid-dynamical transport mechanisms and surface mobility are not crucial in such a chemistry-driven process. For similar reasons, there is no need to control reactant flux homogeneity, nor of line-of-sight substrates, and the only limit to the growth area is the chamber size. Furthermore, sequencing of the reactants prevents undesired gas phase reactions and allows to use highly reactive substances as precursors, as well as to achieve complex film structures in the same chamber. Amorphous or crystalline films can be effectively deposited, and the low growth temperatures are suitable also for sensitive and challenging substrates.
- *Industrial scaling*: the reproducibility of the technique and the possibility to extend it to very large are and batched substrates make it of great appeal for industrial use. Commercial ALD reactors are already available.

The main drawback of the process is the low deposition rate, since even with fast precursor alternation one ALD step ideally provides a single monoatomic layer. Moreover, equipment can be rather expensive, as sequencing requires either fast and efficient gas valving or moving substrates.

Processing requirements

ALD processes can be performed in MBE or CVD systems, provided that reactants are supplied sequentially, one at a time, under conditions which result in a saturated monolayer for each of the reactants used (see *"The importance of saturation"* at the end of this section).

Within the saturation regime, during each exposure step the precursor will react with the surface sites and desorb from the surface areas where the reaction has already reached completion. In particular, the second half-reaction concludes the cycle and restores the surface initial state, either by adding a second monolayer (which is composed by different atomic species in the case of compounds) or by reacting with complementary sites in the underlying layer, thus completing it. A purging sequence is generally required to remove the residual reactant traces and possible by-products, thus avoiding spurious CVD during the next step (Figure 2.6).

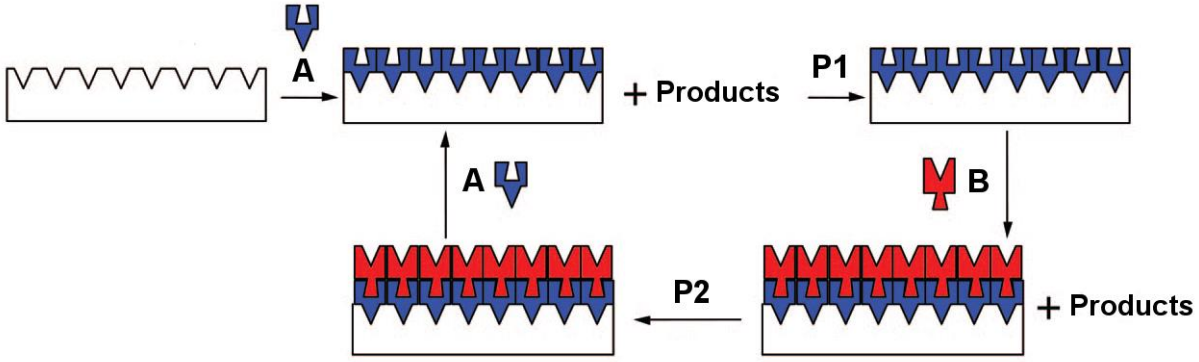

Figure 2.6: Schematic representation of a single ALD cycle using precursors A and B, and purge sequences P1 and P2[156].

Under these conditions, in order to drive reactions to completion during each cycle, ideally leaving no sites behind and achieving uniform deposition, it is hence enough to provide just a sufficient reactant dose. For one sequence, the dose needed is determined by several surface-related properties: total surface area of the substrates, saturation density, reaction probability per hit and hitting efficiency[154,155]. However, two limiting cases for monolayer saturations can be identified. With immediate desorption of excess atoms, no surface mobility and no desorption of the formed solid surface, the effective dose per unit area needed for a reasonable saturation must be well in excess of the saturation density (overdosing). If on the contrary residence time and surface migration of reactants are assumed, the effective dose approaches the surface sites. Overdosing is however generally preferable, provided that a purge sequence is employed.

Nucleation during the initial phases of the growth is the most critical step for formation of continuous, conformal and pinhole-free ultrathin films[156]. The precursors need to react with the initial surface species on the very first ALD cycle, allowing the growth to proceed via the *Frank-van der Merwe* layer-by-layer mechanism. On the contrary, lack of uniform nucleation can result in island growth (*Volmer-Weber* mechanism). The effect is substrate-dependent. Efficient ALD nucleation is given for instance by metal-organic precursors on OH-terminated metal-oxide surfaces, while inefficient ALD nucleation can occur in the case of metals deposited on oxides surfaces.

When performing ALD within a MBE chamber, reactants are supplied by Knudsen cells with standard shutters for sequencing (or valves for gas sources). Ultra-high vacuum conditions allow to achieve high layer perfection and in situ surface analysis is often embedded in the chamber. In CVD systems, reagents are generally diluted in an inert gas in viscous flow, and sequencing is achieved either by independent gas or by moving the substrate between differently exposed regions inside the reactor.

The CVD-derived processing is more productive and grants more freedom in choosing the reaction dynamics[156]. *Thermal-ALD* involves solid ALD reactions with negative enthalpies, which occur spontaneously at various temperatures. Most of the deposited materials are binary compounds and the process is derived from the corresponding CVD binary reactions. On the contrary, *plasma-* or *radical-*

enhanced-ALD is mostly used for single-element materials which can be deposited by a binary reaction sequence. A plasma or another high energy source generates energetic species, such as radicals, that help to induce reactions which would not be possible using just the thermal energy. A comparison between the characteristics of ALD and standard CVD processes is summarised in Table 2.1.

Table 2.1: Comparison between some characteristics of ALD and CVD processes.

ALD	CVD
Equipment which enables fast reactant sequencing and purging.	Precursors react at the same time on the substrate.
High reactivity of the reactants.	Less reactive precursors.
Precursors must not decompose at the process temperature.	Precursors can decompose at the process temperature.
Gas-phase reactions prevented through sequencing.	Elimination of gas-phase reactions requires a reaction threshold.
Surface-controlled: uniformity only requires sufficient reactant dose.	Flow-controlled: uniformity requires uniform flows and temperature.
Thickness control by counting the number of ALD cycles.	Thickness control by precise process control and monitoring.

Surface reactions

When depositing elemental materials, a single compound reactant or a pair of different compound reactants can be used. The first reaction adds a monolayer of the desired material and is followed by a separated reduction sequence. The latter can be activated either by simple heating or by an additional reaction with a different precursor and re-establishes the surface for a new monolayer. For compound materials, even if additive reactions of pure elemental precursors with sufficient volatility are possible, the most frequent scenario involves binary exchange-reactions between compound reactants. For the deposition of the solid $AB(s)$ from precursors $AX_n(g)$ and $BY_n(g)$ the simplest reaction form can be expressed as:

$$BY_k(s) + AX_n(g) = BAX_{n-k}(s) + kXY(g) \quad (2.12)$$

$$AX_{n-k}(s) + BY_n(g) = ABY_k(s) + (n-k)XY(g) \quad (2.13)$$

where the index $k = [0; \mathrm{n}]$ determines the reaction pathway. In this case, the presence of a precursor state requires an activation energy.

It is often possible to distinguish between a ligand precursor, which prepares the surface for the next layer and defines the kind of material which will be deposited (oxide, nitride…), and a main precursor containing the metal atom. The latter should fulfil the following requirements:

- Volatility and thermal stability at the operating temperature.
- High reactivity with the surface.
- Non-competitive by-products for surface sites.
- Self-terminating reactions with the previous layer.
- No etching of the film surface/substrate or dissolution inside it.
- Sufficient purity and availability.

Deposition of Al_2O_3 from trimethylaluminium (TMA) and water, schematically depicted in Figure 2.7, is often employed as model system for ALD processes, since its high exothermic enthalpy of -376 kcal results in very efficient, self-limiting surface reactions:

$$AlOH^* + Al(CH_3)_3 \rightarrow AlOAl(CH_3)_2^* + CH_4 \quad (2.14)$$

$$AlCH_3^* + H_2O \rightarrow AlOH^* + CH_4 \quad (2.15)$$

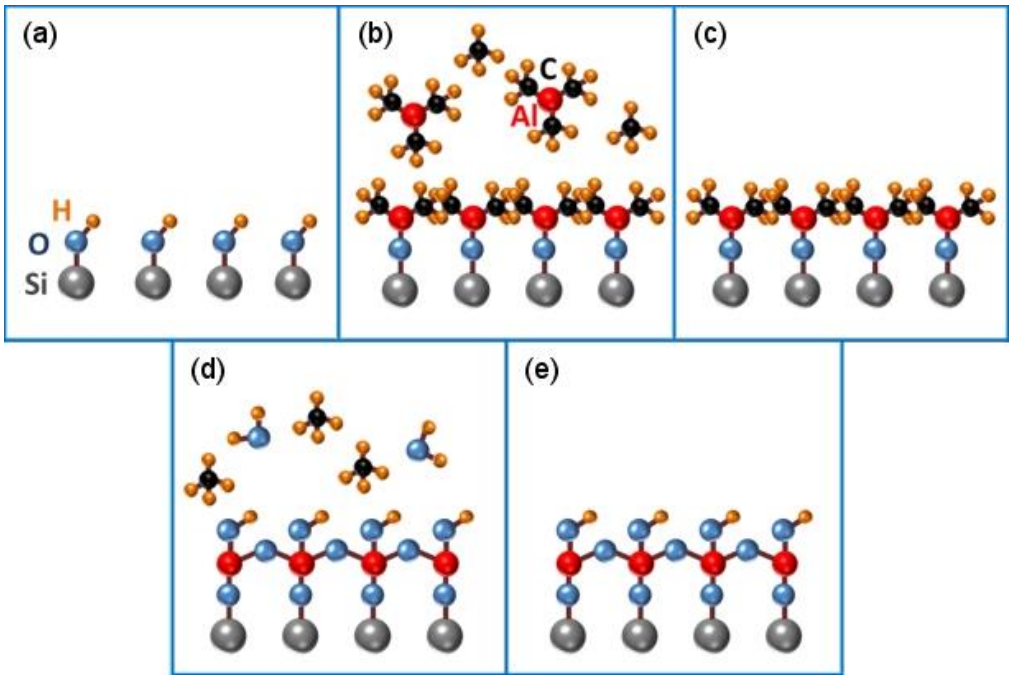

Figure 2.7: Schematic steps of Al_2O_3 ALD on Si surface. (a): Hydroxylation of the substrate surface by exposure to air. (b): TMA injection and reaction with OH* group similar to Eq. 2.14. (c): Purge. (d): H_2O injection and reaction following Eq. 2.15. (e): Purge and re-establishment of the initial surface conditions. (From Ensure Scientific Group[158])

Note that the surface species are denoted by an asterisk. This model is also particularly interesting for the analogies with the system trimethylgallium-water that was employed in this thesis for the deposition of ε-Ga_2O_3 thin films.

The importance of saturation

Saturation is the most important mechanism defining ALD regimes[154,155], as it controls not only the growth rate and the uniformity, but also the density of each deposited layer, which can be less than a full monolayer (see Figure 2.8).

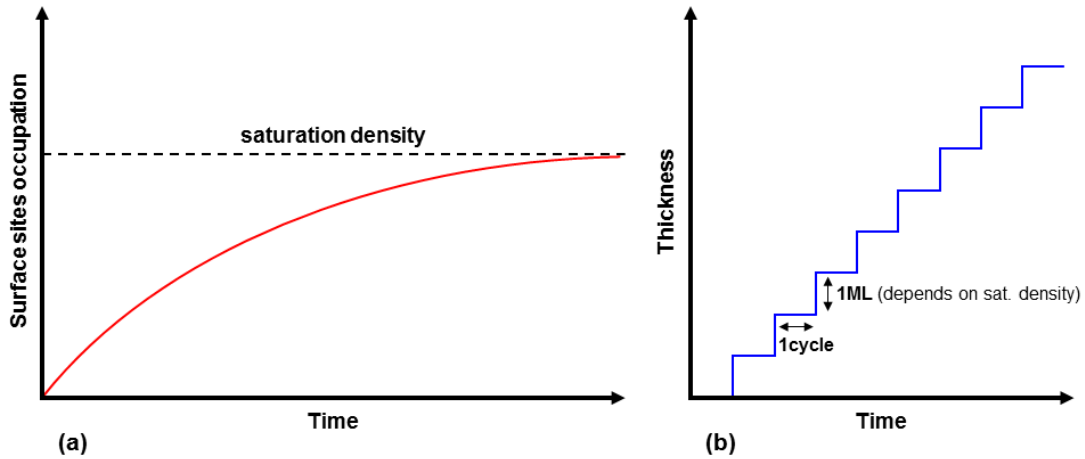

Figure 2.8: Schematic representation of (a): surface sites occupation converging to the saturation density (partial or full monolayer) and (b): dependence of the deposited thickness on the number of ALD cycles. If saturation conditions are fulfilled, each cycle results in the deposition of a single monolayer (ML), with a thickness that depends on the saturation density.

Conditions for saturation, i.e. the formation during a single ALD reaction sequence of a surface monolayer (full or partial) in which all the *available* surface sites are occupied, require that a sufficient reactant dose is provided and a selective desorption regime to be established. The latter implies no condensation of extra vapour on the forming solid layer and surface stability until reaction with the next precursor. This requires an optimal operation temperature, as it will be discussed later.

Besides temperature, other factors can influence saturation, for instance the sequencing time, that should be sufficient to provide the required dose but not too long, in order to prevent undesired long-term desorption and to maintain an acceptable growth rate. The high reactivity of surface and reactants is another important parameter, since it promotes an efficient saturation and a high material utilisation factor. Reactants should however display a good thermal stability at the processing temperature, as thermal release of ligands or dissociation of the reactants may produce impurities and make saturation even more sensitive to temperature, timing, dosing and type of inert gas. The presence of a purge step is crucial in order to remove surplus of reactant vapour, as well as reaction- and decomposition-products.

As anticipated, however, even in saturation conditions monolayers can be only partially occupied. This *saturation density* depends on various factors, such as the energetically most favourable surface reconstruction at the operation temperature, which is a function of the crystalline face, and the steric hindrance of the reactant molecules or ligands. The latter can affect both surface bond-energies of the surrounding species and the preferred surface reconstruction, or even suppress the latter, leading to the formation of a full monolayer per cycle.

Despite many parameters are involved in determining the saturation conditions, temperature is notoriously the most important[154,155], and the ALD temperature window, shown in Figure 2.9, is often employed to get a first indication of the limiting mechanisms of the overall ALD process.

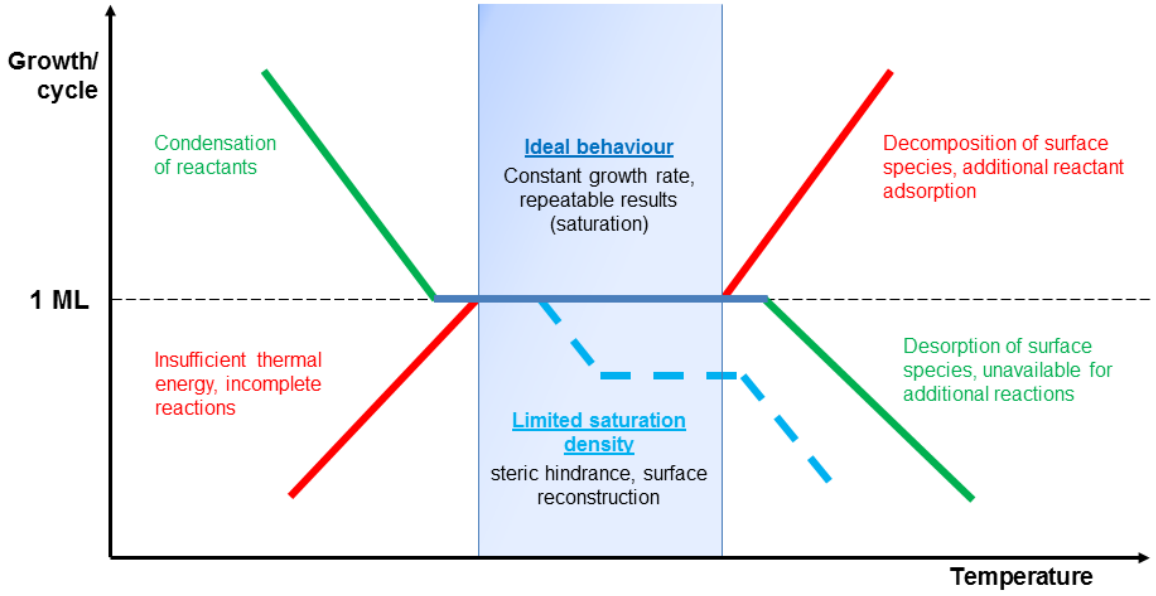

Figure 2.9: ALD temperature window and deviations from ideal behaviour.

Within the window, the system displays nearly ideal behaviour, characterised by a constant growth rate. Operating here grants reliable and reproducible results, as the growth is saturated and self-limited. All bonding sites, corresponding to the number of atoms in a crystal plane, are occupied and result in a growth rate of one monolayer (or lattice unit) per cycle. Even within the window, however, in some cases a less-than-one complete unit per cycle might be observed, because of the aforementioned role played by surface reconstruction and ligand-related effects. In some cases, undecomposed molecules might also result in saturation density above unity.

At lower temperatures, the growth rate can increase due to condensation of reactants, or decrease because the supplied thermal energy is not enough to activate the required surface reactions. Processes providing extra energy, such as photo-excitation or plasma, can help widening the ALD window at lower temperatures.

At upper limits of the substrate temperature, an increase in the growth rate is usually associated to condensation of decomposition products. On the contrary, the growth rate can decrease due to desorption of surface species, which are thus made unavailable for additional reactions.

2.1.3 Pulsed laser deposition

Pulsed laser deposition (PLD) is a far-from-equilibrium technique involving the ablation of a target material by means of high-energy laser pulses. The ablation process results in a transient and highly luminous plasma plume, composed by a collection of atoms, molecules, ions and electrons, that expands rapidly from the target and condenses on the surface of an opportunely placed substrate, resulting in the nucleation and growth of a thin film.

Development of high-power lasers with high pulse energy and short pulse duration, such as excimers, made the breakthrough of this technique possible, and nowadays it is a well-established method for the deposition of a variety of materials. Several advantages are provided by PLD[159–161]:

- Since the relative concentration of elemental species within the plasma corresponds to the chemical composition of the target material, stoichiometric transfer from the target to the substrate is usually possible. This allows for the growth of both granular crystalline and amorphous thin films with complex stoichiometry. For instance, a wide variety of oxides can be directly grown by using a reactive oxygen background, with no need of additional processing steps. Furthermore, multilayer materials can be readily obtained by alternate ablation of different targets.
- The process is versatile and fast, with average growth rates of tens of nm/min, while thickness can be directly controlled by the number of ablation pulses.
- It is a clean method, as using the laser as external energy source makes heating filaments or a plasma gas inside the deposition chamber unnecessary, thus avoiding contamination. The growth can hence take place within an inert or reactive gas environment, with nearly no constraints on the employed pressure.
- Under some circumstances, species appearing only in the plasma can also be deposited on the film surface. For instance, metastable phases can be obtained by PLD.

However, some intrinsic drawbacks have so far limited the application of PLD to research fields, while industrial development still proceeds slowly. These impediments are mostly associated with the overall low efficiency of the PLD process. For instance, the volume deposition rate is generally around 10^{-5} cm^3/s, much lower than other physical vapour techniques. The spatial confinement of the plasma plume, which is highly forward-directed, further hinders the upscaling to large substrates, and an additional lateral scanning of the substrate is required if sufficient thickness and uniform deposition on areas larger than 1 cm^2 are to be achieved.

Moreover, particulate and droplets are often found on the film surface after deposition, limiting the layer quality and performance. As it will be discussed in the last part of this section, some expedients have been proposed which however reduce the deposition rate and make the overall process more complex.

As a final point, because of their strong non-equilibrium character, the fundamental mechanisms governing PLD are not completely understood. It is thus difficult to provide effective theoretical models to assist the experimental activity, and an initial period of pure empirical optimisation is usually required when novel materials are studied.

PLD mechanisms

PLD is a complex process that can be controlled through the combination of different parameters: laser characteristics (fluence, wavelength, pulse duration and repetition rate), target-to-substrate distance, substrate type and temperature, background gas composition and pressure, target

composition and properties, deposition geometry. Three main process steps can be identified[159,160], as schematically depicted in Figure 2.10:

- *Ablation*: the involved phenomena can be primary or secondary laser-target interactions, taking place simultaneously at times scales within the order of nanoseconds.
    - *Thermal ablation*: is produced by the interaction of the laser energy with phonons, resulting in melting and evaporation of the target material.
    - *Electronic sputtering*: is associated with interactions of the laser with the electronic levels and can result in the breaking of chemical bonds. It is more evident when very short pulses are employed (sub-picoseconds).
    - *Macroscopic sputtering:* it can manifest itself in different forms, such as hydrodynamic ejection of droplets as a consequence of transient melting, or exfoliation of flakes from the target surface caused by repeated thermal shocks.
    - *Indirect sputtering*: it involves secondary mechanisms such as back-sputtering from already ablated species or additional heating transfer from the plasma itself. These secondary phenomena usually involve a larger area than the initial ablation spot and can affect the final film stoichiometry if their efficiency is component-dependent.

  It is worth noting however that for the actual optimisation of the growth of a particular material, the detailed ablation mechanisms are of minor importance. What is more determining from a practical point of view is to ensure that the ablations takes place on a short time scale, in order to minimise the dissipation of the laser energy beyond the ablated region, thus avoiding thermal destruction of the target and phase segregation.
- *Plume expansion*: the ablated material partially absorbs the laser radiation, producing a heated and excited plasma plume which expands transferring the depositing material towards the target. Plume expansion behaviour is strongly influenced by the presence of an ambient gas and by its pressure, as it scatters, attenuates and thermalises the plume, thus modifying the spatial distribution, deposition rate and kinetic energy of the deposited species. Plume expansion in a background gas occurs within microseconds.
- *Condensation and film growth*: arriving particles are adsorbed on the substrate surface, upon which they diffuse and react with each other before starting to nucleate. A stable nucleation-growth sequence is achieved provided that the time constants of these surface atomic processes are much smaller than the period of the PLD cycle and that the growth rate per laser pulse is less than one molecular building block. Under this assumption, nucleation and growth on the substrate surface can be described by the same models which are valid for other deposition techniques (Volmer-Weber three-dimensional islands, Frank-van der Merwe two-dimensional monolayer and Stranski-Krastanov monolayer-plus-islands). Growth and quality of the film strongly depend on the substrate temperature and on the kinetic energy/arrival rates of the various species composing the plume. The former primarily controls thermally activated processes such as adsorption/desorption, diffusion and nucleation, while the latter, besides favouring rearrangements of the surface species when the energy is low, can result in surface penetration or even in detrimental sputtering of the deposited film when highly energetic particles are involved.

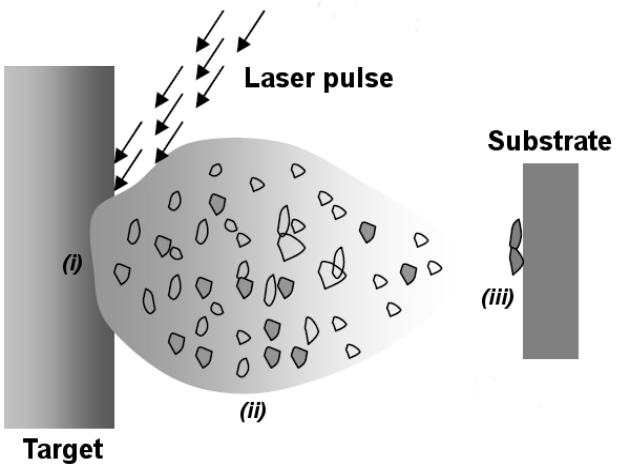

Figure 2.10: Schematic steps involved in a PLD process: (*i*): laser-target interaction and ablation; (*ii*): plume formation; (*iii*): condensation and film growth[162].

Avoiding damaging particles and droplets

As discussed above, during laser irradiation the target undergoes thermal and mechanical shocks, resulting in explosive spouting of cluster particles or droplets with varying size, shape and composition. These can scatter on the grown film surface or even damage it, compromising its structural and electrical quality. Among the proposed expedients to overcome this problem, *eclipse* and *off-axis* methods displayed in Figure 2.11 are some of the most successful.

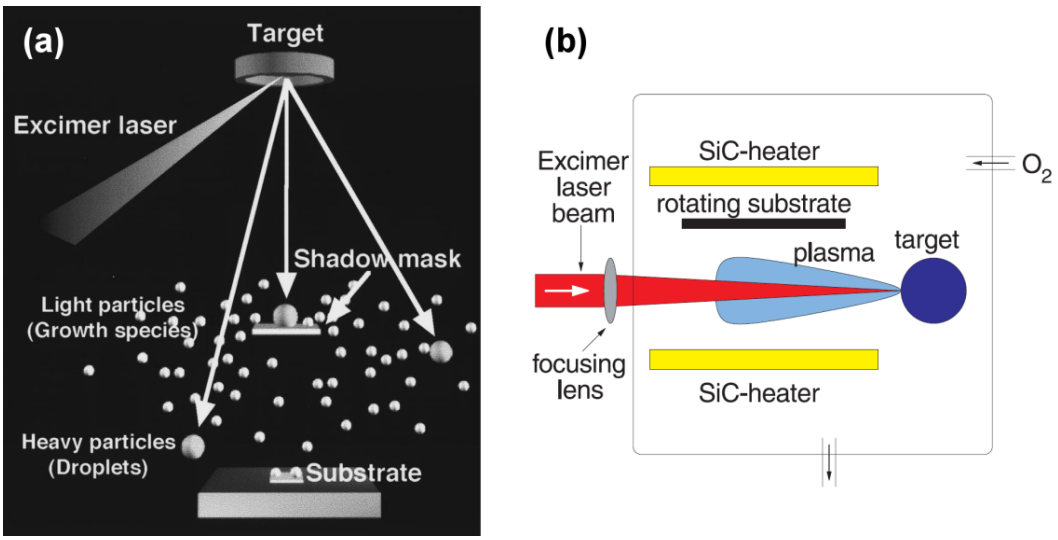

Figure 2.11: Variants of the PLD technique designed to prevent highly energetic particles from reaching the substrate. (a): Eclipse[163]. (b): Off-axis[164].

In eclipse PLD a shadow mask is positioned between target and substrate[165,166]. The heavier particles are completely shielded by the mask, as they tend to fly in a straight line because of their small scattering angle. Hence, deposition proceeds by means of diffusion of the lighter species through the ambient gas. However, especially for the deposition of oxides, it was often pointed out that the quality of layers grown with this method, though improved, was still not perfect[167]. This persistent

degradation of crystallinity was ascribed to the fact that a fewer number of activated growth species and oxygen radicals reach the substrate, as they are shielded by the shadow mask similarly to the heavier clusters. By adding an inert gas like argon to the chamber atmosphere, almost perfect transfer of reactive species can be achieved also by eclipse PLD[163,168], as the plume becomes more diffused and the species are more effectively excited and ionised[169]. Due to its many vibrational and rotational levels, O_2 is in fact more likely to collide inelastically with the electrons, lowering the plasma temperature. Moreover, oxygen tends to form negative ions, disturbing the formation of high-energy electrons[163].

Off-axis PLD involves a change in the substrate orientation, usually by positioning its surface parallel to the plume axis[170,171]. Under these conditions, deposition can take place only if the particles have a non-zero velocity component perpendicular to the main plume expansion direction. This is the case for light particles, which undergo a Brownian-like motion as the result of collisions with oxygen molecules, while larger fragments or droplets are less affected by these impacts and tend to pass by the substrate without being deposited. The film deposition takes place once again via a diffusion-like process out of the main plume, even though in this case the heavier clusters are not completely excluded. In the most common configuration, the substrate intercepts the plume axis, thus allowing for deposition on both sides, even though different variants are possible (see Figure 2.11b).

2.2 Experimental setups

2.2.1 MOCVD/ALD home-made reactor

The epitaxial growth of ε-Ga_2O_3 thin films was performed at IMEM-CNR Institute, in collaboration with Dr. Matteo Bosi and Dr. Giovanni Attolini. The system consists of a home-made, horizontal MOCVD reactor, equipped with a refurbished stainless steel chamber (Figure 2.12). The substrate is placed on a graphite plate, heated by resistive cartridges. The growth temperature can be tuned through the supplied electric power by means of a proportional-integral-derivative (PID) controller, receiving its feedback from a thermocouple inserted into the centre of the graphite.

Trimethylgallium (TMG) and ultrapure water, both stored in dedicated stainless steel bubblers and kept at 1–5 °C and 30 °C, respectively, were used as precursors. In particular, water was preferred to molecular O_2, since a series of preliminary experiments showed that the oxidation by pure gas was less effective, as previously observed also by other authors[15]. Both precursors are delivered through a standard double-dilution line; however, the dilution step was here employed almost exclusively in the case of TMG, in order to operate in water-excess conditions.

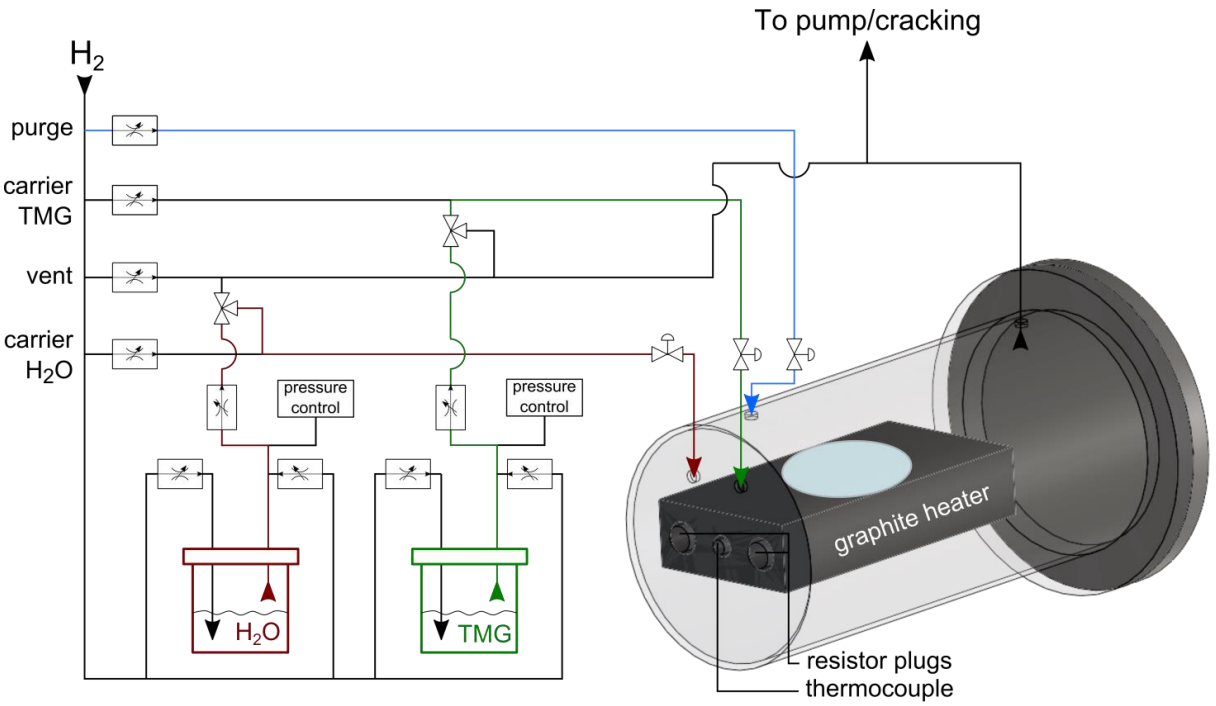

Figure 2.12: Schematic representation of the MOCVD/ALD reactor for the growth of ε-Ga_2O_3 thin films. The graphite heater is supported by three hollow tubes, soldered to the internal reactor wall, in which two resistor plugs and a thermocouple are inserted from the outside.

Delivery to the growth chamber is performed by means of two separate gas lines, using palladium-purified H_2 as carrier, since tests carried out with helium resulted in no appreciable improvement. Each line is intercepted by a valve just before the chamber inlet. This configuration allows either the simultaneous injection of the reagents (standard MOCVD mode) or the alternate supply of individual reagents, thus avoiding any pre-mixing of TMG and H_2O in the gas phase and enabling a pure ALD regime, as depicted schematically in Figure 2.13. During the purge, both reagent supplies are shut off and only hydrogen from a separated gas line is flushed into the chamber.

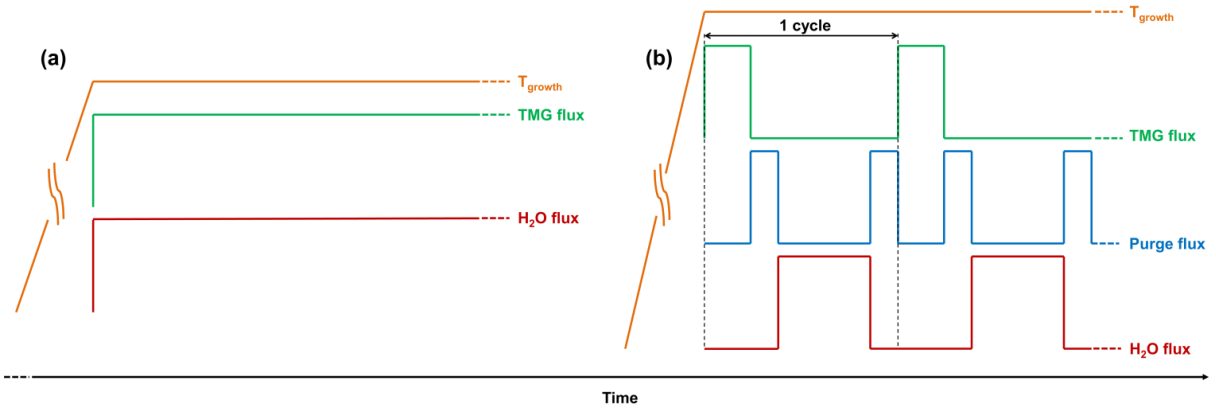

Figure 2.13: Operation regimes of the reactor used for the deposition of ε-Ga_2O_3 thin films. (a): MOCVD mode, simultaneous injection of the reactants. (b): ALD mode, reactants sequencing and purge.

The pressure inside the chamber is controlled by a rotary pump and can be varied from ambient to ~ 30 mbar, while a cracking furnace set at 650 °C allows to decompose potentially unreacted residuals before unloading the gases at atmospheric pressure. Valves operation and gas delivery systems are fully automated, the latter by means of mass flow controllers (MFCs).

The partial pressure p_i of the i-th reactant inside the chamber can be controlled directly through the sccm flows F set by the MFCs, but also by changing the respective bubblers temperature $T_{i,bub}$ and pressure $P_{i,bub}$:

$$p_i = \frac{F_{i,bub}\, F_{i,inj}}{F_{tot}\, P_{i,bub}\left(F_{i,dil} + F_{i,bub}\right)} P_{i,vap} \tag{2.16}$$

where $F_{i,bub}$, $F_{i,dil}$ and $F_{i,inj}$ are respectively the flows entering into the bubbler, diluting the bubbler output, and finally injected into the reactor (following the scheme of Figure 2.12). F_{tot} is the total gas flow that reaches the chamber. Note that p_i is here expressed relatively to the total chamber pressure. The temperature dependence is given through the term $P_{i,vap}$, which is the vapour pressure of TMG and water inside the respective bubblers and depends only on the bubbler temperature $T_{i,bub}$:

$$log_{10}\, P_{TMG} = \left(8.07 - \frac{1703}{T_{TMG,bub}}\right) \tag{2.17}^{[172]}$$

$$ln\, P_{H_2O} = \left(20.386 - \frac{5132}{T_{H_2O,bub}}\right) \tag{2.18}^{[173]}$$

Here vapour pressures are expressed in mmHg and the temperature in K. The relative quantity of a reactant in the chamber with respect to the other can thus be increased by increasing its bubbler flow, injection flow or bubbler temperature, or equivalently by decreasing its dilution or bubbler pressure.
The total deposition reaction can be expressed as:

$$2Ga(CH_3)_3 + 3H_2O \rightarrow Ga_2O_3 + 6CH_4 \tag{2.19}$$

TMG is known to pyrolyse through a two-step uni-molecular reaction with the loss of methyl groups and the formation of monomethylgallium[174–176]:

$$Ga(CH_3)_3 \rightarrow Ga(CH_3)_2 + CH_3 \tag{2.20}$$

$$Ga(CH_3)_2 \rightarrow Ga(CH_3) + CH_3 \tag{2.21}$$

However, at the moment there are no detailed studies on the reaction mechanisms between TMG sub-products and H_2O to form Ga_2O_3. Baldini *et al.*[117] hypothesised that monomethylgallium tends to hydrolyse in water to form first $Ga(OH)_3$ and finally Ga_2O_3, through the following mechanism:

$$Ga(CH_3) + 3H_2O \rightarrow Ga(OH)_3 + CH_4 + H_2 \tag{2.22}$$

$$2Ga(OH)_3 \rightarrow Ga_2O_3 + 3H_2O \tag{2.23}$$

In analogy to the deposition of Al_2O_3 from TMA and H_2O, one can suppose the two ALD steps to be roughly:

$$GaOH^* + Ga(CH_3)_3 \rightarrow GaOGa(CH_3)_2^* + CH_4 \quad (2.24)$$

$$GaCH_3^* + H_2O \rightarrow GaOH^* + CH_4 \quad (2.25)$$

where asterisks again denote surface species, while the second step re-establishes the initial surface conditions.

2.2.2 PLD chamber

PLD growth of Si-doped β-Ga_2O_3 layers was performed at Leipzig University in collaboration with Holger Hochmuth. The main deposition apparatus is shown schematically in Figure 2.14.

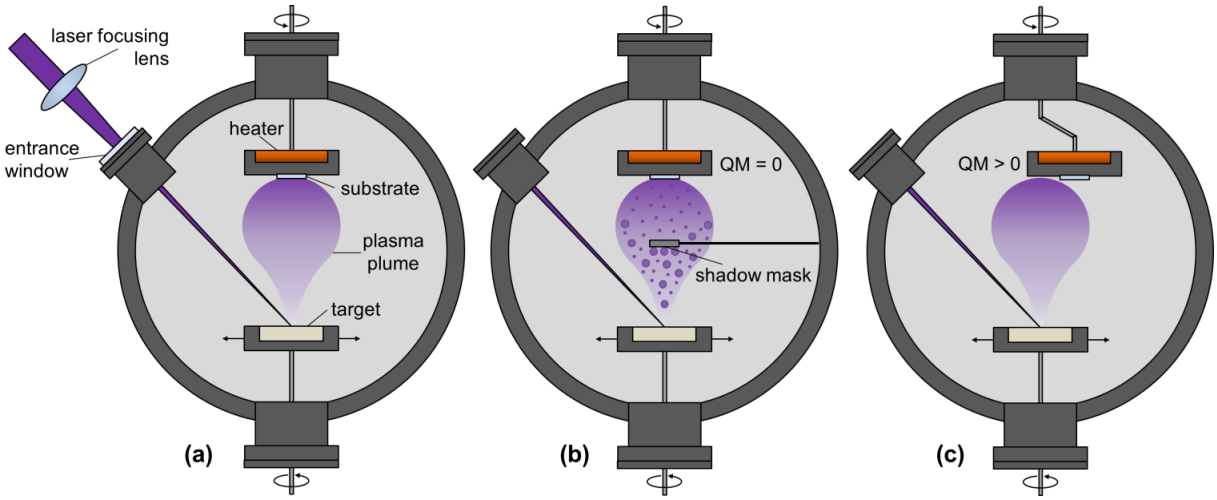

Figure 2.14: Experimental PLD setups. (a): Standard configuration. (b): Eclipse PLD. (c): Off-axis PLD.

A KrF excimer laser with an emission wavelength of λ = 248nm is used as high energy source and the deposition is carried out in a vacuum chamber equipped with a turbomolecular drag pump, with pure oxygen as background gas. A UV fused-silica lens focuses the laser through a UV fused-silica entrance window and onto the target. The employed ceramic targets were prepared by homogenisation of gallium oxide and SiO_2 in different concentrations, subsequent pressing and sintering in air by Gabriele Ramm at Leipzig University. Target is positioned at a normal distance of 110 mm from a heated substrate holder. When operating in eclipse mode, a circular metallic shadow mask is set halfway between target and substrate (see Figure 2.14b). Further, target and substrate holder manipulators allow for respective rotation and lateral translation. In particular, the substrate offset is exploited to operate in off-axis mode. As mentioned in the above section, in the most common off-axis PLD configuration substrate and target are reciprocally perpendicular. In the present case, we attempted to exploit the same effect with a modified geometry (Figure 2.14c): the substrate faces the

target but is laterally shifted with respect to its normal by an offset value QM, ranging between 0 and 30 (1 QM ~ 1.4 mm).

By means of a dedicated software, it is possible to divide the process in several steps, for each of which many different parameters can be automatically controlled: laser-related parameters, chamber pressure, heating power, target movement. This feature was exploited to design the deposition of nucleation layers with different laser pulses and frequencies, as well as to programme post-growth thermal treatments.

Besides the settable parameters, the final film quality can be influenced by other inner factors that always need to be accounted for. Accuracy and reproducibility of laser pulse energy, for instance, require constant monitoring of the laser system. Regular cleaning of the laser entrance window is also necessary, in order to remove ablation deposits that progressively shield the laser energy as the deposited thickness increases. The ablation state of the target has to be routinely assessed, as well, since the ablation efficiency changes with increasing depth. The latter two effects are particularly crucial when operating at low pressure or in eclipse/off-axis mode. Within these conditions, the deposition rate is in fact strongly reduced and the desired film thickness cannot be simply obtained by increasing the number of laser pulses indefinitely, since target consumption and thickening of the window deposit constantly modify the ablation efficiency.

2.3 Growth parameters

2.3.1 MOCVD and ALD samples

Epi-ready *c*-sapphire wafers with 1 or 2 inch diameter were employed as standard substrates, while test depositions were performed on (0001) GaN, (001) 3C-SiC and (111) 3C-SiC templates previously grown at IMEM-CNR Institute by Dr. Matteo Bosi.

In this case, the growth process was started anew. During the initial period it was thus necessary to identify a suitable parameter window for reproducible growth, followed by an optimisation phase (still ongoing) to increase deposition homogeneity while maintaining acceptable growth rates. A collection of the most representative MOCVD growth runs is reported in Table 2.2. With respect to MOCVD, progress in ALD are still at an early stage; however, as it will be discussed in the following chapter, the first results are quite promising. Typical ALD growth parameters are shown in Table 2.3.

Table 2.2: Representative collection of samples grown by MOCVD. Partial pressures are calculated according to Eqs. 2.16–2.18 and expressed relatively to the total chamber pressure.

Sample #	Chamber		Flows (sccm)				Partial pressures			Time (min)
	T (°C)	P (mbar)	Carrier H_2O	Carrier TMG	Inj. H_2O	Inj. TMG	H_2O	TMG	H_2O/ TMG	
cvd38	550	100	200	200	100	20	$6.63\cdot10^{-3}$	$1.18\cdot10^{-3}$	6	30
cvd40	650	100	200	200	112	10	$4.89\cdot10^{-2}$	$4.57\cdot10^{-4}$	107	30
cvd50	650	100	200	200	112	10	$8.72\cdot10^{-2}$	$4.57\cdot10^{-4}$	191	30
cvd52	650	100	200	200	112	10	$8.72\cdot10^{-2}$	$4.57\cdot10^{-4}$	191	5
cvd53	650	100	200	200	112	10	$8.72\cdot10^{-2}$	$4.57\cdot10^{-4}$	191	10
cvd54	715	100	200	200	112	10	$8.72\cdot10^{-2}$	$4.57\cdot10^{-4}$	191	15
cvd132	650	100	200	200	200	20	$1.34\cdot10^{-1}$	$8.98\cdot10^{-4}$	149	30
cvd134	650	100	200	200	400	20	$2.02\cdot10^{-1}$	$6.79\cdot10^{-4}$	297	30
cvd135	650	100	200	200	300	20	$1.72\cdot10^{-1}$	$5.67\cdot10^{-4}$	304	30
cvd138	650	100	200	200	200	20	$1.34\cdot10^{-1}$	$6.59\cdot10^{-4}$	203	30
cvd139	650	100	200	200	200	20	$1.34\cdot10^{-1}$	$6.59\cdot10^{-4}$	203	30
cvd141	650	100	200	200	200	20	$1.34\cdot10^{-1}$	$6.59\cdot10^{-4}$	203	10
cvd142	650	100	100	300	200	20	$1.34\cdot10^{-1}$	$6.59\cdot10^{-4}$	203	10
cvd143	650	100	200	400	200	20	$1.01\cdot10^{-1}$	$4.98\cdot10^{-4}$	203	10
cvd144	650	100	200	200	200	20	$1.34\cdot10^{-1}$	$6.59\cdot10^{-4}$	203	15
cvd145	650	100	0	200	200	20	$1.97\cdot10^{-1}$	$9.72\cdot10^{-4}$	203	15
cvd146	650	100	200	200	200	20	$1.34\cdot10^{-1}$	$6.59\cdot10^{-4}$	203	15
cvd149	650	100	200	200	200	20	$1.34\cdot10^{-1}$	$6.59\cdot10^{-4}$	203	120
cvd153	650	100	200	200	200	20	$1.34\cdot10^{-1}$	$6.59\cdot10^{-4}$	203	120
cvd210	650	50	200	200	200	10	$2.71\cdot10^{-1}$	$1.75\cdot10^{-4}$	1550	30
cvd213	650	50	200	200	200	10	$2.71\cdot10^{-1}$	$1.75\cdot10^{-4}$	1550	60
cvd223	650	60	1000	1000	200	10	$6.24\cdot10^{-2}$	$4.83\cdot10^{-5}$	1291	30
cvd224	650	60	1000	1000	200	10	$6.24\cdot10^{-2}$	$4.83\cdot10^{-5}$	1291	60
cvd225	650	60	1000	1500	200	10	$5.09\cdot10^{-2}$	$3.94\cdot10^{-5}$	1291	60
cvd226	650	60	1000	1000	200	10	$6.24\cdot10^{-2}$	$2.64\cdot10^{-5}$	2368	60
cvd227	650	65	1000	1500	400	10	$8.75\cdot10^{-2}$	$3.67\cdot10^{-5}$	2384	60
cvd246	615	60	1000	1000	110	10	$3.58\cdot10^{-2}$	$6.05\cdot10^{-5}$	592	30
cvd247	615	60	1000	1000	110	10	$3.58\cdot10^{-2}$	$1.13\cdot10^{-4}$	316	30
cvd248	615	60	1000	1500	110	10	$2.90\cdot10^{-2}$	$9.18\cdot10^{-5}$	316	30
cvd249	615	60	1000	1500	110	10	$2.90\cdot10^{-2}$	$9.18\cdot10^{-5}$	316	30
cvd250	615	60	1000	1000	150	10	$4.79\cdot10^{-2}$	$1.11\cdot10^{-4}$	430	30
cvd251	600	60	1000	1000	110	10	$3.58\cdot10^{-2}$	$1.13\cdot10^{-4}$	316	30
cvd252	600	60	1000	1000	110	10	$3.58\cdot10^{-2}$	$1.89\cdot10^{-4}$	189	30
cvd253	600	60	700	700	110	10	$4.99\cdot10^{-2}$	$1.58\cdot10^{-4}$	316	30
cvd255	600	60	1000	1000	110	10	$3.58\cdot10^{-2}$	$1.13\cdot10^{-4}$	316	420
cvd256	600	60	1000	1000	110	10	$3.58\cdot10^{-2}$	$8.25\cdot10^{-5}$	434	30
cvd259	600	60	1000	1000	50	10	$1.26\cdot10^{-2}$	$1.17\cdot10^{-4}$	108	30
cvd263	600	60	1000	1000	220	10	$6.81\cdot10^{-2}$	$1.08\cdot10^{-4}$	631	30

Table 2.3: Representative collection of samples grown by ALD. Carrier flows were set to 200 sccm each. Partial pressures are calculated according to Eqs. 2.16–2.18 and expressed relatively to the total chamber pressure.

Sample #	Chamber			Partial pressures		ALD sequence (s)				Cycles #
	T (°C)	P (mbar)	Purge (sccm)	TMG	H_2O	TMG	Purge	H_2O	Purge	
ald41	550	100	-	$2.79 \cdot 10^{-3}$	$1.47 \cdot 10^{-1}$	5	3	10	3	200
ald43	550	100	-	$2.79 \cdot 10^{-3}$	$1.47 \cdot 10^{-1}$	5	3	10	3	1000
ald47	650	100	-	$2.79 \cdot 10^{-3}$	$1.47 \cdot 10^{-1}$	5	3	10	3	200
ald152	620	100	500	$1.86 \cdot 10^{-3}$	$2.07 \cdot 10^{-1}$	5	3	10	3	200
ald154	620	100	500	$1.86 \cdot 10^{-3}$	$2.07 \cdot 10^{-1}$	5	3	10	3	400
ald156	550	100	500	$1.86 \cdot 10^{-3}$	$2.07 \cdot 10^{-1}$	5	3	10	3	400
ald260	550	60	500	$1.37 \cdot 10^{-3}$	$2.90 \cdot 10^{-1}$	5	3	10	3	400
ald261	580	60	500	$1.37 \cdot 10^{-3}$	$2.90 \cdot 10^{-1}$	5	3	10	3	400
ald262	525	60	500	$1.37 \cdot 10^{-3}$	$2.90 \cdot 10^{-1}$	5	3	10	3	400
ald264	500	60	500	$1.37 \cdot 10^{-3}$	$2.90 \cdot 10^{-1}$	5	3	10	3	400
ald265	525	60	1000	$1.37 \cdot 10^{-3}$	$2.90 \cdot 10^{-1}$	3	5	3	5	400
ald266	500	60	1000	$1.37 \cdot 10^{-3}$	$2.90 \cdot 10^{-1}$	3	5	3	5	400
ald267	475	60	1000	$1.37 \cdot 10^{-3}$	$2.90 \cdot 10^{-1}$	3	5	3	5	400
ald268	475	60	500	$1.37 \cdot 10^{-3}$	$2.90 \cdot 10^{-1}$	5	3	10	3	400

2.3.2 PLD samples

PLD growth was carried out using a laser pulse energy of 600 mJ at 17 kV, keeping a constant power supply of 500 W to the substrate heating system (~ 700 °C) and rotating the substrate holder at 60 rpm. Most processes were performed at low oxygen pressure (0.001 mbar) in order to further reduce the kinetic energy of the particles reaching the substrate and to increase their surface mobility. The two main parameters determining film quality for standard PLD processes previously developed at Leipzig University, namely temperature and pressure, were thus maintained unvaried for all growth runs.

After the deposition, all samples underwent two additional treatments inside the chamber: 1 minute relaxation under the same conditions employed during the growth, in order to promote the rearrangement of the last atomic layers, and 5 minutes further heating, this time lowering the rotation speed to 10 rpm and increasing the oxygen back pressure to 800 mbar, in order to improve the film quality and complete the oxidation.

More than 50 sample were grown, exploring different process parameters. Here, only a collection of the most representative ones will be shown. Depositions were performed on 1×1 cm epi-ready *c*-sapphire substrates in the case of eclipse PLD (Table 2.4) and off-axis PLD (Table 2.5) experiments. Some tests were also made on ε-Ga_2O_3 templates previously grown at IMEM-CNR (Table 2.6).

Table 2.4: Deposition parameters for most significant eclipse PLD samples. Process temperature was ~ 700 °C.

Sample #	SiO_2 (%)	O_2 pressure (mbar)	Pulses #		Pulse frequency (Hz)		Mask diameter (mm)	
			Nucleation	Growth	Nucleation	Growth		
w3268	0.1	0.01	300	150k	1	20	18	mask diameter series
w3269	0.1	0.01	300	150k	1	20	14	
w3270	0.1	0.001	300	150k	1	20	14	
w3310	0.5	0.01	300	150k	1	20	18	silicon content series
w3311	1	0.01	300	150k	1	20	18	
w3312	2.5	0.01	300	150k	1	20	18	

Table 2.5: Deposition parameters for most significant off-axis PLD samples. Process temperature and oxygen pressure inside the chamber were about 700 °C and $1 \cdot 10^{-3}$ mbar respectively.

Sample #	SiO_2 (%)	Pulses #		Pulse frequency (Hz)		Laser lens shift (mm)	QM	
		Nucleation	Growth	Nucleation	Growth			
w3306	0.5	300	90k	1	20	/	30	QM series
w3307	0.5	300	90k	1	20	/	25	
w3308	0.5	300	90k	1	20	/	22	
w3309	0.5	300	90k	1	20	/	14	
w3337	0.5	3.2k	/	5	/	/	22	optimisation of the nucleation layer
w3338	0.5	6.4k	/	5	/	/	22	
w3339	0.5	19.2k	/	5	/	/	22	
w3340	0.5	3.2k	/	20	/	/	22	
w3341	0.5	6.4k	/	20	/	/	22	
w3342	0.5	19.2k	/	20	/	/	22	
w3343	0.5	3.2k	/	10	/	/	22	
w3344	0.5	6.4k	/	10	/	/	22	
w3345	0.5	19.2k	/	10	/	/	22	
w3382	0.5	2000	50k	5	20	/	22	nucleation layer + film series
w3383	0.5	2000	50k	10	20	/	22	
w3384	0.5	2000	30k	10	20	/	22	
w3385	0.5	50k	/	10	/	/	22	
w3386	0.5	50k	/	20	/	/	22	
w3387	0.5	2000	50k	10	20	/	22	
w3394	0.5	300	90k	1	20	/	25	QM series
w3395	0.5	300	90k	1	20	/	28	
w3396	0.5	300	90k	1	20	/	25	
w3398	0.5	300	90k	1	20	10	22	lens position series
w3399	0.5	300	90k	1	20	5	22	
w3400	0.1	300	50k	1	20	/	22	dopant content series
w3401	1	300	50k	1	20	/	22	
w3402	2.5	300	50k	1	20	/	22	
w3403	5	300	50k	1	20	/	22	

Table 2.6: Deposition parameters for PLD test runs on ε-Ga_2O_3 templates. Process temperature and oxygen pressure inside the chamber were about 700 °C and $1 \cdot 10^{-3}$ mbar respectively.

Sample #	SiO_2 (%)	Pulses #		Pulse frequency (Hz)		QM	
		Nucleation	Growth	Nucleation	Growth		
w3409 (ref)	1	300	3.5k	1	15	5	standard PLD
w3410 (on cvd143)	1	300	3.5k	1	15	5	
w3411 (on ald156)	1	300	3.5k	1	15	5	
w3375 (ref)	0.5	300	50k	1	20	22	off-axis PLD
w3412 (on cvd143)	0.5	300	50k	1	20	22	
w3413 (on ald156)	0.5	300	50k	1	20	22	

CHAPTER 3 - Characterisation of epitaxial layers and fabrication of test devices

The structural, morphological, optical and electrical properties of the grown ε- and β-Ga_2O_3 epilayers were extensively investigated by different techniques, as it will be discussed in the following. Obviously, such a wide range of experimental methods implies the active collaboration with many colleagues, whose names and contributions are further detailed in the acknowledgement section.

3.1 Experimental techniques

Surface morphology of MOCVD/ALD layers was investigated in collaboration with Dr. Tatiana Berzina and Dr. Matteo Bosi. A Zeiss Auriga Compact scanning electron microscope (SEM) was employed at a typical acceleration voltage of 10 kV, applying carbon-tape/Cu stripes to the sample in order to minimise charge accumulation on the surface and consequent image drifting. Atomic force microscopy (AFM) was performed in contact mode with a Digital Instruments Nanoscope IIIa microscope. The film thickness was determined by interferometry, measuring the reflectivity fringes with a JASCO UV-VIS V-530 spectrometer. A calibration curve for the wavelength-dependent refractive index $n(\lambda)$, obtained from ellipsometric analysis (see section 3.2.4), was employed. For PLD films, the thickness was standardly determined by using a M2000 spectroscopic ellipsometer (90.73–3.23 eV, J.A. Woollam Co., Inc.) while surface morphology was studied by AFM, employing a Park System XE-150 in dynamic non-contact mode.

Crystallographic structural quality of the grown epilayers was routinely assessed by ω-2θ X-ray diffraction (XRD) scans. Measurements on ε-Ga_2O_3 MOCVD/ALD films were carried out in collaboration with Dr. Elisa Buffagni and Dr. Claudio Ferrari, by using a modified, high-resolution Philips X-ray diffractometer equipped with a Goebel mirror as monochromator to select only the CuKα lines. The beam divergence and the energy resolution were 0.01° and 10^{-3}, respectively, which permitted to resolve the CuKα_1 and CuKα_2 diffraction peaks at Bragg angles larger than about 30° and to remove the majority of instrumental artefacts. Residual small errors in the evaluation of the peak position, due to parallax error in the sample positioning, were eliminated by using the (00$\underline{12}$) sapphire peak position as a reference (θ_B = 45.354°, for c = 12.991586 Å[177] and λ(CuKα_1) = 1.54056 Å). Reciprocal lattice high-resolution maps were registered with a xPert-Pro PANalytical diffractometer, using a 4 reflection Ge 220 monochromator and a Ge 220 three-bounces crystal analyser, thus reducing the beam divergence to 10 seconds of arcsec, and achieving a wavelength

dispersion $\Delta\lambda/\lambda < 1.5 \cdot 10^{-4}$. PLD layers were measured by means of a Philips X'pert X-Ray diffractometer, equipped with a Bragg-Brentano goniometer.

Optical properties were studied in collaboration with Prof. Pier Paolo Lottici and Prof. Andrea Baraldi. Raman spectra were recorded in a backscattering geometry using a Horiba-Jobin-Yvon LabRAM micro-spectrometer, equipped with a 632.8 nm He-Ne laser, an integrated Olympus BX40 microscope and a Peltier-cooled CCD detector. The laser power was set to less than 5 mW on the sample, to avoid uncontrolled thermal effects. Spectra were collected by using an ultra-long working distance 50x microscope objective, with typical exposures of 360 s, repeated 3 times. Unpolarised absorption was measured at room temperature and normal incidence in the 800–200 nm range by means of a Varian 2390 spectrophotometer. For all absorption measurements, an epi-ready sapphire substrate was taken as reference.

Fabrication of electrical contacts on CVD films and relative electrical testing was carried out in collaboration with Dr. Enos Gombia. Electrical characterisation of PLD samples was performed in collaboration with Daniel Splith and Stefan Müller, by using a semi-automatic Süss Waferprober System P 200 and an Agilent 4155C Semiconductor Parameter Analyzer.

Crystal structure of ε-Ga_2O_3 thin films was investigated by Dr. Francesco Mezzadri and Prof. Gianluca Calestani at the Chemistry Department of Parma University by single-crystal XRD. Data were collected with a Bruker AXS Smart diffractometer, equipped with an APEX II CCD area-detector and graphite-monochromatised MoKα radiation.

Transmission electron microscopy (TEM) analysis was performed at MFA Institute (Budapest) by Dr. Ildikó Cora and Dr. Béla Pécz. Bright-field (BF) images and selected area electron diffraction (SAED) patterns were acquired onto an imaging plate detector using a Philips CM 20 TEM working at 200 kV. High-resolution TEM images and the relative SAED patterns were acquired at 300 kV using a JEOL 3010 microscope equipped with a LaB_6 cathode and a Gatan Orius CCD camera. The scanning transmission electron microscope (STEM) images were taken at 200kV in a JEOL ARM microscope, equipped with a FEG cathode and spherical-aberration correction.

Ferroelectric properties of ε-Ga_2O_3 layers were assessed at room temperature by Dr. Davide Delmonte. The measurements were performed by using a TF-Analyzer 2000E AixACcT system equipped with the Ferroelectric Module (FE-Module), according to the Dynamic Hysteresis Measurement (DHM) protocol. DHM consists in a current measurement under the application of alternate triangular voltage pulses of variable frequencies and intensities. The range of signal frequencies, provided by the FE module, ranges from 10 mHz to 5 kHz, while the maximum applied voltage amplitude can be extended from 25 V to 2 kV by using a TREK 2200 High-Voltage Amplifier (sensitivity < 1 V). By means of real-time current intensity acquisition during the application of the voltage transient, and of signal filtering with the Virtual Ground circuit methodology (VG signal), it is possible to use the frequency of the triangular bias to select the dielectric branch of the material, thus discriminating the capacitive impedance from the resistive one. This operation deeply limits the

influence of dielectric loss currents and cleans the displacement current signal from other spurious contributions (mainly the leakage currents).

Radiative recombination processes were investigated at room temperature by cathodoluminescence (CL) measurements, performed by Dr. Filippo Fabbri. A commercial Gatan monoCL system, mounted onto an S360 Cambridge Scanning Electron Microscope was used to this purpose, equipped with grating and a multi-alkali photomultiplier sensitive in the range 350–830 nm (3.6–1.5 eV). The spectra were collected with a constant power density.

Ellipsometry measurements on ε-Ga_2O_3 layers were carried out by Dr. Péter Petrik at MFA Institute, using a Woollam M-2000DI rotating-compensator spectroscopic ellipsometer, with a spot size of approximately 2 mm by 6 mm.

Photocurrent spectroscopy (PCS) measurements were performed by Prof. Maura Pavesi, using an ORIEL Mod. 66882 light source system equipped with an ORIEL Xenon - 300 W lamp and a CornerStone 130TM 1/8 m Mod. 74000 monochromator, covering the range 200–1600 nm, with wavelength-resolution of 3 nm. The chopped monochromatic light was focused on the free surface of the ε-Ga_2O_3 films between two metal contacts. The spectral distribution of the light beam was measured using a Hamamatsu Photonic Multi-Channel Analyzer PMA-11. The photon flux was varied by intercepting the light beam with optical neutral filters having optical density in the range 0.1–8.0. Voltage was applied to the contacts by means of a Source-Meter Keithley Mod. 2400.

Differential scanning calorimetry (DSC) analysis was courtesy of Dr. Detlef Klimm and was performend at Leibniz Institute for Crystal Growth (Berlin), by means of a STA 449C "Jupiter" calorimeter.

X-ray reflectivity (XRR) measurements were carried out by Michael Bonholzer, using a PANalytical X'Pert MRD PRO diffractometer.

3.2 Characterisation of ε-Ga_2O_3 CVD films

3.2.1 Standard parameters

The crystalline and morphological quality of the grown layers, that will be discussed in section 3.2.2, was reproducible over a wide range of conditions. After a series of preliminary experiments, a set of standard growth parameters was identified, as reported in Table 3.1:

Table 3.1: Reproducibility range and standard growth parameters for MOCVD of ε-Ga_2O_3 on *c*-sapphire.

Parameter type	Temperature (°C)	Pressure (mbar)	Partial pressures ratio (H_2O/TMG)	Growth rate (μm/h)
Reproducibility range	600–650	50–100	100–2500	0.35–6.5
Standard parameters	650	100	200	1.2 (avg.)

Low pressure was necessary in order to achieve acceptable values of the growth rate, while the high reactivity of TMG required to operate in water excess conditions in order to get an ordered growth. However, by increasing the H_2O/TMG partial pressure ratio the growth rate was found to decrease accordingly, so that a suitable compromise was found in the value of H_2O/TMG ~ 200. More than actual best parameters, this set represented a landmark of high-quality samples around which all the other growths were engineered. Variation of carrier flows, chamber pressure and precursors concentration, within a reasonable amount, only led to changes in the growth rate and in the homogeneity of the growth front, with only a slight influence on the surface roughness and no appreciable effect on the crystalline quality.

The sample thickness as a function of the growth time is shown in Figure 3.1 for standard growths of different duration. It is worth noting that the standard growth rate value reported in Table 3.1 is only an average, as it was seen to slightly decrease after an initial, faster growth stage. Moreover, due to the horizontal reactor geometry and to lack of substrate rotation, the growth rate was higher at the inlet with respect to the outlet side of the substrate. This gradient varied strongly when changing partial pressures, gas flows and growth times, ranging between 30–50% for 1 inch wafers and 50–80% for 2 inch wafers. As it will be shown in section 3.2.6, in the final period of this thesis some improvements to the reactor were brought about, which also allowed to increase the thickness homogeneity.

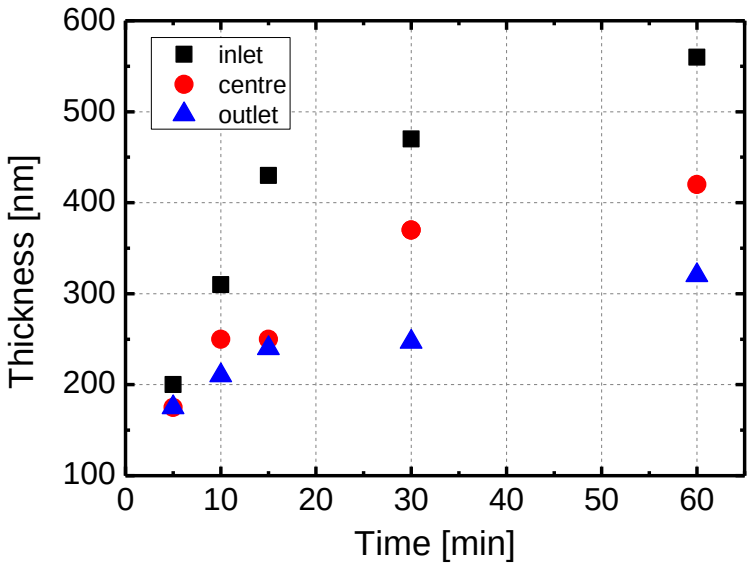

Figure 3.1: Thickness of standard samples after different growth times.

Contrary to other parameters, the temperature window played a crucial role in determining both film quality and the grown phase. Figure 3.2a and Figure 3.2b show SEM images and high-resolution XRD profiles, respectively, of samples grown at different temperatures on *c*-sapphire substrates.

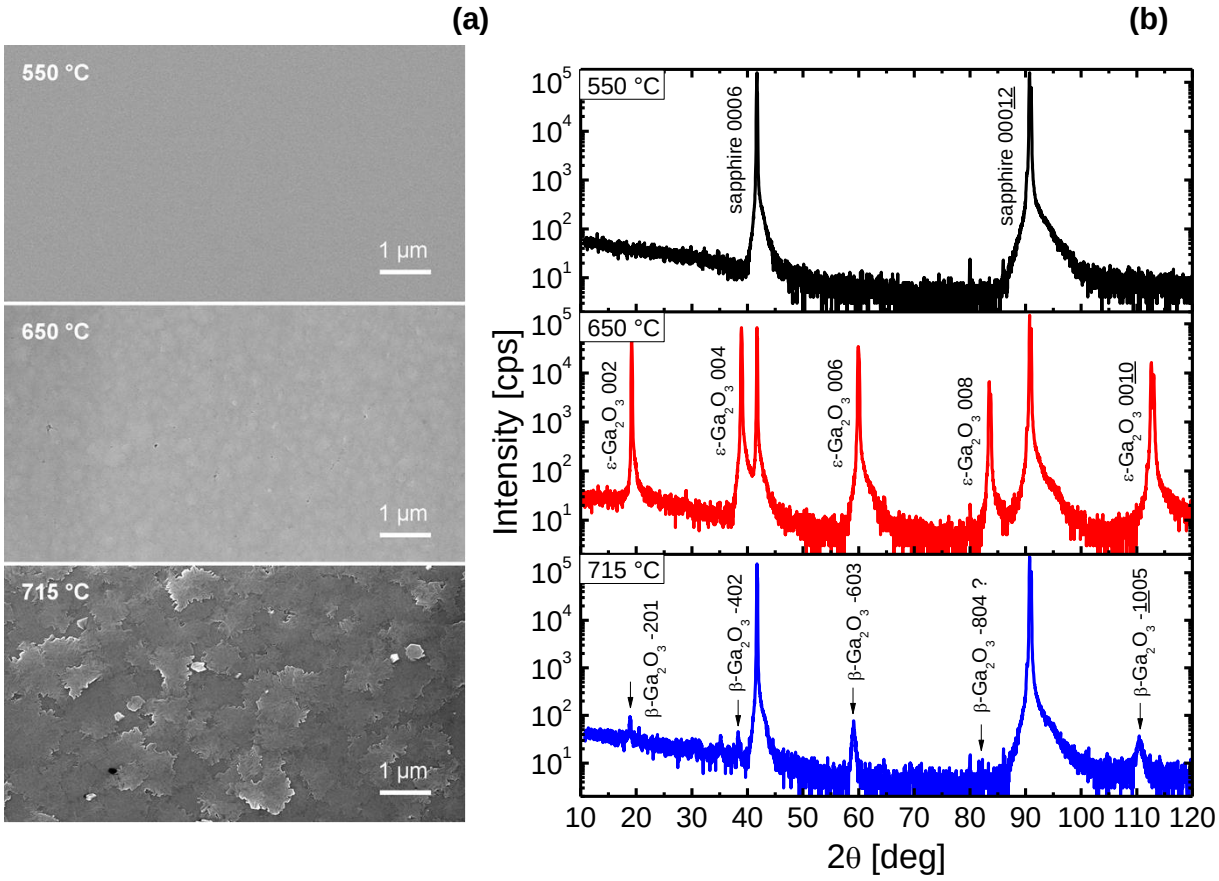

Figure 3.2: Ga_2O_3 samples grown at different temperatures on *c*-plane sapphire: (a) SEM images and (b) high-resolution XRD scan profiles. The thickness of the layers is 270, 200 and 250 nm corresponding to T = 550, 650 and 715 °C, respectively. (From Boschi *et al.*[148])

For a growth temperature of 550 °C, very smooth layers were obtained, as confirmed by the presence of interference fringes in reflectivity spectra. However, despite their excellent morphology shown by SEM analysis, X-ray profile scans only displayed the typical α-Al_2O_3 reflections from the substrate, thus suggesting the amorphous character of the deposited layers.

At a deposition temperature of 715 °C, weak and broad peaks corresponding to (-201) planes of β-Ga_2O_3 were observed, in addition to those of sapphire. The lattice parameters extracted from these XRD profiles matched well those of the (-201) plane of the bulk material[37], namely: a = 12.21 Å, b = 3.04 Å, c = 5.80 Å and β = 103.8°. The poor crystalline quality of these layers, connected to the low intensity and wide angular spread of the XRD peaks, was also reflected by an irregular surface morphology. This result is not surprising, since good crystalline β-Ga_2O_3 is usually obtained at much higher deposition temperatures[15,119,120].

On the other hand, films grown between 600 and 650 °C were reproducibly smooth, with five very intense and narrow X-ray diffraction peaks in the 2θ interval 0–120°. These peak positions, located at 19.2°, 38.9°, 59.9° 83.5° and 112.6°, are commonly ascribed to the {001} diffraction planes of ε-Ga_2O_3[32,149].

3.2.2 Crystalline and morphological quality

Layers grown with standard parameters, or within the reproducibility interval, exhibited both high crystalline and morphological quality. Figure 3.3 shows 4th and 5th order diffractions of a 1.6 μm ε-Ga_2O_3 epitaxial layer grown on *c*-sapphire compared to a (-201)-oriented β-Ga_2O_3 bulk sample. The film peaks are so sharp that the splitting CuKα$_1$-CuKα$_2$ is clearly visible at their very top, while their intensity is almost comparable to the one of the bulk material. From the (00$\underline{10}$) peak position (2θ = 112.58 ± 0.02), assuming full relaxation, a lattice spacing *d* = 9.258 ± 0.001 Å is obtained, which corresponds to the *c* lattice parameter and is slightly larger with respect to the one reported by Playford *et al.*[35] in a microcrystalline ε-β mixed phase. At this point, it is important to stress that in order to discern β- from ε-Ga_2O_3 via ω-2θ scans a good crystal quality, as in the present case, and the measurements of high order XRD peaks are necessary. Due to similar inter-plane spacing along the growth direction, respectively (-201) and (001), the first three Bragg diffractions are in fact almost overlapping. It could be that this fact was overlooked in some of the previous reports on β-Ga_2O_3 thin films grown at low temperature.

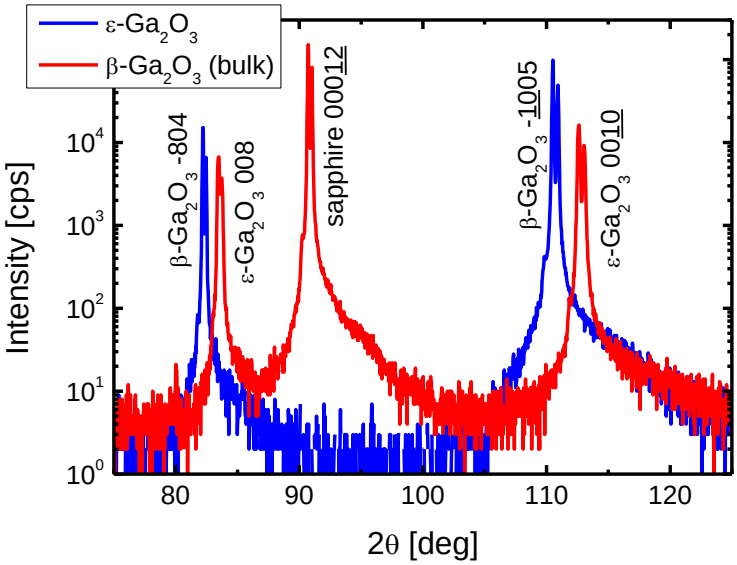

Figure 3.3: High-order diffraction peaks of a 1.6 μm ε-Ga_2O_3 epitaxial film grown at 650 °C on *c*-sapphire compared to bulk (-201) β-Ga_2O_3. (From Boschi *et al.*[148])

More quantitative information about the crystallinity of the deposited layers were obtained by reciprocal space maps, which were recorded in the vicinity of the (004) diffraction peak (see Figure 3.4) in order to allow comparison with other works. The measured mosaic spread, corresponding to a transverse omega-scan, was limited to 0.3°. This value is comparable to previously reported rocking-curves FWHMs of ε-Ga_2O_3 epitaxial films grown on β-Ga_2O_3, and about twice smaller than the values obtained on other heterosubstrates[32,149]. In the orthogonal direction of the reciprocal space, the peak FWHM is less than 0.02°. This quantity is reversely related to the dimension of the crystallites, and a small value is thus usually regarded as an index of good crystallinity. In the present case, it is a further evidence that the lattice spacing along the growth direction is very well defined.

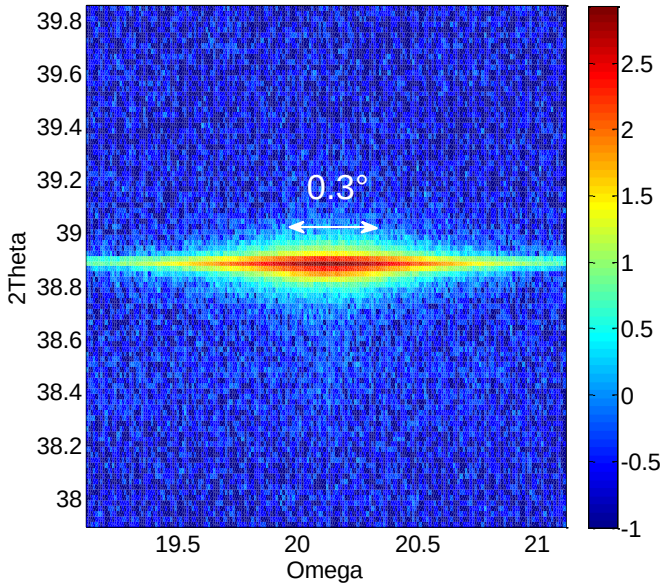

Figure 3.4: Reciprocal lattice map reporting the Log of the diffracted intensity in angular coordinates near the (004) diffraction peak of a 1.3 μm thick ε-Ga_2O_3 sample grown on *c*-sapphire. The map shows a mosaic spread of 0.3° and a negligible FWHM (about 0.02°) along the orthogonal axis.

Surface morphology was investigated by SEM and AFM (Figure 3.5), revealing a root mean square (RMS) roughness ranging between 1 nm and 4 nm. The latter value usually corresponds to sample areas close to the gas inlet, where, as previously discussed, the growth rate is higher due to non-optimised flow-dynamic conditions and lack of substrate rotation.

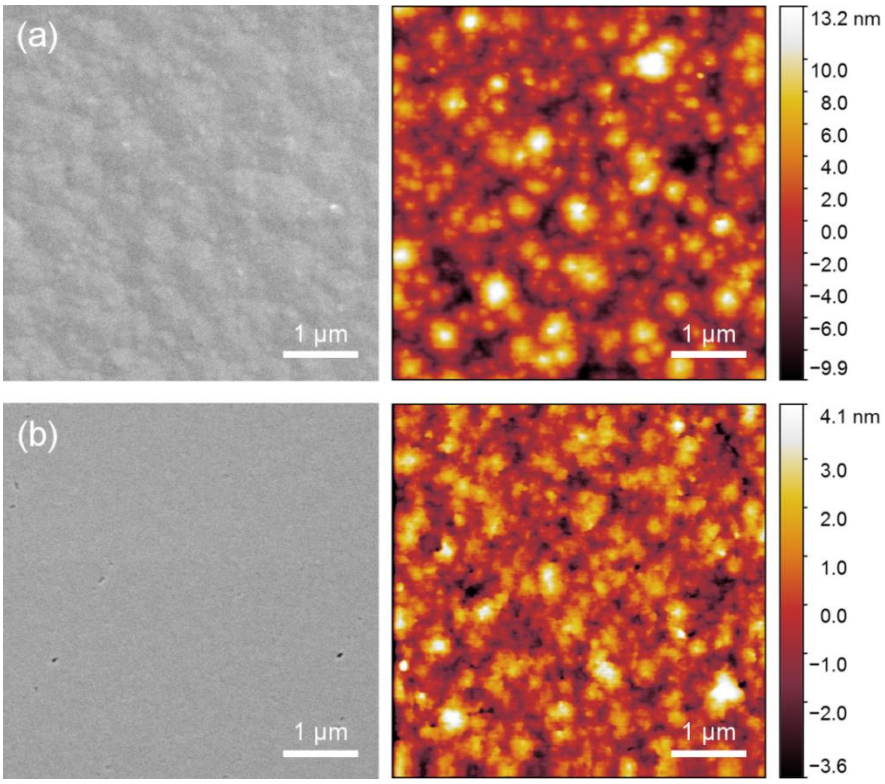

Figure 3.5: SEM and AFM scans of inlet (a) and outlet (b) regions of a sample grown at 650 °C on *c*-sapphire. Thickness is 300 nm and 210 nm and the measured RMS roughness is 3.8 nm and 1.2 nm, respectively in (a) and (b). (From Boschi *et al.*[148])

This difference in thickness between inlet and outlet regions was however exploited in very thin ε-Ga_2O_3 samples to get useful hints about the growth mechanisms on *c*-sapphire, as far away from the reagent inlets the film did not cover the substrate entirely. A sequence of three images recorded on the same sample while moving from the outlet to the inlet side, thus capturing growth interruption at different stages, is shown in Figure 3.6. It is clear that the growth proceeds via formation of small oriented nuclei (5–10 nm in size, see left side of Figure 3.6a) that expand up to give large and flat hexagonal islands (size of 200–400 nm), which ultimately merge producing a flat and homogeneous film (Figure 3.6b), up to complete closure (Figure 3.6c).

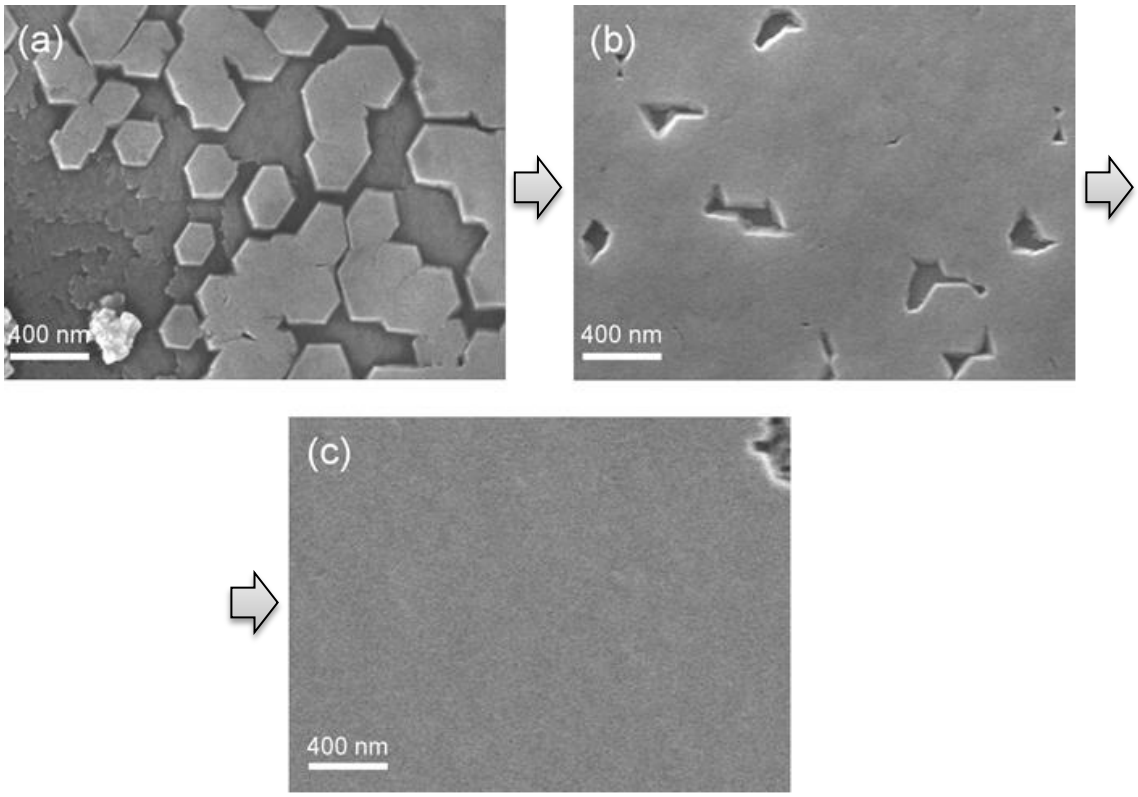

Figure 3.6: SEM images showing three regions of the same sample in which the growth has reached three different stages. (a): Starting nucleation and coalescence of hexagonal islands. (b): Islands merging, where hexagon-shape edges are still visible. (c): Film closure. (Adapted from Boschi *et al.*[148])

In order to get further insight about formation of the ε-phase, the effects of employing different substrates were also investigated. SEM images and XRD scan profiles of samples deposited on (0001) GaN, (111) 3C-SiC and (001) 3C-SiC templates, at the same growth temperature of 650 °C, are shown in Figure 3.7 and Figure 3.8, respectively.

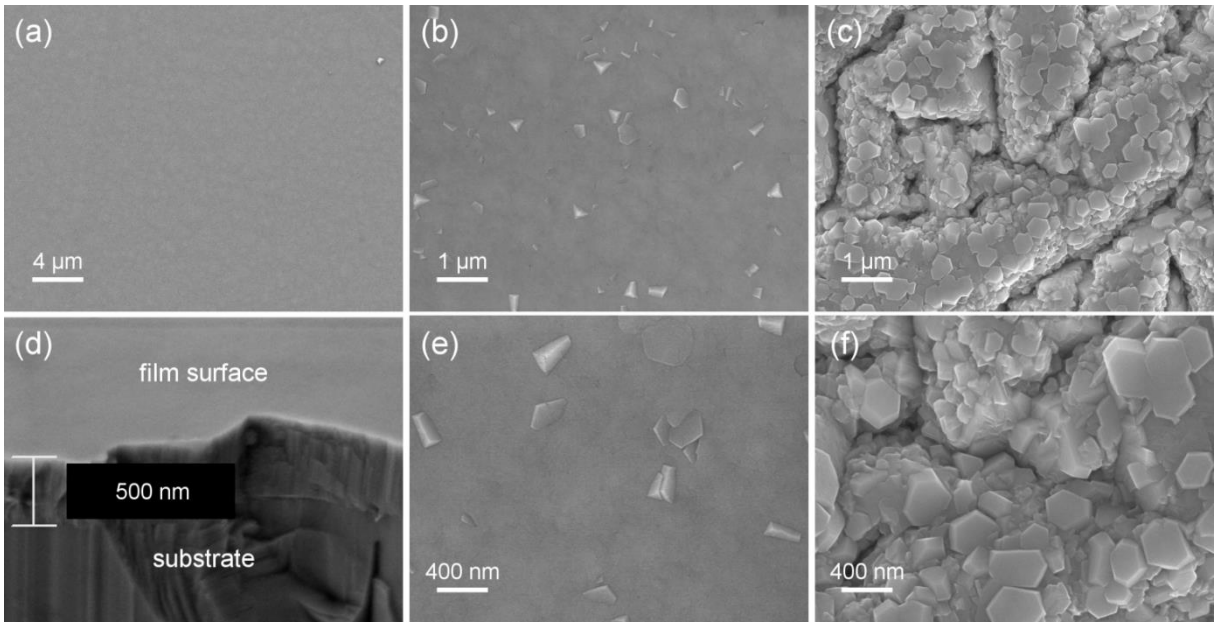

Figure 3.7: SEM images of the surface of ε-Ga_2O_3 samples grown at 650 °C on different templates. (a),(d): Surface and cross-section of a film grown on a *c*-plane GaN template. (b),(e): Different magnifications of a 610 nm thick film on (111) 3C-SiC. (c),(f): Different magnifications of a 530 nm thick film on (001) 3C-SiC. (Partially adapted from Boschi *et al.*[148])

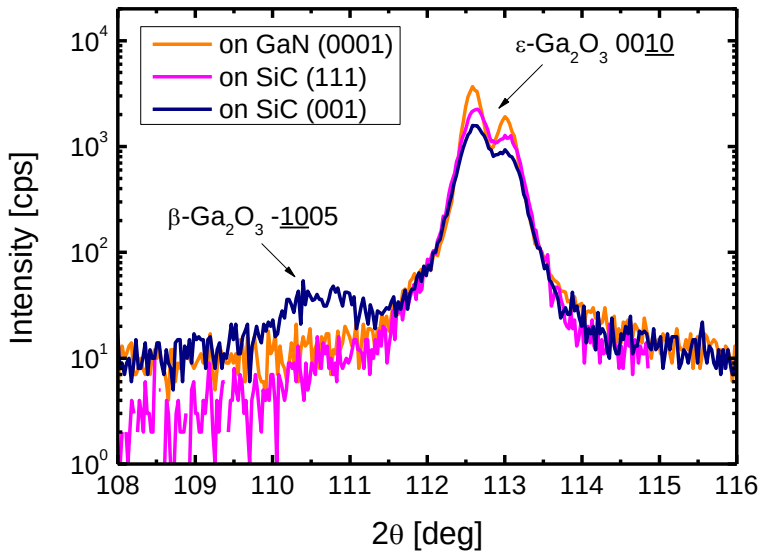

Figure 3.8: (00$\underline{1}$0) diffraction profiles of ε-Ga_2O_3 grown at 650 °C on different templates. Lower-order peaks are not shown in order to avoid an overcrowding of the spectrum, as the contributions from different templates and substrates are present. (From Boschi *et al.*[148])

The good matching to GaN, also discussed by Oshima *et al.*[32], was confirmed by both surface smoothness and XRD high perfection, proving GaN to be another promising substrate for hetero-epitaxial growth of ε-Ga_2O_3.

The XRD profile exhibited comparable intensity and sharpness also in the case of the film grown on (111) 3C-SiC template, despite the cubic symmetry of this material. This can be explained by taking into consideration the hexagonal arrangement (ternary symmetry) of the atoms along this specific plane of 3C-SiC. Note that the ε-Ga_2O_3 film also maintained an acceptable morphology and exhibited

only scattered faceted defects on the surface. On the contrary, the different crystal structures between substrate and thin-film had drastic consequences when growth was performed on the (001) plane of 3C-SiC. Here, morphological and structural disorder increased dramatically, and even β-Ga_2O_3 was revealed as secondary phase by XRD. However, it is worth stressing that the ε-phase remained dominant, as demonstrated by both XRD and SEM analysis. In particular, the latter suggests that, after a first step in which the growth was disordered or even polycrystalline, hexagonal islands took over and expanded up to coalesce on the top of different large grains. This behaviour becomes even more evident in thicker regions of the same sample (Figure 3.9). Despite the substrate having a completely different symmetry, the ε phase is hence clearly the dominant one. This is a further proof that within these growth conditions ε-Ga_2O_3 is favoured and reproducible.

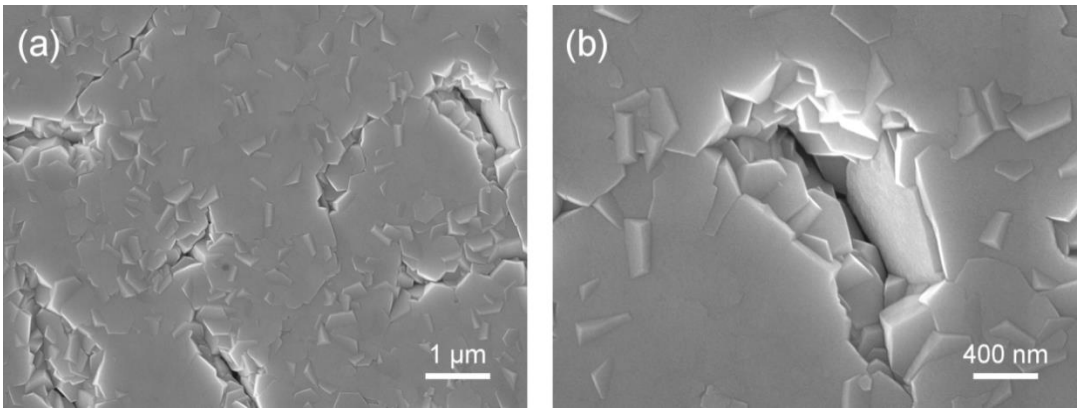

Figure 3.9: SEM images of the same ε-Ga_2O_3 sample grown on (001) 3C-SiC shown in Figure 3.7c, acquired at different magnifications and within a thicker region.

Hence, even though the presence of a substrate with an in-plane hexagonal arrangement of the atoms appears to be more favourable for nucleation and coalescence of ε-Ga_2O_3 hexagonal islands, the results obtained on different templates confirm that, within our MOCVD process, the growth temperature is the crucial factor which ultimately decides the crystal structure of the epilayers.

However, this experimental evidence seems to contradict previous results, where a more marked dependence of the obtained phase on the employed substrate was observed. For example, mist-CVD of Ga_2O_3, carried out at low temperature and atmospheric pressure, resulted in the formation of the α-phase when performed on *c*-sapphire[178] and of the γ phase when performed on (100) $MgAl_2O_4$[179]. Further, Oshima *et al.*[180] reported that HVPE of Ga_2O_3 on *c*-sapphire at 550 °C actually produced a pure α-phase. In a later work on HVPE of ε-phase[32], the same authors confirmed that the low deposition temperature was important in order to prevent the formation of the β phase, but also stated that the key factor for obtaining the ε polymorph was to use a substrate with hexagonal structure, such as GaN or AlN, which indeed belongs to the same space group $P6_3mc$ proposed by Playford *et al.*[35] for ε-Ga_2O_3. In our case, low-pressure MOCVD between 600 and 650 °C always resulted in single-phase ε-Ga_2O_3, independently on the employed substrates, including *c*-sapphire and even cubic silicon carbide, provided that the latter was (111) oriented. The type of reagents and the lower pressure of our

system, together with the different surface kinetics and lower growth rates, probably play a major role in nucleating the ε phase. The substrates and templates employed in the present work are summarised in Table 3.2.

Table 3.2: Substrates and templates employed for the MOCVD growth of ε-Ga_2O_3 thin films, with the respective surface orientation and 2D in-plane lattice parameters.

Material	Plane	In-plane lattice parameters		Lattice mismatch
		a (Å)	Angle (°)	
ε-Ga_2O_3	00(0)1	2.9036[35]	120°	-
		2.880 (present)	120°	-
α-Al_2O_3	0001	4.7592[177]	120°	+65% (nominal) +4.8% (real, due to lattice rotation)
GaN	0001	3.1890[181]	120°	+10.7% (nominal)
3C SiC	001	4.3596[182]	90°	-
3C SiC	111	3.0827	120°	+7.0% (nominal)

Despite all previous considerations, growth of ε-Ga_2O_3 on *c*-sapphire may still seem unfavourable due to the large difference in lattice parameters. In order to understand why it takes places successfully, the relative orientation of the two lattices was investigated. In particular, the high crystalline quality of the thin films allowed to perform single-crystal XRD measurements. In Figure 3.10 the precession images reconstructed on the basis of reciprocal space data collected on a 3 μm thick sample are reported.

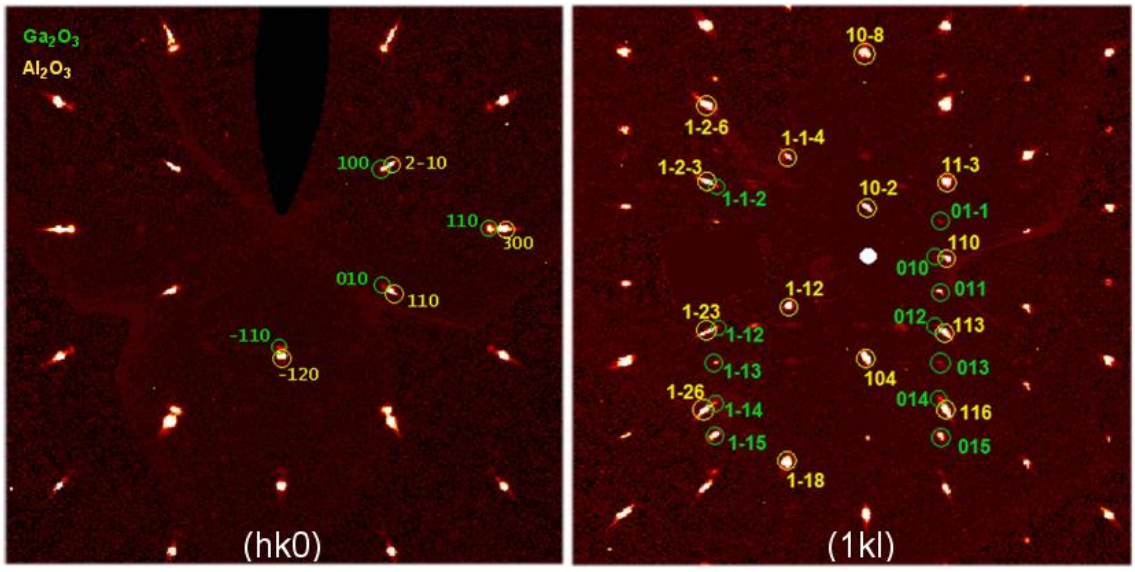

Figure 3.10: (*hk*0) and (1*kl*) precession images reconstructed by single-crystal diffraction data. Reconstruction was carried out by using the Precession Images plugin available in the Bruker APEX2 software. (Partially adapted from Mezzadri *et al.*[183])

While the difference in the ***c***-axes gives rise to a more complex pattern in the (1*kl)* plane, the (*hk*0) image shows the presence of two almost coincident hexagonal lattices with slightly different *d*-spacing. In spite of the small film thickness, ε-Ga_2O_3 diffraction peaks are well defined and relatively intense. No extra peaks or powder rings were detected, thus further highlighting the good quality of the layers. The [10-10] direction of Ga_2O_3 is aligned with the Al_2O_3 [11-20] one, indicating that the two hexagonal Bravais lattices are rotated in the *ab* plane by 30° with respect to one another, as depicted schematically in Figure 3.11.

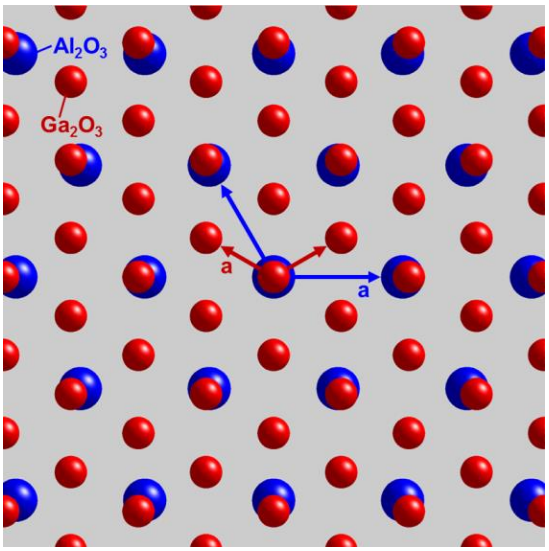

Figure 3.11: Superimposition of the *c*-plane, 2D Bravais lattices of Al_2O_3 and Ga_2O_3, rotated by 30 degrees with respect to each other in order to reduce the effective mismatch.

The in-plane lattice parameter *a* was assessed by high resolution XRD in ω-2θ configuration, by measuring the asymmetric (11-26) diffraction profiles in grazing incidence and emergence conditions, with a ϕ = 53.1° inclination of the (11-26) planes with respect to the (0001) surface (Figure 3.12).

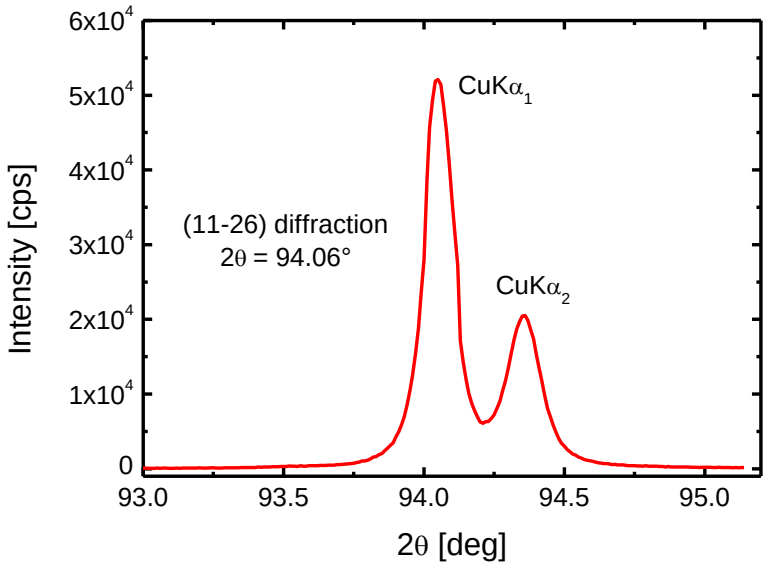

Figure 3.12: Asymmetric (11-26) diffraction profile of a representative ε-Ga_2O_3 film.

Since in a hexagonal crystal the lattice spacing *d* is expressed as a function of Miller indices (*h, k, l*) and lattice parameters (*a, c*) by the formula[184]:

$$\frac{1}{d^2} = \frac{4}{3}\left(\frac{h^2 + hk + k^2}{a^2}\right) + \frac{l^2}{c} \tag{3.1}$$

by taking the averaged measured (11-26) peak position 2θ = 94.06 ± 0.01° for the CuKα_1 line, and by using the previously calculated c = 9.258, we obtain a value for the in-plane lattice parameter a = 2.880 ± 0.001 Å, which is slightly smaller than the one reported by Playford *et al.*[35] (see Table 3.2). Based on this result, it can be concluded that the 30° rotation between film and substrate allows to strongly reduce the lattice mismatch between ε-Ga_2O_3 and *c*-sapphire from +64% to +4.8%.

However, as it will be thoroughly discussed in the following section, it must be stressed in advance that this hexagonal symmetry, always observed by XRD in standard samples, is only an averaged behaviour which is connected directly to the hexagonal lattice formed by oxygen ions. The latter is exactly described by the aforementioned lattice parameters, while at the nanoscale the distribution of gallium sites gives rise to a shorter-range order, lowering the local symmetry. Nevertheless, the description in terms of the hexagonal oxygen lattice remains valid, and effectively helps to describe both the orientation with respect to the sapphire substrate and the supposed growth mechanism.

3.2.3 Crystal structure determination and ferroelectricity

As anticipated during the introductory section, the exact crystal structure of ε-Ga_2O_3 has been up to now matter of debate, especially regarding its space group being hexagonal or orthorhombic. This gave rise to contradictory publications, none of which managed to provide an ultimate solution that could reconcile both points of view. Being among the first to have pure ε phase samples at our disposal for characterisation, we were able to carry out a full structural investigation with the aim to solve the ambiguities found in literature. The excellent quality of the ε-Ga_2O_3 layers grown at IMEM-CNR made observations within a single-crystal diffractometer possible, while TEM analysis corroborated the results and gave further fundamental insights about the local film structure. The results of these analysis were summarised in two publications[183], one of which is currently under review (see Appendix B).

Two samples with different thickness (3 μm and 10 μm, respectively) were specifically grown for single crystal XRD measurements and were then properly prepared in order to maximise the diffraction intensities of the film with respect to the ones of the sapphire substrate. For the thinner sample, the substrate thickness was mechanically reduced with a lapping machine down to about 200 μm by using 60 grit sandpaper. Further mechanical cleavage ultimately allowed to obtain a small fragment with approximate dimensions 193×64×16 μm^3, the latter being the total thickness of sapphire plus the 3 μm film, thus reducing by orders of magnitude the intensity of the reflections from the substrate. At the same time, by increasing the sample-to-detector distance from 50 to 70 mm, it

was possible to isolate the diffraction spots of the Ga_2O_3 phase. In this way, the ε-Ga_2O_3 intensities could be accurately determined despite the strong Al_2O_3 reflections, which in a first instance impeded accurate measurements, in particular at low theta values. On the other hand, a sample suitable for single crystal diffraction experiments was obtained from the 10 μm film by simple mechanical removal of a 100×100×10 μm^3 fragment.

Cross-sectional and plan-view samples for TEM analysis were prepared by Ar ion beam milling from a 250 nm film, expressly grown for the purpose. A few nm thin amorphous carbon layer was evaporated on the film surface, in order to reduce charging effects.

Averaged structure

Despite the presence of Al_2O_3 on one side of the 3 μm sample, the quality of the data was not dramatically influenced by asymmetrical absorption, allowing for reliable structural solution and refinement. These procedures were carried out within the SIR2011[185] suite and the SHELXL[186] software, respectively. The cell parameters, refined by using the positions of 46 reflections in the theta range 4.401–19.914°, are a_h = 2.9081(7) and c_h = 9.262(3) Å. Despite the different technique and instrumentation employed, these values are in good agreement with those reported in section 3.2.2. The analysis of systematic absences, showing reflection conditions hh-2hl = 2n and 000l = 2n, is compatible with the $P6_3/mmc$, $P\bar{6}2c$ and $P6_3mc$ space groups. While the structure solution process failed in the first two cases, a plausible result was obtained for the $P6_3mc$ space group. Crystal data and refined parameters are summarised in Table 3.3, while the structure model is shown in Figure 3.13.

Table 3.3: Crystal structure and refined parameters obtained by single-crystal XRD of a 3 μm thick ε-Ga_2O_3 film. (From Mezzadri *et al.*[183])

s.g. $P6_3mc$ (n. 186)
a = 2.9081(7), c = 9.262(3) Å
V = 67.8(5) $Å^3$
ρ = 6.106 g/cm^3

Atom	Site	x	y	z	s.o.f	Ueq.
GA1	2b	0.66667	0.33333	0.4269(9)	0.6667	0.0291(15)
GA2	2b	0.66667	0.33333	0.2167(11)	0.35(2)	0.0291(15)
GA3	2b	0.66667	0.33333	0.6210(17)	0.318(18)	0.0291(15)
O1	2b	0.33333	0.66667	0.323(4)	1	0.025(5)
O2	2a	0	0	0.558(3)	1	0.025(5)

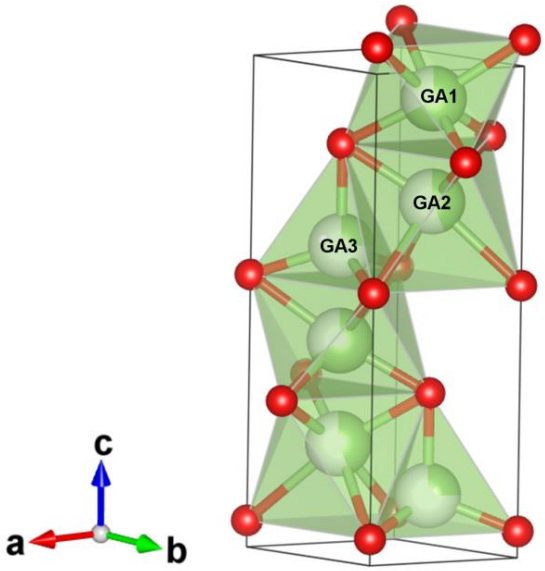

Figure 3.13: ε-Ga_2O_3 $P6_3mc$ structure model. Green balls represent gallium ions, red balls oxygen. (Adapted from Mezzadri *et al.*[183])

The structure obtained by XRD analysis of the thinner sample thus consists of an hexagonal 4H stacking of close-packed oxygen layers, in which, similarly to β-Ga_2O_3, both the octahedral and tetrahedral cavities are occupied by gallium ions. In this case, within two adjacent oxygen layers, the cavities are statistically occupied, so that the correct Ga_2O_3 stoichiometry is guaranteed by Ga vacancies. Two types of layers alternate along the stacking direction: within the first one, only the octahedral cavities (GA1) are occupied in a 2/3 ratio, whereas in the second one both octahedral (GA2) and tetrahedral (GA3) sites are possible. The independent refinement of GA2 and GA3 occupancies indicates that the two sites are statistically occupied in a mutually exclusive way, maintaining the stoichiometric cation-to-oxygen ratio. Indeed, the statistical occupation of the cationic sites in a cell with a reduced volume (to which a low density of reflections in the reciprocal space is related), leads to a noticeable increase of the number of parameters needed for describing the structure, reducing the data-to-variable ratio. Nonetheless, the obtained results are highly reliable and the refinement converged with agreement indices R_1 = 0.0621 for 65 $F_o > 4\sigma(F_o)$ and R_1 = 0.1123 for all 101 data, and a goodness of fit *GOF* = 1.077.

The average bond lengths and the results of charge distribution analysis are reported in Table 3.4. If compared to β-Ga_2O_3, the average bond distances of the ε phase are in general longer. The charge distribution analysis, performed with the CHARDIS99[187] program and by making use of bond strength-bond length relations, indicates formal oxidation states quite close to the 3+ value expected on the basis of the refined stoichiometry.

Table 3.4: Average interatomic distances and effective formal oxidation states divided by the occupancy (Q(ij)/s.o.f.) obtained by single crystal XRD of a 3 μm thick ε-Ga_2O_3 film. (From Mezzadri *et al.*[183])

Atoms	Avg. bond length (Å)	Q(ij)/s.o.f
GA1-O	2.006(18)	2.968
GA2-O	2.087(19)	2.889
GA3-O	1.80 (2)	3.176

The structure refined from the 3 μm samples would thus seem in good agreement with the one proposed by Playford *et al.*[35]. Unfortunately, this kind of approach was unable to clarify whether the fractional occupation of gallium sites is to be ascribed to merely statistical occupancy or to short-range ordered domains. The answer was given unambiguously by TEM analysis, and corroborated by further XRD measurements of the thicker sample.

Local structure

A cross-sectional TEM image of the 250 nm film is shown in Figure 3.14. The ε-Ga_2O_3 layer has a columnar structure, revealed by amplitude and phase contrast, with columns of about 2–5 nm in diameter and characterised by an orthorhombic symmetry. Even though ε-Ga_2O_3 constitutes most of the grown sample, at the interface with the substrate a different phase is observed. SAED investigation of this very thin region (10–20 nm) identifies the latter as cubic γ-Ga_2O_3[39]. The occurrence of this interfacial phase is unexpected and its presence became evident only after specific TEM investigations. Although its role may be important to understand the growth mechanism of ε-Ga_2O_3 on sapphire, its origin and evolution are still unclear. This γ phase could for instance form as buffer layer at the interface to promote the nucleation of the more stable ε-Ga_2O_3 (see for example the stabilisation of α-Ga_2O_3 during heteroepitaxy of β-Ga_2O_3 on *c*-sapphire[96]), or it could be, on the contrary, a degradation product. In order to understand if and how the γ phase evolves with thickness and prolonged growth processes, further TEM analysis is currently in progress on samples grown with different parameters and processing times.

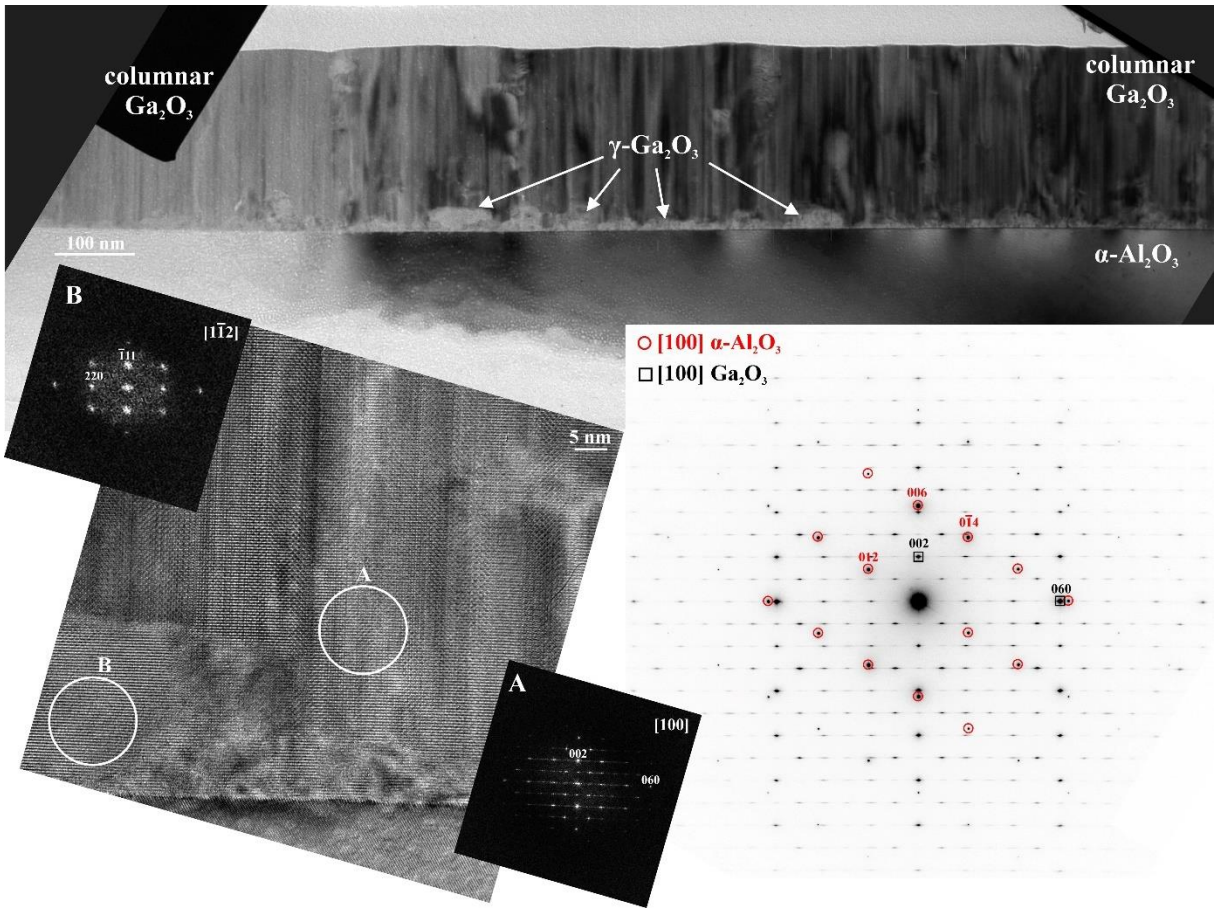

Figure 3.14: Cross-sectional TEM BF image, SAED pattern and HRTEM image with the corresponding FFTs ("A" and "B") of the 250 nm ε-Ga_2O_3 thin film on *c*-sapphire. At the interface, another phase was identified as γ-Ga_2O_3 (region and FFT labelled as "B"). The overlying phase, ε, is dominant and shows a columnar texture. The reflections were here indexed by using an orthorhombic unit cell (region and FFT labelled as "A").

More information on the columnar structure was extracted by combining the cross-sectional and plan-view observations of the film. Figure 3.15 shows the High Resolution TEM (HRTEM) images in planar-section, with the corresponding FFTs calculated from different domains. The latter represent the cross-section of the columns observed in Figure 3.14, whose diameter is confirmed to be 2–5 nm. The experimental and simulated SAED patterns are reported in Figure 3.16. Noteworthy, while the total SAED pattern (Figure 3.16b) displays a hexagonal/trigonal-like symmetry, the FFTs of the individual domains in Figure 3.15 all have the same orthorhombic character. These domains are in fact rotated by 120° with respect to each other and separated by a twin plane, which results in the pseudo-hexagonal symmetry given by the SAED pattern, as the latter originates from the simultaneous scattering by many different columns. The pseudo-hexagonal symmetry is clearly visible also in a FFT of a larger area of the HRTEM image (Figure 3.15f, Figure 3.16a) and has a similar metric and intensity distribution as the SAED pattern in Figure 3.16b.

Based on SAED patterns obtained in both cross-section (Figure 3.14) and plan-view (Figure 3.16b), it was possible to index the diffractions with an orthorhombic unit cell: a_o = 5.0 Å, b_o = 8.68 Å, c_o = 9.23 Å. Along the ***a**** and ***b**** directions some diffuse streaks are observed, confirming the presence of in-plane disorder.

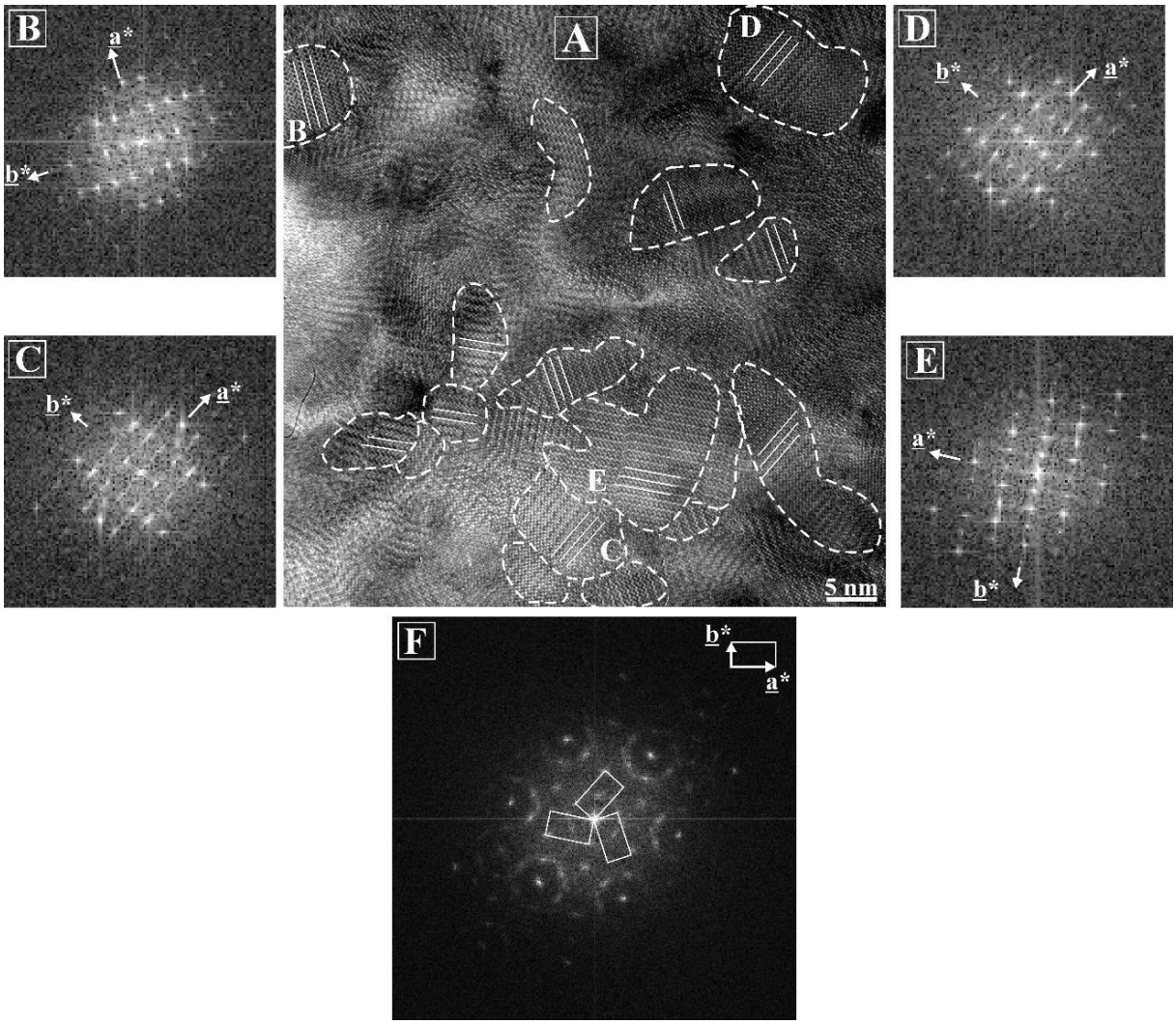

Figure 3.15: HRTEM image (A) of the plan-view section of the sample in [001] projection with 5×5 nm FFTs corresponding to different domains (B-E). Domains show orthorhombic symmetry and are rotated by 120° with respect to each other. FFT of the whole image (F) shows a pseudo-hexagonal symmetry.

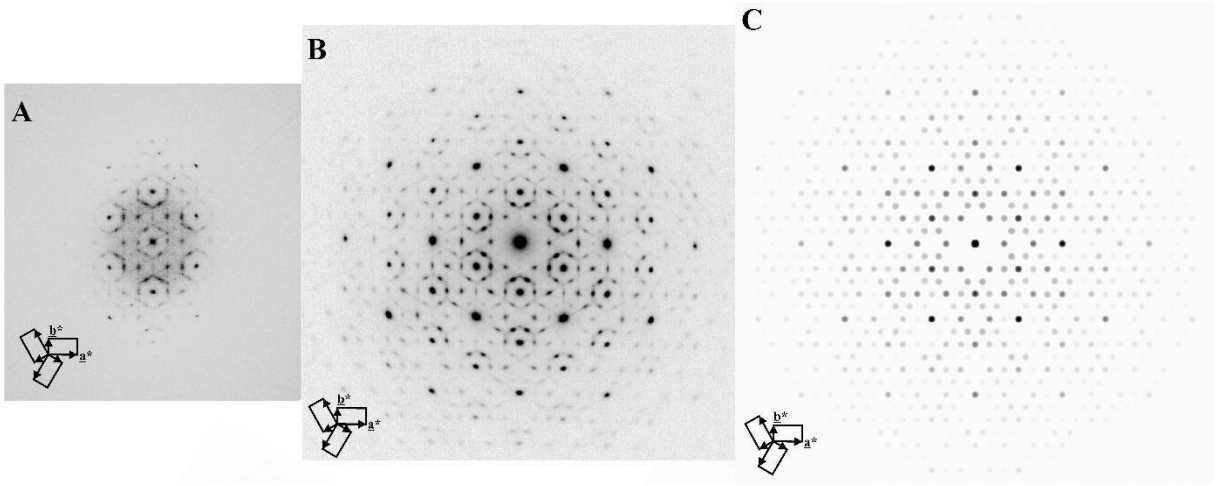

Figure 3.16: (A): Experimental FFT of the HRTEM image shown in Figure 3.15a. (B): Experimental [001] SAED pattern. (C): Simulated diffraction pattern along the [001] direction, obtained from the superimposition of three orthorhombic patterns, rotated by 120° and calculated for a 10 nm thick layer with cell parameters a_o, b_o and c_o. Simulation was performed by applying dynamical approximation for JEOL3010 microscope, using the JEMS software package. All patterns display similar intensity distributions.

Local domain structure and symmetry was further analysed by Scanning Transmission Electron Microscopy (STEM, Figure 3.17). The 2D symmetry in the *bc* plane is *cm* (here *m* is ⊥ to ***b***).

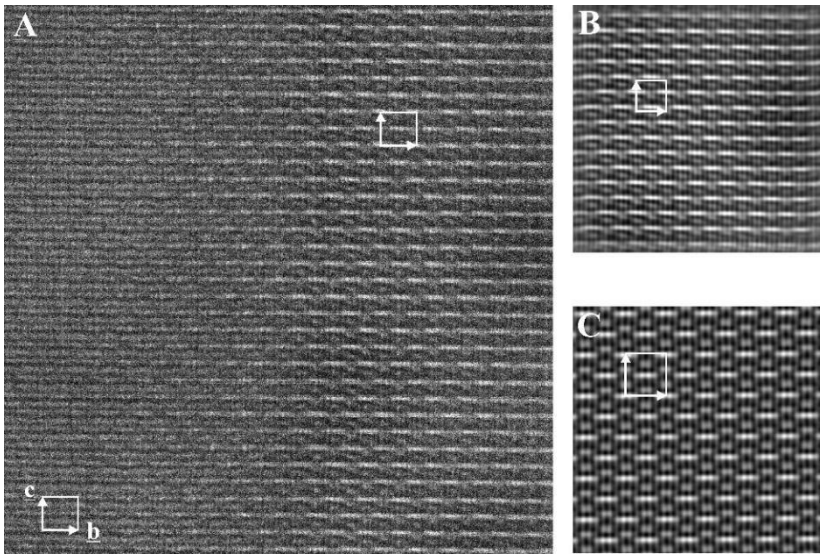

Figure 3.17: STEM images from [100] projection of the columnar ε-Ga_2O_3. (A): Raw STEM image. (B): Fourier-filtered image. (C): Symmetry averaged image using *Crisp*[188] software package. The 2D symmetry was found to be *cm*, with $m \perp \boldsymbol{b}$.

Complementary results to TEM analysis were found when the thicker film (10 μm) was measured by single-crystal XRD. The performed collection of the complete Ewald sphere using a CCD area detector allowed to elaborate the data by using the Precession Images plugin of the Bruker APEX2 software. The reconstructed precession image of the *hk*0 projection is shown in Figure 3.18.

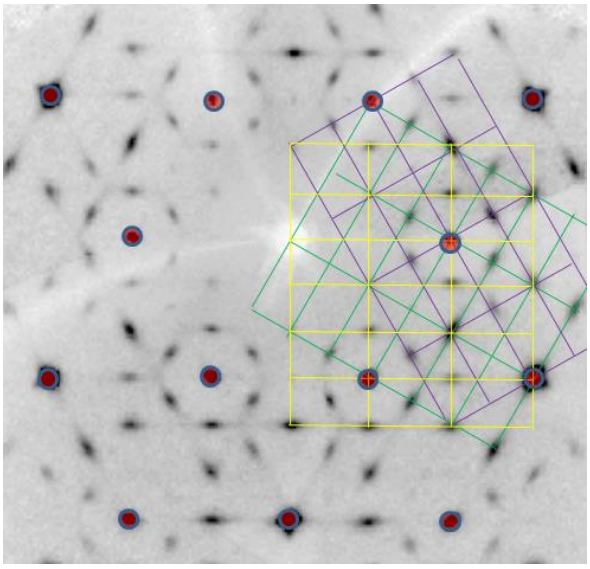

Figure 3.18: Reconstructed *hk*0 precession image of ε-Ga_2O_3, showing the superimposition of the three lattices related to the possible orthorhombic twin variants. Red spots correspond to the reflections of the hexagonal fundamental lattice, with lattice parameters a = 2.9081(7) and c = 9.262(3) Å.

This XRD pattern, showing an apparent $6mm$ symmetry, fully agrees with the SAED reported in Figure 3.16b. The diffraction spots are characterised by streaking features that represent the typical fingerprint of domains, spatially limited along an equivalent direction, rotated by 120° around the projection axis and separated by twin boundaries. Therefore, in agreement with the TEM characterisations reported in Figure 3.15, the XRD pattern can be taken as the superimposition of the diffraction from three orthorhombic lattices, rotated by 120° with respect to each other, according to the twin law:

$$\begin{pmatrix} -\frac{1}{2} & \frac{1}{2} & 0 \\ -\frac{3}{2} & -\frac{1}{2} & 0 \\ 0 & 0 & 1 \end{pmatrix} \tag{3.2}$$

By indexing of the diffraction pattern, the orthorhombic lattice parameters were refined as a_o = 5.0463(15), b_o = 8.7020(9), c_o = 9.2833(16) Å., once again in good agreement with TEM results.

Due to the partial superposition of the reciprocal lattices nodes of the twinning domains, shown in Figure 3.18, the extinction rules could not be determined unambiguously by the integrated intensities. The space group determination therefore was carried out by using the ISODISTORT software, by considering the orthorhombic lattice as a commensurate superstructure generated from the hexagonal, disordered one previously determined for the thinner 3 μm sample ($P6_3mc$, a_h = 2.9081(7), c_h = 9.262(3) Å), where the ordering of Ga-sites occupancy was in this case driven by the modulation vector $\boldsymbol{q}$ = (1/6 1/6 0). This symmetry reduction led to a limited number of possible space group for the superstructure lattice: four orthorhombic ($Pmc2_1$, $Pca2_1$, $Pmn2_1$, $Pna2_1$) and one monoclinic (Pc). Among these, only $Pna2_1$ gave good results to structural solution, in terms of both agreement indices and reliability. The procedure was carried out using the SIR2011[185] programme on merged data produced by TWINABS.

Structure refinement was then successfully carried out with SHELXL[186], the results of which are summarised in Table 3.5, while the unit cell model is shown in Figure 3.19. No deviation from complete occupancy was detected for Ga atoms, yielding the expected 2/3 gallium-to-oxygen ratio. The refined average interatomic distance is 1.83(4) Å for the tetrahedral site (GA4), while for the octahedral ones (GA1, GA2, GA3) it ranges from 2.01(4) to 2.05 (4) Å, in good agreement with the averaged $P6_3mc$ structure.

The complexity of the experimental features, in particular the presence of the twin variants, the streaking of the diffraction spots and the quasi-two dimensional character of the sample, limited to some extent a precise evaluation of the diffraction intensity. This is reflected by the final value of the agreement indices (R_1 = 0.1220, GOF = 1.212). However, the structure obtained by XRD can be considered fully reliable and consolidates the model given by TEM analysis.

Table 3.5: Crystal data and atomic parameters of the orthorhombic ε-Ga_2O_3 phase.

s.g. $Pna2_1$(n. 33)
a = 5.0463(15), b = 8.7020(9), c = 9.2833(16) Å
V = 407.66(15) Å^3
ρ = 6.108 g/cm^3

Atom	Site	x	y	z	s.o.f	Ueq.
Ga1	4a	0.1833(8)	0.3398(4)	0.0287(4)	1	0.0023(7)
Ga2	4a	0.6749(9)	0.5297(5)	0.0360(6)	1	0.0023(7)
Ga3	4a	0.1904(9)	0.6531(8)	0.2504(4)	1	0.0023(7)
Ga4	4a	0.1733(8)	0.6525(8)	-0.1614(4)	1	0.0023(7)
O1	4a	0.357(8)	0.497(3)	0.138(4)	1	0.01
O2	4a	-0.018(9)	0.493(3)	-0.092(5)	1	0.01
O3	4a	0.334(7)	0.156(4)	0.140(4)	1	0.01
O4	4a	0.845(7)	0.674(4)	0.169(4)	1	0.01
O5	4a	0.006(9)	0.830(4)	0.409(4)	1	0.01
O6	4a	0.501(10)	0.665(4)	-0.096(4)	1	0.01

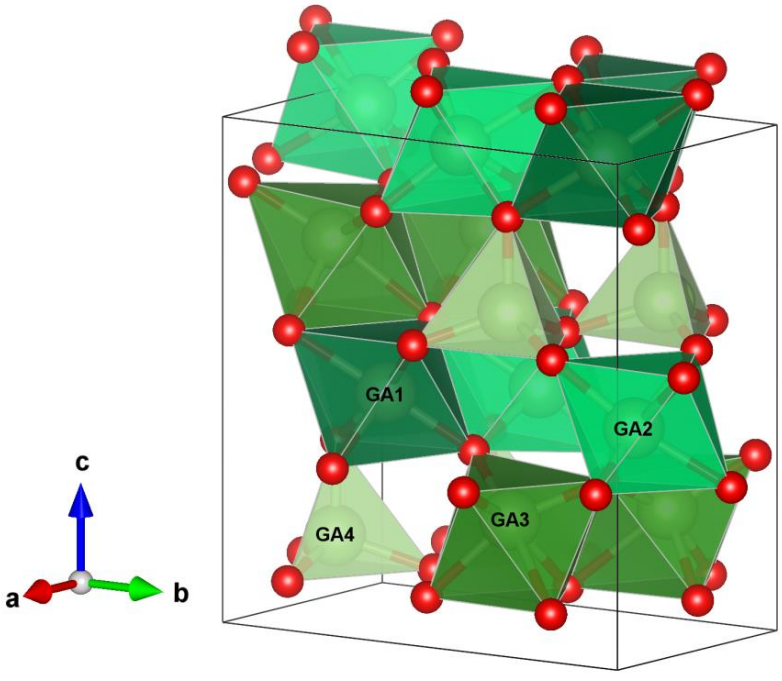

Figure 3.19: ε-Ga_2O_3 $Pna2_1$ structure representation. Green balls are gallium ions, red balls oxygen. Different gallium sites are represented with different shades of green for the respective coordination polyhedra.

Structural model

By taking into account the combined results from XRD and TEM, a comprehensive structural model for the ε-Ga_2O_3 can thus be provided. The structure is unambiguously orthorhombic and can be considered as a 4H (ABAC) close packed stacking of oxygen atoms, in which the cavities are occupied by gallium cations following an ordering scheme that keeps for each layer the 2/3 stoichiometric ratio (Figure 3.20). Two cationic layers alternate along the ***c***-axis, one formed by just octahedrally coordinated Ga and the other one by both tetrahedrally and octahedrally coordinated Ga in 1:1 ratio. The stacking sequence is such that two equivalent layers, shifted by half-cell along ***c***, are inverted in the *ab* plane by action of the 2_1 axis.

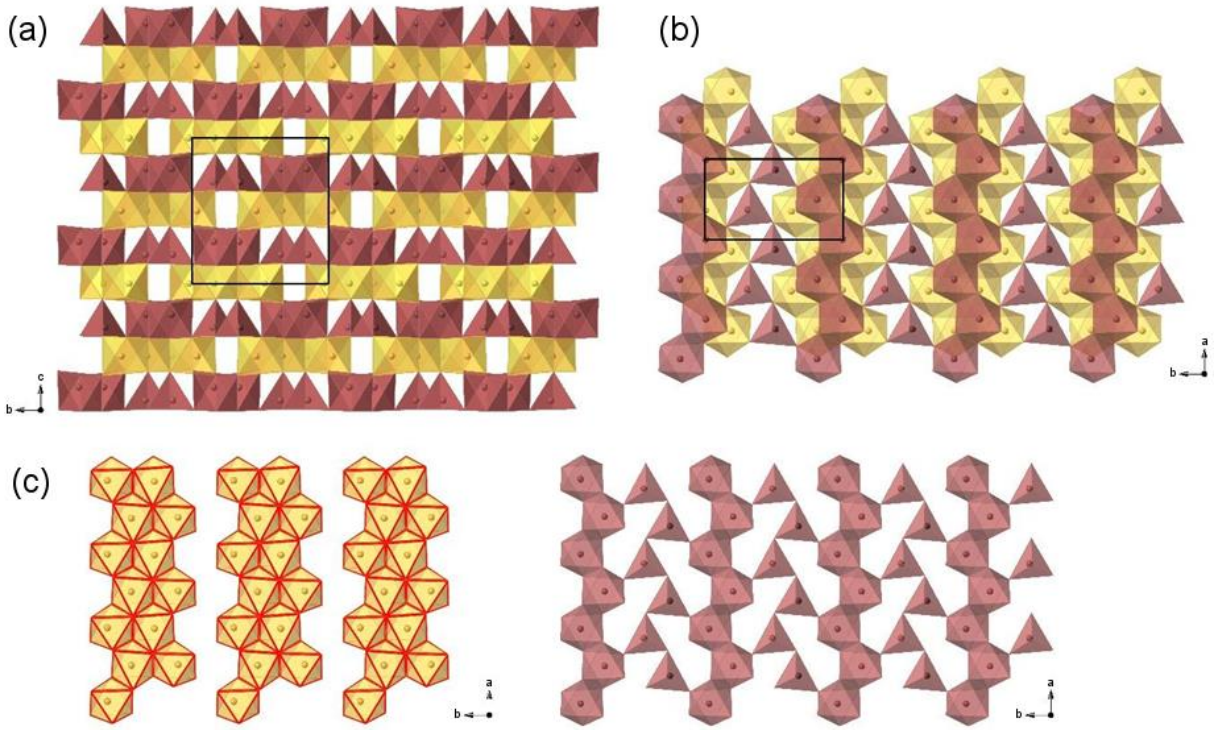

Figure 3.20: ε-Ga_2O_3 structural model in [100] (a) and [001] (b) projections. (c): In the octahedral layers (yellow) octahedra form ribbon-chains parallel to [100], just like tetrahedra and octahedra do in the mixed layers (red). This structure is analogous to the κ phase of Al_2O_3.

As shown in Figure 3.20c, in the $z \sim 0$ and $z \sim 1/2$ layers GaO_6 octahedra form ribbons (zig-zag double chains), running along ***a*** and separated by a strip of vacancies along the ***b***-axis. In mixed layers ($z \sim 1/4$ and $\sim 3/4$), GaO_6 octahedra and GaO_4 tetrahedra form single zig-zag chains, running along ***a*** and alternating along ***b*** with interspersed vacancies. Noteworthy, the scheme of cavities occupancy by the Ga atoms is such to maximise the cation-cation distances.

When it comes to thin films, at least the ones grown in the present work, this orthorhombic structure forms columnar domains, about 2–5nm in diameter and stretching along the entire film thickness. As shown in Figure 3.21, these domains are separated by either twin-boundaries (TB) or anti-phase boundaries (APB).

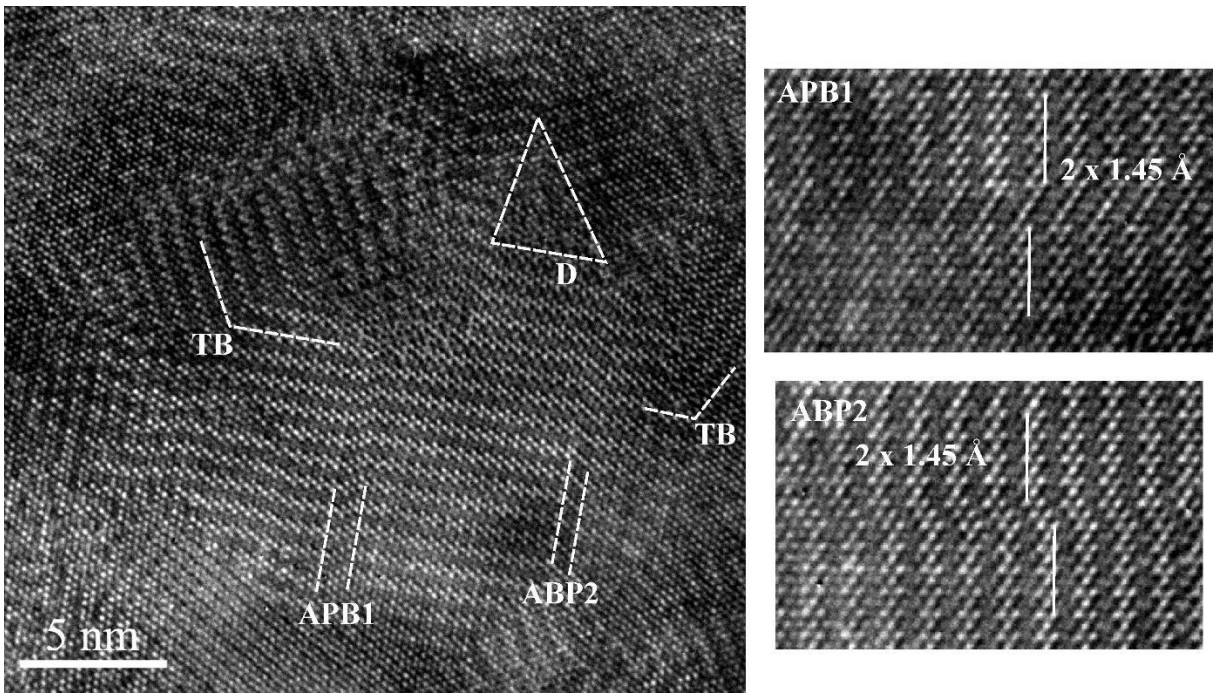

Figure 3.21: Detailed [001] HRTEM plan-view of the 250 nm ε-Ga_2O_3 sample. Twin-boundaries (TB) and anti-phase boundaries (APBs) can be readily identified. Disordered regions (D) are also observed at the boundary of the twin domains. The two magnified images on the right show antiphase boundaries: 2 elementary shifts combined that result in a 2×1.45 Å shift of the structure.

The fact that the structure is commonly twinned is not surprising: indeed, independently from the growth direction of the GaO_6 chains, the hexagonal 4H stacking of the O atoms is preserved (which explains the excellent quality shown by standard XRD measurements), while the local orthorhombic symmetry is driven by the arrangements of the ribbon-chains. Three equivalent domains can be assumed in the ***ab*** plane, rotated by 120° with respect to each other. Furthermore, the non-centrosymmetric nature of the structure further doubles the possible twin variants, by reversing the ***c***-axis. Figure 3.22a shows the polyhedral model representation of a twin boundary in ε-Ga_2O_3, where the transition from one domain to the next takes place by a simple 120° reflection of the ribbon chains in the *ab* plane, whose boundary does not leave any dangling bonds.

Inside twin domains, isolated anti-phase boundaries can occur. As it is clearly shown by HRTEM images (right side of Figure 3.21), the latter imply a shift of the ribbon chains in the direction of ***b***, which can be quantified as a multiple of the vector $\boldsymbol{R} = -1/6\,\boldsymbol{b}$, which is 1.45 Å in module. The region involved in this shift is the anti-phase boundary, of which Figure 3.22b represents a structural model. The largest observed shift-zone was 2.9 Å wide, namely $2\times\boldsymbol{R}$.

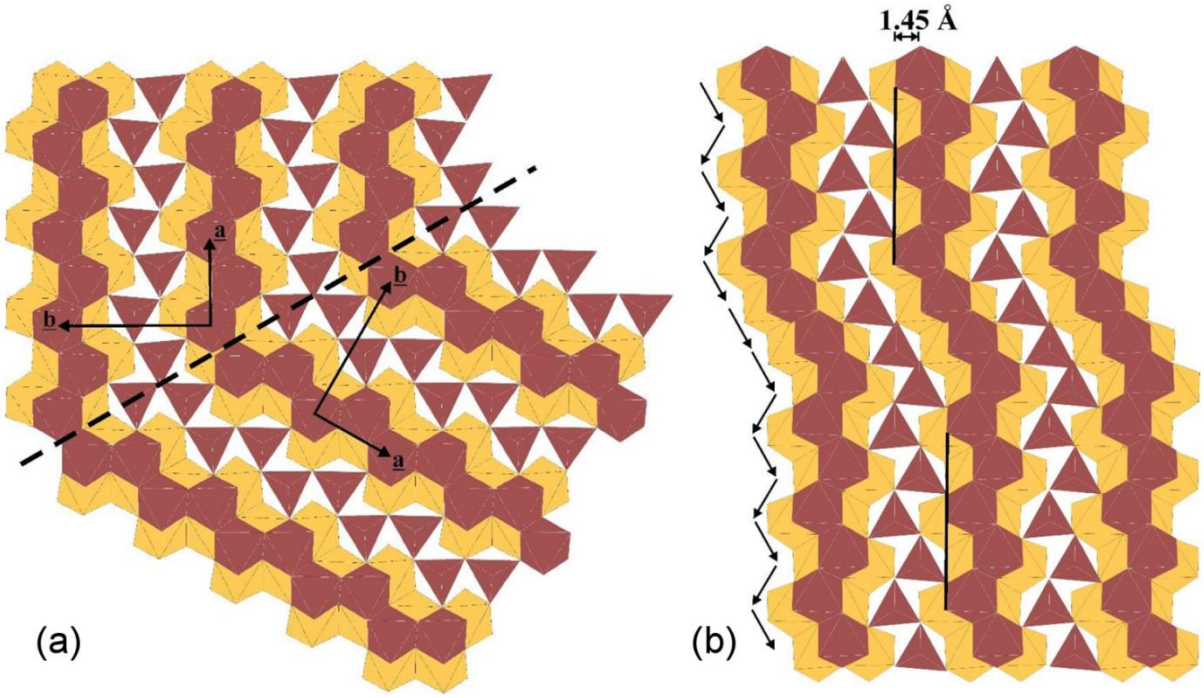

Figure 3.22: Polyhedral structural model of (a): a 120° rotational twin boundary and (b): an anti-phase boundary inside a domain, with 2 elementary shifts resulting in 2×1.45 Å total shift of the structure.

The propagation direction of the GaO_6 chains plays a drastic role in limiting the domain size of the orthorhombic structure along the [100] direction. Noteworthy, when the domain size drops below the coherence length of the radiation used in the XRD or SAED diffraction experiment, an apparent hexagonal symmetry is recovered in the diffraction patterns. In other words, when the ordering scale is below the actual resolution of the probing techniques, one may uniquely see the averaged structure, with its six-fold symmetry and $P6_3mc$ space group.

These findings are of crucial importance for a correct understanding of the ε-Ga_2O_3 structure, as they do account for all the contradictory data of the literature, and ultimately solve the hexagonal-orthorhombic ambiguity. However, the implications of this peculiar domain structure, with gallium chains twins at the borders instead of grain boundaries, are unclear at the moment and indeed call for further in-depth investigation. For instance, the reason why it was possible to observe the orthorhombic superstructure by XRD in the 10 μm thick sample is probably related to an increased lateral size of the domains: how the latter changes with thickness and, in case, by changing the growth parameters, will be the object of a future study, as well as the possibility to eventually supress domain formation. It will be of great interest also to determine how and if domain size variation would affect the properties of the layers, in particular the electrical ones.

As a final point of the structural analysis, the polar character of the structure was demonstrated, in agreement with the polar character of $Pna2_1$ space group. As shown in Figure 3.23, a positive resultant of the cationic displacements with respect to the mean oxygen layers is observed along the positive direction of the ***c***-axis, generating a net dipole moment in the same direction. This dipole

moment, calculated from the refined atomic coordinates, results to be 0.20 μC/cm^2, thus suggesting the compound to be at least pyroelectric.

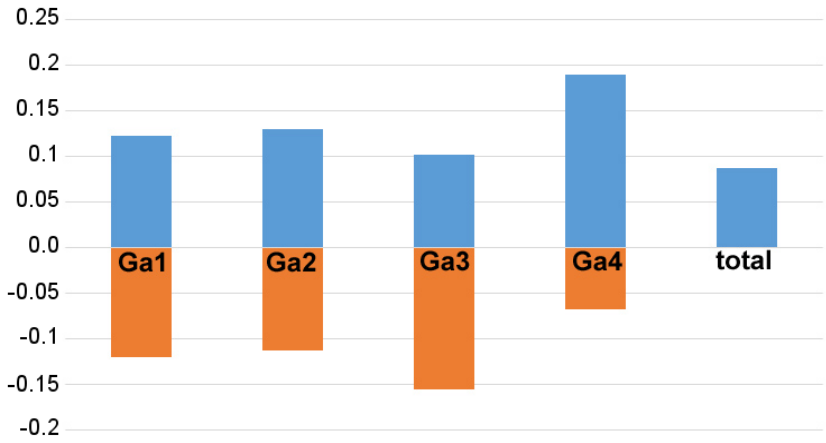

Figure 3.23: "Out of plane" distances (Å) of the gallium atoms from the mean oxygen layers adjacent along the polar ***c***-axis.

Ferroelectricity

In order to check the effective pyroelectric and/or ferroelectric character of this Ga_2O_3 polymorph, additional measurements were carried out. A 3 μm sample deposited on *c*-sapphire was mechanically lapped on the back side down to about 200 μm, by using 60 grit sandpaper. Metallisation was performed by sputtering 100 nm Au on both sides, in the so-called parallel-plate capacitor configuration, followed by 24 h annealing at 100°C. The shape of the selected specimen was rectangular, with a surface area of 3.55 mm^2.

An AC triangular bias between 0 kV and 1 kV was applied to the sample, exploring the frequency range below 1500 Hz. The current flowing through the dielectric was registered as a function of the real-time value of the applied voltage during the triangular wave signal. In order to get the maximum contribution from the polar-induced current produced by ε-Ga_2O_3 and to reduce the relative weight of the displacement current promoted by sapphire, the current was collected from the gold plate on the film side. Blank measurements were performed also on a sapphire sample. The obtained data were analysed using the MATLAB platform.

In the whole frequency range, the layer behaves as a good dielectric material with negligible leakage current. The registered value of the relative dielectric constant is around 7.17 at 1 kHz (lower than the value of about 10.5–11.5 expected for bulk sapphire along the ***c***-axis[189]) while the measured resistivity is $1.74 \cdot 10^{12}$ Ω·cm. Under 1 Hz bias-condition, an electrical polarisation loop $P(E)$ was successfully obtained after data elaboration. The result of this study is shown in Figure 3.24, where the V-invariant displacement current of sapphire was deleted and the very weak leakage currents were taken into account.

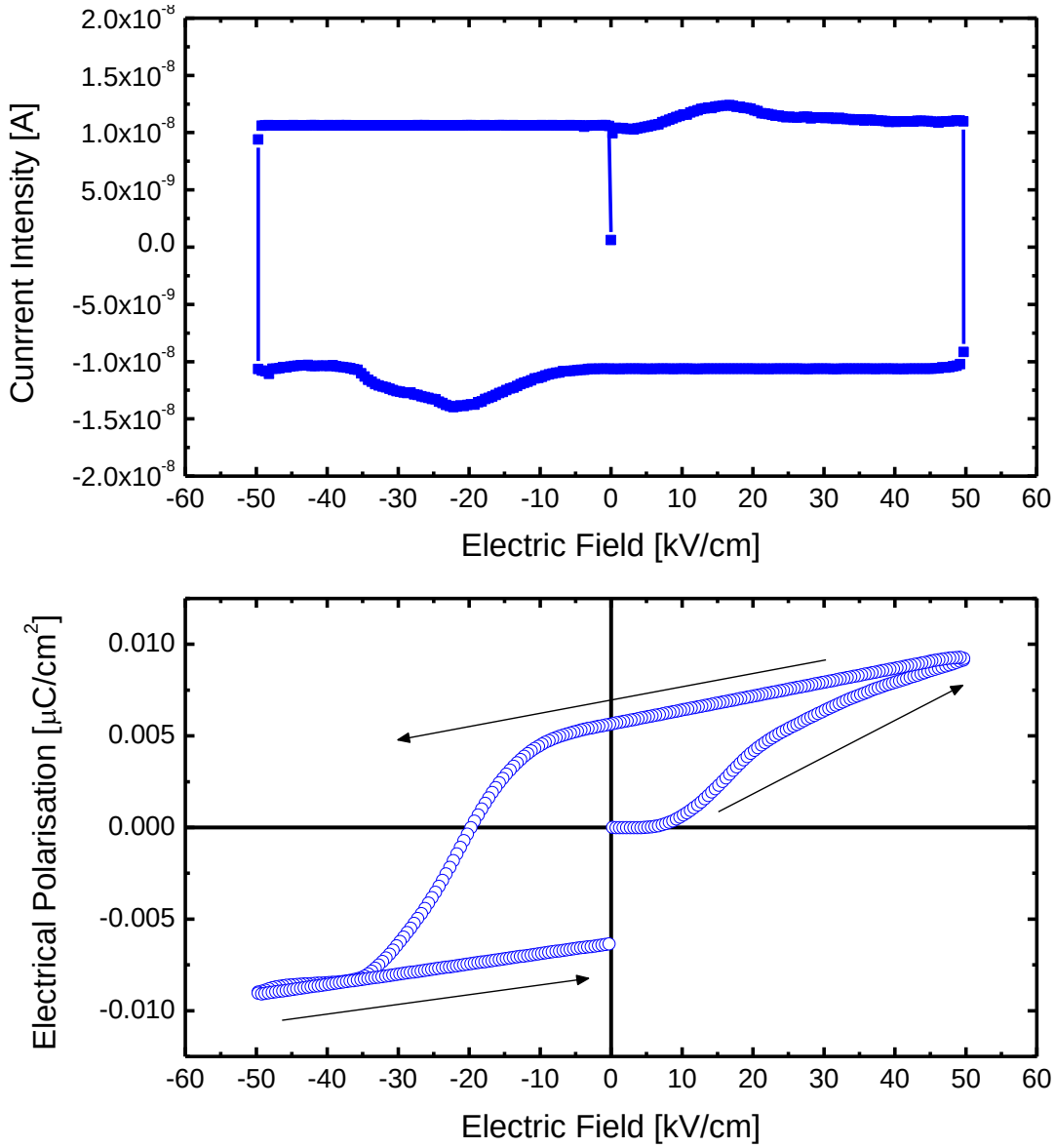

Figure 3.24: Top: Current intensity flowing through the ε-Ga_2O_3 film during the poling/reading procedure of the DHM protocol, performed at room temperature by applying (1Hz, 1 kV) triangular pulses; the detection of broad positive and negative polarisation peaks, superimposed to the standard rectangular loop, unveils the ferroelectric character of the sample. Bottom: Electrical polarisation hysteresis obtained by integration of the current signal reported in (top). (Adapted from Mezzadri *et al.*[183])

A net polarisation is clearly present, with a maximum value of $9.2 \cdot 10^{-3}$ μC/cm^2 arising from a depolarised state. However, the hysteresis characteristic shows that the polarisation is not saturated, at least within fields up to 50 kV/cm. Unfortunately, dielectric breakdown always occurred at about 60 kV/cm, even when different samples were measured, thus preventing saturation from being reached in these ε-Ga_2O_3 films. Hence, the one shown in Figure 3.24 is just a minor loop, which accounts for the consistent difference between the measured polarisation and the one estimated from structural analyses (namely 0.20 μC/cm^2). Nevertheless, by taking the polarisation change of sign it was possible to determine the coercive field E_C = 19.7 kV/cm. The coexistence of semiconducting and ferroelectric properties is unusual and makes this material worth of further studies, aiming in particular at the development of novel application fields.

3.2.4 Optical and electrical properties

Absorption spectroscopy

Optical absorption measurements were performed on a large set of films, with thickness ranging between 175 nm and 2 μm. The most significant results are shown in Figure 3.25.

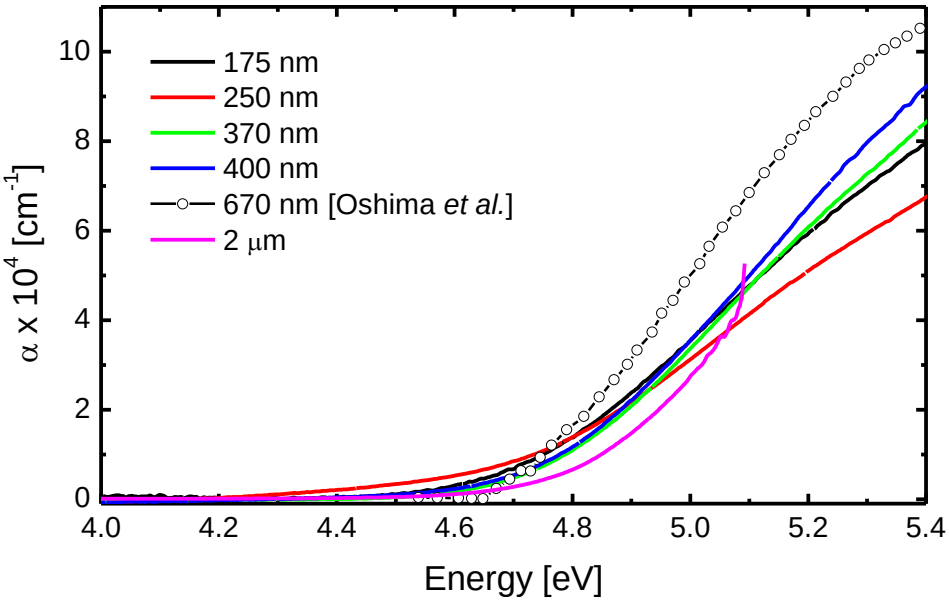

Figure 3.25: Absorption coefficient α of ε-Ga_2O_3 films having different thickness. The reference values for a 670 nm thick sample were taken from Oshima *et al.*[32].

The measured absorption coefficients α are in good agreement with those extrapolated from the data of Oshima *et al.*[32]. Noteworthy, for all curves the onset starts at about 4.6 eV. On the other hand, any attempt to extract an univocal gap value from a Tauc plot failed, which casts some doubts on the possibility of applying the standard interpretation based on direct transitions between parabolic bands to the case of ε-Ga_2O_3. This issue, currently under investigation, is further complicated by the fact that the band structure of the ε phase is still unknown. For this reason, in order to avoid artefacts related to the Tauc plot when assessing the bandgap of the layers, the absorption coefficient behaviour as a function of energy was analysed, instead. This analysis led to an estimation of the optical bandgap of ε-Ga_2O_3 falling most likely between 4.6 eV and 4.7 eV, hence close to that observed in bulk β-Ga_2O_3. Indeed, a slightly smaller gap value with respect to β is consistent with the slightly larger average interatomic distances measured by XRD (section 3.2.3).

Raman spectroscopy

Unpolarised Raman spectra were measured in back scattering configuration, with a 632.8 nm red laser perpendicularly incident on the sample surface. Figure 3.26 shows the results obtained on a 10 μm layer compared with a reference sapphire substrate, both measured under the same experimental conditions. On standard samples with thickness below 3 μm the signal was too low to be significant.

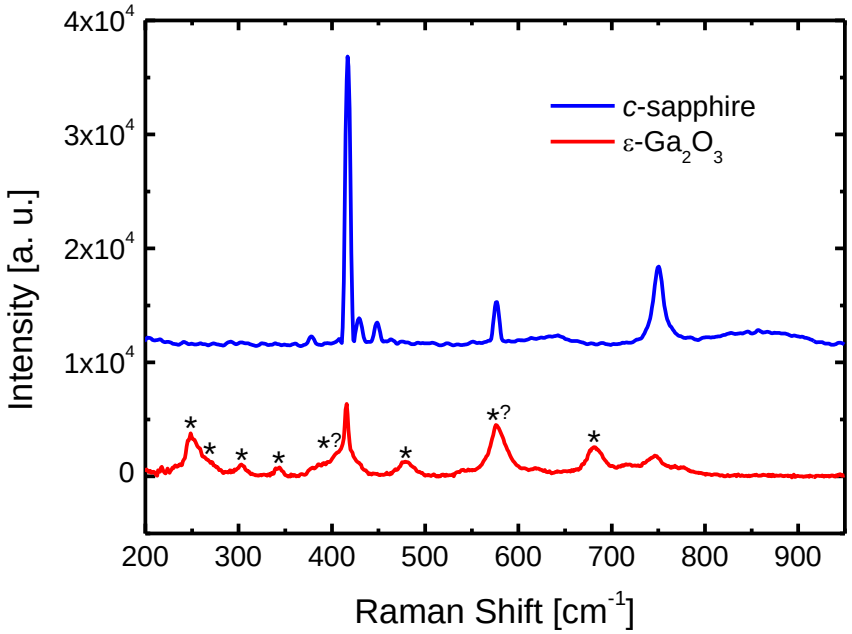

Figure 3.26: Raman spectrum of a 10 μm thick ε-Ga_2O_3 thin film compared with the one of a sapphire substrate, acquired under the same experimental conditions. Asterisks denote the peaks which are only present in the ε-Ga_2O_3 spectrum.

Despite its high thickness and good crystallinity, only low-intensity and relatively broad peaks were observed for the ε-Ga_2O_3 layer. This can be tentatively ascribed to the disorder of gallium ribbon-chains within the *ab* plane (see section 3.2.3), i.e. the one explored with this experimental configuration. Wavenumbers below 200 cm^{-1} were particularly noisy and are not shown in the plot. However, between 200 and 800 cm^{-1} it is possible to identify a number of features that clearly do not belong to the sapphire substrate, and can therefore be labelled as ε-Ga_2O_3 Raman modes. These are located at 248 cm^{-1}, with a shoulder at about 260 cm^{-1}, followed by 303, 343, 479 and 682 cm^{-1}. Besides these "certain" ε-Ga_2O_3 peaks, it is worth mentioning at least one possible feature at about 400 cm^{-1}, between the residual substrate peaks, while the high and broadened 577 cm^{-1} sapphire residual is probably superimposed on some additional peak from the film.

Unfortunately, so far neither experimental nor theoretical studies were made on Raman properties of ε-Ga_2O_3 single crystals. There is hence no data available for comparison, except from the plot previously shown in Figure 1.14, where the quality of the measured ε-β Ga_2O_3 mixed crystallites was however poor, as reflected by very wide bands in their Raman spectrum. In case it will be possible to suppress domain formation during the growth of ε thin films, a more in-depth study of Raman properties will be necessary, backed-up with theoretical calculations of the expected modes.

Ellipsometry

The refractive index n of ε-Ga_2O_3 was measured by ellipsometry. As a first approximation, possible anisotropy was not taken into account. Multi-sample analysis of the ellipsometric spectra in the photon energy region below the gap energies, recorded at multiple angles of incidence, led to the fitting of n

with a Cauchy dispersion model[190]. The refractive index can be expressed as a slowly-varying function of the wavelength λ, which depends on the three Cauchy parameters A, B and C:

$$n(\lambda) = A + \frac{B}{\lambda^2} + \frac{C}{\lambda^4} \tag{3.3}$$

For the measured ε-Ga_2O_3 films, the obtained values were A = 1.9508, B = 0.010398, and C = 0.00061257. The resulting trend of $n(\lambda)$ is reported in Figure 3.27.

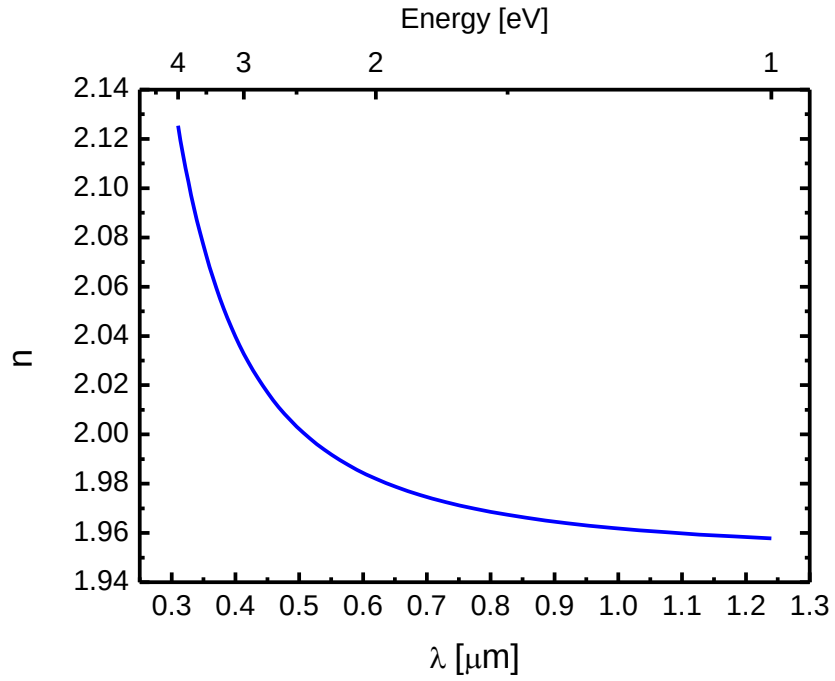

Figure 3.27: Wavelength-dependent refractive index of ε-Ga_2O_3 measured by ellipsometry. Estimated Cauchy coefficients were A = 1.9508, B = 0.010398, and C = 0.00061257.

For the whole range, these values are larger than those reported for β-Ga_2O_3 (see for example Figure 1.8). Since no literature data were available about the refractive index of the ε phase, Figure 3.27 was employed as a calibration curve of $n(\lambda)$ for the assessment of ε-Ga_2O_3 films thickness from the interference fringes measured by reflectometry.

Cathodoluminescence

Radiative recombination phenomena were investigated by means of cathodoluminescence spectroscopy (CL) at room temperature. In Figure 3.28 the CL spectra for a representative ε-Ga_2O_3 thin film are reported as a function of different accelerating voltages, corresponding to different electron penetration depths.

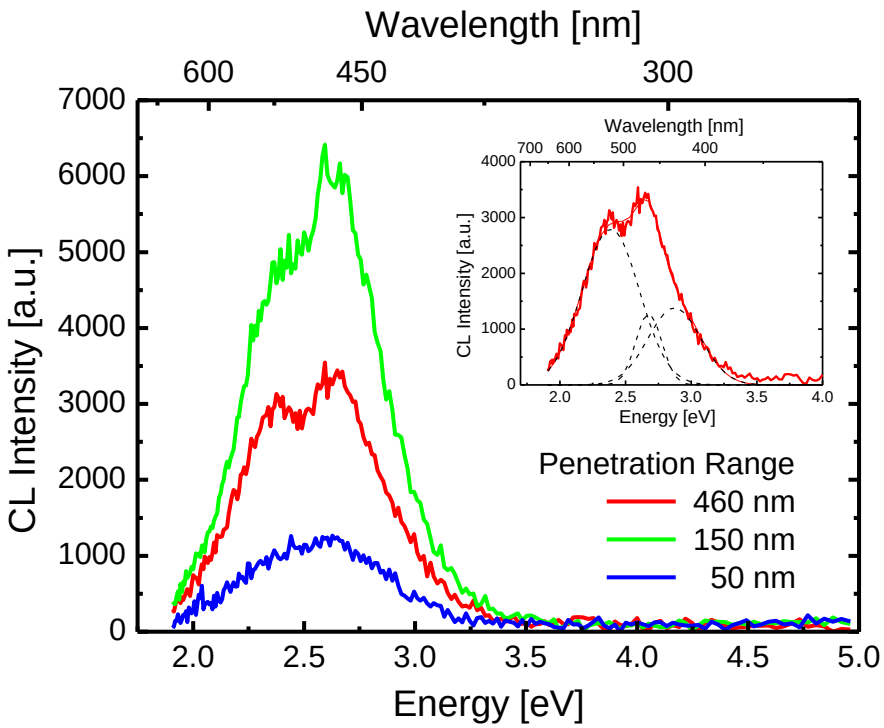

Figure 3.28: Depth-resolved CL analysis of a 380 nm thick film at fixed injection power (10^{-5} W) for three different electron penetration ranges. Inset: Gaussian deconvolution of the 5 keV CL spectrum.

As in the case of β-Ga_2O_3 single crystals, no band-edge emission was detected here for ε-Ga_2O_3. The deconvolution shown in the inset of Figure 3.28 reveals the presence of three bands at 2.34 eV (530 nm), 2.67 eV (464 nm), and 2.75 eV (450 nm). For depth-resolved CL analysis, the accelerating voltage was varied between 2.5 keV and 10 keV, in order to change the electron penetration range from ~ 50 nm to ~ 450 nm and to study the distribution of the radiative recombination centres along the vertical cross-section of the layers[191,192].

In Figure 3.29 the integrated intensity of the single emissions (from Figure 3.28) is reported as a function of the electron penetration depth, which was modelled by Montecarlo simulations. A great inhomogeneity of the radiative recombination centres distribution is clearly visible. The maximum intensity of the three bands occurs at acceleration voltages of 5 kV (penetration depth of about 150 nm), while lower and higher voltages resulted in lower integrated intensities. While the lower CL emission close to the film surface is possibly related to higher density of non-radiative defects, it is worth noting that for an acceleration voltage of 10 keV the generation-recombination volume reaches the interface with the sapphire substrate. Therefore, a part of the energy released by the electron beam is lost to the substrate, which did not allow for a quantitative analysis of the actual concentration of radiation levels in the deeper region of the film. Further detailed studies are necessary in order to identify the origin of the CL emissions in ε-Ga_2O_3.

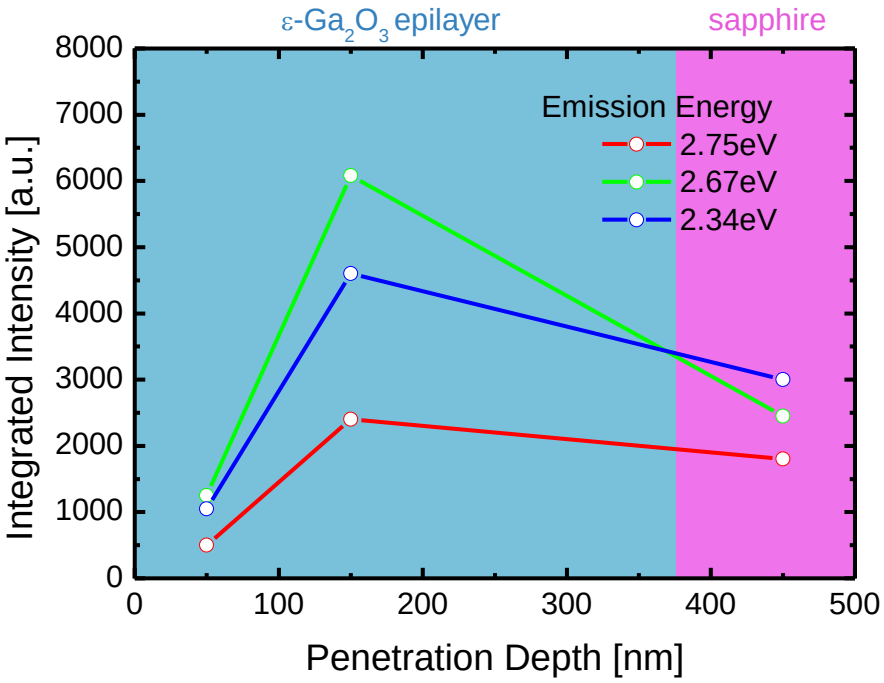

Figure 3.29: Integrated CL intensity as a function of the electron penetration depth in a 380 nm thick film.

Photoconductivity and UV detection

The photoresponse properties of ε-Ga_2O_3 thin films were studied in air, at fixed temperature (25°C) and constant humidity. Simple and cost-effective photo-resistors were fabricated in planar metal-semiconductor-metal geometry (Figure 3.30), hence ruling out complicated heterojunctions. The electrodes, consisting of Au (250 nm) / Ti (20 nm) bilayers, were deposited through a metal mask by thermal evaporation, followed by 10 minutes annealing at 500 °C, thus employing one of the simplest procedures to deposit Ohmic contacts to β-Ga_2O_3 discussed in section 1.1.5. A typical distance of 2 mm between electrodes was used for this study.

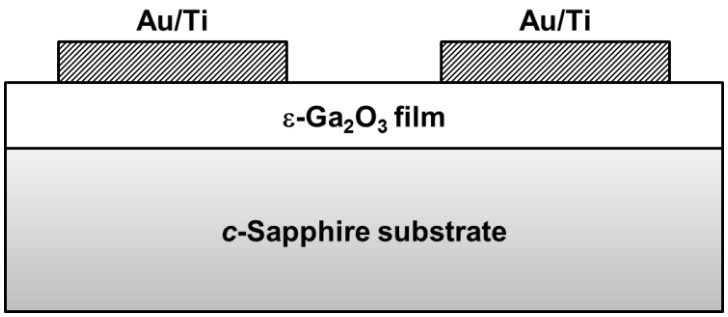

Figure 3.30: Schematic model of a planar photoresistor based on an ε-Ga_2O_3 thin film. The metal contacts consist of Au (250 nm) / Ti (20 nm) bilayers and are located at a mutual distance of about 2 mm.

Current-voltage curves, carried out in dark and under illumination at different wavelength between 0 and 200 V, are shown in Figure 3.31 and confirm a linear behaviour over a wide range of applied biases.

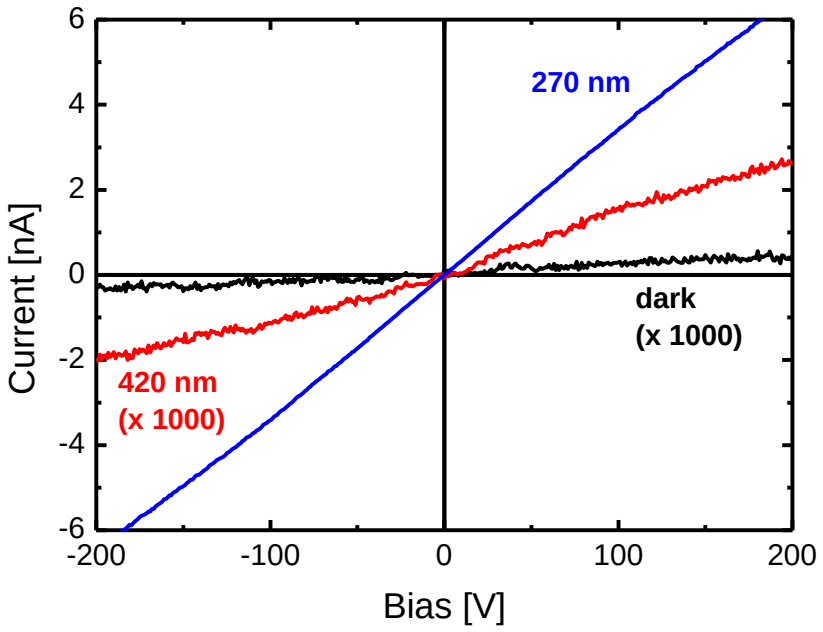

Figure 3.31: Current-voltage curves in dark and under illumination at different wavelengths. Note that the currents corresponding to dark and 420 nm illumination are multiplied by a factor 1000. The mean irradiance on the active surface of the detectors (i.e. outside the metal contacts) in the spectral region 270–420 nm was around 1 mW cm^{-2}.

The temperature behaviour of the electrical contacts was assessed in dark up to 300 °C and found to be Ohmic in most of the explored range, as well as stable after several temperature cycles. Measurements of the dark current at a function of temperature in the range 20–300 °C showed that the film conductance increases by three orders of magnitude with the temperature. The corresponding Arrhenius plot is linear and presents an activation energy of 0.695 eV (Figure 3.32). This effect is possibly related to the thermal ionisation of an electronic level located at about 0.7 eV below the conduction band. Electronic states with comparable energies were previously detected by deep-level transient spectroscopy (DLTS) in β-Ga_2O_3 single crystals[21].

Possible non-linear effects on the photocurrent signal were analysed by changing the incident UV photon flux. A set of neutral optical filters was used to intercept the light beam and to vary the light intensity at the bandgap wavelength from about 0.2 and 1.6 mW cm^{-2}. The UV photoresponse of the detector was observed to be linear in this power range.

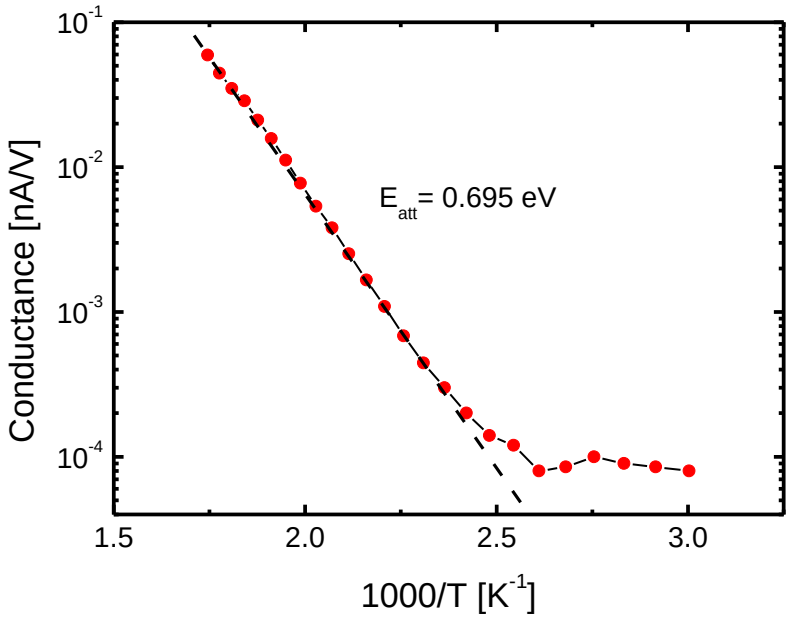

Figure 3.32: Arrhenius plot for the dark current in the temperature range 20–300 °C.

The photoconductivity spectrum (PCS) of a representative thin film is shown in Figure 3.33 and compared to the corresponding optical absorption spectrum. It is worth stressing that a correction factor was introduced for all the measured photocurrent spectra, taking into account the spectral distortion of Au/Ti contacts, which was measured for a reference Au/Ti layer of the same thickness deposited on quartz. All investigated samples showed a very similar behaviour.

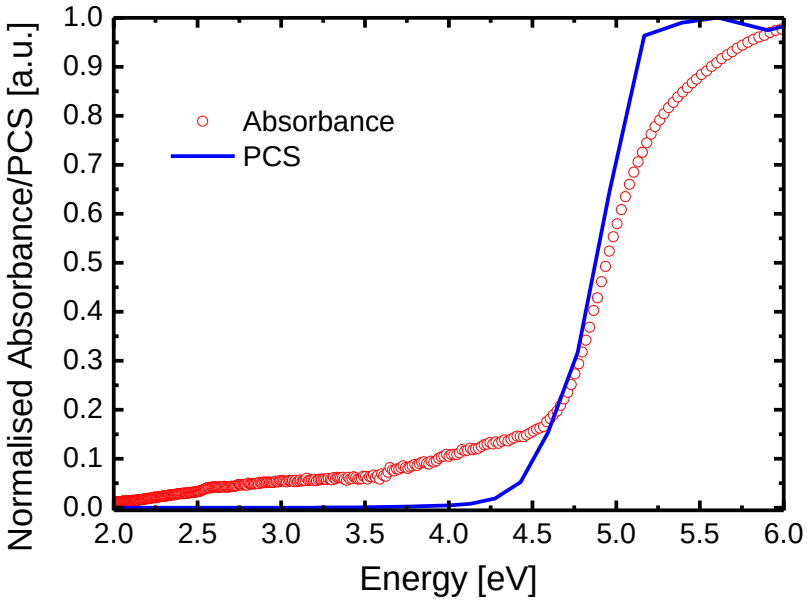

Figure 3.33: Spectral photocurrent and optical absorption edge (normalised curves).

Though similar, the two curves present some non-negligible differences. The normalised PCS curve, reported in a linear scale, shows a relatively mild onset at about 4.2 eV that becomes much sharper at about 4.6 eV. The onset of photoconductivity occurs below the estimated bandgap and can

be ascribed to the presence of energy levels connected with point defects or complexes, as already observed for β-Ga_2O_3[193,194].

On the other hand, in optical absorption spectra a non-negligible response is present already at 2 eV, which increases monotonically up to the band-edge. This long tail below the energy gap may include other components in addition to excitation of photo-carriers from deep levels, for example light scattering by precipitates or inclusions, interface defects, etc. Photocurrent values in the same spectral region, far from the bandgap edge, are too low to be appreciable in the same linear plot of Figure 3.33. Photo-generated current can in fact be low even when the absorbance is non-negligible, because a primary requirement for photocurrent detection is that photo-carriers have to live and diffuse long enough to reach the collection electrodes.

This simple photoresistor based on ε-Ga_2O_3 can be effectively employed as a solar-blind UV-photodetector, whose performance is shown in Figure 3.34. The photo-generated signal shows good stability over a long time (a few hundred seconds) while the response time to on/off UV illumination is about ~ 25 s. After multiple illumination cycles the photodetector maintained a practically identical response, demonstrating robustness and good reproducibility. The noise affecting the current output under illumination was estimated to be well below 1%.

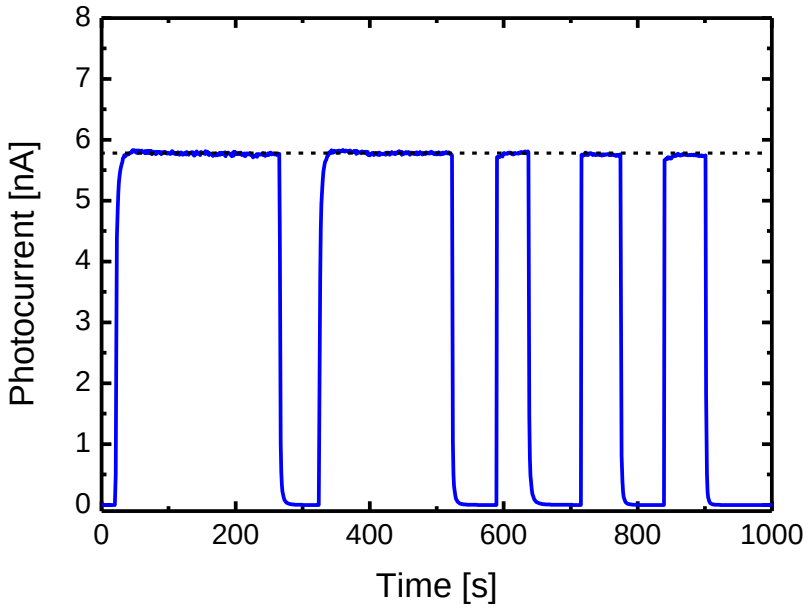

Figure 3.34: Time-dependent photoresponse to UV light (270 nm) under an applied bias of 200 V.

All these features, together with the sharp drop of PCS signal below 4 eV (about three orders of magnitude with respect to the UV region), make ε-Ga_2O_3 a very promising material for solar-blind photodetecting applications. Even though its on/off response time is of several seconds, this performance indeed compares well with that of detectors based on β-Ga_2O_3, a proven material for UV detection, at least when the device is built in metal-semiconductor-metal configuration[25].

3.2.5 Thermal stability

Thermal stability of ε-Ga_2O_3 was evaluated for fragments about 0.5×0.5 cm in size, cut from samples having similar thickness and annealed for three hours in O_2 at different temperatures, namely 500, 750 and 1000 °C. One sample was kept as reference, un-annealed. Figure 3.35 and Figure 3.36 respectively show the XRD ω-2θ scan profiles and the CL spectra of the annealed layers, compared to the reference one.

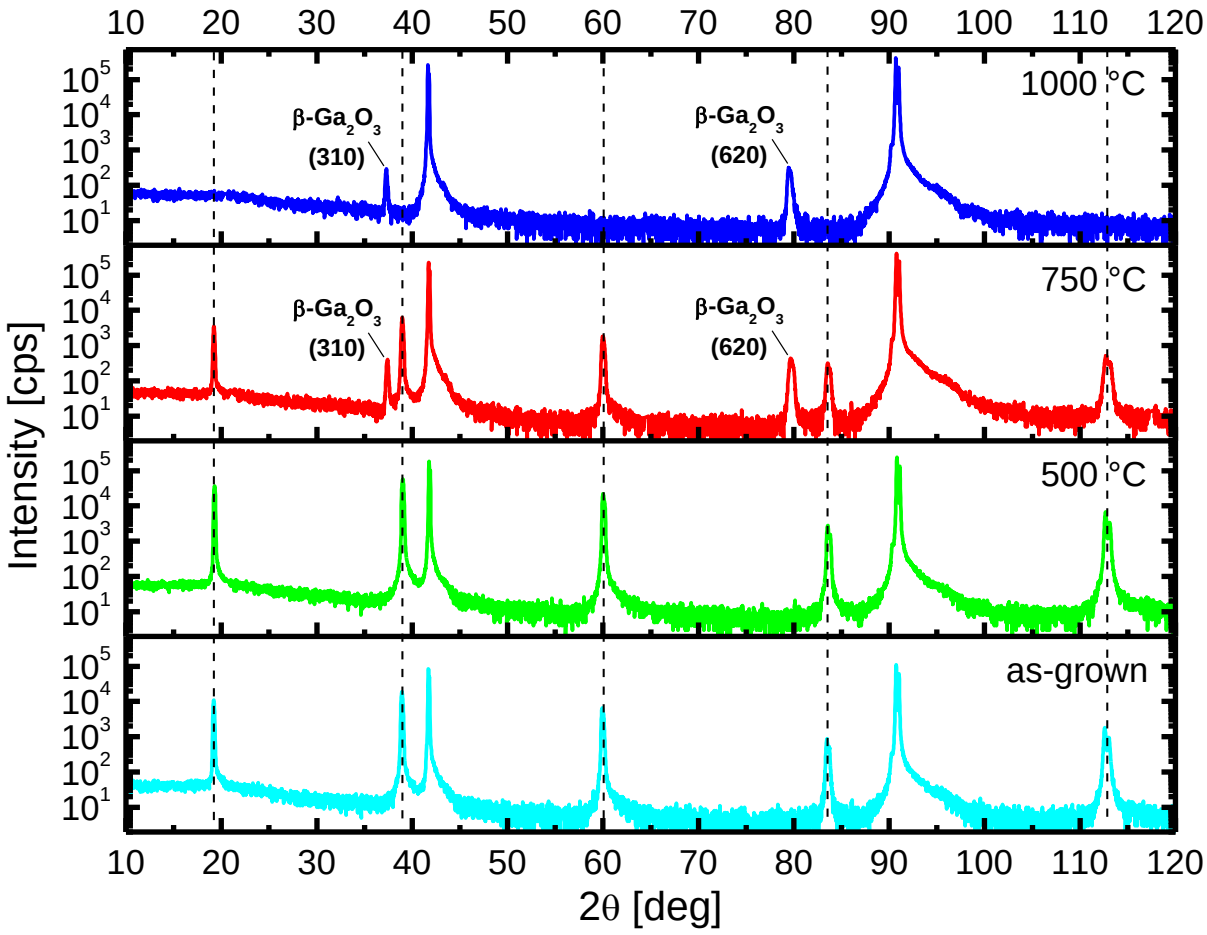

Figure 3.35: XRD scan profiles of ~ 400 nm thick ε-Ga_2O_3 layers grown on *c*-sapphire, after thermal annealing at different temperatures. The profile of an as-grown sample is shown for the sake of comparison. Dashed lines represent the position of ε-Ga_2O_3 peaks.

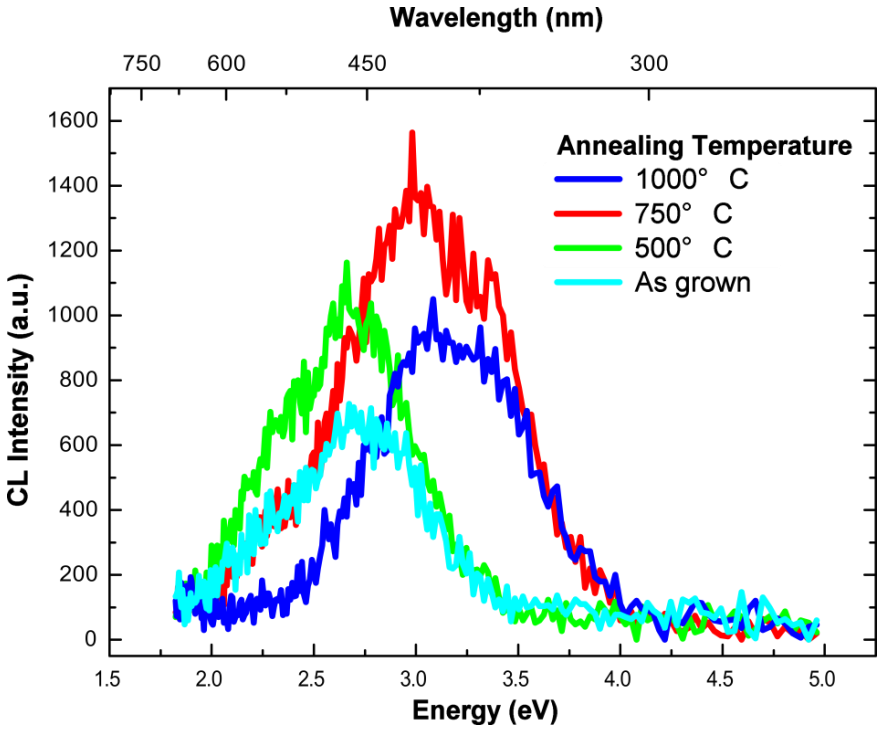

Figure 3.36: CL spectra of ~ 400 nm thick ε-Ga_2O_3 layers grown on *c*-sapphire, after thermal annealing at different temperatures. An as-grown sample is shown for the sake of comparison.

The treatment performed at 500°C did not result in any appreciable structural change revealed by XRD, while CL spectra only highlighted a slightly increased emission intensity. This might be ascribed to an increased concentration of radiative centres, as well as to a reduction of traps due to a favourable rearrangement of defects upon heating. On the other hand, at 750 °C peaks corresponding to the β phase begin to emerge in the XRD scan profiles, followed through by a reduction of ε-Ga_2O_3 diffracted intensities, while CL spectra show a clear blue-shift. At 1000 °C, only the XRD peaks of β-Ga_2O_3 remain and the CL emission is further shifted to higher energies, reaching the position expected for the β-phase (see section 1.1.4).

The orientation of the layers after transition to β-Ga_2O_3 was identified as (310), which is unusual for the growth on *c*-sapphire. However, the typical (-201) arrangement was recovered by increasing the cooling-down time after annealing at 1000 °C, from six to twelve hours (Figure 3.37). These findings were further confirmed by TEM analysis. As reported in Figure 3.38, after annealing the layer becomes polycrystalline β-Ga_2O_3 (a = 12.21 Å; b = 3.03 Å; c = 5.75 Å; β = 103.6°). In each crystalline domain, the (-201) plane is always perpendicular to the growth axis, while four different in-plane orientations are possible: [010], [1-10], [1-32] and [1-12].

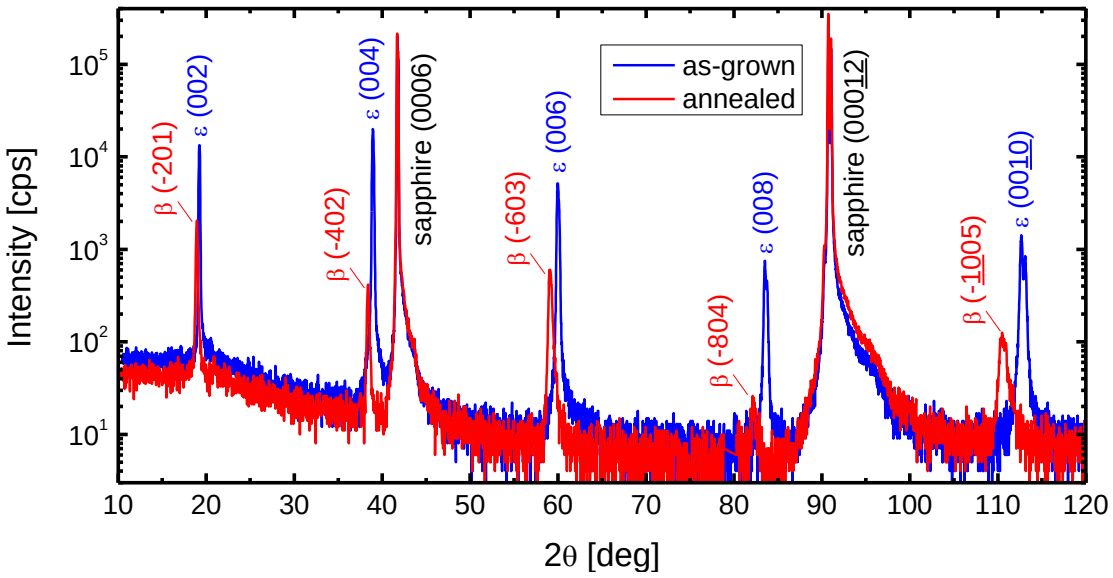

Figure 3.37: XRD scan profiles of an ε-Ga_2O_3 sample annealed at 1000 °C compared to an as-grown layer. The cooling-down time was here increased to about twelve hours.

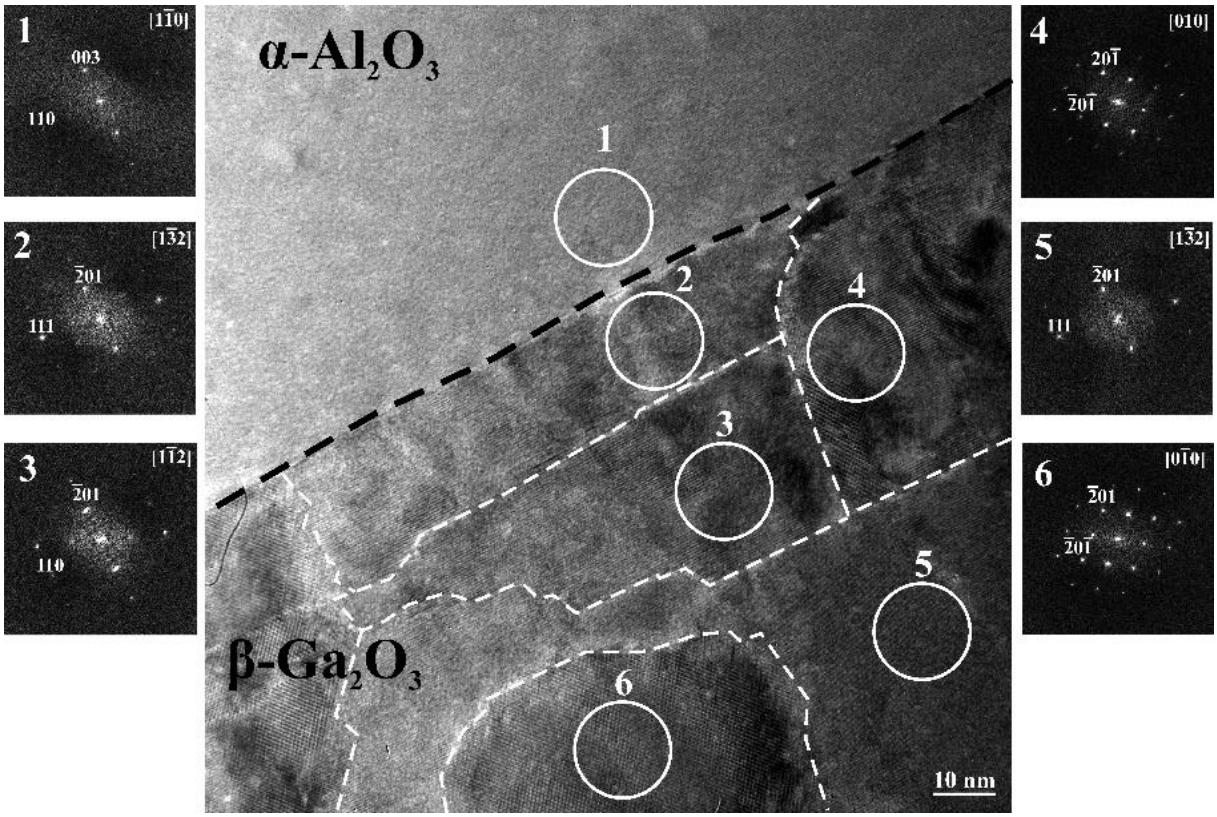

Figure 3.38: Cross-sectional HRTEM image and corresponding indexed FFTs of an ε-Ga_2O_3 sample annealed at 1000 °C and then cooled-down in about twelve hours.

In order to better understand the stability range of the ε phase, DSC analysis was also started. Preliminary results suggest that the transition to β strongly depends on the rate at which the heat is transferred to the material (Figure 3.39). This dependence is particularly evident at lower temperatures, where some kind of transformation starts to take place already at 600–700 °C, while the real phase transition is likely to happen between 870–900 °C, the latter being sharper when the sample temperature is raised slowly.

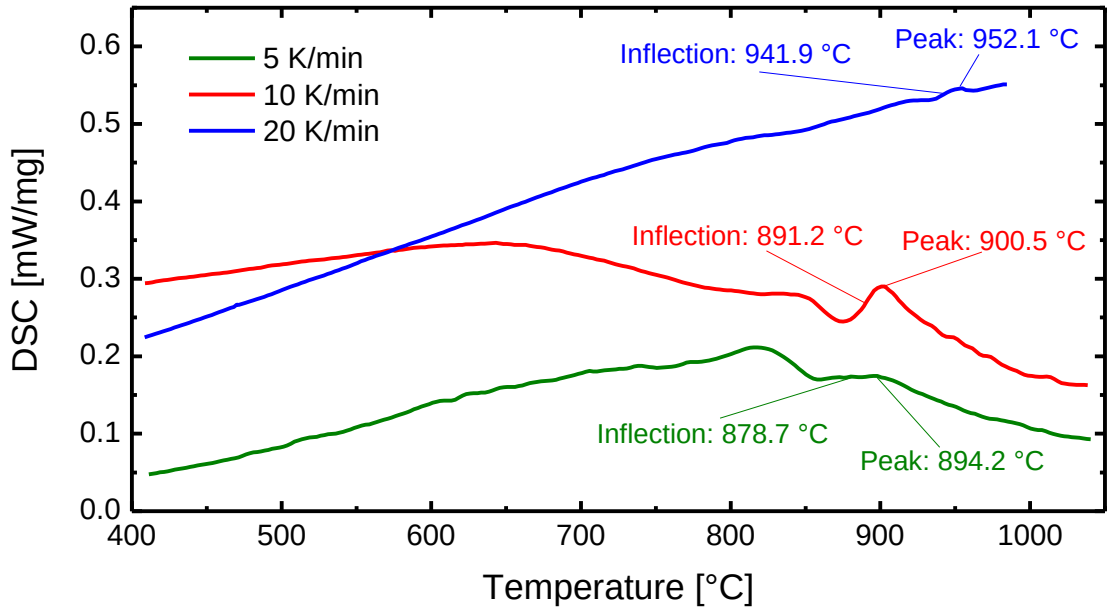

Figure 3.39: DSC preliminary analysis of the ε-to-β transition in Ga_2O_3 thin films. Samples were directly mounted onto the sensor and kept in helium atmosphere (20 ml/min).

Even though further investigation of ε-Ga_2O_3 thermal stability is required, all characterisations performed until now suggest that the effective conversion to β happens above 850 °C and that the crystalline quality of the obtained phase is strongly affected by the heating-cooling pathway. At lower temperatures, some kind of transition takes place, whose nature is still unclear. However, the ε phase is definitely stable at least up to 600–650 °C.

3.2.6 Enhancement of the initial growth setup

The important advantage of the employed homemade MOCVD reactor was that it allowed to obtain reproducible results despite the chamber simple layout and cost-effectiveness. However, a very basic thermo-fluid dynamical simulation can help visualise its limitations.

The study was carried out within the COMSOL Multiphysics software, simultaneously exploiting the *heat transfer in solids*, *laminar flow* and *non-isothermal flow* modules. The aim was to qualitatively determine gas flow velocities and thermal profiles in standard conditions. To the ends of

this very schematic analysis, the reactants were not added to the model, as at the macroscopic level the velocity field of the gas flow and the global thermal profile are mainly determined by the carrier gas.

Boundary conditions were defined for both laminar flow (carrier) and heat transmission (all domains). Inside the chamber, the initial pressure was set at 100 mbar and the velocity field to zero. Slip or sliding of the gas were neglected on both reactor walls and graphite surface. The carrier flow was imposed through the two inlet holes and outside the outlet hole towards a fixed 100 mbar pressure. As for thermal conditions, initial temperatures of all domains were set at 20 °C and heat transmission in fluids was enabled. Three regions were defined, in which the final temperature was fixed: the cylindrical steel tubes inserted into the graphite and containing the heating cartridges (650 °C); the gas surface at the inlet side, since gas lines were constantly heated (60 °C); the surface of the closing flange, as it was cooled by a copper coil filled with flowing water, in order to prevent damage to the O-ring joint (10 °C). Radiative heat transmission from the graphite surface was accounted for by imposing a prescribed radiosity with grey-body radiation. As a last point, an outgoing heat flux was imposed through the outlet hole and a convective thermal flux was assumed for heat exchange with air outside the reactor chamber.

The simulated thermal profile is shown in Figure 3.40. A relatively uniform radial distribution of the temperature around the graphite heater can be observed, which drops to about 300 °C while approaching the chamber walls (Figure 3.40a). On the graphite surface (Figure 3.40b), as expected, the hotter regions are those closer to the cartridges, which however never reach the imposed 650 °C temperature (max ~ 647.5 °C). Moving towards the border in contact with the reactor wall, the temperature drops rapidly. However, in the central region where the substrate is placed during growth, temperature variations are below 3 °C. Hence, from the thermal point of view it is not the presence of a gradient in the growth region to be a limiting factor for the reactor performance, but the strong thermal dissipation highlighted by the radial profile.

As shown in Figure 3.41, gas flow velocity profiles are strongly asymmetric. In the transversal direction, the effect is amplified by the imposed asymmetry of the flows, usually employed in these growth experiments in order to increase the water excess. The fact that the two inlet holes are physically separated results in a not-optimal injection, since it is a source of inhomogeneity especially when asymmetric flows are employed.

A further aspect that emerges from velocity profiles is the evident change, this time in the longitudinal direction, of the boundary layer thickness, even in the proximity of the growth region at the centre of the graphite surface (Figure 3.41b). As expected, this is most likely the main factor determining thickness inhomogeneity of the deposited films.

In Figure 3.42 the pathway of the calculated flow lines is displayed. Even if vortexes or of turbulent behaviour are apparently avoided, the gas is inefficiently dispersed around the heater before exiting from the outlet hole.

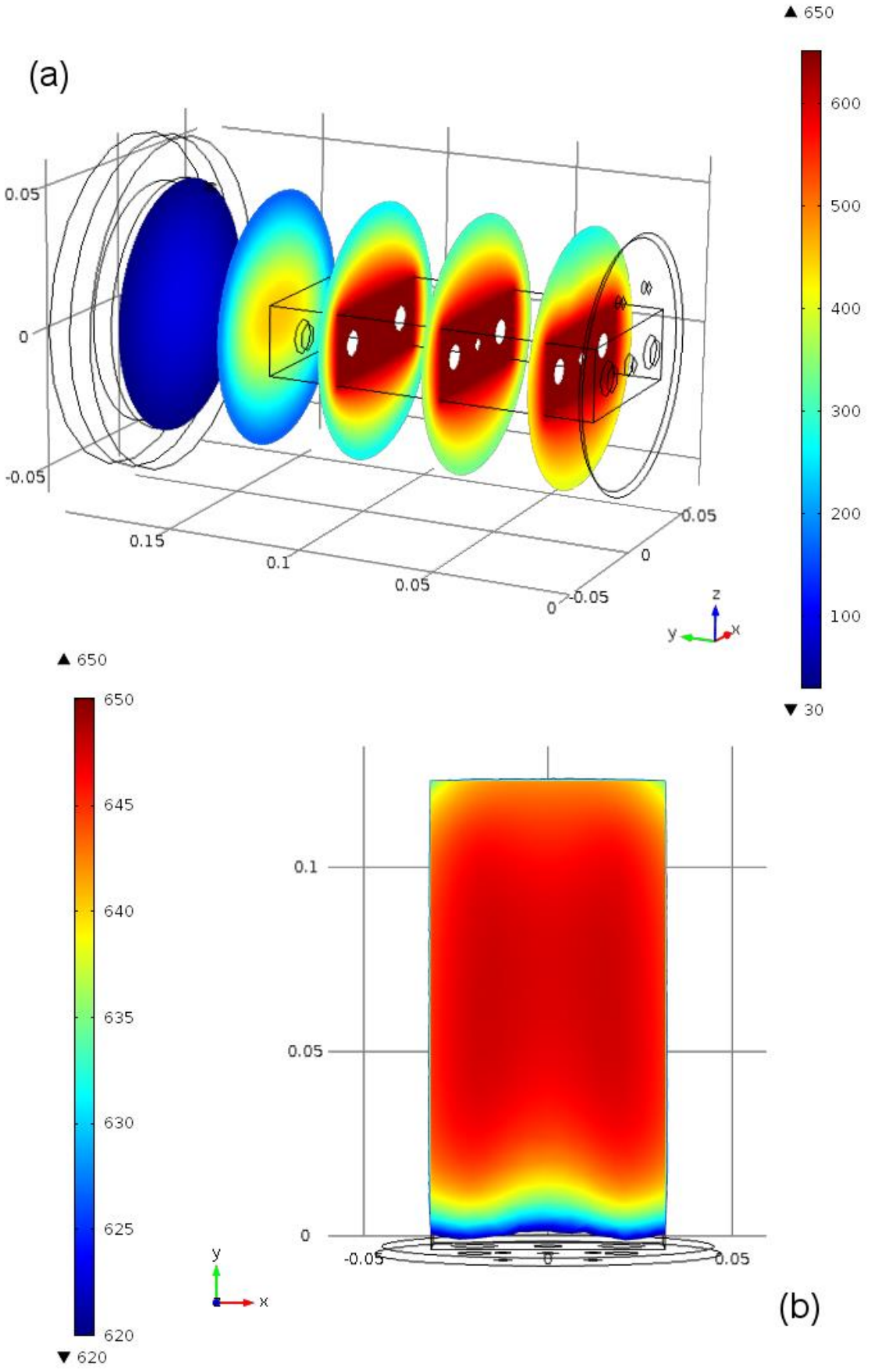

Figure 3.40: Simulated temperature profiles inside the reactor chamber. (a): Radial profile. (b): Graphite surface.

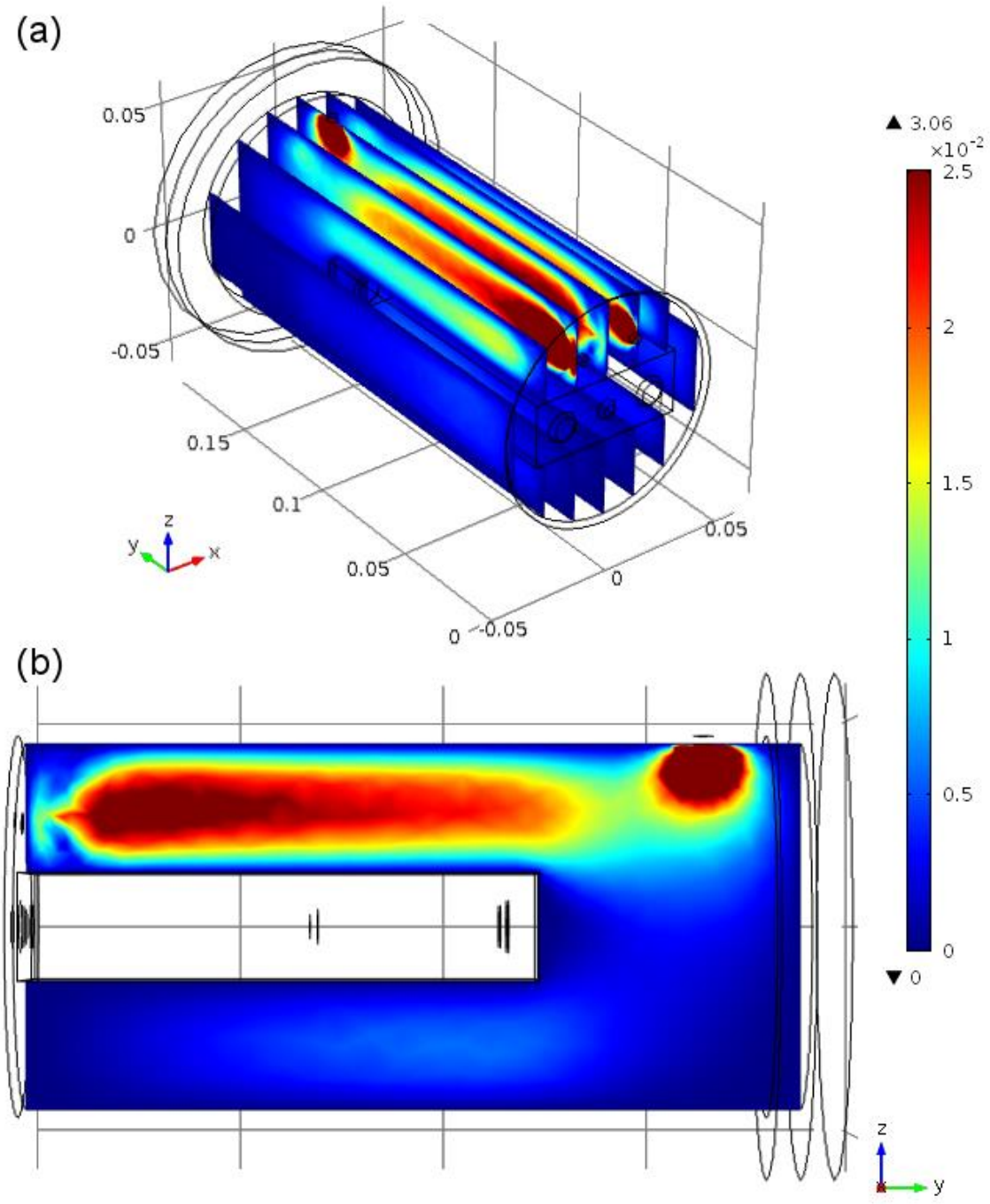

Figure 3.41: Gas flow velocity profiles in planes parallel to the flow direction and perpendicular to the graphite surface. (a): Whole chamber. (b): Central section.

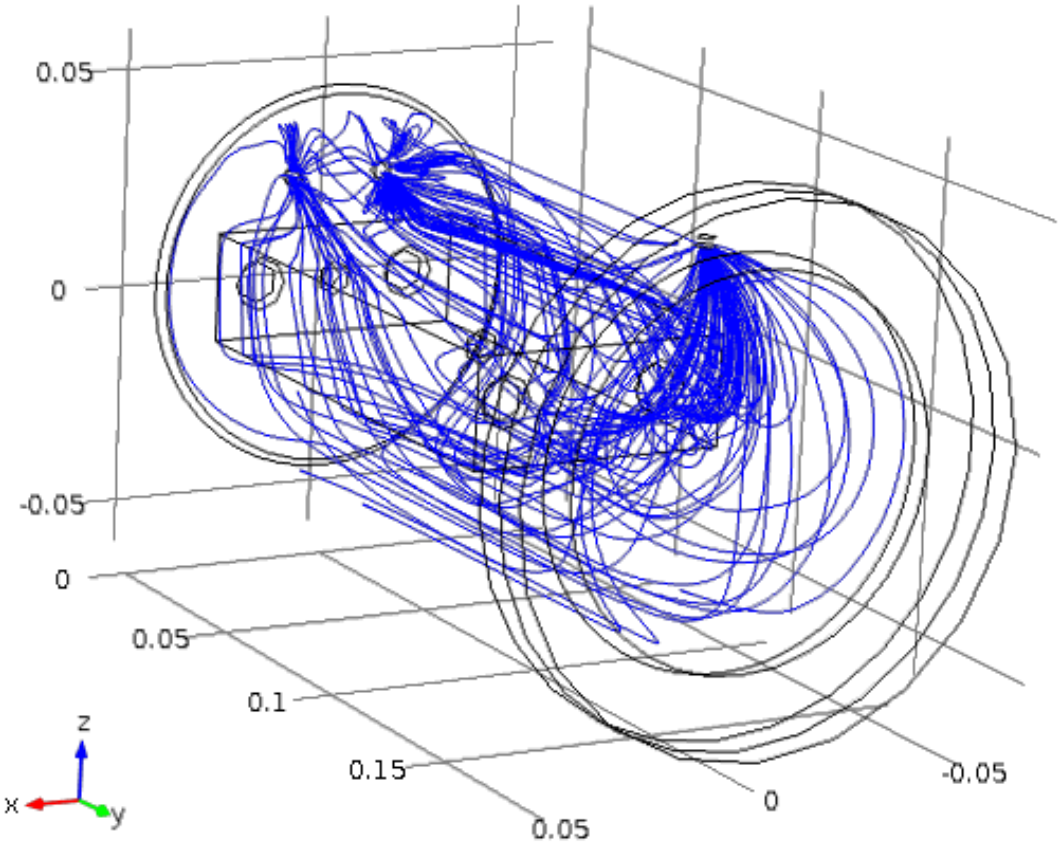

Figure 3.42: Flow lines entering from the inlet holes and exiting from the outlet one.

Based on these considerations, the reactor chamber setup was recently upgraded, in order to make it more efficient and to further increase the quality of the deposited layers. As a first step, the graphite heater was re-designed in order to let the substrate form a small angle with respect to the incoming horizontal flows, aiming to increase the boundary layer uniformity. A 5° slope was identified as a good compromise for the range of the employed carrier flows. A translucent quartz cap was added to contain the carrier gas within the growth region and to further promote a laminar flow regime. Furthermore, the cap provides protection against contaminants and precipitates, as well as some degree of radiation containment. In order to further reduce heat dissipation, a porous graphite insulator was placed around the heater. A schematic of these upgrades is shown in Figure 3.43.

The results of the first growth runs were indeed quite encouraging. More efficient heating was achieved, with stable growth at 600 °C, while the inlet-outlet thickness gradient was significantly reduced, down to 5–30% for 1 inch substrates and to about 30–40 % for 2 inch wafers.

However, the problem of double injection remains and it will be addressed in the near future. Further developments of the deposition system will also require a more in-depth modelling of both fluid-dynamics and particle tracing, including chemical reactions pathways. As mentioned in the previous chapter, the latter are still poorly understood in the case of TMG and H_2O giving Ga_2O_3.

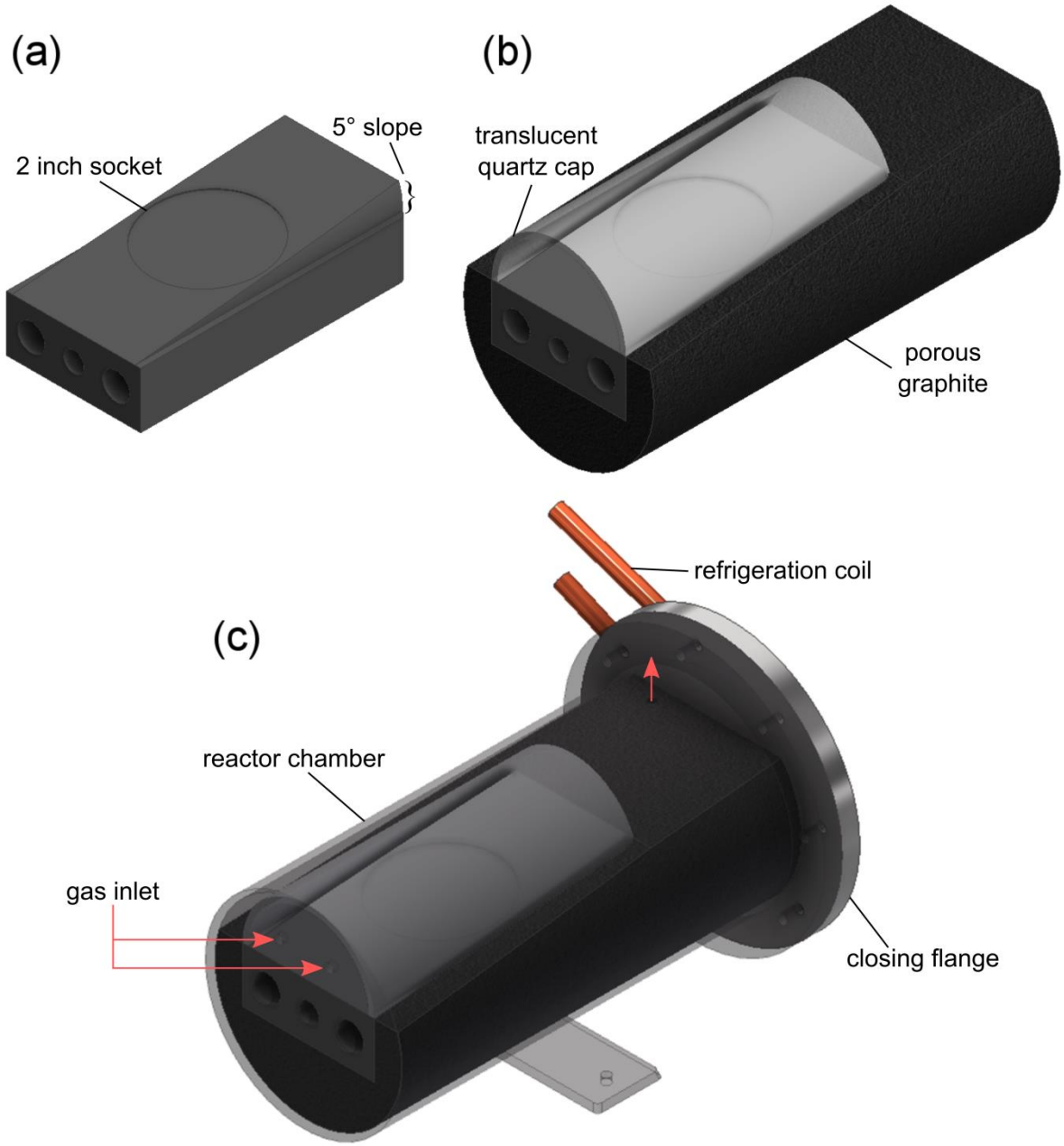

Figure 3.43: Upgraded reactor setup. (a): Graphite heater with a 5° slope and a 2 inch socket. (b): Heater embedded into the porous graphite insulator and topped with the translucent quartz cap. (c): Whole system inserted into the reactor chamber.

3.2.7 ALD mode

As anticipated in section 2.3.1, the development of an ALD process within the CVD reactor is still at its early stages, and standard deposition parameters still need to be defined and optimised. Preliminary growth runs were however quite promising, and will represent an important landmark to address the future growth activity. During these first runs, the best results were obtained with the parameters reported in Table 3.6.

Table 3.6: Best ALD parameters for preliminary growth runs.

T (°C)	P (mbar)	ALD sequence (s)				Growth rate (nm/h)
		TMG	Purge	H_2O	Purge	
550	100	5	3	10	3	50

ALD proved extremely successful in decreasing the crystallisation temperature threshold of ε-Ga_2O_3, from 650 °C down to at least 550 °C, as highlighted by the characteristic diffractions in XRD scan profiles (Figure 3.44). Furthermore, the capability of the technique to achieve uniform deposition was confirmed, as well, with a measured gradient of 20 nm over the entire diameter of 2 inch *c*-sapphire substrates. The cost was a significant reduction of the growth rate, down to ~ 50 nm/h (about 3 Å/cycle), which is however typical of ALD processes, and in this case it was quite close to the expected value for a single Ga-O monolayer in (001)-oriented ε-Ga_2O_3 (~ 2.3 Å). Adding an inert gas flow during the purge sequence was observed to be crucial in order to remove the residual precursor from the chamber and to avoid undesired CVD contributions to the growth. By solely relying on the vacuum pump, the growth rate was in fact several times larger.

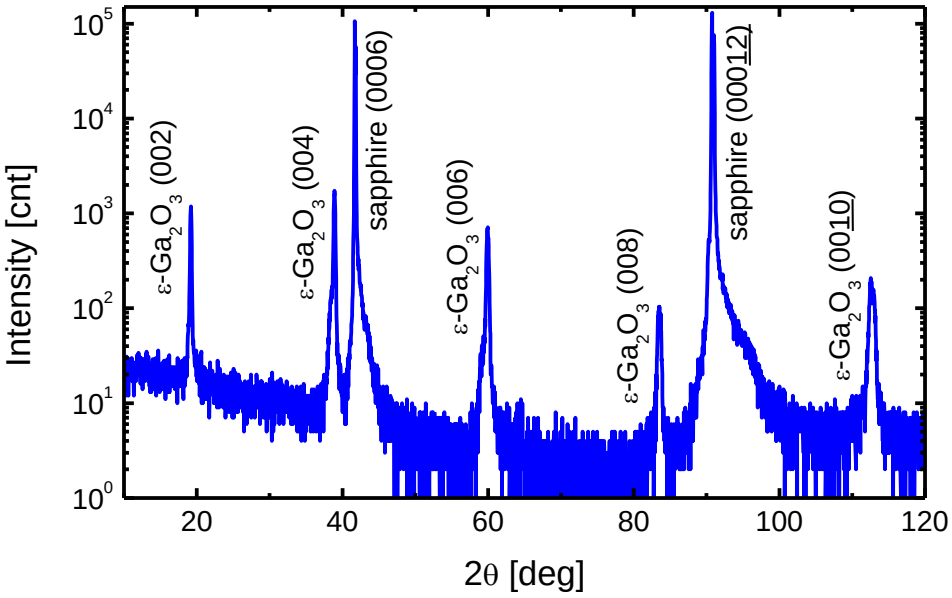

Figure 3.44: XRD scan profiles of a 120 nm ε-Ga_2O_3 ALD thin film grown on *c*-sapphire at 550 °C. (Adapted from Boschi *et al.*[148])

The surface morphology of ALD films was however not as good as in their MOCVD counterparts, with a non-negligible RMS roughness of about 2 nm (Figure 3.45). This implies that the ALD regime conditions were still not optimised, as it is also suggested by the fact that the effective growth rate still exceeds, though slightly, the exact monolayer/cycle. Nevertheless, the strong dependence of the ALD process on the deposition temperature window and gas switching times leaves a large margin for further experimentation and improvement towards higher morphological perfection.

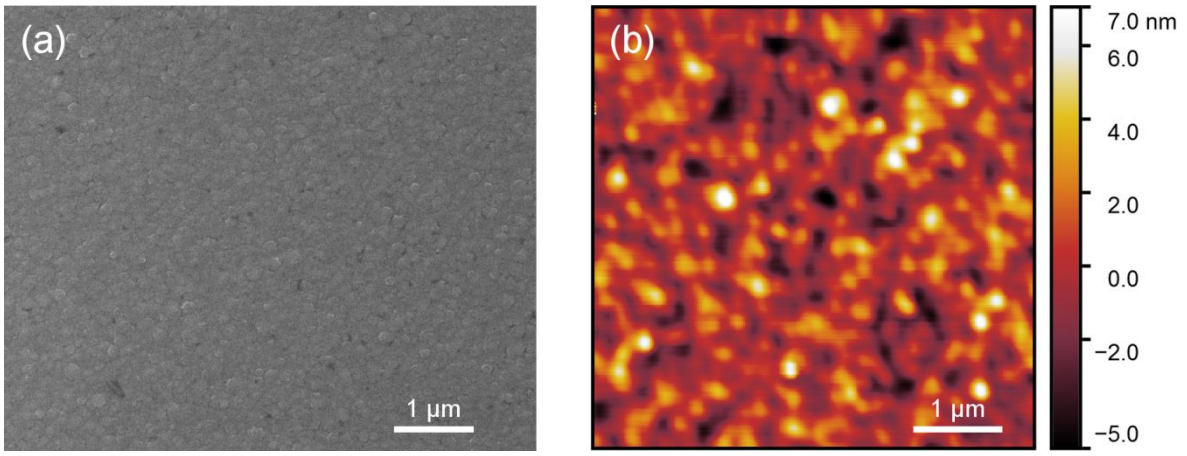

Figure 3.45: (a): SEM and (b): AFM images of a 120 nm ε-Ga_2O_3 ALD film grown on *c*-sapphire at 550 °C. The measured RMS roughness is 1.94 nm. (Adapted from Boschi *et al.*[148])

Furthermore, it is important to underline that this was the first report on the growth of a crystalline gallium oxide phase by ALD[148], while previous works focused on amorphous dielectric films, in which crystallisation was eventually induced only by annealing at high temperature[121,124,125]. Achieving crystalline deposition of gallium oxide in a pure, layer-by-layer ALD regime will be one of the main goals for the future of this research activity.

3.3 Characterisation of β-Ga_2O_3 PLD films

At Leipzig University, deposition of β-Ga_2O_3 heteroepitaxial films by conventional PLD was already at a developed stage[80,81]. However, layers deposited in a standard on-axis configuration exhibited a strong dependence of the electrical conductivity on the thickness. In particular, an abrupt increase in film resistance was observed when the thickness dropped below 100 nm. Unfortunately, the latter includes the range of interest when it comes to fabrication of thin-film based MESFETs, as the channel (i.e. the film itself) must be thin enough to be closed by applying relatively low voltages.

For all eclipse and off-axis samples studied in the present work, a preliminary assessment of the electrical response was thus carried out, by measuring the resistance between triangular contacts positioned at the four corners of the samples. From now on, the latter will be referred to as "edge-contacts". These were fabricated by thermal evaporation of Au/Al/Ti (70/25/25 nm) multilayers on the four sample corners through metal masks, followed by annealing at 500 °C for 10 minutes in nitrogen atmosphere (800 mbar). Distance between contacts was kept constant, in order to get comparable resistance values.

Eclipse PLD did not provide any improvement of electrical nor morphological properties with respect to the conventional setup. Even by changing the diameter of the shadow-mask and by variating the dopant content within the target, no sign of electrical conductivity was detected in films thinner than ~ 150 nm, i.e. well beyond an acceptable threshold for working effectively as channel layers. For this reason, this setup was soon abandoned. As discussed in section 2.1.3, the mask probably shields

not only the heavier, highly energetic particles, but also the activated species and oxygen radicals necessary to promote the film growth, thus resulting in an overall degradation of crystallinity. Adding an inert gas like argon in the deposition chamber might enhance the process.

On the other hand, the off-axis configuration proved to be both faster in terms of growth rate and more flexible. Moreover, preliminary conductivity measurements were carried out on a first series of samples deposited at 90k pulses with different offset values (QM), showing not only a better stability with respect to eclipse PLD, but also a significantly reduced resistance between edge-contacts. In particular, the latter was orders of magnitude lower than the values obtained in on-axis configuration, the respective film thickness being equal (Figure 3.46).

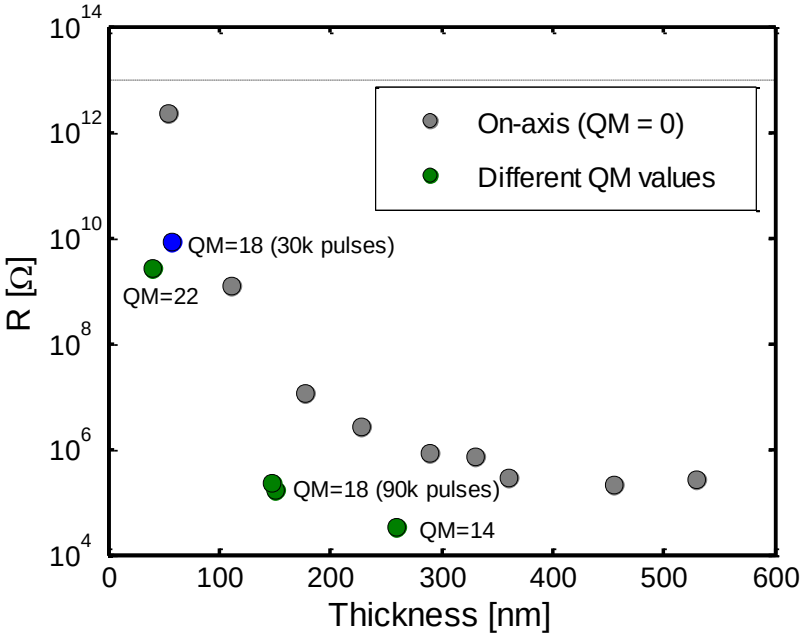

Figure 3.46: Resistance of β-Ga_2O_3 PLD films measured between edge-contacts having the same geometry, and deposited at the same distance. Film thickness being equal, on-axis samples (grey dots) display resistance values which are orders of magnitude larger than the off-axis series, deposited with 90k pulses and different QM values (green dots). A 30k pulses, QM = 18 sample (blue dot) having similar thickness as the QM = 22 one is shown as comparison.

As expected, the thickness decreased with increasing QM value, i.e. with the horizontal offset from the plume axis (remember that 1 QM ~ 1.4 mm shift). QM = 22 was selected as the most promising setup, as lower QMs resulted in higher resistance at comparable thickness (see for example the QM = 18 dot in Figure 3.46).

3.3.1 Field-effect transistors based on PLD β-Ga_2O_3 layers

The best performance FETs were built on sample *w3308* (Table 3.7). Despite its low thickness of ~ 40 nm, the resistance detected by preliminary I-V measurements between edge-contacts decreased from over 10^{12} Ω (on-axis configuration, see Figure 3.46) down to ~ 10^9 Ω. Furthermore, thanks to the off-axis geometry, its surface was almost completely droplet-free (Figure 3.47).

Table 3.7: Main deposition parameters and properties of sample *w3308*, on which the highest performance MESFETs were fabricated.

Sample *w3308*	
QM	22
Silicon content	0.5%
Pulses #	300 @ 1Hz + 90k @ 20 Hz
Thickness	40 nm
Avg. resistance between edge contacts	10^9 Ω
RMS roughness	0.3 nm

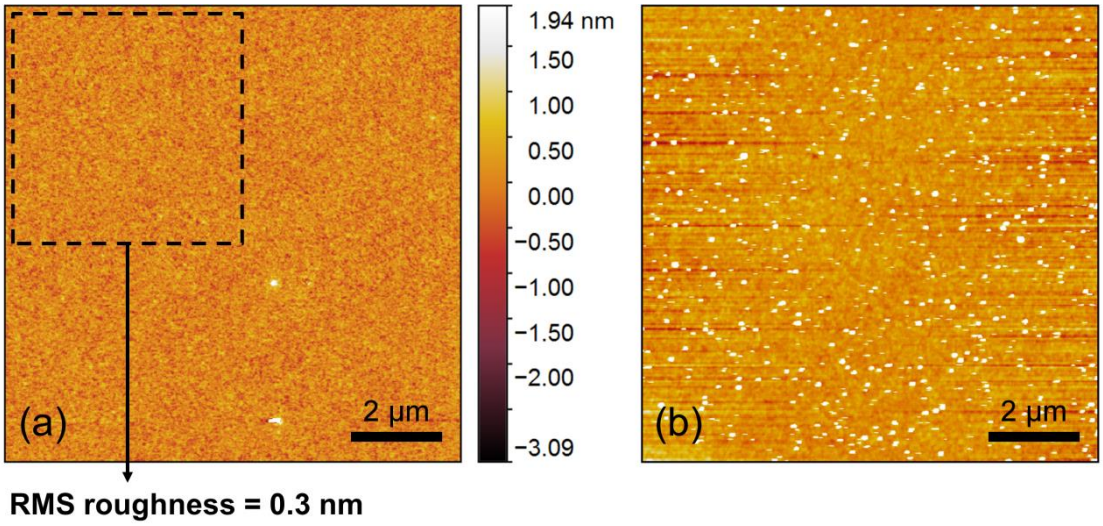

Figure 3.47: AFM image of the almost droplet-free surface of sample *w3308* deposited at QM = 22 (a) compared with a standard on-axis PLD film having the same thickness (b).

MESFETs were fabricated in a ring-geometry similar to the one previously reported for homoepitaxial β-Ga_2O_3 thin films (Figure 1.12a[28]), in order to avoid complicated etching procedures. The pattern used in the present work is shown in Figure 3.48 and consists of a series of ring-FETs with different diameters, replicated multiple times on the sample surface by photolithography. For each FET device, inner and outer regions (namely drain and source, respectively) were Ohmic contacts, obtained by thermal evaporation of Au/Al/Ti (70/25/25 nm) multilayers, followed by 10 min annealing at 500 °C under 800 mbar nitrogen atmosphere. As a last step, Schottky gate-rings were deposited by sputtering Pt in Ar/O_2 atmosphere. The large number of devices allowed to build a significant statistics, also considering the fact that close to the sample border the films are usually slightly thinner. Data analysis and elaboration were performed by Daniel Splith in MATLAB environment.

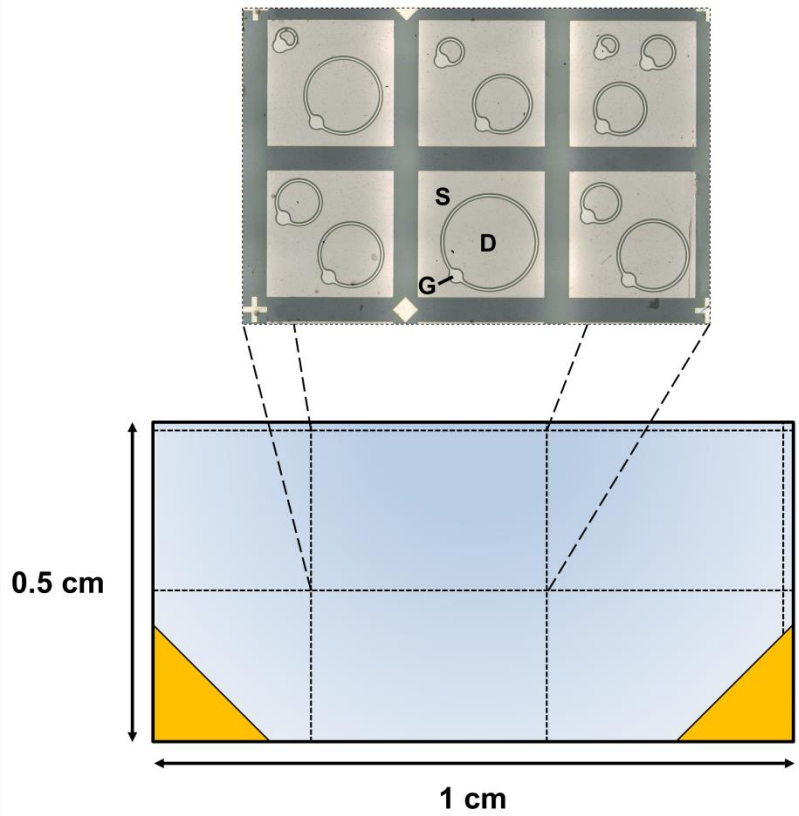

Figure 3.48: Schematic model of the ring-MESFETs deposited on the surface of sample *w3308*. In the upper section of the image, the actual pattern-unit is shown. The diameter of the different gate-rings was 150, 200, 250, 300, 350, 400, 450, 500, 550, 600 and 750 μm. For each FET, the source-to-drain distance was 40 μm, with a gate length of 10 μm. The shading effect on the sample surface is meant to highlight the slight thickness reduction when getting closer to the outer borders. Note that the sample was cut in half (1×0.5 cm^2) previous to FETs deposition, so that only two edge-contacts remained. These will be used as reference to identify the "bottom part" of the sample in the following figures.

Figure 3.49 shows the resistance measured between each couple of drain-source contacts in logarithmic scale. The relatively low resistance (at least considering the film thickness) was here confirmed for the majority of the measured contacts. Note that for this structure the resistance is up to two orders of magnitude lower than the one measured between edge-contacts, due to the shorter distance between drain and source (~ 40 μm).

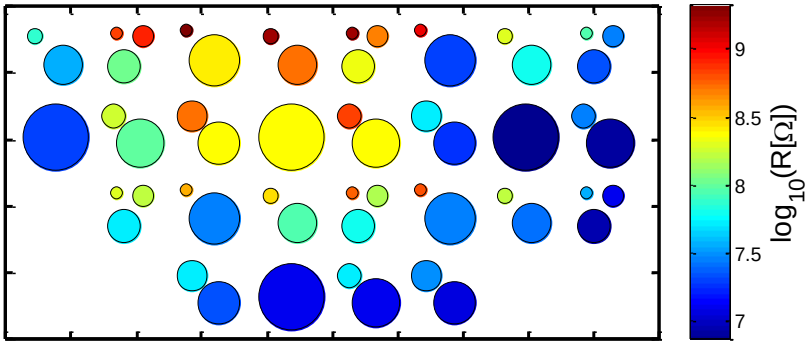

Figure 3.49: Source-drain resistance in logarithmic scale measured for the whole FETs batch. Each dot corresponds to a single FET, reproducing both its diameter and position on the sample surface, following the same pattern shown in Figure 3.48.

The transfer characteristics of a representative FET is shown in Figure 3.50, together with the related physical quantities measured for the whole batch, and highlights the clear presence of a field-effect. On-currents are in the range of 10^{-8} –10^{-7} A, with on/off-ratios between 3 and 5.5 orders of magnitude, while the channel can be closed by applying relatively low threshold voltages (V_T ~ 1.5–3.2 eV).

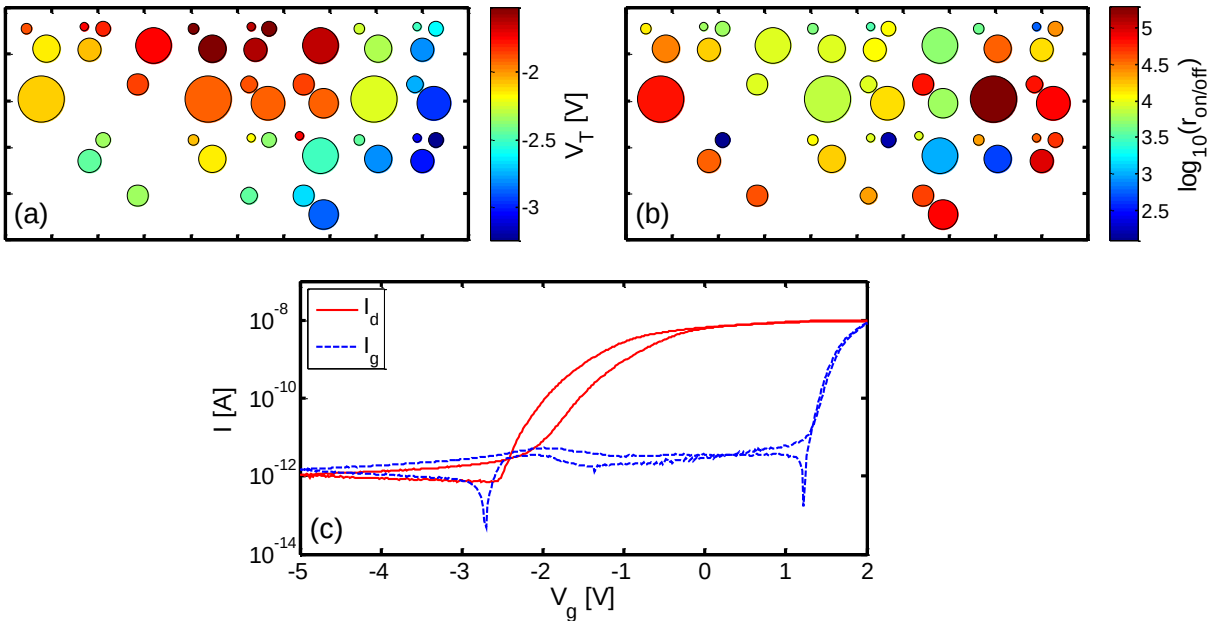

Figure 3.50: (a): Map of threshold voltages V_T. (b): Map of logarithmic drain current (I_d) on/off ratios. (c): Transfer characteristics of a representative FET, showing drain (I_d) and gate (I_g) currents as a function of the gate voltage V_g.

Further information on the physical properties in the film region underneath the transistors were extracted from quasi-static capacitance-voltage (CV) measurements, by fixing drain (V_d) and source voltages (V_s) to 0 V while variating the gate voltage (V_g) (Figure 3.51, Figure 3.52). Within the assumption that the capacitance can be expressed as a function of the depletion-region depth as:

$$C = \frac{\epsilon}{w} \tag{3.4}$$

where ϵ is the film dielectric constant, the doping concentration $N(w)$ was calculated by:

$$N(w) = \frac{2}{q\epsilon}\left(\frac{d(1/C^2)}{dV}\right)^{-1} \tag{3.5}$$

where q is the elementary charge. The average values of channel width (w_{ch}) and doping concentration inside the channel (N_{ch}), respectively shown in Figure 3.52a and Figure 3.52b, were extracted from fitting $N(w)$ with a logistic function (Figure 3.51b). Built-in voltages (V_{bi}) reported in Figure 3.52c were extrapolated by plotting $\frac{1}{C^2}$ as a function of V_g (Figure 3.51c). Furthermore, values of the mobility (μ) are displayed in Figure 3.52d for all the measured FETs. Noteworthy, a thickness

dependence of the mobility seems to emerge, as shown in Figure 3.53. The larger is the channel, the higher the mobility.

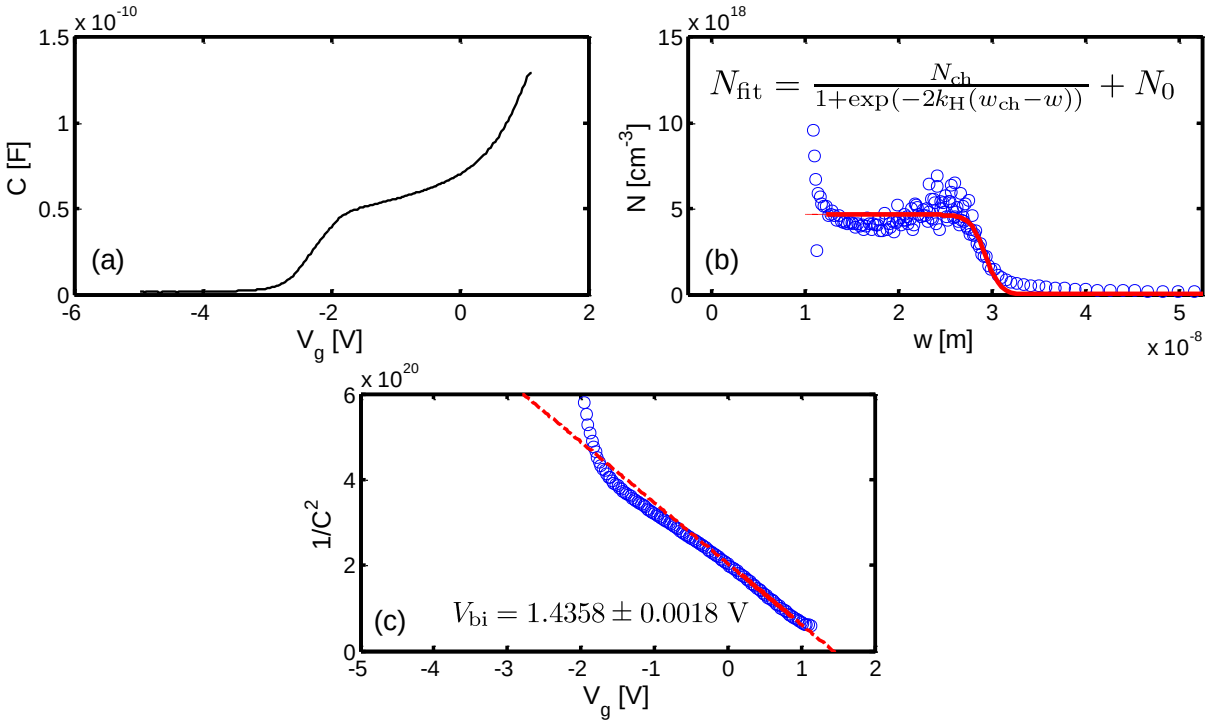

Figure 3.51: Capacitance-voltage measurements of a representative FET. (a): CV characteristics. (b): Extraction of the average doping concentration inside the channel N_{ch} and of the average channel width w_{ch} from fitting of the doping concentration N as a function of the depletion region w. In the fitting function N_{fit}, N_0 is an offset value representing the doping concentration inside the substrate, while k_H is the steepness of the fitting curve. (c): Extrapolation of the built-in voltage V_{bi} from the plot of $1/C^2$ as a function of the gate voltage V_g.

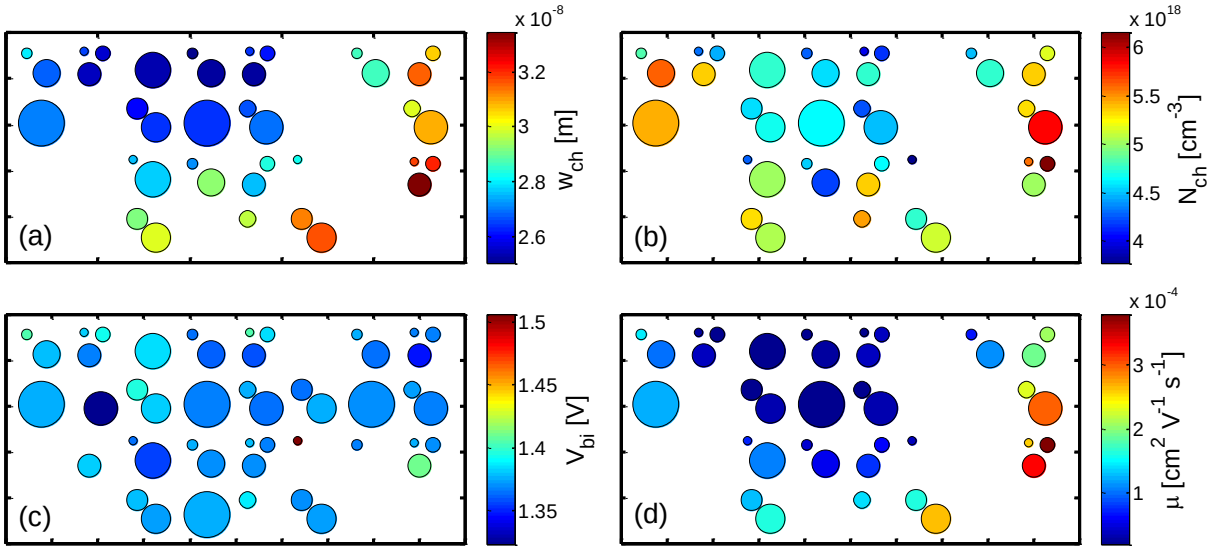

Figure 3.52: Spatial maps of (a): channel widths w_{ch}; (b): doping densities inside the channel N_{ch}; (c): built-in voltages V_{bi}; (d): electron mobilities μ.

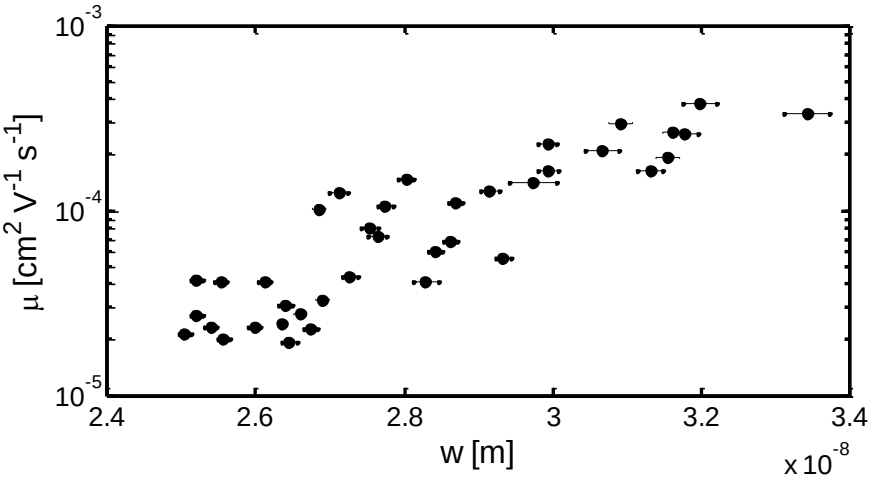

Figure 3.53: Behaviour of the mobility as a function of the channel width.

As a final point, the transistors displayed a stable behaviour over a wide range of applied voltages, with no evidence of breakdown at least up to 100 V (Figure 3.54).

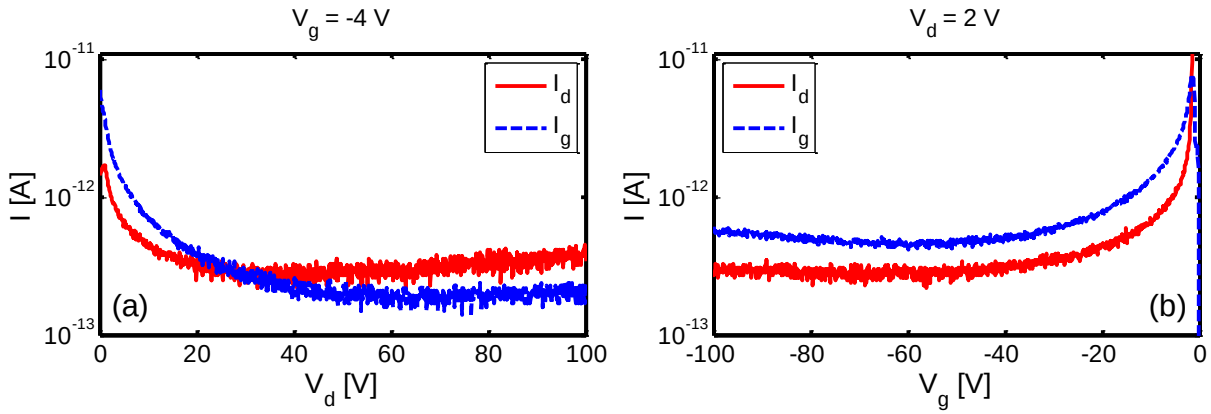

Figure 3.54: Behaviour of drain and gate currents for a representative transistor in the range 0–100 V as a function of (a): V_d at constant V_g and (b): V_g at constant V_d. Note that the channel remains closed within the entire range.

These results are extremely promising, as they demonstrate that field-effect transistors based on heteroepitaxial β-Ga_2O_3 can be successfully fabricated by off-axis PLD and pave the way for further optimisation.

However, attempts to reproduce the very same electrical properties of the first QM = 22 samples failed mostly. In particular, the resistance values, though lower than their on-axis counterparts, were the most difficult to replicate, despite the number of different explored parameters, as shown in Figure 3.55.

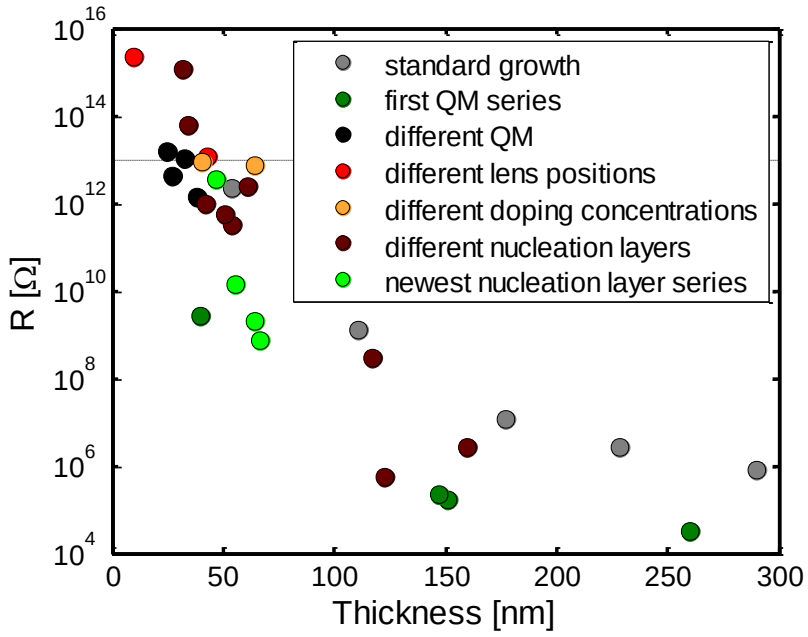

Figure 3.55: Resistance of β-Ga_2O_3 PLD films measured between edge-contacts. Comparison between standard PLD growth, first QM series and reproducibility attempts.

The reasons for these reproducibility issues are unclear at the moment. It is possible that a combined effect of laser oscillating power and focus shifting occurred during the first QM series, as suggested by the thickness increase observed for all the new layers. QM = 22 was probably not the optimal offset value, and further studies will require a combined optimisation of QM, nucleation layer and focusing lens position. Lower QM values could be explored, too, since they allow for higher growth rates and for more freedom in changing the other parameters.

Though still not exactly comparable to the quality of the transistors fabricated on sample *w3308*, the best results were indeed obtained by optimisation of the nucleation layer at QM = 22, as it will be discussed in the following section.

3.3.2 Effect of the nucleation layer

In standard, on-axis PLD processes, nucleation layers were deposited at 1 Hz with 300 pulses. In off-axis configuration, due to the significant drop of the deposition rate, this resulted in practically no deposition at all during the nucleation-layer step. A dedicated study was thus carried out, by investigating the combined effect of different pulse frequencies (5, 10, 20 Hz) and number of pulses.

XRD confirmed the presence of the β-Ga_2O_3 phase for all deposited samples. As expected, the thickness has a clear trend when compared to the number of pulses, with only minor changes due to the pulse frequency (Figure 3.56). Due to the low values involved, in order to get accurate results the thickness was measured by X-ray reflectivity.

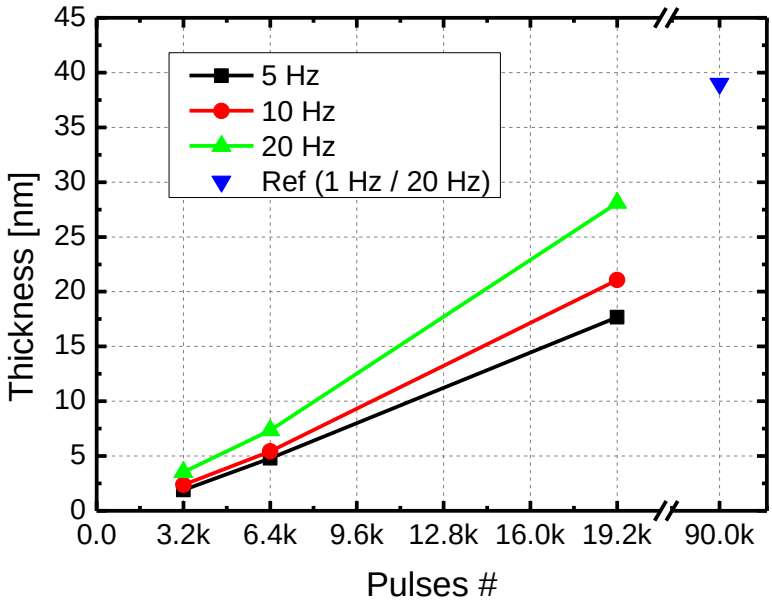

Figure 3.56: Dependence of the thickness on the number of pulses for nucleation layers deposited with different laser frequencies. For the sake of comparison, the thickness of sample *w3308* is also shown, confirming that the deposition rate was here significantly increased.

However, the most significant effect was related to the morphology. RMS roughness, measured by AFM, was below 0.5 nm for all samples grown at 5 Hz and 10 Hz, but it increased up to 1–3 nm for the 20 Hz series (Figure 3.57). The best compromise between growth rate and surface roughness was identified in the 10 Hz frequency.

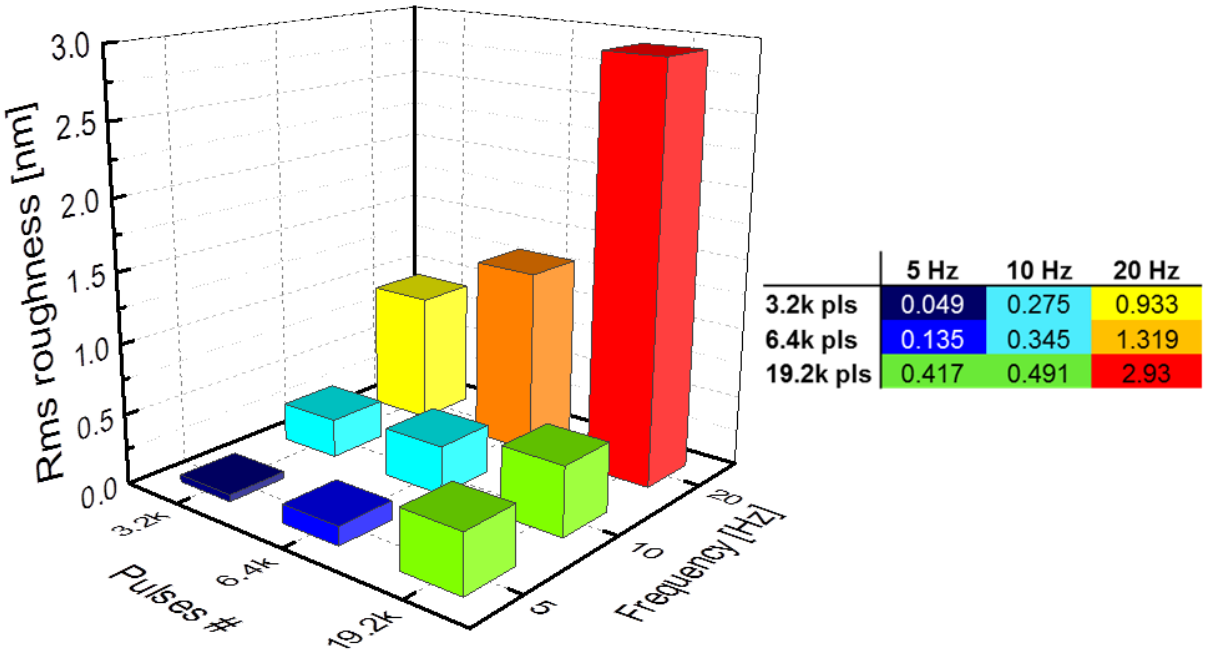

	5 Hz	10 Hz	20 Hz
3.2k pls	0.049	0.275	0.933
6.4k pls	0.135	0.345	1.319
19.2k pls	0.417	0.491	2.93

Figure 3.57: RMS roughness of different nucleation layers, measured by AFM.

A beneficial effect of the 10 Hz nucleation layer on the final morphology was confirmed also when employed as actual buffer for the deposition of 20 Hz films, with a further reduction of the surface roughness down to 0.1–0.3 nm in the case of ~ 40 nm thick samples.

As anticipated, for all these films the resistance measured between edge-contacts was higher than for *w3308*. Nevertheless, it was again an improvement with respect to previous on-axis samples, allowing for fabrication of ring-FETs. The presence of a 10 Hz nucleation layer further helped reducing the film resistivity and increasing the on-off ratio of ring-FETs (Figure 3.58).

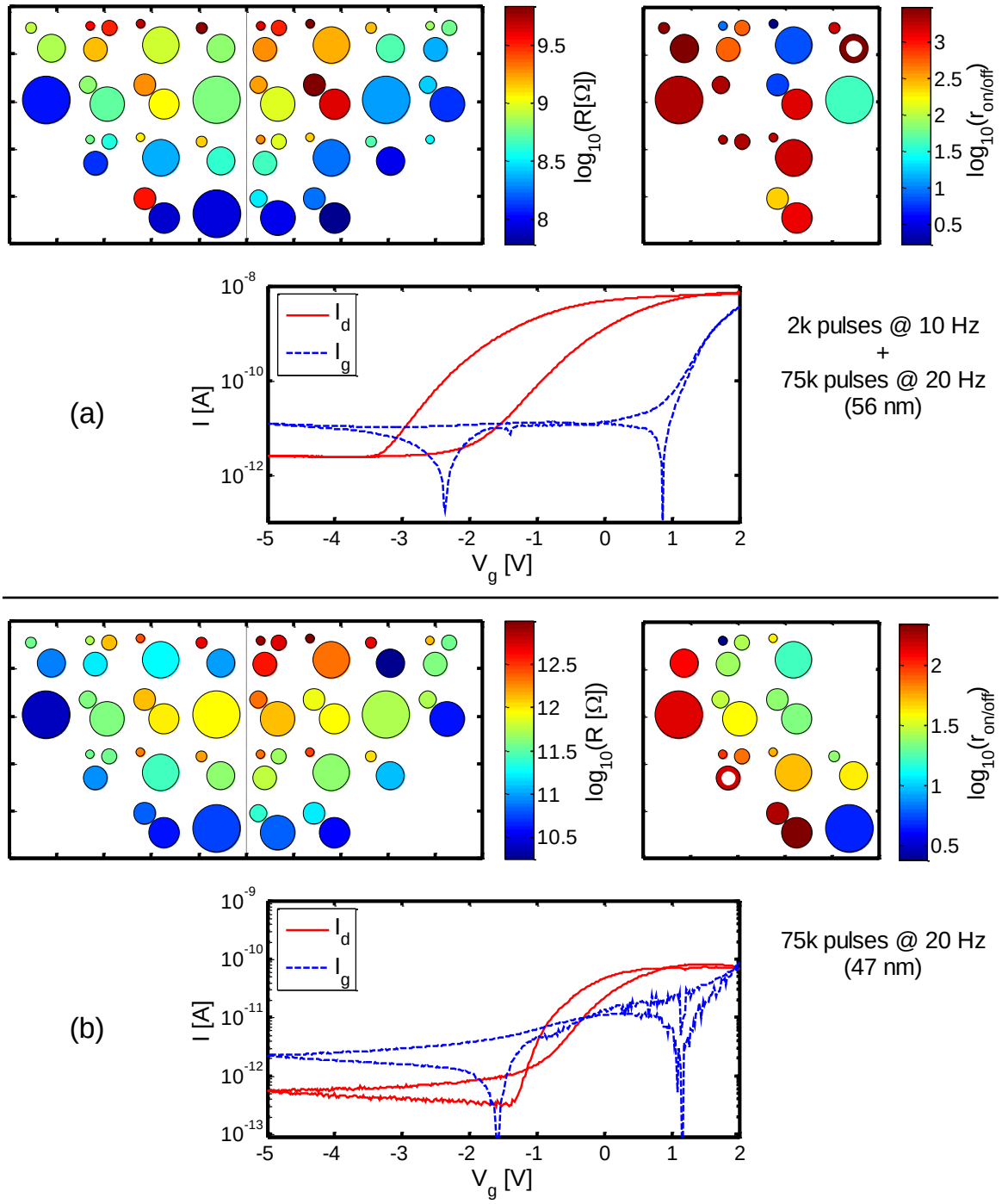

Figure 3.58: Map of drain-source resistance, map of logarithmic drain current on-off ratios and representative transfer characteristics of (a): a sample grown onto a 10 Hz nucleation layer and (b): a sample grown without a nucleation layer.

3.3.3 Deposition on ε-Ga_2O_3 templates

In a series of preliminary experiments, PLD samples were deposited on MOCVD and ALD ε-Ga_2O_3 templates fabricated on *c*-plane sapphire at IMEM-CNR. Both standard and off-axis (QM = 22) PLD were explored. For each process, a PLD sample of ~ 40 nm was chosen as reference for setting the growth parameters in order to get a comparable thickness. Further details on the employed parameters can be found in Table 2.6.

The most interesting outcome for these preliminary series of experiments emerges from XRD analysis. Figure 3.59 shows the scan profiles of a representative sample before and after PLD growth. While the employed templates were and remained pure-ε phase, intense peaks corresponding to the nominal β-Ga_2O_3 positions arose when PLD growth was performed. In order to facilitate the distinction of the peaks belonging to the two different phases, only the higher order diffractions are shown.

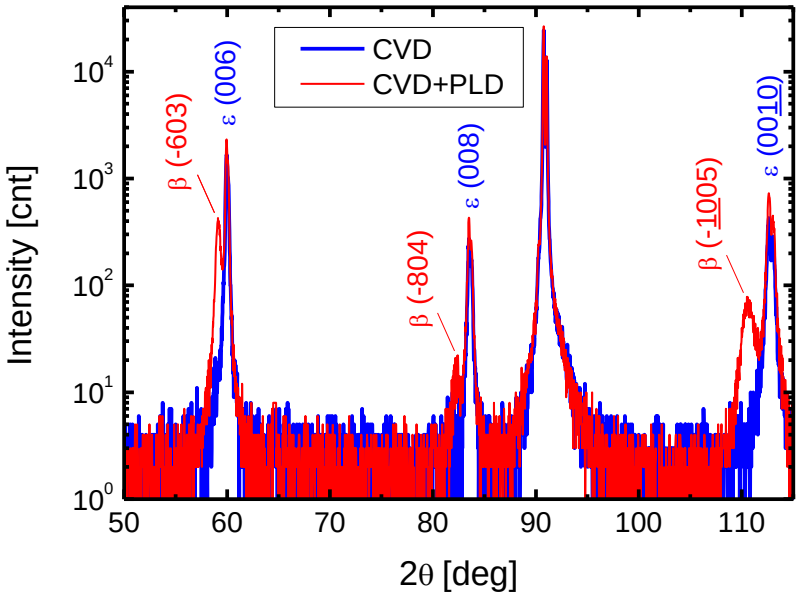

Figure 3.59: XRD scan profiles of a "heteroepitaxial" β-G_2O_3 PLD sample and of the corresponding ε-Ga_2O_3 layer used as template. Only high order diffractions are shown, for the sake of clarity.

All the measured "heteroepitaxial" PLD layers shared the same behaviour. These findings seem to further confirm the decisive role of both the growth temperature and of employing a chemical deposition method in the formation of stabilised ε-Ga_2O_3 thin films.

CHAPTER 4 - Anisotropic properties of β-Ga_2O_3 bulk crystals

The initial period of this Ph.D. activity, while the deposition process for ε-Ga_2O_3 thin films by MOCVD was still under development, was dedicated to the investigation of β-Ga_2O_3 bulk samples provided by a Japanese partner (Tamura Corp.). The aim was to get acquainted with the material, understanding at the same time some fundamental properties that were either controversial or poorly discussed in the existing literature. In particular, this chapter will focus on the anisotropic behaviour of β-Ga_2O_3, concerning optical properties (Raman and absorption), as well as thermal expansion at high temperature.

The study of Raman properties was carried out in collaboration with Prof. Pier Paolo Lottici. Raman-active A_g and B_g modes were selectively observed depending on the experimental geometry, and their assigned wavenumber was compared with previous works. Furthermore, Raman tensor elements of A_g modes were obtained by angular fitting of the respective intensities. Different approaches and models are here compared, including the one proposed by Kranert *et al.* in recent works[70,71], which accounts for birefringence effects.

Anisotropic optical absorption of β-Ga_2O_3 is a well-known experimental fact, as previously discussed in section 1.1.4[30,49]. However, it is surprising that many recent papers reported bandgap values of β-Ga_2O_3 without providing any information about sample orientation and measurement geometry. In order to shed more light on the relationship between optical properties and band structure, a combined experimental and theoretical assessment of anisotropy in the optical absorption edge as a function of light polarisation was here carried out, in collaboration with Prof. Andrea Baraldi and with the group of Prof. Vincenzo Fiorentini. From the experimental point of view, different sample orientations were explored, which were not investigated so far. The experimental bandgap values were critically discussed in view of the results of *ab initio* computation, and a physical interpretation of the optical anisotropy was provided. This study resulted in a publication[59].

As a last point, thermal expansion coefficients of lattice parameters were accurately measured at high temperature by XRD and compared with previous, low-temperature data[51]. This information, surprisingly missing in literature, is of crucial importance for epitaxy, since it allows to determine the *thermal mismatch* between film and substrate. Contrary to *lattice mismatch*, the latter holds when the lattice parameters of substrate and layer have a good matching at room temperature but, owing to different thermal expansion, they tend to diverge as soon as the temperature is raised. Therefore, the "ideal" substrate/film combination at room temperature does not ensure the obtainment of a defect-free layer, as the film may undergo a considerable strain during the heating-growth-cooling cycle of

typical epitaxial processes. Knowing the behaviour of the lattice parameters at high temperature thus allows to foresee the formation of extended defects in epilayers and to further improve their quality. This study was performed in collaboration with the crystallography group of the Chemistry Department (University of Parma), and the results were the object of a publication[57].

4.1 Samples specifications

The investigated samples were high-quality bulk crystals, (010)- and (-201)- oriented, provided by Tamura Corporation and cut from single-crystalline ribbons grown from the melt by the EFG technique (Figure 4.1). Table 4.1 reports the specifications kindly provided by the supplier. All samples were 10×15 mm^2 in size and unintentionally doped, with carrier densities around $2 \cdot 10^{17}$ cm^{-3}.

Table 4.1: β-Ga_2O_3 bulk samples specifications, as kindly provided by the supplier (Tamura Corp., Japan[45]), along with the characterisations performed in this work. CMP stands for "*chemical-mechanical polishing*".

Bulk #	Size (mm^2)	Thickness (µm)	Surface orientation	N_d-N_a (cm^{-3})	Surface front /back	Characterisations
EUN03	10×15	≈ 600	(010)	$1.9 \cdot 10^{17}$	CMP / CMP	Raman, expansion
EUN05	10×15	≈ 650	(-201)	$1.7 \cdot 10^{17}$	CMP / Rough	Absorption
EUN06	10×15	≈ 650	(010)	$2.4 \cdot 10^{17}$	CMP / Rough	Absorption

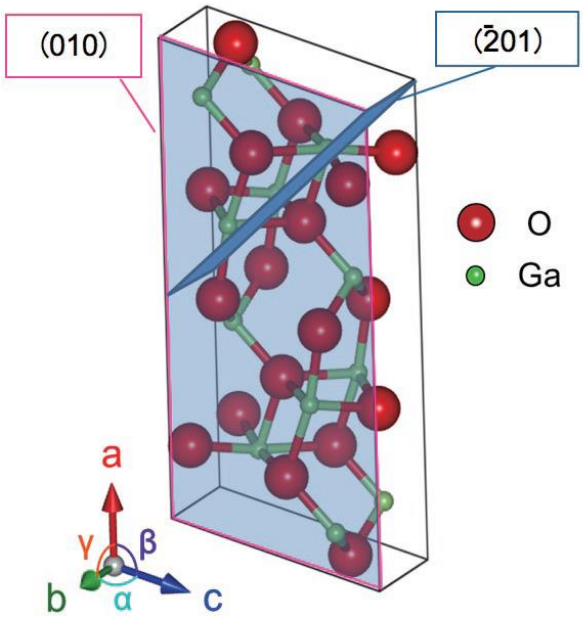

Figure 4.1: Crystal structure and orientation of the bulk β-Ga_2O_3 samples studied in this chapter (kindly provided by Tamura Corp.[45]).

4.2 Raman spectra and tensor elements determination

4.2.1 Raman tensor formalism for β-Ga_2O_3

According to the factor group analysis, fifteen Raman-active modes are expected for β-Ga_2O_3[66]:

$$\Gamma_{Raman} = 10A_g + 5B_g \tag{4.1}$$

Raman activity and selection rules of the vibrational modes are described by the Raman tensor, a second-rank symmetric tensor, which is a function of the crystal structure. In monoclinic structures, the two-fold ***b***-axis is an indicatrix axis, while the other two, mutually perpendicular, lie in the plane perpendicular to ***b***, but at some angle to the crystallographic axes ***a*** and ***c***. In order to be consistent with previous works[66,68,71], a reference system was here chosen by imposing Z parallel to ***b***, as this axis lies perpendicularly to the (010) face, while Y was set parallel to ***a*** and X at an angle of about 14° from ***c*** in the *ac* plane. Consequently, one obtains the following form for the second-rank Raman tensors $\mathcal{R}$ of the A_g and B_g modes at $\boldsymbol{k} = 0$[195]:

$$\mathcal{R}(A_g) = \begin{pmatrix} a & d & 0 \\ d & b & 0 \\ 0 & 0 & c \end{pmatrix} \quad ; \quad \mathcal{R}(B_g) = \begin{pmatrix} 0 & 0 & e \\ 0 & 0 & f \\ e & f & 0 \end{pmatrix} \tag{4.2}$$

where a, b, c, d, e, and f here denote the Raman tensor elements (RTEs). As a general rule, the relative intensities of a given Raman mode is related to the corresponding tensor by[195]:

$$I \propto |\boldsymbol{e}_i \, \mathcal{R} \, \boldsymbol{e}_s|^2 \tag{4.3}$$

where I is the Raman intensity, $\boldsymbol{e}_i$ and $\boldsymbol{e}_s$ are the unit polarisation vectors of the electrical field of the incident and scattered beams, respectively, and $\mathcal{R}$ represents the Raman scattering tensor of the particular mode under consideration, while the proportionality coefficient depends on the experimental conditions.

For monoclinic β-Ga_2O_3, A_g modes are therefore allowed for the $(X\,X)$, $(Y\,Y)$, $(Z\,Z)$ and $(X\,Y)$ polarisation configurations, while B_g modes are allowed for the $(Y\,Z)$ and $(Z\,X)$ configurations. The two terms in brackets indicate the direction of the electric field vector for the incident and backscattered light, respectively (*Porto formalism*, Table 4.2).

This allows for selective observation of the modes, depending on the employed experimental geometry. If light propagates along Z, i.e. perpendicular to the (010) face, only A_g modes can be observed. This case is the most straightforward when analysing (010) samples. On the contrary, when light propagates perpendicular to Z, operating in parallel- or cross-polarisation configuration allows to discriminate between A_g and B_g modes, respectively. This geometry can be achieved also for (010) samples, provided that the thickness is sufficient to focus the laser on one of the lateral edges.

Table 4.2: Selection rules for β-Ga_2O_3 Raman modes in different backscattering geometries, expressed by the *Porto formalism*. The two terms in brackets indicate the direction of the electric field vector for the incident and backscattered light, respectively, while the terms outside brackets stand for the direction of incident (left) and scattered (right) radiation. Primed values indicate negative directions. Note that while Z is kept parallel to the crystallographic ***b***-axis, x and y can be any two directions, mutually perpendicular, within the XY plane (with X and Y axes chosen in the same way described in the main text).

Backscattering geometry	Allowed Raman modes
$Z(x\ x)Z'$	A_g
$Z(x\ y)Z' = Z(y\ x)Z'$	A_g
$Z(y\ y)Z'$	A_g
$x(Z\ Z)x'$	A_g
$x(y\ Z)x' = x(Z\ y)x'$	B_g
$y(x\ Z)y' = y(Z\ x)y'$	B_g

Concerning A_g modes, if light propagates along Z within a backscattering geometry, the observed intensities should be directly related to the corresponding RTEs in Eq. 4.2 by:

$$I_{XX} \propto a^2 \tag{4.4}$$

$$I_{YY} \propto b^2 \tag{4.5}$$

$$I_{XY} = I_{YX} \propto d^2 \tag{4.6}$$

where I_{XX} and I_{YY} are the intensities measured in parallel polarisation along X and Y, respectively, while I_{XY} = I_{YX} is the intensity measured in cross polarisation along X or Y, equivalently. However, from the experimental point of view it is not straightforward to exactly align the polarisation to the real X and Y, and furthermore even small fluctuations in the signal can prevent a correct intensity value from being extracted. A more accurate result can be obtained by fitting the intensity of each mode as a function of the rotation angle θ around the Z axis, considering that:

$$\mathcal{R}_{ij}(\theta) = (M_{rot}\mathcal{R}M_{rot}^T)_{ij} \tag{4.7}$$

where R_{ij} is the i,j-th element of the tensor, while M_{rot} and M_{rot}^T are the 2D rotation matrix and its transposed, respectively. In the following, this approach will be referred to as *classic model*.

However, for some anisotropic materials a non-ideal angular dependence of the intensity can be observed, with features that cannot simply be modelled by combining Eqs. 4.3 and 4.7. In some cases, this anomalous behaviour is accounted for by introducing Raman tensors with complex elements[196–198]. For A_g modes in β-Ga_2O_3 the most general Raman tensor form would thus be (*phase-angles model*):

$$\mathcal{R}(A_g) = \begin{pmatrix} |a|e^{i\alpha} & |d|e^{i\delta} & 0 \\ |e|e^{i\varepsilon} & |b|e^{i\beta} & 0 \\ 0 & 0 & |c|e^{i\gamma} \end{pmatrix} \tag{4.8}$$

Although these complex RTEs can obviously lead to a better convergence of angular-fitting curves to data due to the increased number of fitting parameters, the phase angles do not have a well-defined physical meaning. In this regard, Kranert *et al.*[70] recently proposed a model which accounts for birefringence effects, thus providing a physical explanation to deviations from ideality in optically anisotropic crystals. According to the authors, in the case of (010)-oriented β-Ga_2O_3 studied in backscattering geometry, Raman properties would be described by a 2D effective tensor:

$$\mathcal{R}_{Eff}(\theta, z) = \mathcal{R}_0(\theta) + \mathcal{R}_1(\theta)e^{i\chi(z)} + \mathcal{R}_2(\theta)e^{i2\chi(z)} \tag{4.9}$$

with:

$$\mathcal{R}_0(\theta) = a\begin{pmatrix} cos^2\theta & sin\,\theta\,cos\,\theta \\ sin\,\theta\,cos\,\theta & sin^2\theta \end{pmatrix} \tag{4.10}$$

$$\mathcal{R}_1(\theta) = d\begin{pmatrix} -2\,sin\,\theta\,cos\,\theta & cos^2\theta - sin^2\theta \\ cos^2\theta - sin^2\theta & 2\,sin\,\theta\,cos\,\theta \end{pmatrix} \tag{4.11}$$

$$\mathcal{R}_2(\theta) = b\begin{pmatrix} sin^2\theta & -\,sin\,\theta\,cos\,\theta \\ -\,sin\,\theta\,cos\,\theta & cos^2\theta \end{pmatrix} \tag{4.12}$$

$\mathcal{R}_{eff}$ thus depends both on the in-plane rotation angle θ and on the scattering depth z, through a function $\chi(z)$. However, in the limit of an infinite scattering depth, which is a suitable approximation for typical thicknesses of β-Ga_2O_3 bulk samples, Raman intensity would no longer follow Eq. 4.3, but instead:

$$I \propto |\boldsymbol{e}_s\mathcal{R}_0\boldsymbol{e}_i|^2 + |\boldsymbol{e}_s\mathcal{R}_1\boldsymbol{e}_i|^2 + |\boldsymbol{e}_s\mathcal{R}_2\boldsymbol{e}_i|^2 \tag{4.13}$$

which makes the birefringence contribution depth-independent (*birefringence model*). Further details on the three discussed models can be found in Appendix A.

4.2.2 Experimental details

Raman spectra were recorded in a backscattering geometry, using a Horiba-Jobin-Yvon LabRAM micro-spectrometer, equipped with a 632.8 nm He-Ne laser, an integrated Olympus BX40 microscope and a Peltier-cooled CCD detector. The laser power was set to less than 5 mW on the sample, to avoid uncontrolled thermal effects. Spectra were collected by using an ultra-long working distance 50x microscope objective, with typical exposures of 30 s, repeated 3 times. The sample was a (010)-oriented, unintentionally doped β-Ga_2O_3 wafer (see Table 4.1).

The wavenumbers of A_g and B_g Raman modes were determined in different sample and polarisation geometries. Scattered light polarisation (parallel or cross) was controlled by means of polarising filters.

Furthermore, it was possible to estimate the RTEs of A_g modes, by studying the related intensity changes with crystal rotation around the (010) axis. As depicted schematically in Figure 4.2, the sample was arranged in the starting position (θ = 0), with the X-axis parallel to the incident laser

polarisation, and was then rotated 360° counter-clockwise around the Z-axis, by using a backlash-free goniometer stage. Since alignment to the initial position was performed roughly with an optical microscope by taking a cleaved edge parallel to the (100) plane as reference, the condition for θ = 0° was later optimised during fitting and found to be about -2° with respect to Figure 4.2.

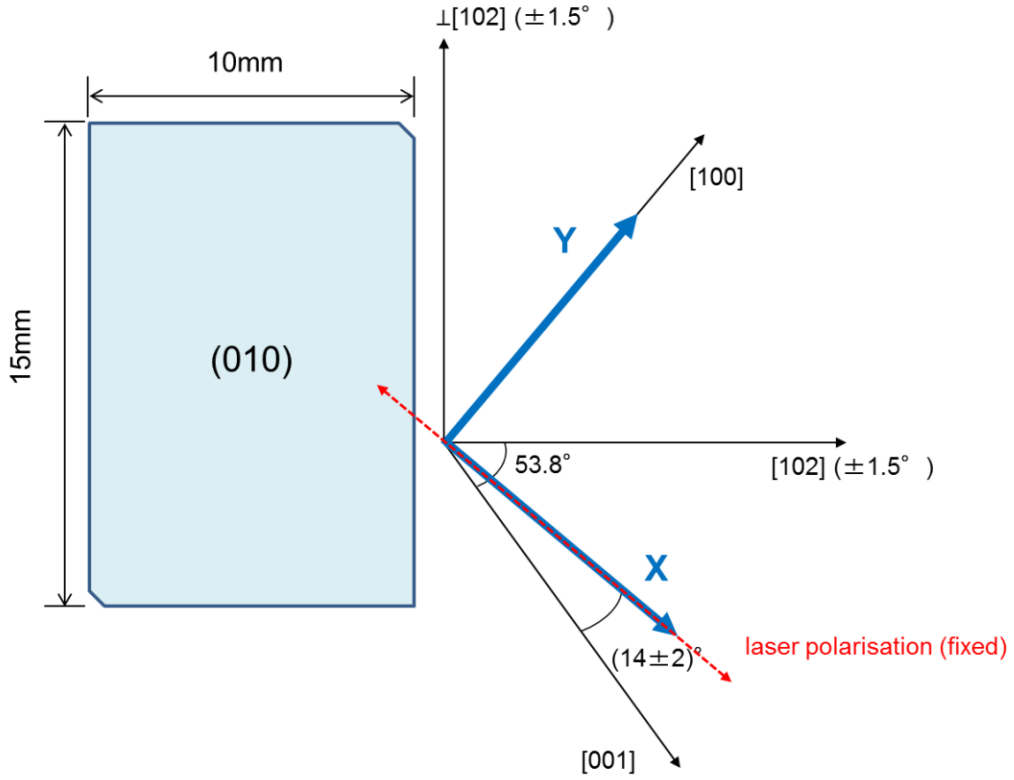

Figure 4.2: Top-view of the starting setup (θ = 0°) for angular Raman measurements. From this configuration, the sample is rotated counter clockwise by 15° steps, up to 360°.

In order to assign the peak wavenumbers, peaks were identified and fitted with Lorentzian functions. For A_g modes, in particular, an average over the whole rotation range and over different types of baseline corrections (8th degree polynomial, linear, automatic and manual) was evaluated.

In order to determine a, b and d RTEs of A_g modes, i.e. the ones accessible in a (010) oriented sample, peak areas were extracted keeping constant both position and width of the Lorentzian functions. For each mode, a mean value for the area was evaluated at each angle, averaging between different baseline corrections. For the sake of optimal data visualisation, only the interval 0–180° was considered and the corresponding intensity values were averaged with those measured at 180–360°. Angular behaviour was fitted by using the three models discussed in the above section: *classic*, *phase-angles* and *birefringence*. Further details about the employed model equations can be found in Appendix A.

Raw-data manipulation was performed within the LabSpec suite, while Raman tensor determination and curve fitting were carried out in MATLAB environment.

4.2.3 Wavenumbers of the Raman modes

From the polarisation selection rules reported in Table 4.2, only A_g modes are expected to appear in Raman backscattering spectra on the (010) surface. For each value of the angle θ, spectra were acquired with parallel and crossed polarisers (Figure 4.3). A representative spectrum, in which all ten expected A_g modes are visible, is reported in Figure 4.4.

Whereas laser propagation along [010] direction allows only A_g symmetry modes to be observed, backscattering on the perpendicular surface (i.e. with the laser propagating in the XY plane) allows to distinguish (in parallel- and cross-polarisation, respectively) the diagonal Raman tensors components, displayed by A_g symmetry modes only, from the crossed components ($x\ Z$) and ($y\ Z$), which are non-zero only for B_g modes. The obtained spectra are shown in Figure 4.5. Note that, just like in Table 4.2, x and y represent two arbitrary directions, mutually perpendicular, within the XY plane.

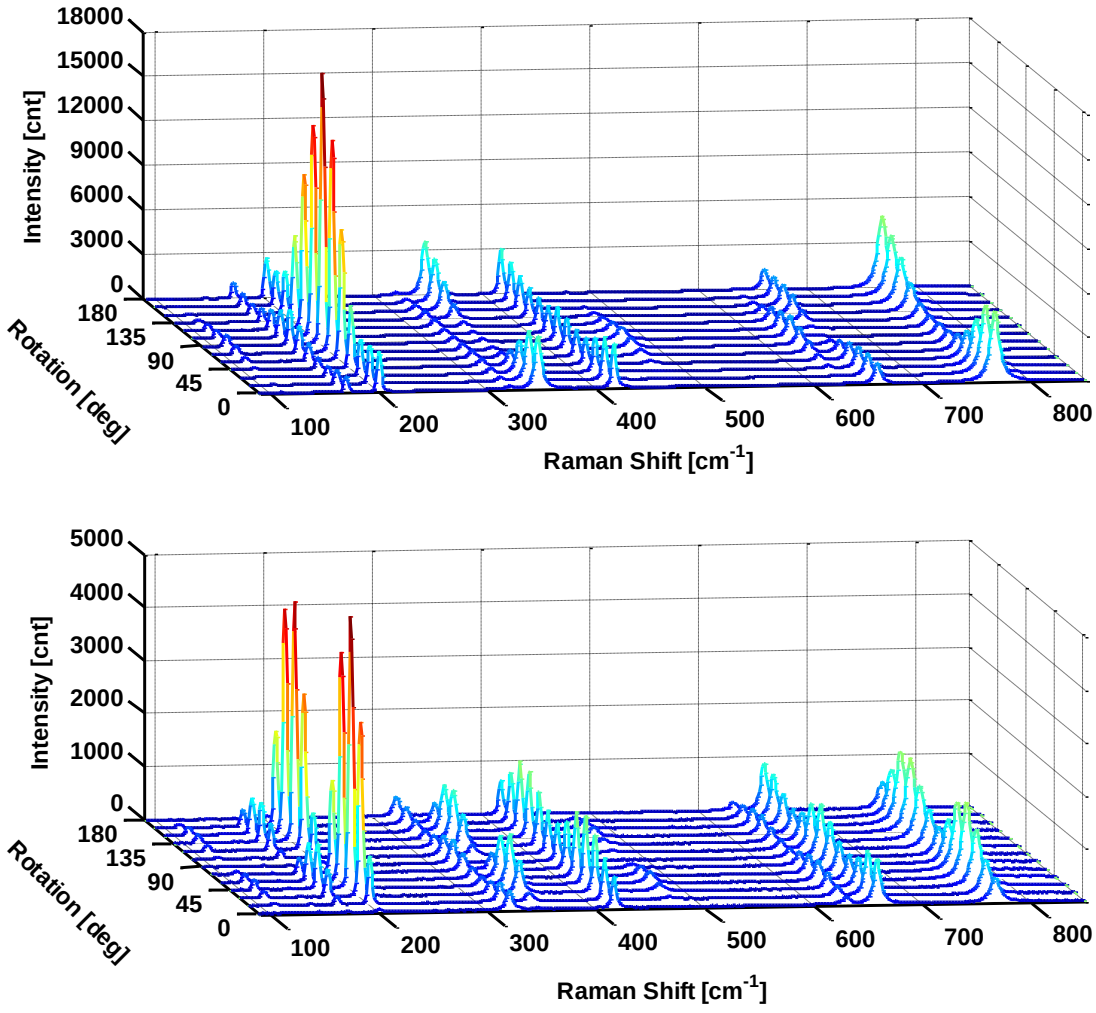

Figure 4.3: Parallel (top) and cross (bottom) spectra for different values of rotation angle θ. For the sake of clarity, only the interval 0–180° is shown. Colours from blue to red cover the intensity range from the minimum to the maximum value, respectively.

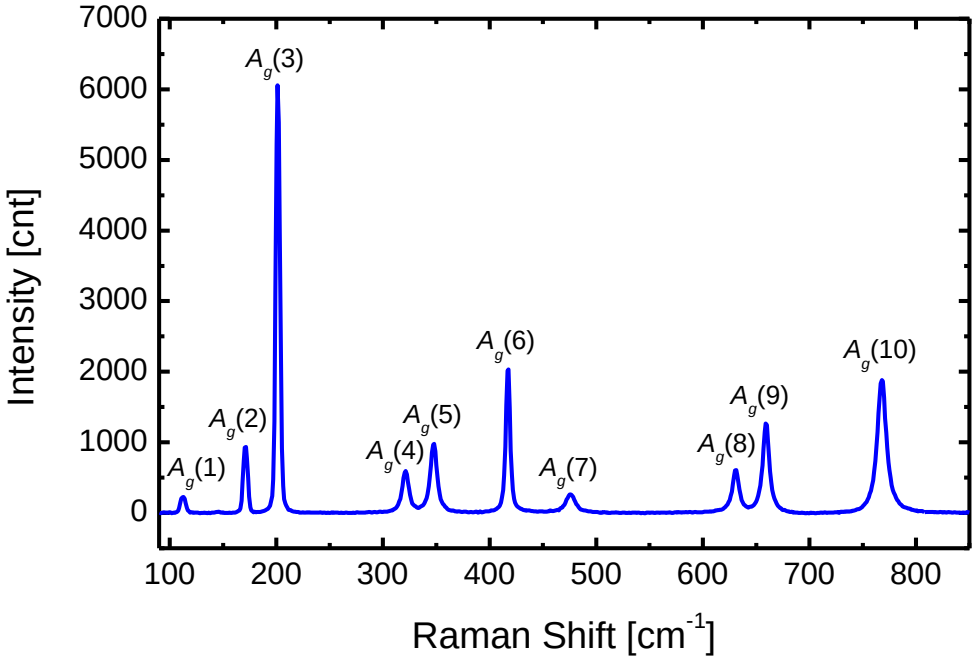

Figure 4.4: Representative spectrum measured in parallel polarisation on the (010) surface, where all A_g modes are clearly visible.

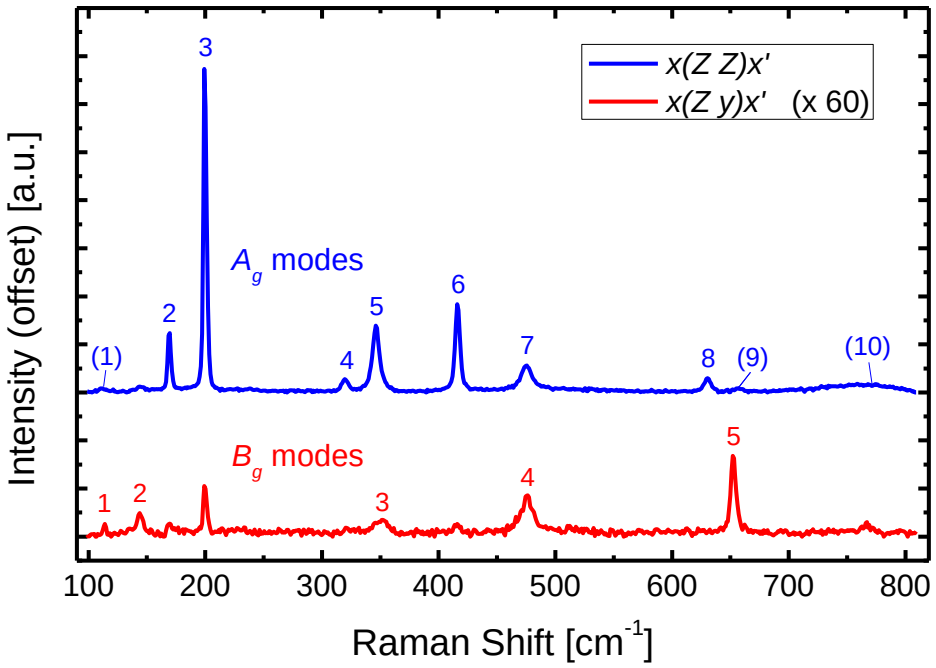

Figure 4.5: Backscattering Raman spectra in parallel $x(Z\ Z)x'$ and cross $x(Z\ y)x'$ configurations, with the laser propagating parallel to the XY plane, i.e. incident on the 600 μm thick surface perpendicular to the (010) plane of the sample. Since the exact orientation of the electric field in this not-optimal geometry is not known accurately, here x and y represent two arbitrary directions, mutually perpendicular, within the XY plane. In order to get comparable intensities, cross-polarised spectra were multiplied by a factor 60.

Since the measured sample was (010) oriented, the latter backscattering condition was not straightforward to achieve. The sample was in fact mounted vertically and the laser was focused on the lateral edge, only 600 μm thick. Despite this not-optimal geometry, B_g modes emerge at 114, 144, 352, 475 and 652.5 cm^{-1}. Some leakage of the most intense A_g modes is present, as well, due mainly to the wide angle of collection. The feature at 475 cm^{-1} is displayed by both spectra and therefore its A_g and B_g symmetry character is confirmed[66].

A complete list of the obtained phonon wavenumbers for β-Ga_2O_3 is reported in Table 4.3, compared with previous works. Due to the more favourable geometric conditions, statistics could be applied more efficiently to A_g modes, whose wavenumbers were averaged over the whole sample rotation range and for different types of baseline correction. Nevertheless, B_g modes wavenumbers were assigned within a reasonable degree of confidence.

Table 4.3: Raman shift values (cm^{-1}) for all A_g and B_g Raman modes, compared with previous works.

Mode	Present work	Dohy *et al.*[66]	Onuma *et al.*[68]	Kranert *et al.*[71]
A_g (1)	112.1 ± 0.5	111	112	111.0
B_g (1)	114.0 ± 0.5	114	115	114.8
B_g (2)	144.5 ± 0.5	147	149	144.8
A_g (2)	170.7 ± 0.3	169	173	169.9
A_g (3)	201.5 ± 0.2	199	205	200.2
A_g (4)	320.4 ±0.5	318	322	320.0
A_g (5)	347.6 ± 0.1	346	350	346.6
B_g (3)	352.0 ± 0.5	353	355	353.2
A_g (6)	417.2 ± 0.3	415	421	416.2
A_g (7)	475.9 ± 0.7	475	479	474.9
B_g (4)	475 ± 1	475	480	474.9
A_g (8)	630.6 ± 0.3	628	635	630.0
B_g (5)	652.5 ± 0.5	651	659	652.3
A_g (9)	659.3 ± 0.6	657	663	658.3
A_g (10)	767.5 ± 0.5	763	772	766.7

As it can be noticed, these data confirm previous symmetry assignments, and a particularly good agreement with the results obtained in the pioneering work of Dohy *et al.*[66] is evident, as well as with those recently reported by Kranert *et al.*[71]. All peak positions reported by Onuma *et al.*[68] appear to be slightly blue-shifted (2–5 cm^{-1}) with respect to the present results.

4.2.4 Crystal rotation and Raman tensor elements for the A_g modes

The results of angular fitting are shown in Figure 4.6 for each peak and for each employed model. For the sake of optimal visualisation, all curves are normalised to the respective maximum.

The *classic model* qualitatively reproduces the angular behaviour of most peaks, but fails significantly with modes $A_g(4)$, $A_g(6)$ and $A_g(9)$. In particular, it is unable to replicate some specific features, such as non-zero minima and shifted periodicity for cross-polarisation curves, and secondary maxima for parallel-polarisation curves. A significant improvement is achieved when a complex Raman tensor is used (*phase-angles model*). While the modulus of the diagonal elements (*d* and *e* in Eq. 4.8) can be set as equal, phase angles need to be different in order to obtain a satisfactory fitting such as the one shown in Figure 4.6. The optimal fit is however achieved with the *birefringence model* (further details about goodness of fit are available in Appendix A).

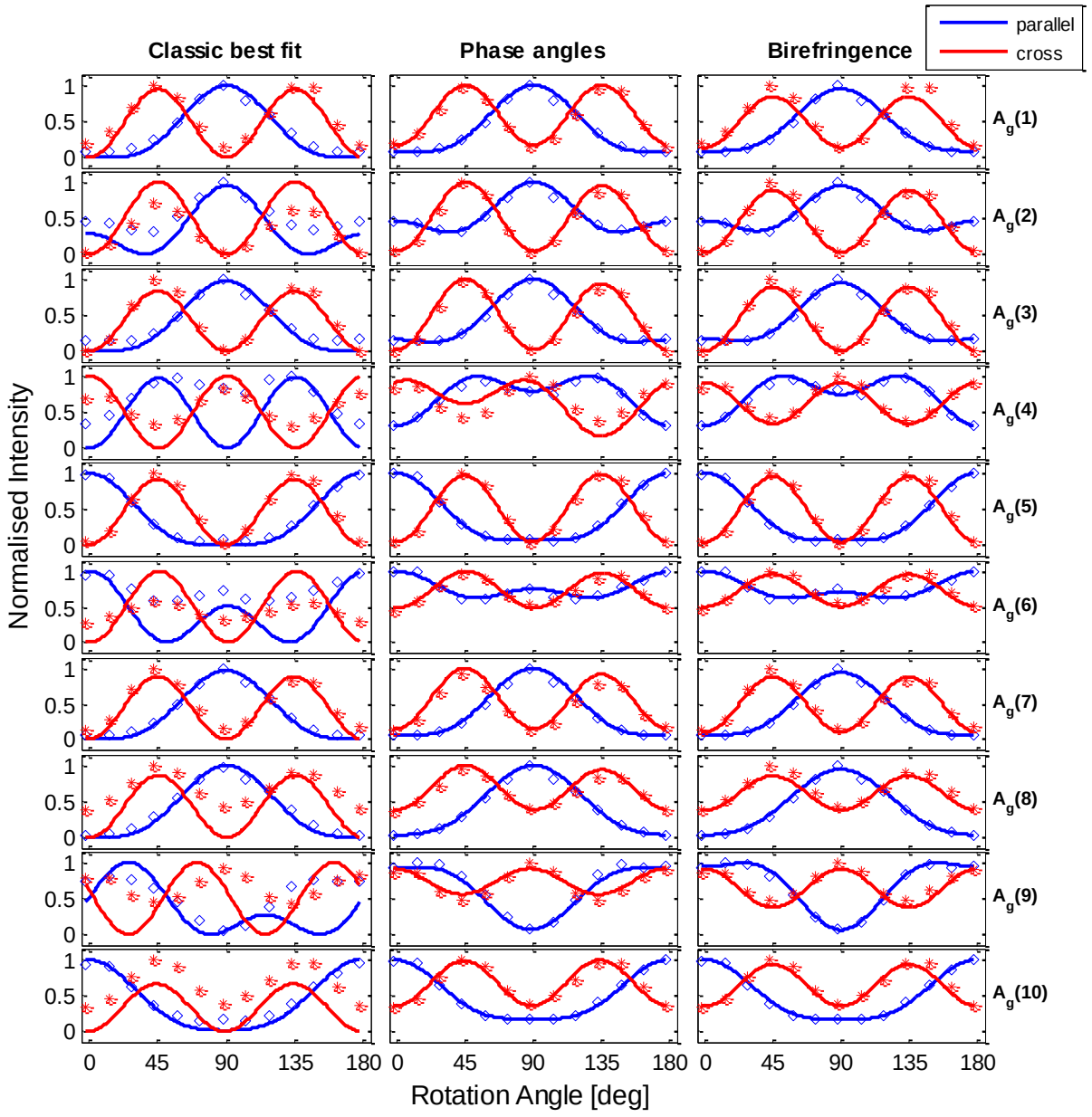

Figure 4.6: Angular dependence of normalised Raman intensity for all A_g modes in both parallel (blue) and cross (red) configurations: experimental data (scatter symbols) and fitting curves (solid lines).

Table 4.4: Raman tensor elements of A_g modes obtained by fitting from different models. Values of a, b and d are normalised to $A_g(3)$ and scaled by a factor of 1000. Phase angles are expressed in degrees.

A_g mode	Model	Raman tensor elements						
		a	b	d	α	β	δ	ϵ
1	classic	-18	233	2	-	-	-	-
	phase angles	66	231	53	47	-41	391	215
	birefringence	69	232	48	-	-	-	-
2	classic	-193	357	5	-	-	-	-
	phase angles	244	361	46	147	239	0	191
	birefringence	254	362	39	-	-	-	-
3	classic	-34	1000	4	-	-	-	-
	phase angles	398	1000	72	265	0	114	302
	birefringence	420	1000	37	-	-	-	-
4	classic	7	-6	231	-	-	-	-
	phase angles	132	210	199	232	232	0	283
	birefringence	134	208	203	-	-	-	-
5	classic	-606	3	-1	-	-	-	-
	phase angles	590	156	64	-195	-106	240	-298
	birefringence	611	158	62	-	-	-	-
6	classic	-447	319	18	-	-	-	-
	phase angles	432	376	205	307	9	-15	162
	birefringence	446	375	210	-	-	-	-
7	classic	-6	348	1	-	-	-	-
	phase angles	85	349	73	1	278	-2	178
	birefringence	86	348	60	-	-	-	-
8	classic	5	385	4	-	-	-	-
	phase angles	70	377	129	350	-39	224	42
	birefringence	71	377	127	-	-	-	-
9	classic	-309	101	262	-	-	-	-
	phase angles	371	99	301	25	-149	294	-66
	birefringence	384	98	309	-	-	-	-
10	classic	829	99	9	-	-	-	-
	phase angles	792	327	263	-24	399	40	224
	birefringence	818	327	269	-	-	-	-

Table 4.5: Square root of the Raman intensity values reported by Dohy *et al.*[66], obtained with the same experimental geometry used in the present work. Note that the authors indicated with an asterisk the bands of low intensity, probably due to polarisation leaks into forbidden components (< 2%).

A_g mode	Dohy *et al.*[66]		
	$\sqrt{I_{XX}}(\propto a)$	$\sqrt{I_{YY}}(\propto b)$	$\sqrt{I_{XY}}(\propto d)$
1	212	-	-
2	367	255	-
3	1000	418	122
4	212	141	158
5	141	430	*
6	354	418	187
7	274	*	*
8	339	*	100
9	*	354	265
10	255	771	158

Due to the excellent agreement with experimental data and to a more solid physical background with respect to the introduction of arbitrary phase angles, these results confirm the model proposed by Kranert *et al.*[70] to be very suitable for prediction of Raman intensities in anisotropic samples, at least within the depth-independence limit.

The resulting Raman tensor elements, expressed relatively to the most intense mode $A_g(3)$, are reported in Table 4.4. For the sake of comparison, the square root of the Raman intensities obtained by Dohy *et al.*[66], which should be in the same ratio as the corresponding RTEs, is shown in Table 4.5.

By looking at the modulus of the tensor elements, only minor differences are observed between *phase-angles* and *birefringence* models. Note that for the first one, only phase angles were varied during the fitting procedure, while moduli were kept fixed at a value which was directly obtained from the Raman intensity I measured when light was polarised along the direction of optic indicatrices of the sample X, Y and Z (see Appendix A for further details on model equations). I_{XX}, I_{YY} and I_{XY} are thus confirmed to be in general a good indication of the corresponding Raman tensor element (a, b, d respectively), whichever model is used. The model itself becomes important in order to describe the angular behaviour of the intensity: in this regard, phase angle and depth-independent birefringence seem to be almost equivalently effective ways to describe the same phenomenon. As discussed above, we are strongly inclined to prefer the latter, due to its deeper physical meaning.

As for the comparison with the results from Dohy *et al.*[66], the qualitative behaviour of I_{XX} and I_{YY} intensities appears to be in good agreement with the present results only if an inversion between X and Y axes is performed. Since the crystallographic directions of the sample investigated here were

unambiguously determined by single-crystal XRD, we are confident the reported results to be the most coherent with the chosen axes reference system.

A comparison between the original experimental spectra and the ones recalculated by using the average wavenumbers in Table 4.3 and the RTEs obtained by fitting with the depth-independent *birefringence model* is shown in Figure 4.7.

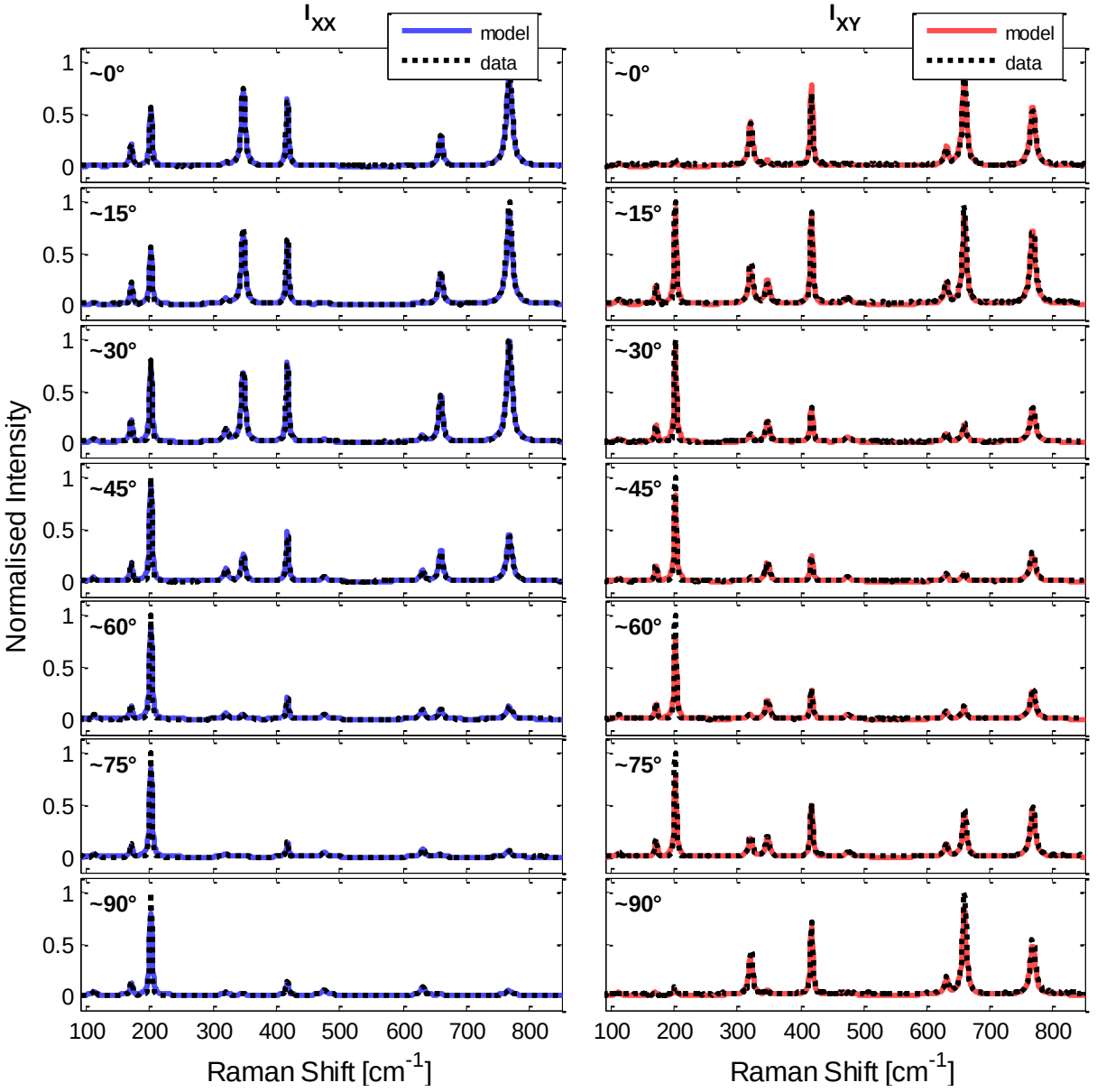

Figure 4.7: Comparison between the experimental spectra, shown in parallel- and cross-polarisation at different rotation angles, and the recalculated ones. In the latter case, peak wavenumbers and widths are the average ones obtained by fitting of the original spectra with lorentzian functions, while the corresponding intensities (i.e. the areas) were calculated by using the RTEs from the *birefringence model*. For the sake of clarity, only the interval 0–90° is shown.

As a final point, in order to compare the RTEs of different modes between each other, as well as with the results commonly obtained by DFT calculations, it must be noted that the proportionality coefficient in Eqs. 4.3 and 4.13 includes a wavenumber-dependent corrective factor which can be approximated as[71]:

$$C(\omega_i) = \frac{\omega_0(\omega_0 - \omega_i)^3}{\omega_i\left[1 - exp\left(-\frac{hc\omega_i}{k_B T}\right)\right]} \tag{4.14}$$

where ω_i is the Raman shift of the i-th mode from the laser absolute frequency ω_0 (expressed in wavenumber units). The factor also includes a temperature-dependent term in the form of a Boltzmann distribution. Hence, the RTEs given by the fitting procedures need to be further divided by $\sqrt{C(\omega_i)}$. The corrected RTEs for the depth-independent *birefringence model* are summarised in Table 4.6, along with the recent theoretical and experimental results by Kranert *et al.*[71]. An overall good qualitative and quantitative agreement is observed. All RTEs are expressed relatively to the most intense one, namely the element a of mode $A_g(10)$.

Table 4.6: Raman tensor elements (from the *birefringence model*) corrected by considering the factor $C(\omega_i)$. All RTEs are expressed relatively to the element a of mode $A_g(10)$. A comparison with other literature results is also reported, including DFT calculations. Note that while the signs of RTEs were inaccessible for the geometry employed in the present work, the signs of the other reported data are assigned with respect to the element a of each mode, which is conventionally considered as positive.

A_g mode	Present work			Kranert *et al.*[71]			Kranert *et al.*[71] (DFT)		
	a	b	d	a	b	d	a	b	d
1	20	67	14	19	-59	13	79	-70	9
2	105	150	16	100	146	0	142	214	-34
3	199	475	18	187	445	27	154	431	-16
4	91	142	138	111	147	128	124	113	146
5	441	114	44	441	111	-5	479	12	-18
6	367	308	173	357	289	158	320	358	146
7	78	313	54	47	-300	-52	31	-369	9
8	77	408	138	59	393	-135	55	414	-164
9	427	109	343	408	77	325	468	61	364
10	1000	400	329	1000	353	-283	1000	248	-409

Besides the fundamental interest in determining Raman tensor elements, studying the angular behaviour of Raman intensities can help recognising different modes when information about their wavenumber is not reliable, as well as orienting crystals as a faster (tough less accurate) alternative to XRD.

4.3 Optical absorption anisotropy

4.3.1 Experimental and theoretical methods

Polarised optical absorption was accurately measured at room temperature and normal incidence in the 800–200 nm range, by means of a Varian 2390 spectrophotometer and a Glan-Taylor polariser. These experiments were carried out on high-quality melt-grown gallium oxide substrates, in order to verify whether the conclusions of previous works[30,49] apply to different materials and crystal orientations. New experimental data were obtained for (-201)- and (010)-oriented samples, which were not investigated so far (see Table 4.1). The different sample geometries allowed to effectively orient the electric field vector ***E*** parallel to the crystallographic axes ***a***, ***b***, and ***c***. It must be noted that, in the following, ***E*****||*****a*** will denote for simplicity the direction orthogonal to the *bc* plane, which indeed is about 14° away from the actual ***a***-axis.

Additional measurements were carried out on Sn-doped samples (~ 10^{18} cm^{-3}), whose absorption edges well matched those of their undoped counterparts, as long as the same set-up geometry was employed. The effect of doping only manifested itself in the infrared region of the absorption spectra, but had no appreciable effect in the vicinity of the bandgap. Therefore, the following discussion will essentially focus on the results obtained on undoped β-Ga_2O_3.

In order to interpret and support the experimental results, *ab initio* calculations were performed by Francesco Ricci and Prof. Vincenzo Fiorentini, using several density functional theory (DFT) methods. The level of agreement with experimental data was generally good, always well within 10%. The best performance in comparison with experiment was achieved by employing self-interaction corrected functionals (VPSIC[199,200]) within the generalised gradient approximation (GGA).

4.3.2 Analysis of the absorption edge anisotropy

Figure 4.8 shows the absorption spectra of nominally undoped β-Ga_2O_3, obtained at normal incidence on the (010) surface, with polarisations ***E*****||*****c*** and ***E*****||*****a***. Absorption edges at 4.54 and 4.57 eV were observed, respectively. Hence, the absorption anisotropy between ***E*****||*****c*** and ***E*****||*****a*** is limited to about 0.03 eV.

In Figure 4.9 the absorption spectra obtained on the (-201) surface are reported. In this geometry, it is easy to probe the ***E*****||*****b*** configuration as well as the perpendicular direction ***E***|| [102]. As expected from [102] being a combination of ***a*** and ***c*** vectors, the absorption edge along this direction (4.52 eV) is in line with those just reported for ***E*****||*****c*** and ***E*****||*****a***. On the contrary, for ***E*****||*****b*** the extrapolated onset is at 4.72 eV, namely 0.2 eV higher in energy. This significant shift of the absorption edge is a direct evidence for anisotropy and confirms previous observations. In summary, the lowest absorption edge at 4.54 eV is for polarisation ***E*****||*****c***, followed by the close 4.57 eV onset when ***E*****||*****a***, while ***E*****||*****b*** gives a clearly separated 4.72 eV.

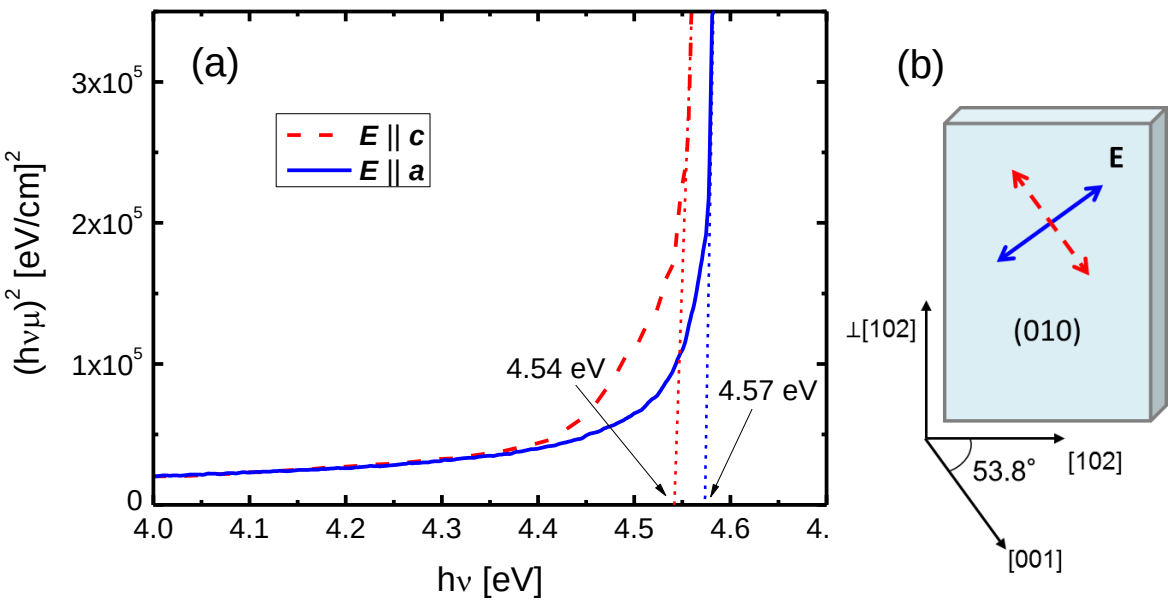

Figure 4.8: (a): Tauc plot of the absorption spectra of a (010)-oriented β-Ga_2O_3 sample at normal incidence for polarisation ***E*||*c*** and ***E*||*a***. Here, $h\nu$ and μ represent the photon energy and the absorption coefficient, respectively. (b): Schematic representation of the employed experimental geometries. (From Ricci *et al.*[59])

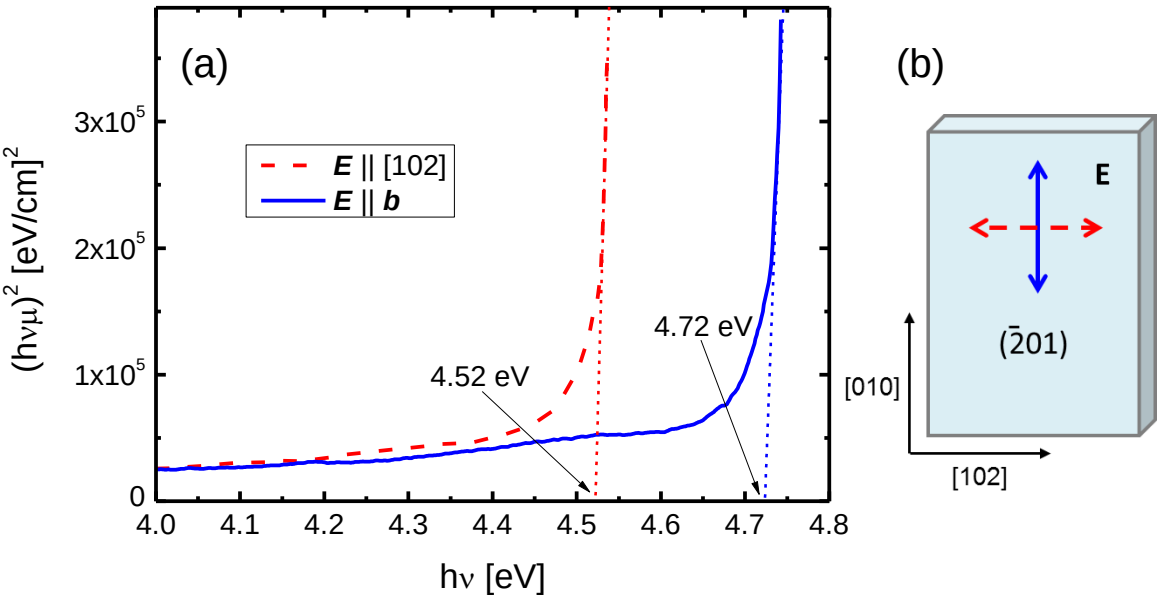

Figure 4.9: (a): Tauc plot of the absorption spectra of a (-201)-oriented β-Ga_2O_3 sample at normal incidence for polarisation ***E*||*b*** and ***E***||[102]. Here, $h\nu$ and μ represent the photon energy and the absorption coefficient, respectively. (b): Schematic representation of experimental geometry. (From Ricci *et al.*[59])

The behaviour of the absorption coefficient μ was obtained also by VPSIC-GGA, from the calculated imaginary part of the frequency-dependent dielectric tensor. The results for different polarisations are reported in Figure 4.10, where μ is plotted in Tauc form for the sake of consistency with Figure 4.8 and Figure 4.9.

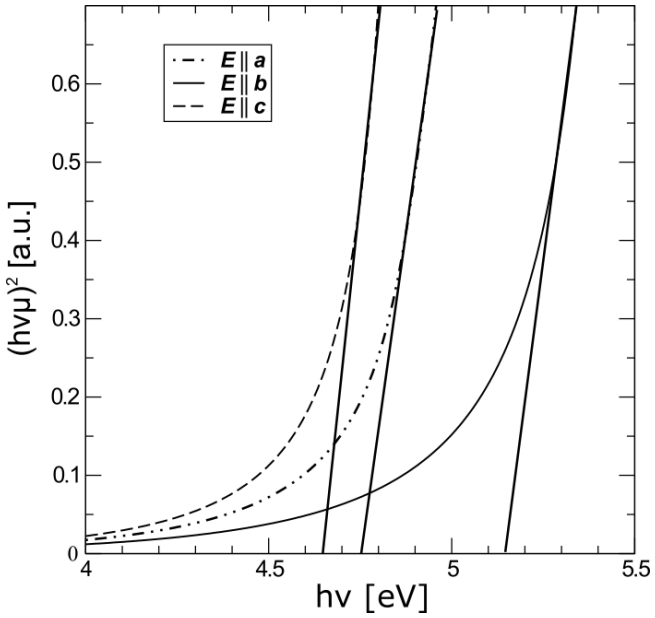

Figure 4.10: DFT-calculated Tauc plot of the absorption coefficient, showing the polarisation-dependent onsets. (From Ricci *et al.*[59])

In agreement with experimental results, distinct absorption edges can be observed as a function of polarisation, and their energetic order is again $\boldsymbol{E}\|\boldsymbol{c} < \boldsymbol{E}\|\boldsymbol{a} < \boldsymbol{E}\|\boldsymbol{b}$. For $\boldsymbol{E}\|\boldsymbol{c}$ the onset is at 4.65 eV, only 2% larger than the experimental value of 4.54 eV, which represents an excellent agreement for the standards of *ab initio* theory. For $\boldsymbol{E}\|\boldsymbol{a}$ the onset is higher by just 0.1 eV, which compares well with the 0.03 eV shift observed experimentally (see Figure 4.8), also considering that the measurement geometry was not exactly matching the ***a***-axis. For $\boldsymbol{E}\|\boldsymbol{b}$, the theoretical onset is 0.5 eV higher than for $\boldsymbol{E}\|\boldsymbol{c}$, once again in good agreement with experimental data in Figure 4.9. Although the VPSIC theoretical results are able to give a semi-quantitative description of the absorption anisotropy, we have to note that all experimental bandgap values are systematically lower than theoretical predictions. This may be related to the high absorbance of the measured thick wafers, which can ultimately lead to a slight underestimation of the bandgap edges.

As a final point, it was observed that the upwards shift of the onset for $\boldsymbol{E}\|\boldsymbol{b}$ originates from a suppression of the matrix elements determining the transition from the top valence bands to the conduction band. Optical absorption is indeed proportional to $|\boldsymbol{e} \cdot \boldsymbol{P}_{VC}|^2$, where $\boldsymbol{e}$ is the polarisation and $\boldsymbol{P}_{VC} = (< P_a >, < P_b >, < P_c >)$ is the transition matrix between valence and conduction states, whose elements represent momentum components along ***a***-, ***b***- and ***c***-axis, respectively. Figure 4.11 shows the calculated transition matrix elements along the three axes at Γ point, along with the relevant bands and wave functions. It can be noticed that $< P_b >$ from the top three valence bands is essentially zero, which ultimately suppresses the corresponding absorption. As sketched in Figure 4.12, the reason is that, besides valence states having a very small amplitude, the initial and final wave functions have the same parity along ***b***, and therefore the matrix-element integral is zero. The recovery of the matrix element at the fourth-from-top valence band shows that the observed anisotropic shift is essentially the distance of that specific band from the valence top.

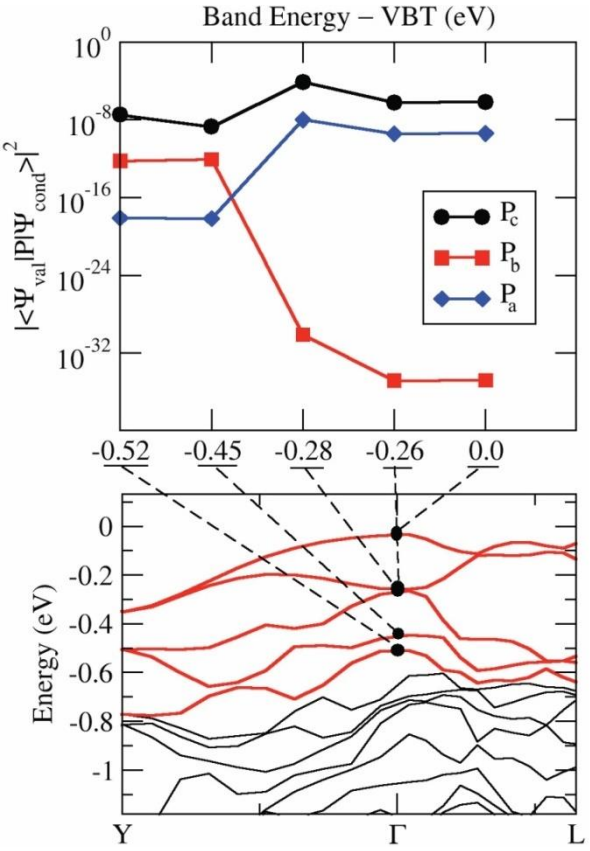

Figure 4.11: Top: Transition matrix elements along different crystal axes vs energy shift from the valence top. Along ***b***, the corresponding matrix element is suppressed (note the log scale). Bottom: Calculated band structure in the vicinity of the valence top, showing that the shift of the ***E*||*b*** onset is related to the distance between the top band and fourth-from-top one. (From Ricci *et al.*[59])

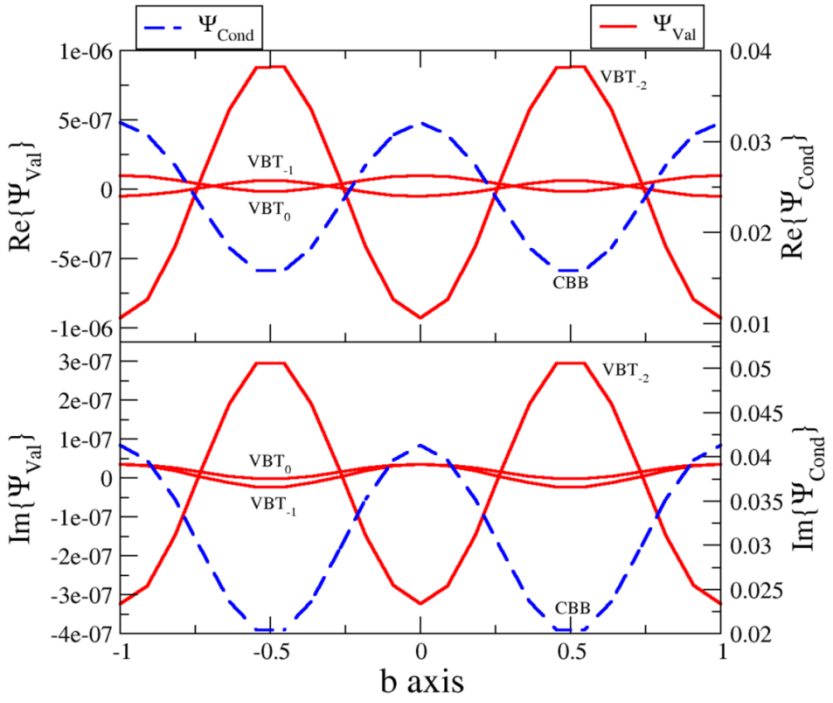

Figure 4.12: Wave functions $\Psi(n, y;\ x = z = k = 0)$ at the Γ-point of the three top valence bands along the ***b***-axis, compared with the conduction band (top: real part; bottom: imaginary part; note the different scales). Wave functions of valence bands are much smaller, and furthermore have the same parity, as the conduction band ones. (From Ricci *et al.*[59])

Theoretical analysis thus supports the experimental observation that optical absorption of β-Ga_2O_3 is anisotropic as a function of incident light polarisation, and provides a physical interpretation of the phenomenon.

4.4 Lattice expansion at high temperature

4.4.1 Experimental details

Lattice expansion of bulk β-Ga_2O_3 was studied by means of powder-XRD, using a Thermo ARL X'tra diffractometer equipped with Cu Kα radiation and a Si(Li) Thermo Electron solid-state detector. The temperature-dependent patterns were collected in the range 300–700 K, by using an Anton Paar TTK450 chamber. The explored 2θ range was 28–65.5° and the lattice parameters were extracted by means of a Le Bail fit, using the Jana2006 software[201].

Bulk samples supplied by Tamura Corp. (see Table 4.1) were milled to obtain a fine powder, which was then loaded into the sample holder of the diffractometer. Measurements were performed by Dr. Fabio Orlandi.

4.4.2 Determination of thermal expansion coefficients

At room temperature, powder diffraction measurements confirm the crystallographic parameters of β-Ga_2O_3 commonly reported in literature[37,41], namely a monoclinic structure (space group $C2/m$) with lattice constants a = 12.23(2) Å, b = 3.04(1) Å, c = 5.80(1) Å, and an angle β =103.7(3)° between a and c. As the temperature is increased between 300 and 700 K, all three lattice constants undergo a linear expansion, but with different angular coefficients. Expansion along ***a***-, ***b***- and ***c***-axis is shown in Figure 4.13, Figure 4.14 and Figure 4.15 respectively.

The slopes of the linear plots above 300 K are $1.88 \cdot 10^{-5}$ ÅK^{-1}, $1.027 \cdot 10^{-5}$ ÅK^{-1} and $1.828 \cdot 10^{-5}$ ÅK^{-1}, for *a*, *b* and *c*, respectively, with corresponding lattice constants variations between 300 and 700 K (in percent) of 0.061, 0.135 and 0.126 %, respectively. The expansion of the elementary cell is thus anisotropic, and one has to expect a cell deformation with increasing temperature, as actually proved by the behaviour of angle β shown in Figure 4.16.

Although the experimental values below 400 K are somewhat scattered, β exhibits a clear tendency to increase with increasing temperature, thus accentuating the monoclinic character of this compound. It is also interesting to note that, whilst for *b* and *c* the monotonic increase with temperature starts from the very first measurements above 300 K, for the parameter *a* the effect of temperature becomes more appreciable above 370 K (see Figure 4.13). This change of slope is certainly not fortuitous and effectively links up with the data of Víllora *et al.*[51], also plotted in Figure 4.13 for comparison. This discontinuity is reflected also by the change in cell volume with temperature (Figure 4.17), which indeed shows a double slope: higher between 370 and 700 K, and lower between 300 and 370 K.

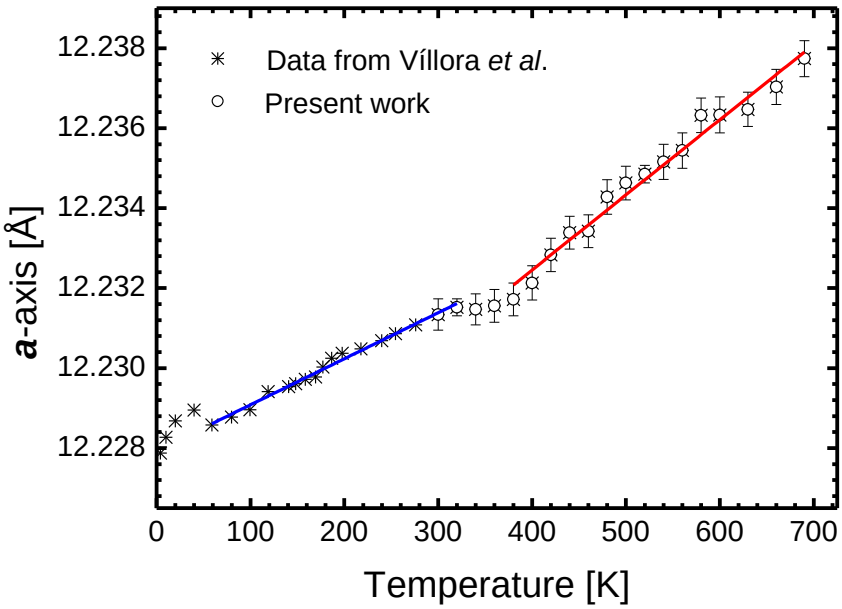

Figure 4.13: Expansion of lattice parameter *a* along the ***a***-axis as a function of the temperature. Circles represent data from the present work, fitted by a red line with a slope of $1.88 \cdot 10^{-5}$ ÅK^{-1}. and an intercept of 12.2249 Å. Asterisks are experimental data obtained from Víllora *et al.*[51], fitted by a blue line with a slope of $1.15 \cdot 10^{-5}$ ÅK^{-1} and an intercept of 12.2289 Å. (From Orlandi *et al.*[57])

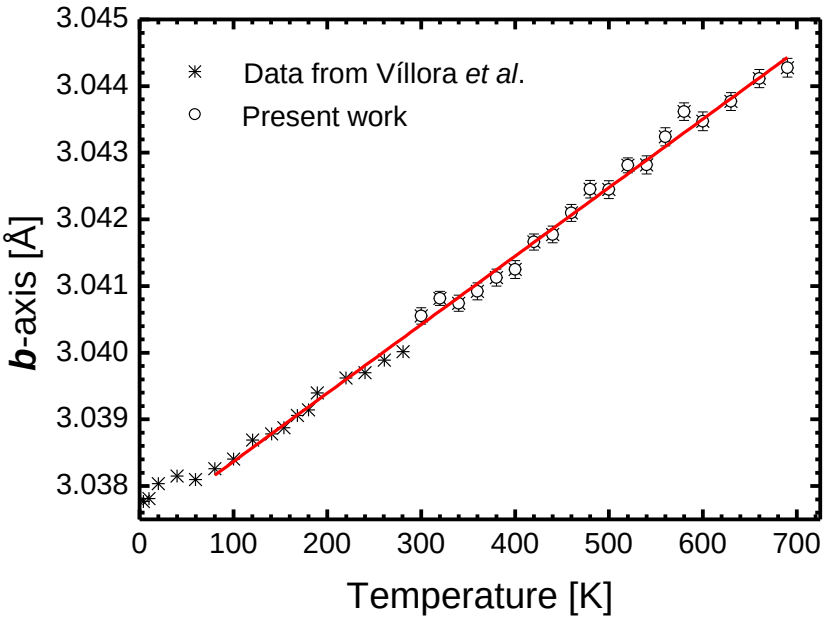

Figure 4.14: Expansion of lattice parameter *b* along the ***b***-axis as a function of the temperature. Circles and asterisks represent data from the present work and from Víllora *et al.*[51], respectively. Both data sets are fitted by the same line, with a slope of $1.027 \cdot 10^{-5}$ ÅK^{-1} and an intercept of 3.03734 Å. Only data below 70 K deviate from the linear fit. (From Orlandi *et al.*[57])

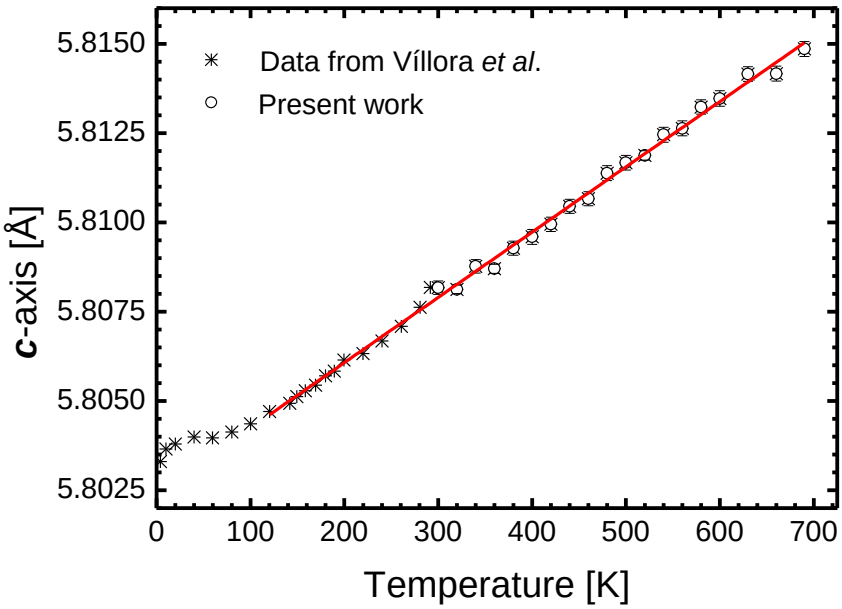

Figure 4.15: Expansion of lattice parameter *c* along the ***c***-axis as a function of the temperature. Circles and asterisks represent data from the present work and from Víllora *et al.*[51], respectively. Both data sets are fitted by the same line, with a slope of $1.828 \cdot 10^{-5}$ $ÅK^{-1}$ and an intercept of 5.8024 Å. Only data below 100 K deviate from the linear fit. (From Orlandi *et al.*[57])

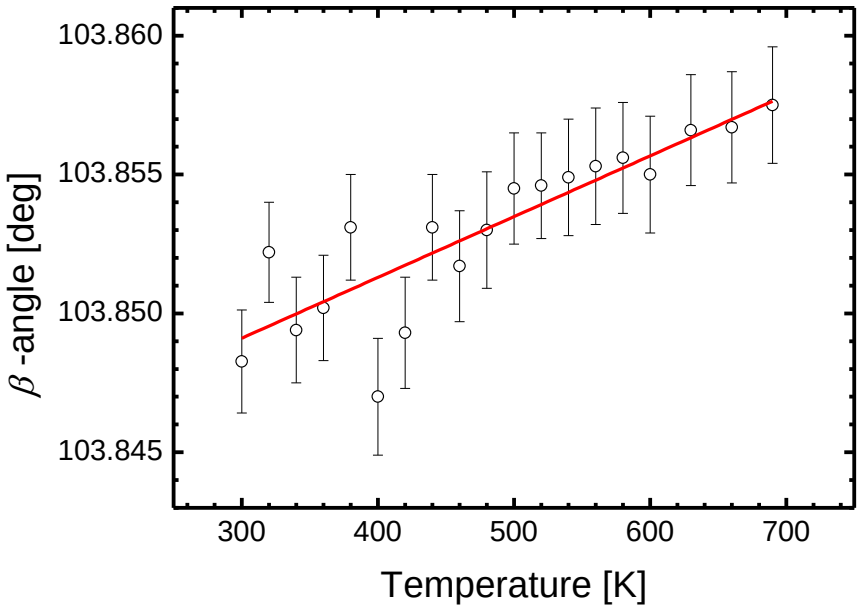

Figure 4.16: Behaviour of the angle *β* between ***a***- and ***c***-axes as a function of the temperature. The best fit line, calculated by the least-squares method, has a slope of $2.23 \cdot 10^{-5}$ °/K and an intercept of 103.8425°. (From Orlandi *et al.*[57])

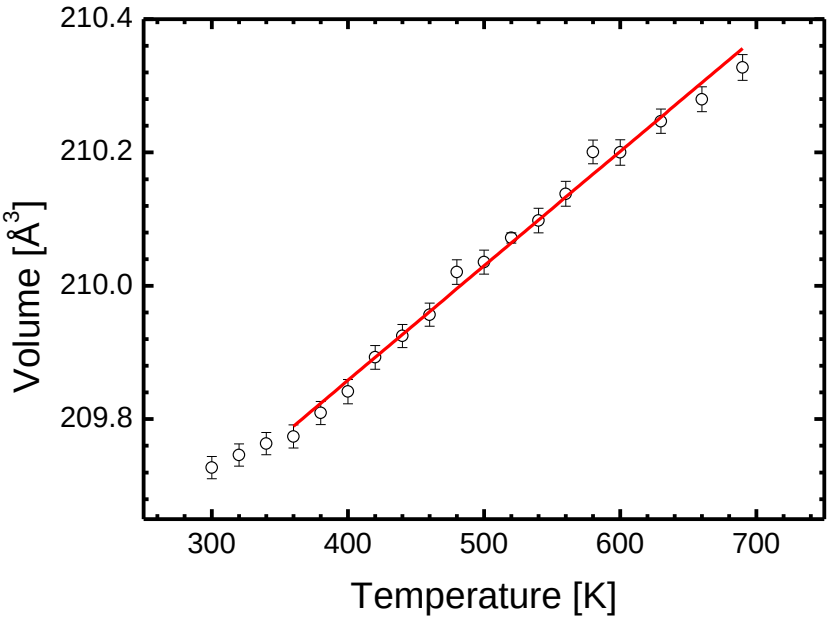

Figure 4.17: Expansion of the elementary cell volume as a function of the temperature. The best fit line, calculated by the least-squares method, has a slope of $17.24 \cdot 10^{-4}$ Å^3/K and an intercept of 209.172 Å^3. Note that the experimental points below 350 K deviate from linearity, in agreement with the discontinuity observed in Figure 4.13. (From Orlandi *et al.*[57])

The reason for such discontinuity is unknown at present, and requires additional investigation. This phenomenon might be related to variable contributions of lattice vibrations and electronic conductivity to heat transfer, as suggested by Víllora *et al.*[51] for another type of discontinuity observed between 50–100 K.

As a final point, expansion coefficients α were calculated by following the standard definition:

$$\alpha_p = \frac{p_T - p_{300K}}{(T - 300)\,p_{300K}} \tag{4.15}$$

where T is the absolute temperature and p a generic lattice parameter. From Figure 4.13, Figure 4.14 and Figure 4.15 the following values were obtained: $\alpha_a = 1.54 \cdot 10^{-6}$ K^{-1}, $\alpha_b = 3.37 \cdot 10^{-6}$ K^{-1}, and $\alpha_c = 3.15 \cdot 10^{-6}$ K^{-1}. Noteworthy, coefficients of *b* and *c* are practically identical and roughly double that of *a*., as also pointed out by Víllora *et al.*[51]. However, the absolute values of the expansion coefficients determined in the present work are systematically lower by 16–25%. We could not find a plausible explanation for such discrepancy, since all the presented fittings are accurate, below as well as above room temperature, and so is the determination of their slopes, which allows to determine the expansion coefficients. Therefore, we are confident that the values of α_b and α_c reported here are reliable in the temperature range of 100–700 K. On the other hand, the behaviour of *a* is more complex, and the given $\alpha_a = 1.54 \cdot 10^{-6}$ K^{-1} can be considered valid only within the interval 380–700 K.

The quantitative evaluation of the thermal expansion coefficients performed in the frame of this thesis is of great technological interest for the deposition of β-Ga_2O_3 films on foreign substrates, as well as for the deposition of different materials (such as GaN) on β-Ga_2O_3.

CHAPTER 5 - Conclusions and future work

Gallium oxide is the object of great scientific and technological interest, justified by its proven applicability in the fields of deep-UV detection and power electronics. Despite the exponential increase in the number of related publications, Ga_2O_3 is still a relatively new material from the point of view of its crystalline and semiconducting properties, as well as of growth and deposition techniques.

The research activity presented here ranges from technological aspects of ε- and β-Ga_2O_3 thin films growth, to their comprehensive characterisation and first fabricated devices. Furthermore, fundamental studies on the β bulk material were carried out, and new information on this polymorph was provided. The principal findings can be summarised as follows.

ε-Ga_2O_3 CVD films

A chemical vapour deposition process was successfully developed for reproducible growth of ε-Ga_2O_3 thin films on *c*-sapphire at relatively low temperature. Between 600 and 650 °C, the deposited layers display good crystalline and morphological quality, with intense and sharp XRD peaks and surface RMS roughness values down to about 1 nm. The growth mechanisms were investigated in very thin samples, observing that growth occurs via nucleation and coalescence of hexagonal islands. It was understood that film and substrate share the same ***c***-axis, however the *ab* plane of the film is rotated by 30 ° with respect to the one of sapphire. This crystallographic arrangement reduces the effective mismatch from 60% down to 4.8%. Despite the favourable influence of other hexagonal substrates or pseudo-hexagonal templates in favouring the successful nucleation of ε-Ga_2O_3 islands, the most crucial parameter was found to be the growth temperature. We are confident that the latter, combined with the employment of a chemical deposition method, is decisive in order to obtain ε-Ga_2O_3 without critically deviating from equilibrium or using expedients such as heavy doping. The effect of other growth parameters, such as chamber pressure or reactants partial pressure ratios, was mainly related to adjustments in surface morphology and growth rate.

Crystal structure of ε-Ga_2O_3 was accurately determined by TEM and XRD, providing a model which reconciles the different literature reports. The films consist of orthorhombic, columnar domains, with diameters of some nanometres and stretching through the whole film thickness. The oxygen atoms are arranged in a fixed 4H packing, which remains unaltered over the entire structure. Between oxygen layers, gallium octahedral and tetrahedral sites are stacked along the ***c***-axis, again maintaining constant periodicity, while in the *ab* plane they form ribbon-chains. What drives the formation of the domains is indeed the arrangement of these chains, which can change direction by a reflection of 120° in the *ab* plane, leading to six possible arrangements (including inversion). Adjacent domains are

separated by twin boundaries. Noteworthy, the way the crystallographic structure can be described depends on the sensitivity of the probing technique and on the lateral dimension of these domains. Using a technique like HRTEM, with atomic resolution, leads to identify an orthorhombic structure, belonging to $Pna2_1$ space group. On the contrary, if the domain size is smaller than the coherence length of the probing radiation, for example X-Ray, the diffraction pattern will be essentially determined by the fixed 4H packing of oxygen atoms, while gallium sites will appear statistically occupied, leading to an averaged, hexagonal $P6_3mc$ symmetry.

A first consequence of the determined structure, which belongs to a polar space group and is characterised by a positive displacement of cationic sites from the centre of the respective coordination polyhedra along the ***c***-axis, is pyroelectricity. DHM measurements confirmed this assumption and further proved the presence of ferroelectricity. Even though it was not possible to reach full saturation due to dielectric breakdown, a partial hysteresis cycle was measured, with a determined coercive field of about 20 kV/cm, thus providing for the first time an evidence of ferroelectric behaviour in a gallium oxide polymorph.

By comparison between optical absorption and photocurrent onsets, the bandgap of the material was estimated to fall between 4.6 and 4.7 eV. Raman spectroscopy highlighted the contributions of ε-Ga_2O_3 phonon modes excited in the *ab* plane, which displayed however low intensities, probably due to the twin-domains nature of the layers. Ellipsometric analysis allowed to determine the wavelength-dependent refractive index of ε-Ga_2O_3, which was employed to calculate the film thickness from the interfringe spacing measured by reflectivity. Deconvolution of CL spectra revealed three bands at 530, 464 and 450 nm, suggesting the presence of radiative centres related to intra-gap states.

A simple, solar-blind UV-detector was built using a metal-semiconductor-metal planar geometry. It proved to be stable over several illumination cycles, with on/off current ratios of several orders of magnitude and noise well below 1%. The only drawback was the relatively long response time of about 20 seconds, quite comparable to analogous devices based on β-Ga_2O_3.

Thermal stability was assessed by annealing at different temperatures and DSC analysis. While the ε phase remains stable up to 600–650 °C, at 700 °C a conversion to β starts, which reaches completion only above 850 °C. The crystalline quality of the obtained phase is strongly affected by the heating-cooling pathway, with a slow cooling-down step apparently increasing the order of the crystallites.

Basic thermo-fluid dynamical simulation allowed to visualise the main limitations of the initial reactor setup and to design some modifications, which allowed to reduce heat dissipation and to increase the homogeneity of the deposited layers. In particular, preliminary results show a reduction in the inlet-outlet thickness gradient down to 5–30% for 1 inch substrates and to about 30–40 % for 2 inch wafers.

As a last point, by means of automatic valves it was possible to alternate precursors and purge flows inside the reactor chamber, allowing for operation in ALD mode. Though the related processing is at

an initial development stage, first results are quite encouraging, as they confirm the potential of ALD to provide crystalline growth at lower temperature, as well as to increase thickness uniformity.

β-Ga_2O_3 PLD films

Though not straightforward, off-axis geometry is a promising way to improve electrical properties of heteroepitaxial, very thin β-Ga_2O_3 PLD films. Off-axis PLD indeed allowed to reduce the amount of highly energetic clusters that hit the sample surface, thus limiting the degradation of film properties and making the deposited layers suitable for the successful fabrication of MESFETs devices. The best-achieved working MESFETs displayed on/off ratios of up to 5 orders of magnitude and low threshold voltages (about 2 V), while no breakdown was observed for drain voltages in the range ± 100 V.

On the other hand, eclipse PLD did not lead to the expected results. It is possible that, as often suggested in literature, an argon source is needed to enhance both process speed and deposition quality.

Noteworthy, PLD films grow as β phase onto the ε templates, as confirmed by the presence of the (-201) diffractions in XRD scan profiles, thus further suggesting the key role of both the growth temperature and the use of a chemical deposition method in the formation of ε-Ga_2O_3.

Anisotropic properties of bulk β-Ga_2O_3

Vibrational properties were investigated by means of Raman spectroscopy. Normal modes with A_g and B_g symmetry were selectively observed by varying the experimental geometry, and the respective wavenumbers were compared with those previously reported. By studying the angular behaviour of the intensity of A_g modes, it was also possible to determine the a, b and d Raman tensor elements for each mode. Different models were employed for data fitting, the most effective of which was found to be the one accounting for depth-independent birefringence, recently proposed by Kranert *et al.*[70]. Besides giving the minimum variance for the majority of the fitting curves, this model provides a physical interpretation to the unusual angular behaviour of Raman intensity displayed by anisotropic crystals.

The optical absorption of β-Ga_2O_3 was seen to be anisotropic as a function of incident light polarisation and crystal orientation, thus confirming previous reports. In the course of the thesis, the experimental measurements were extended to unexplored wafer orientations. The lowest onset is around 4.55 eV in (010)-oriented wafers. In this case, whatever the polarisation in the *ac* plane, only minor shifts of the bandgap were detected. For the (-201)-oriented samples, the light polarisation along ***b*** has the strongest effect, as it shifts the absorption edge towards a higher energy by 0.2 eV. Theoretical analysis (especially by the VPSIC method) supports these observations and provides a physical interpretation of the absorption anisotropy. In the specific case of the higher absorption edge for $\boldsymbol{E}||\boldsymbol{b}$, theory indicates that the higher energy is actually due to suppression of the transition matrix elements of the three uppermost valence bands.

The lattice parameters of β-Ga_2O_3 single crystals were determined by accurate powder diffraction measurements, performed in the temperature range 300–700 K. The estimated expansion coefficients are $1.54 \cdot 10^{-6}$, $3.37 \cdot 10^{-6}$, and $3.15 \cdot 10^{-6}$ K^{-1} for *a*, *b*, and *c*, respectively, in reasonable agreement with previously published data measured at lower temperatures. This quantitative evaluation of the thermal expansion coefficients is of great technological interest for effectively planning the deposition of β-Ga_2O_3 films on foreign substrates as well as the deposition of different materials (such as GaN) on Ga_2O_3.

Future perspectives

Despite the extremely promising results, the activity on Ga_2O_3 epilayers is of course still far from being fully ripe, and many questions remain open, calling for both further investigation of material properties and technological improvement of the deposition processes.

One of the short-term priorities will be to understand the implications of ε phase domains on the physical properties of the CVD layers, as well as to explore the possibility of controlling their size and eventually suppressing their formation. For this purpose, investigating the origin of the interfacial γ-Ga_2O_3 phase may provide further information on the actual growth mechanisms.

The possibility of effectively controlling the ε-to-β transition has to be studied more in detail, through specifically tailored annealing experiments at different temperatures and different heating-cooling pathways.

An extensive study of electrical properties of the ε epilayers is currently in progress, including Ohmic contact formation, contact resistance measurements, possible implications of the ferroelectricity and Hall Effect measurements at different temperatures. Again, it will be of major importance to understand the correlation between these properties and the structural domains. Different geometries for the fabrication of UV detectors should be explored, as well.

From the point of view of ε-Ga_2O_3 deposition technology, improvements will be implemented, aiming to optimise the reactants injection process. The ultimate goal will be to achieve crystalline layers with negligible surface roughness when operating in ALD mode. A series of preliminary experiments will be necessary, in order to identify the ALD temperature window and the optimal sequencing times for reactants exposure and purge steps, thus avoiding undesired CVD contributions to what should be in principle a perfect layer-by-layer growth.

As for the activity carried out at Leipzig University, at the moment off-axis PLD remains the most promising setup for trying to improve the quality of very thin β-Ga_2O_3 layers. Tuning the offset (QM) value, together with shifting the focusing lens position, could be an effective approach towards further optimisation. In particular, exploring lower offset values should in principle allow for higher growth rates, and hence for more freedom in changing other parameters, for instance the focusing lens position itself. Of course, nucleation layers will need to be optimised at each employed offset.

As a final remark, it should be added that this Ph.D. thesis started in January 2014, in parallel with the establishment of gallium oxide as strategic research topic at the Physics Department of Parma University and IMEM-CNR Institute. The results achieved in the frame of this thesis substantially contributed to make the activity on Ga_2O_3, especially the ε phase, of Parma team well known and appreciated by the international community. In recognition of these accomplishments, the second International Workshop on Gallium Oxide and Related Materials (IWGO-2017) will be held in the Campus of Science and Technology of Parma University.

APPENDIX A - Further details about Raman tensor determination

Raman tensor formalism

General form of the Raman tensor for monoclinic $C/2m$ space group, with Z//$\boldsymbol{b}$, Y//$\boldsymbol{a}$, X//($\boldsymbol{c}$+13.7° in the *ac* plane):

$$\mathcal{R}_{A_g} = \begin{pmatrix} |a|e^{i\alpha} & |d|e^{i\delta} & 0 \\ |e|e^{i\varepsilon} & |b|e^{i\beta} & 0 \\ 0 & 0 & |c|e^{i\gamma} \end{pmatrix} \tag{A.1}$$

General relationship with the observed intensity:

$$I \propto |\boldsymbol{e}_s \mathcal{R} \boldsymbol{e}_i|^2 \tag{A.2}$$

Raman tensor elements after a counter-clockwise rotation θ of the sample (i.e. the Raman tensor) around the Z-axis:

$$\mathcal{R}_{ij}(\theta) = (M_{rot}\mathcal{R}M_{rot}^T)_{ij} = \begin{pmatrix} cos\,\theta & -sin\,\theta & 0 \\ sin\,\theta & cos\,\theta & 0 \\ 0 & 0 & 1 \end{pmatrix} \mathcal{R} \begin{pmatrix} cos\,\theta & sin\,\theta & 0 \\ -sin\,\theta & cos\,\theta & 0 \\ 0 & 0 & 1 \end{pmatrix} \tag{A.3}$$

Possible forms of the Raman tensor $\mathcal{R}_{A_g}(\theta)$ in the XY plane after rotation, ordered by decreasing complexity:

- Case 1 - Complex tensor elements, $d \neq e$:

$$\begin{pmatrix} |a|e^{i\alpha}\,cos^2\theta + |b|e^{i\beta}\,sin^2\theta - \left(\frac{|d|e^{i\delta} + |e|e^{i\varepsilon}}{2}\right) sin\,2\theta & \left(\frac{|a|e^{i\alpha} - |b|e^{i\beta}}{2}\right) sin\,2\theta + |d|e^{i\delta}\,cos^2\theta - |e|e^{i\varepsilon}\,sin^2\theta \\ \left(\frac{|a|e^{i\alpha} - |b|e^{i\beta}}{2}\right) sin\,2\theta + |e|e^{i\varepsilon}\,cos^2\theta - |d|e^{i\delta}\,sin^2\theta & |b|e^{i\beta}\,cos^2\theta + |a|e^{i\alpha}\,sin^2\theta + \left(\frac{|d|e^{i\delta} + |e|e^{i\varepsilon}}{2}\right) sin\,2\theta \end{pmatrix} \tag{A.4}$$

- Case 2 - Complex tensor elements, $|d|=|e|$:

$$\begin{pmatrix} |a|e^{i\alpha}\,cos^2\theta + |b|e^{i\beta}\,sin^2\theta - |d|\,sin\,2\theta\left(\frac{e^{i\delta} + e^{i\varepsilon}}{2}\right) & \left(\frac{|a|e^{i\alpha} - |b|e^{i\beta}}{2}\right) sin\,2\theta + |d|\left(e^{i\delta}\,cos^2\theta - e^{i\varepsilon}\,sin^2\theta\right) \\ \left(\frac{|a|e^{i\alpha} - |b|e^{i\beta}}{2}\right) sin\,2\theta + |d|\left(e^{i\varepsilon}\,cos^2\theta - e^{i\delta}\,sin^2\theta\right) & |b|e^{i\beta}\,cos^2\theta + |a|e^{i\alpha}\,sin^2\theta + |d|\,sin\,2\theta\left(\frac{e^{i\delta} + e^{i\varepsilon}}{2}\right) \end{pmatrix} \tag{A.5}$$

- Case 3 - Complex tensor elements, d=e:

$$\begin{pmatrix} |a|e^{i\alpha}\cos^2\theta + |b|e^{i\beta}\sin^2\theta - |d|e^{i\delta}\sin 2\theta & \left(\frac{|a|e^{i\alpha} - |b|e^{i\beta}}{2}\right)\sin 2\theta + |d|e^{i\delta}\cos 2\theta \\ \left(\frac{|a|e^{i\alpha} - |b|e^{i\beta}}{2}\right)\sin 2\theta + |d|e^{i\delta}\cos 2\theta & |b|e^{i\beta}\cos^2\theta + |a|e^{i\alpha}\sin^2\theta + |d|e^{i\delta}\sin 2\theta \end{pmatrix} \tag{A.6}$$

- Case 4 (classic) - Real tensor elements, d=e:

$$\begin{pmatrix} a\cos^2\theta + b\sin^2\theta - d\sin 2\theta & \left(\frac{a-b}{2}\right)\sin 2\theta + d\cos 2\theta \\ \left(\frac{a-b}{2}\right)\sin 2\theta + d\cos 2\theta & b\cos^2\theta + a\sin^2\theta + d\sin 2\theta \end{pmatrix} \tag{A.7}$$

- Case 5 (Kranert *et al.*[70]) - Depth-depending effective 2D Raman tensor (birefringence):

$$\mathcal{R}_{Eff}(\theta, z) = \mathcal{R}_0(\theta) + \mathcal{R}_1(\theta)e^{i\chi(z)} + \mathcal{R}_2(\theta)e^{i2\chi(z)} \tag{A.8}$$

with:

$$\mathcal{R}_0(\theta) = a\begin{pmatrix} \cos^2\theta & \sin\theta\cos\theta \\ \sin\theta\cos\theta & \sin^2\theta \end{pmatrix} \tag{A.9}$$

$$\mathcal{R}_1(\theta) = d\begin{pmatrix} -2\sin\theta\cos\theta & \cos^2\theta - \sin^2\theta \\ \cos^2\theta - \sin^2\theta & 2\sin\theta\cos\theta \end{pmatrix} \tag{A.10}$$

$$\mathcal{R}_2(\theta) = b\begin{pmatrix} \sin^2\theta & -\sin\theta\cos\theta \\ -\sin\theta\cos\theta & \cos^2\theta \end{pmatrix} \tag{A.11}$$

In the limit of infinite scattering depth (but the approximation also holds for sufficiently large Δz integration range) the Raman intensity no longer follows Eq. A.2, but instead:

$$I \propto |\boldsymbol{e}_s\mathcal{R}_0\boldsymbol{e}_i|^2 + |\boldsymbol{e}_s\mathcal{R}_1\boldsymbol{e}_i|^2 + |\boldsymbol{e}_s\mathcal{R}_2\boldsymbol{e}_i|^2 \tag{A.12}$$

Additional experimental details

With the employed experimental setup, parallel- (PP) and cross-polarisation (CP) intensities could not be directly correlated, due to the different response of the detector diffraction grating depending on the direction of incident polarisation. It was thus necessary to introduce a scale factor k, which allows I_{PP} and I_{CP} to be correctly described in terms of the same tensor elements:

$$I_{PP} = I_{PP}(a, b, d, e) \tag{A.13}$$

$$I_{CP\,sc}(a,b,d,e) = \frac{I_{CP\,exp}(a',b',d',e')}{k^2} = I_{CP\,exp}\left(\frac{a'}{k},\frac{b'}{k},\frac{d'}{k},\frac{e'}{k}\right) \quad \text{(A.14)}$$

where the subscripts *sc* and *exp* respectively stand for *scaled* and *experimental*.

To achieve this in practice, PP and CP spectra were recorded using a white light source, and a calibration curve for k as a function of the Raman shift ω was extrapolated by linear fit of $\sqrt{I_{CP}/I_{PP}}$ (Figure A. 1). The raw CP spectra of β-Ga_2O_3 could hence be rescaled to their correct intensity value by dividing by the obtained $[k(\omega)]^2$. Background removal from all spectra was performed only after this rescaling procedure.

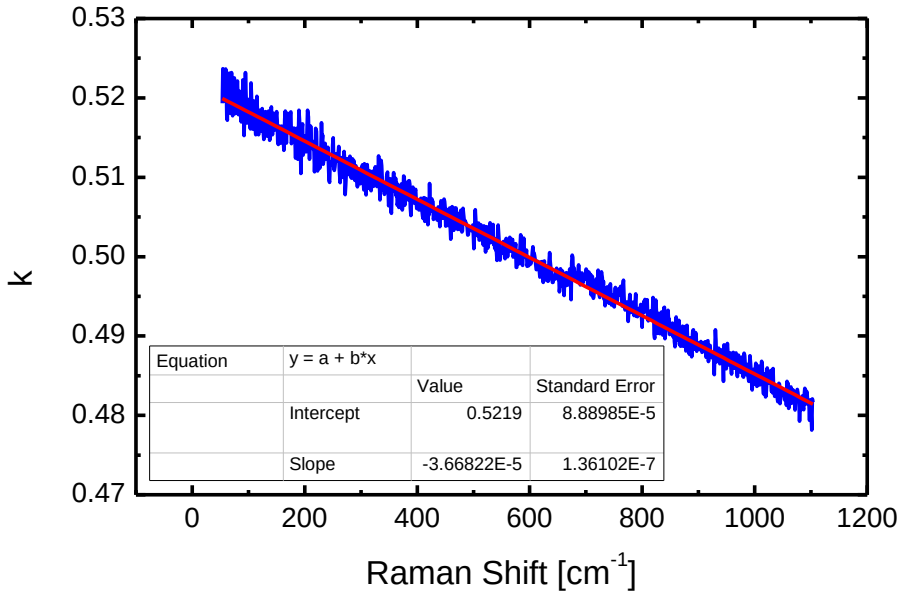

Figure A. 1: Calibration curve for CP intensity rescaling through the wavenumber-dependent factor $k = \sqrt{I_{CP}/I_{PP}}$.

Model equations

Angular dependence of Raman intensity was modelled as follows, depending on the considered case.

- Real and symmetric Raman tensor (*classic model*):

$$I_{PP} = [a\cos^2\theta + b\sin^2\theta - d\sin 2\theta]^2$$
$$I_{CP} = \left[\left(\frac{a-b}{2}\right)\sin 2\theta + d\cos 2\theta\right]^2 \quad \text{(A.15)}$$

- Complex Raman tensor (*d=e*, *phase-angles model 1*):

$$I_{PP} = \left[|a|e^{i\alpha}\cos^2\theta + |b|e^{i\beta}\sin^2\theta - |d|e^{i\delta}\sin 2\theta\right]^2$$
$$I_{CP} = \left[\left(\frac{|a|e^{i\alpha} - |b|e^{i\beta}}{2}\right)\sin 2\theta + |d|e^{i\delta}\cos 2\theta\right]^2 \quad \text{(A.16)}$$

- Complex Raman tensor ($|d|=|e|$, *phase-angles model 2*):

$$I_{PP} = \left[|a|e^{i\alpha}\, cos^2\,\theta + |b|e^{i\beta}\, sin^2\,\theta - |d|\, sin\, 2\theta \left(\frac{e^{i\delta} + e^{i\varepsilon}}{2}\right)\right]^2$$
$$I_{CP} = \left[\left(\frac{|a|e^{i\alpha} - |b|e^{i\beta}}{2}\right) sin\, 2\theta + |d|\left(e^{i\varepsilon}\, cos^2\,\theta - e^{i\delta}\, sin^2\,\theta\right)\right]^2 \quad \text{(A.17)}$$

- Real and symmetric Raman tensor (*birefringence model*):

$$I_{PP} = (a\, cos^2\,\theta)^2 + (b\, sin^2\,\theta)^2 + (-d\, sin\, 2\theta)^2$$
$$I_{CP} = \left(\frac{a}{2} sin\, 2\theta\right)^2 + \left(-\frac{b}{2} sin\, 2\theta\right)^2 + (d\, cos\, 2\theta)^2 \quad \text{(A.18)}$$

Note that, for the sake of rigor, the real intensity should be only proportional (not equal) to the employed functions: this means that the values of the Raman tensor elements obtained with these models do not have an absolute meaning, since they are all multiplied by a constant. However, the information about the relative magnitudes of RTEs within the same mode is maintained, while in order to compare different modes one needs to divide the obtained RTEs by the corrective, wavenumber-dependent factor $\sqrt{C(\omega_i)}$ (see main text, section 4.2.4).

Fitting procedures

- *Definition of initial parameters sets.*
  From all model equations, it can be noticed that a first reliable approximation of RTEs is given by:

$$|a| = |a_{PP}| = mean\left(\sqrt{I_{PP}(0°, 180°, 360°)}\right) \quad \text{(A.19)}$$
$$|b| = |b_{PP}| = mean\left(\sqrt{I_{PP}(90°, 270°)}\right) \quad \text{(A.20)}$$
$$|d| = |d_{CP}| = mean\left(\sqrt{I_{CP}(0°, 180°, 360°)}\right) \quad \text{(A.21)}$$
$$|e| = |e_{CP}| = mean\left(\sqrt{I_{CP}(90°, 270°)}\right) \quad \text{(A.22)}$$

  Obviously, if d=e or $|d|=|e|$ the expression for d becomes:

$$|d| = |d_{CP}| = mean\left(\sqrt{I_{CP}(0°, 90°, 180°, 270°, 360°)}\right) \quad \text{(A.23)}$$

  As a first step, Eq. A.19, Eq. A.20 and Eq. A.23 were hence employed to obtain the modulus of a, b, d for each peak, in the classic assumption of real and symmetric Raman tensor. For each mode, a set of eight vectors was then created with all the possible sign combinations of the three tensor elements. These vectors were then inserted into the *classic model* equations for PP and CP (Eqs. A.15), and the total residual $\sigma^2 = (\sigma_{PP}^2 + \sigma_{CP}^2)$ with respect to the

experimental data was evaluated, allowing to determine the best initial parameter set (p_0) for all the following fittings. In summary:

$$a_0 = \pm |a_{PP}| \qquad b_0 = \pm |b_{PP}| \qquad d_0 = \pm |d_{CP}| \qquad (best\ sign\ combination) \qquad \text{(A.24)}$$

- *Best fit of the classic model*
  The previously obtained p_0 were then employed as starting parameters for the model equations A.15 and optimised with a fitting procedure, using the MATLAB *fminsearch* function to minimise the total residual σ^2 between the experimental data and the model (PP and CP, simultaneously). In summary:

$$a_{class} = a_{fit} \qquad b_{class} = b_{fit} \qquad d_{class} = d_{fit} \qquad \text{(A.25)}$$

- *Best fit of phase angles*
  Since introducing phase angles should not affect I_{PP} and I_{CP} for θ = (0 ± n·180)° and for θ = (90 ± n·180)°, respectively, the modulus of a, b and d was assumed to be fixed and equal to the modulus of the respective p_0 (Eqs. A.24). Only tensor elements phases α, β, δ and ϵ were thus fitted, again with the *fminsearch* function, exploring all possible combination of 0 and π as initial values and taking the best one as result. In summary:

$$|a| = |a_0| \qquad |b| = |b_0| \qquad |d| = |d_0| \qquad \text{(A.26)}$$

$$\alpha = \alpha_{fit} \qquad \beta = \beta_{fit} \qquad \delta = \delta_{fit} \qquad \epsilon = \epsilon_{fit} \qquad \text{(A.27)}$$

Fitting was performed first by considering the complex Raman tensor as fully symmetric (*phase-angles model 1* in Eqs. A.16) and was then repeated for the case in which d and e have equal modulus but different phases (*phase-angles model 2* in Eqs. A.17). Only the results of the fitting with *phase-angles model 2* are presented in the main text, as using a complex but fully symmetric tensor led to a poorer fitting quality which could not properly account for some of the features observed in modes 4, 6 and 10 (see Figure A. 2).

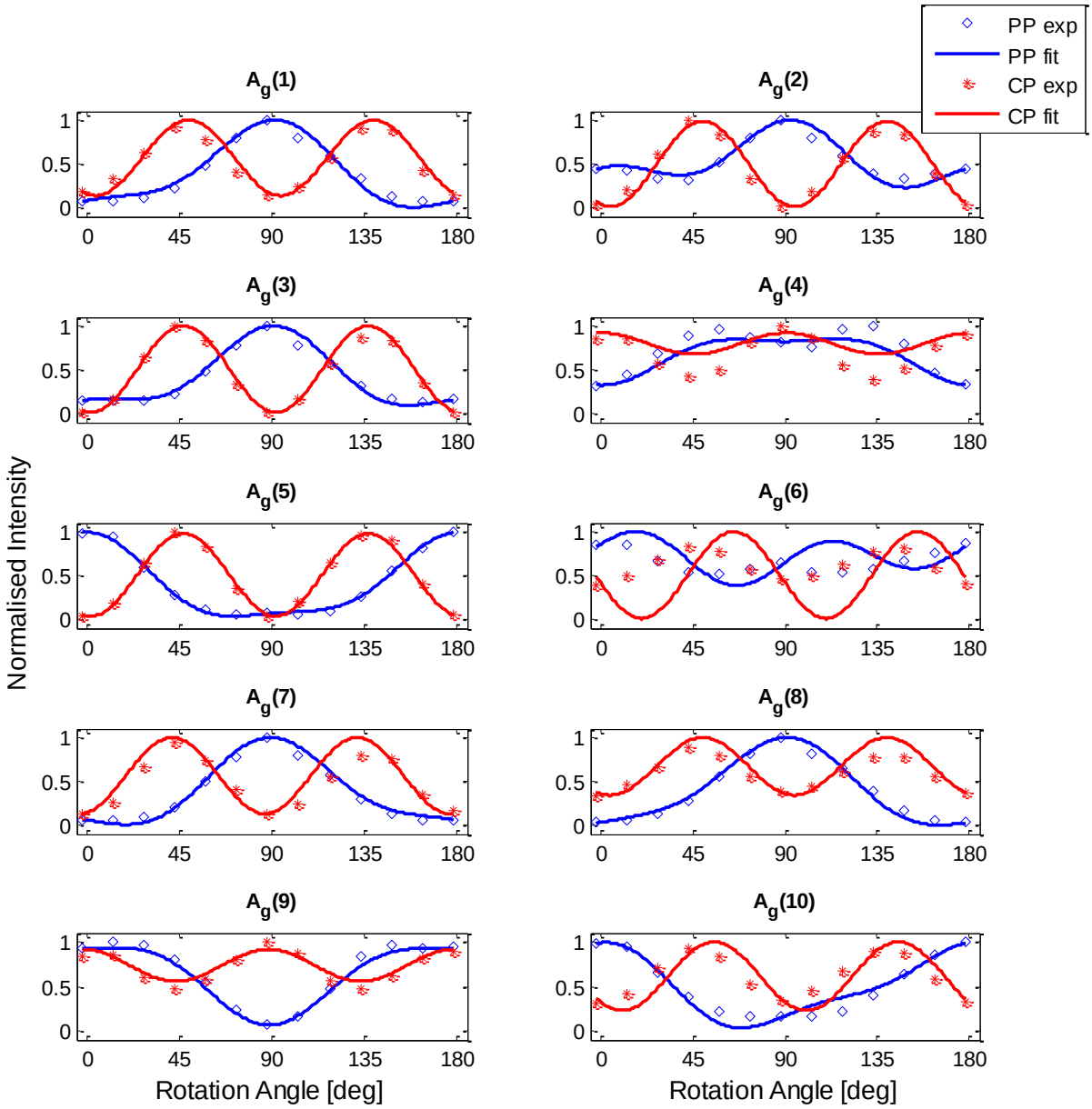

Figure A. 2: Angular behaviour of A_g modes intensities fitted by using *phase-angles model 1* (equations A.16). Note that this model fails to reproduce modes 4, 6 and 10 satisfactorily.

- *Best fit in the depth-independent birefringence limit*

  The same procedure used for the classic best fit was employed, except that here model equations for depth-independent birefringence were used (Eqs. A.18). As starting parameters for the fitting, only the absolute values of p_0 were employed, since any minus sign would have been eliminated by squares, regardless. In summary:

$$a_{biref} = a_{fit\ (biref)} \qquad b_{biref} = b_{fit\ (biref)} \qquad d_{biref} = d_{fit\ (biref)} \tag{A.28}$$

Goodness of fit and residuals

A raw assessment of the goodness of fit was carried out for each mode by using the standard formula for the total variance:

$$\sigma_{fit} = \sqrt{\frac{\sum \sigma^2}{N_m - N_p}} \tag{A.29}$$

where the sum is performed over all the individual squared residuals (σ) of both PP and CP curves, while N_m and N_p stand for the total number of measurements and parameters, respectively.

As shown in Table A. 1, the fitting procedure that considers depth-independent birefringence gives the smaller total variance for the majority of modes, closely followed by the fitting of the phase angles. These two models proved most suitable for describing the angular behaviour of the examined system. In Figure A. 3, the individual normalised residuals for each mode are plotted with the respective variance as error bar, giving a better view of the actual goodness of fit. The most important source of error is here probably due to issues in the reproducibility of laser focusing conditions during sample rotation.

Table A. 1: Total variance for each A_g mode intensity, evaluated with different fitting models. Since the Raman intensity range covered during rotation is significantly different for each mode, it is not straightforward to compare the absolute variance of different modes. For the sake of clarity, for each mode all variances are hence normalised to the one evaluated for the *classic model*, which is always the larger.

A_g mode	Total variance (PP+CP)		
	Classic	Phase angles	Birefringence
1	1.00	0.56	0.60
2	1.00	0.18	0.15
3	1.00	0.44	0.33
4	1.00	0.34	0.15
5	1.00	0.55	0.51
6	1.00	0.10	0.09
7	1.00	0.87	0.57
8	1.00	0.41	0.36
9	1.00	0.14	0.13
10	1.00	0.20	0.21

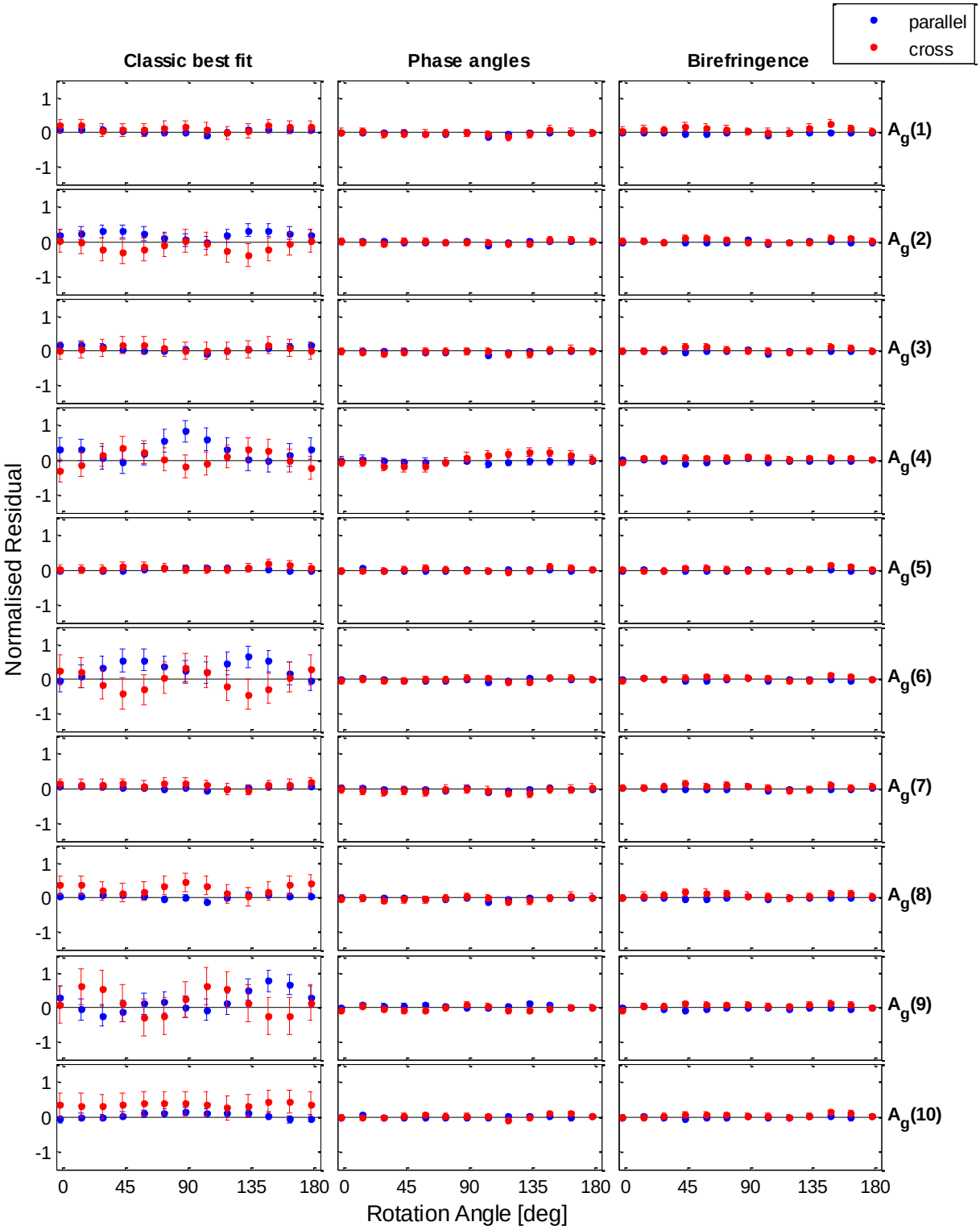

Figure A. 3: Individual fitting residuals for each A_g mode as a function of the rotation angle, shown for different fitting models in both PP and CP configurations. The total variance is plotted for each mode and for each model as error bar. In order to better compare the results from different modes, both residuals and variances are normalised to the maximum value of the respective PP or CP curve.

APPENDIX B - Publications

1. F. Ricci, F. Boschi, A. Baraldi, A. Filippetti, M. Higashiwaki, A. Kuramata, V. Fiorentini and R. Fornari, *"Theoretical and experimental investigation of optical absorption anisotropy in β-Ga_2O_3"*, Journal of Physics: Condensed Matter **28** (2016) 224005.

2. F. Orlandi, F. Mezzadri, G. Calestani, F. Boschi and R. Fornari, *"Thermal expansion coefficients of β-Ga_2O_3 single crystals"*, Applied Physics Express **8** (2015) 111101.

3. F. Boschi, M. Bosi, T. Berzina, E. Buffagni, C. Ferrari, R. Fornari, *"Hetero-epitaxy of ε-Ga_2O_3 layers by MOCVD and ALD"*, Journal of Crystal Growth **443** (2016) 25–30.

4. F. Mezzadri, G. Calestani, F. Boschi, D. Delmonte, M. Bosi, R. Fornari, *"Crystal structure and ferroelectric properties of ε-Ga_2O_3 films grown on (0001)-sapphire"*, Inorganic Chemistry, **55** (2016) 12079.

5. I. Cora, F. Mezzadri, F. Boschi, M. Bosi, M. Caplovicova, G. Calestani, I. Dódony, B. Pécz, R. Fornari, *"The real structure of ε-Ga_2O_3 and its relation to κ-phase"*, submitted to CrystEngComm.

6. M. Pavesi, F. Fabbri, F. Boschi, G. Piacentini, A. Baraldi, M. Bosi, E. Gombia, A. Parisini and R. Fornari, *"ε-Ga_2O_3 epilayers: a study of their physical properties and of their use as solar-blind UV photodetectors"*, to be submitted.

APPENDIX C - Conference contributions

1. B.E. Watts, F. Boschi, R. Fornari, *"Control of gelation during the deposition of alumina films"*, IX Workshop Italiano Sol-Gel, 2014, Parma, Italy. (Talk)

2. F. Ricci, A. Filippetti, V. Fiorentini, A. Baraldi, F. Boschi, R. Fornari, M. Higashiwaki, A. Kuramata, M. Bosi, *"A combined theoretical and experimental study of the bandgap of β-Ga_2O_3 wafers and epilayers"*, E-MRS 2014 Fall Meeting, Warsaw, Poland. (Talk)

3. F. Boschi, M. Bosi, E. Buffagni, T. Berzina, C. Ferrari, R. Fornari, *"A study of Ga_2O_3 hetero-epitaxial layers grown by MOCVD and ALD"*, 5th European Conference on Crystal Growth, 2015, Bologna, Italy (Talk)

4. R. Fornari, A. Baraldi, F. Boschi, A. Parisini, M. Pavesi, F. Ricci, A. Filippetti, V. Fiorentini, *"A reappraisal of anisotropy effects in bulk β-Ga_2O_3"*, International Workshop on Gallium Oxide 2015, Kyoto, Japan. (Talk)

5. F. Boschi, M. Bosi, E. Buffagni, T. Berzina, C. Ferrari, L. Aversa, R. Tatti, R. Verucchi, and R. Fornari, *"Properties of Ga_2O_3 hetero-epitaxial layers grown by MOCVD and ALD"*, International Workshop on Gallium Oxide 2015, Kyoto, Japan. (Poster)

6. F. Boschi, M. Bosi, C. Ferrari, E. Buffagni and R. Fornari, *"Epitaxial growth of ε-Ga_2O_3"*, 18th International Conference on Crystal Growth and Epitaxy, Nagoya, Japan. (Talk)

7. M. Pavesi, F. Fabbri, F. Boschi, A. Baraldi, C. Ferrari, E. Buffagni, M. Bosi, G. Piacentini, E. Gombia, A. Parisini, and R. Fornari, *"Properties of ε-Ga_2O_3 films grown by MOVPE"*, 18th International Conference on Crystal Growth and Epitaxy, Nagoya, Japan. (Talk)

8. F. Mezzadri, F. Boschi, M. Bosi, G. Calestani and R. Fornari, *"Crystal structure of ε-Ga_2O_3 thin films by single crystal X-ray diffraction"*, 18th International Conference on Crystal Growth and Epitaxy, Nagoya, Japan. (Poster)

9. M. Bosi, F. Boschi, T. Berzina, E. Buffagni, C. Ferrari, B. Pécz, I. Cora, G. Calestani, F. Mezzadri, R. Fornari, *"Hetero-epitaxy of ε-Ga_2O_3 layers by MOCVD and ALD"*, 11th European Conference on Silicon Carbide and Related Materials 2016, Halkidiki, Greece. (Poster)

10. M. Bosi, F. Boschi, T. Berzina, E. Buffagni, C. Ferrari , B. Pécz, I. Cora, G. Calestani, F. Mezzadri, R. Fornari, *"Hetero-epitaxy of ε-Ga_2O_3 layers by MOCVD and ALD"*, Materials.it 2016, Catania, Italy. (Poster)

Bibliography

[1] L. de Boisbaudran, *Philos. Mag. Ser. 4* **1875**, *50*, 414–416.

[2] T. Miyata, T. Nakatani, T. Minami, *J. Lumin.* **2000**, *87*, 1183–1185.

[3] P. Wellenius, A. Suresh, J. F. Muth, *Appl. Phys. Lett.* **2008**, *92*, 201111.

[4] B. Zheng, W. Hua, Y. Yue, Z. Gao, *J. Catal.* **2005**, *232*, 143–151.

[5] Y. Hou, L. Wu, X. Wang, Z. Ding, Z. Li, X. Fu, *J. Catal.* **2007**, *250*, 12–18.

[6] S.-J. Chang, Y.-L. Wu, W.-Y. Weng, Y.-H. Lin, W.-K. Hsieh, J.-K. Sheu, C.-L. Hsu, *J. Electrochem. Soc.* **2014**, *161*, H508–H511.

[7] M. Fleischer, J. Giber, H. Meixner, *Appl. Phys.* **1992**, *566*, 560–566.

[8] M. Fleischer, L. Hollbauer, E. Born, H. Meixner, *J. Am. Ceram. Soc.* **1997**, *80*, 2121–2125.

[9] S. Nakagomi, T. Sai, Y. Kokubun, *Sensors and Actuators (B)* **2013**, *187*, 413–419.

[10] M. Orita, H. Ohta, M. Hirano, H. Hosono, *Appl. Phys. Lett.* **2000**, *77*, 4166.

[11] J. Zhang, C. Xia, Q. Deng, W. Xu, H. Shi, F. Wu, J. Xu, *J. Phys. Chem. Solids* **2006**, *67*, 1656–1659.

[12] H. Aida, K. Nishiguchi, H. Takeda, N. Aota, K. Sunakawa, Y. Yaguchi, *Jpn. J. Appl. Phys.* **2008**, *47*, 8506–8509.

[13] Z. Galazka, R. Uecker, K. Irmscher, M. Albrecht, D. Klimm, M. Pietsch, M. Brützam, R. Bertram, S. Ganschow, R. Fornari, *Cryst. Res. Technol.* **2010**, *45*, 1229–1236.

[14] T. Oshima, N. Arai, N. Suzuki, S. Ohira, S. Fujita, *Thin Solid Films* **2008**, *516*, 5768–5771.

[15] G. Wagner, M. Baldini, D. Gogova, M. Schmidbauer, R. Schewski, M. Albrecht, Z. Galazka, D. Klimm, R. Fornari, *Phys. Status Solidi* **2014**, *211*, 27–33.

[16] K. Sasaki, M. Higashiwaki, A. Kuramata, T. Masui, S. Yamakoshi, *J. Cryst. Growth* **2013**, *378*, 591–595.

[17] K. Kaneko, H. Ito, S. D. Lee, S. Fujita, *Phys. Status Solidi* **2013**, *10*, 1596–1599.

[18] N. Ueda, H. Hosono, R. Waseda, H. Kawazoe, *Appl. Phys. Lett.* **1997**, *70*, 3561.

[19] E. G. Víllora, K. Shimamura, Y. Yoshikawa, T. Ujiie, K. Aoki, *Appl. Phys. Lett.* **2008**, *92*, 202120.

[20] J. B. Varley, J. R. Weber, A. Janotti, C. G. Van de Walle, *Appl. Phys. Lett.* **2010**, *97*, 142106.

[21] K. Irmscher, Z. Galazka, M. Pietsch, R. Uecker, R. Fornari, *J. Appl. Phys.* **2011**, *110*, 63720.

[22] K. Shimamura, E. G. Víllora, K. Domen, K. Yui, K. Aoki, N. Ichinose, *Jpn. J. Appl. Phys.* **2005**, *44*, L7–L8.

[23] S. Ohira, N. Suzuki, H. Minami, K. Takahashi, T. Araki, Y. Nanishi, *Phys. Status Solidi* **2007**, *4*, 2306–2309.

[24] S. Nakagomi, T. Momo, S. Takahashi, Y. Kokubun, *Appl. Phys. Lett.* **2013**, *103*, 72105.

[25] D. Guo, Z. Wu, P. Li, Y. An, H. Liu, X. Guo, H. Yan, G. Wang, C. Sun, L. Li, et al., *Opt. Mater. Express* **2014**, *4*, 1067–1076.

[26] M. Higashiwaki, K. Sasaki, A. Kuramata, T. Masui, S. Yamakoshi, *Phys. Status Solidi* **2014**, *211*, 21–26.

[27] J. L. Hudgins, G. S. Simin, E. Santi, M. A. Khan, *IEEE Trans. Power Electron.* **2003**, *18*, 907–914.

[28] M. Higashiwaki, K. Sasaki, A. Kuramata, T. Masui, S. Yamakoshi, *Appl. Phys. Lett.* **2012**, *100*, 13504.

[29] B. J. Baliga, *IEEE Electron Device Lett.* **1989**, *10*, 455–457.

[30] T. Matsumoto, M. Aoki, A. Kinoshita, T. Aono, *Jpn. J. Appl. Phys.* **1974**, *13*, 1578–1582.

[31] M. B. Maccioni, V. Fiorentini, *Appl. Phys. Express* **2016**, *9*, 41102.

[32] Y. Oshima, E. G. Víllora, Y. Matsushita, S. Yamamoto, K. Shimamura, *J. Appl. Phys.* **2015**, *118*, 85301.

[33] K. Sasaki, M. Higashiwaki, A. Kuramata, T. Masui, S. Yamakoshi, *Appl. Phys. Express* **2013**, *6*, 86502.

[34] S. Yoshioka, H. Hayashi, A. Kuwabara, F. Oba, K. Matsunaga, I. Tanaka, *J. Phys. Condens. Matter* **2007**, *19*, 346211–11.

[35] H. Y. Playford, A. C. Hannon, E. R. Barney, R. I. Walton, *Chem. - A Eur. J.* **2013**, *19*, 2803–2813.

[36] M. Marezio, J. P. Remeika, *J. Chem. Phys.* **1967**, *46*, 1862.

[37] J. Åhman, G. Svensson, J. Albertsson, *Acta Crystallogr.* **1996**, *52*, 1336–1338.

[38] H. He, R. Orlando, M. Blanco, R. Pandey, E. Amzallag, I. Baraille, M. Rérat, *Phys. Rev.* **2006**, *74*, 195123.

[39] R. Roy, V. G. Hill, E. F. Osborn, *J. Am. Chem. Soc.* **1952**, *74*, 719.

[40] J. A. Kohn, G. Katz, J. D. Broder, *Am. Miner.* **1957**, *42*, 5–6.

[41] S. Geller, *J. Chem. Phys.* **1960**, *33*, 676.

[42] G. M. Wolten, A. B. Chase, *J. Solid State Chem.* **1976**, *16*, 377–383.

[43] C. Janowitz, V. Scherer, M. Mohamed, A. Krapf, H. Dwelk, R. Manzke, Z. Galazka, R. Uecker, K. Irmscher, R. Fornari, et al., *New J. Phys.* **2011**, *13*, 85014.

[44] S. I. Stepanov, V. I. Nikolaev, V. E. Bougrov, A. E. Romanov, *Rev. Adv. Mater. Sci.* **2016**, *44*, 63–86.

[45] Tamura Corporation, "Single-Crystal Gallium Oxide Substrates Specifications," can be found under http://www.tamura-ss.co.jp/en/gao/, **2016**.

[46] M. Passlack, E. F. Schubert, W. S. Hobson, M. Hong, N. Moriya, S. N. G. Chu, K. Konstadinidis, J. P. Mannaerts, M. L. Schnoes, G. J. Zydzik, *J. Appl. Phys.* **1995**, *77*, 686.

[47] S.-A. Lee, J.-Y. Hwang, J.-P. Kim, S.-Y. Jeong, C.-R. Cho, *Appl. Phys. Lett.* **2006**, *89*, 182906.

[48] H. H. Tippins, *Phys. Rev.* **1965**, *140*, A316–A319.

[49] N. Ueda, H. Hosono, R. Waseda, H. Kawazoe, *Appl. Phys. Lett.* **1997**, *71*, 933.

[50] Z. Guo, A. Verma, X. Wu, F. Sun, A. Hickman, T. Masui, A. Kuramata, M. Higashiwaki, D. Jena, T. Luo, *Appl. Phys. Lett.* **2015**, *106*, 111909.

[51] E. G. Víllora, K. Shimamura, T. Ujiie, K. Aoki, *Appl. Phys. Lett.* **2008**, *92*, 202118.

[52] Z. Galazka, K. Irmscher, R. Uecker, R. Bertram, M. Pietsch, A. Kwasniewski, M. Naumann, T. Schulz, R. Schewski, D. Klimm, et al., *J. Cryst. Growth* **2014**, *404*, 184–191.

[53] I. Bhaumik, R. Bhatt, S. Ganesamoorthy, A. Saxena, A. K. Karnal, P. K. Gupta, A. K. Sinha, S. K. Deb, *Appl. Opt.* **2011**, *50*, 6006–10.

[54] K. Yamaguchi, *Solid State Commun.* **2004**, *131*, 739–744.

[55] L. Zhang, J. Yan, Y. Zhang, T. Li, X. Ding, *Sci. China Physics, Mech. Astron.* **2012**, *55*, 19–24.

[56] H. Peelaers, C. G. Van de Walle, *Phys. status solidi* **2015**, *252*, 828–832.

[57] F. Orlandi, F. Mezzadri, G. Calestani, F. Boschi, R. Fornari, *Appl. Phys. Express* **2015**, *8*, 111101.

[58] E. G. Víllora, M. Yamaga, T. Inoue, S. Yabasi, Y. Masui, T. Sugawara, T. Fukuda, *Jpn. J. Appl. Phys.* **2002**, *41*, L622–L625.

[59] F. Ricci, F. Boschi, A. Baraldi, A. Filippetti, M. Higashiwaki, A. Kuramata, V. Fiorentini, R. Fornari, *J. Phys. Condens. Matter* **2016**, *28*, 224005.

[60] T. Harwig, F. Kellendonk, S. Slappendel, *J. Phys. Chem. Solids* **1978**, *39*, 675–680.

[61] G. Blasse, A. Bril, *Solid State Commun.* **1969**, *7*, iii–iv.

[62] T. Harwig, F. Kellendonk, *J. Solid State Chem.* **1978**, *24*, 255–263.

[63] J. B. Varley, A. Janotti, C. Franchini, C. G. Van de Walle, *Phys. Rev. B* **2012**, *85*, 81109.

[64] T. Onuma, S. Fujioka, T. Yamaguchi, M. Higashiwaki, K. Sasaki, T. Masui, T. Honda, *Appl. Phys. Lett.* **2013**, *103*, 41910.

[65] L. Binet, D. Gourier, *J. Phys. Chem. Solids* **1998**, *59*, 1241–1249.

[66] D. Dohy, L. Lucazeau, A. Revcolevschi, *J. Solid State Chem.* **1982**, *45*, 180–192.

[67] D. Machon, P. McMillan, B. Xu, J. Dong, *Phys. Rev.* **2006**, *73*, 94125.

[68] T. Onuma, S. Fujioka, T. Yamaguchi, Y. Itoh, M. Higashiwaki, K. Sasaki, T. Masui, T. Honda, *J. Cryst. Growth* **2014**, *401*, 330–333.

[69] E. G. Víllora, Y. Morioka, T. Atou, T. Sugawara, M. Kikuchi, T. Fukuda, *Phys. Status Solidi* **2002**, *193*, 187–195.

[70] C. Kranert, C. Sturm, R. Schmidt-Grund, M. Grundmann, *Phys. Rev. Lett.* **2016**, *116*, 127401.

[71] C. Kranert, C. Sturm, R. Schmidt-Grund, M. Grundmann, *Sci. Rep.* **2016**, *6*, 35964.

[72] T. C. Lovejoy, R. Chen, X. Zheng, E. G. Víllora, K. Shimamura, H. Yoshikawa, Y. Yamashita, S. Ueda, K. Kobayashi, S. T. Dunham, et al., *Appl. Phys. Lett.* **2012**, *100*, 181602.

[73] K. Sasaki, A. Kuramata, T. Masui, E. G. Víllora, K. Shimamura, S. Yamakoshi, *Appl. Phys. Express* **2012**, *5*, 35502.

[74] N. Suzuki, S. Ohira, M. Tanaka, T. Sugawara, K. Nakajima, T. Shishido, *Phys. status solidi* **2007**, *4*, 2310–2313.

[75] X. Feng, Z. Li, W. Mi, Y. Luo, J. Ma, *Mater. Sci. Semicond. Process.* **2015**, *34*, 52–57.

[76] L. L. Liu, M. K. Li, D. Q. Yu, J. Zhang, H. Zhang, C. Qian, Z. Yang, *Appl. Phys. A* **2010**, *98*, 831–835.

[77] Y. Tomm, J. . Ko, A. Yoshikawa, T. Fukuda, *Sol. Energy Mater. Sol. Cells* **2001**, *66*, 369–374.

[78] T. Oshima, T. Okuno, S. Fujita, *Jpn. J. Appl. Phys.* **2007**, *46*, 7217–7220.

[79] T. Oshima, T. Okuno, N. Arai, N. Suzuki, S. Ohira, S. Fujita, *Appl. Phys. Express* **2008**, *1*, 11202.

[80] S. Müller, H. von Wenckstern, D. Splith, F. Schmidt, M. Grundmann, *Phys. Status Solidi* **2014**, *211*, 34–39.

[81] D. Splith, S. Müller, F. Schmidt, H. von Wenckstern, J. J. van Rensburg, W. E. Meyer, M. Grundmann, *Phys. Status Solidi* **2014**, *211*, 40–47.

[82] R. Suzuki, S. Nakagomi, Y. Kokubun, N. Arai, S. Ohira, *Appl. Phys. Lett.* **2009**, *94*, 222102.

[83] D. Y. Guo, Z. P. Wu, Y. H. An, X. C. Guo, X. L. Chu, C. L. Sun, L. H. Li, P. G. Li, W. H. Tang, *Appl. Phys. Lett.* **2014**, *105*, 23507.

[84] T. Oshima, T. Okuno, N. Arai, N. Suzuki, H. Hino, S. Fujita, *Jpn. J. Appl. Phys.* **2009**, *48*, 11605.

[85] M. Mohamed, K. Irmscher, C. Janowitz, Z. Galazka, R. Manzke, R. Fornari, *Appl. Phys. Lett.* **2012**, *101*, 132106.

[86] Y. Tomm, P. Reiche, D. Klimm, T. Fukuda, *J. Cryst. Growth* **2000**, *220*, 510–514.

[87] V. N. Maslov, V. M. Krymov, M. N. Blashenkov, A. A. Golovatenko, V. I. Nikolaev, *Tech. Phys. Lett.* **2014**, *40*, 303–305.

[88] A. O. Chase, *J. Am. Ceram. Soc.* **1964**, *47*, 470–470.

[89] M. R. Lorenz, J. F. Woods, R. J. Gambino, *J. Phys. Chem. Solids* **1967**, *28*, 403–404.

[90] J. Zhang, B. Li, C. Xia, G. Pei, Q. Deng, Z. Yang, W. Xu, H. Shi, F. Wu, Y. Wu, et al., *J. Phys. Chem. Solids* **2006**, *67*, 2448–2451.

[91] E. G. Víllora, K. Shimamura, Y. Yoshikawa, K. Aoki, N. Ichinose, *J. Cryst. Growth* **2004**, *270*, 420–426.

[92] S. Ohira, N. Suzuki, N. Arai, M. Tanaka, T. Sugawara, K. Nakajima, T. Shishido, *Thin Solid Films* **2008**, *516*, 5763–5767.

[93] K. Shimamura, E. G. Villora, K. Matsumura, K. Aoki, M. Nakamura, S. Takekawa, N. Ichinose, K. Kitamura, *Nihon Kessho Seicho Gakkaishi* **2006**, *33*, 147.

[94] S. Nakagomi, Y. Kokubun, *J. Cryst. Growth* **2012**, *349*, 12–18.

[95] W. Seiler, M. Selmane, K. Abdelouhadi, J. Perrière, *Thin Solid Films* **2015**, *589*, 556–562.

[96] R. Schewski, G. Wagner, M. Baldini, D. Gogova, Z. Galazka, T. Schulz, T. Remmele, T.

Markurt, H. Von Wenckstern, M. Grundmann, et al., *Appl. Phys. Express* **2015**, *8*, 11101.

[97] Y. Oshima, E. G. Víllora, K. Shimamura, *J. Cryst. Growth* **2015**, *410*, 53–58.

[98] Y. Chen, H. Liang, X. Xia, P. Tao, R. Shen, Y. Liu, Y. Feng, Y. Zheng, X. Li, G. Du, *J. Mater. Sci. Mater. Electron.* **2015**, 3231–3235.

[99] Y. Lv, J. Ma, W. Mi, C. Luan, Z. Zhu, H. Xiao, *Vacuum* **2012**, *86*, 1850–1854.

[100] V. Gottschalch, K. Mergenthaler, G. Wagner, J. Bauer, H. Paetzelt, C. Sturm, U. Teschner, *Phys. Status Solidi* **2009**, *206*, 243–249.

[101] W. Mi, J. Ma, C. Luan, H. Xiao, *J. Lumin.* **2014**, *146*, 1–5.

[102] L. Kong, J. Ma, C. Luan, Z. Zhu, *J. Solid State Chem.* **2011**, *184*, 1946–1950.

[103] J. Hao, Z. Lou, I. Renaud, M. Cocivera, *Thin Solid Films* **2004**, *467*, 182–185.

[104] Z. Ji, J. Du, J. Fan, W. Wang, *Opt. Mater. (Amst).* **2006**, *28*, 415–417.

[105] T. Minami, *Solid. State. Electron.* **2003**, *47*, 2237–2243.

[106] T. Miyata, T. Nakatani, T. Minami, *Thin Solid Films* **2000**, *373*, 145–149.

[107] T. Minami, T. Shirai, T. Nakatani, T. Miyata, *Jpn. J. Appl. Phys.* **2000**, *39*, L524–L526.

[108] V. N. Maslov, V. I. Nikolaev, V. M. Krymov, V. E. Bugrov, A. E. Romanov, *Phys. Solid State* **2015**, *57*, 1342–1346.

[109] D. P. Butt, Y. Park, T. N. Taylor, *J. Nucl. Mater.* **1999**, *264*, 71–77.

[110] S. Penner, B. Klötzer, B. Jenewein, F. Klauser, X. Liu, E. Bertel, *Thin Solid Films* **2008**, *516*, 4742–4749.

[111] P. Marwoto, S. Sugianto, E. Wibowo, *J. Theor. Appl. Phys.* **2012**, *6*, 17.

[112] K. Matsuzaki, H. Yanagi, T. Kamiya, H. Hiramatsu, K. Nomura, M. Hirano, H. Hosono, *Appl. Phys. Lett.* **2006**, *88*, 92106.

[113] Russell Binions, Claire J. Carmalt, I. P. Parkin, K. F. E. Pratt, G. A. Shaw, *Chem. Mater.* **2004**, *16*, 2489–2493.

[114] K. Nomura, K. Goto, R. Togashi, H. Murakami, Y. Kumagai, A. Kuramata, S. Yamakoshi, A. Koukitu, *J. Cryst. Growth* **2014**, *405*, 19–22.

[115] M. Higashiwaki, K. Konishi, K. Sasaki, K. Goto, K. Nomura, Q. T. Thieu, R. Togashi, H. Murakami, Y. Kumagai, B. Monemar, et al., *Appl. Phys. Lett.* **2016**, *108*, 133503.

[116] D. Gogova, M. Schmidbauer, A. Kwasniewski, *CrystEngComm* **2015**, *17*, 6744–6752.

[117] M. Baldini, M. Albrecht, A. Fiedler, K. Irmscher, D. Klimm, R. Schewski, G. Wagner, *J. Mater. Sci.* **2016**, *51*, 3650–3656.

[118] P. Ravadgar, R. H. Horng, T. Y. Wang, *ECS J. Solid State Sci. Technol.* **2012**, *1*, N58–N60.

[119] D. Gogova, G. Wagner, M. Baldini, M. Schmidbauer, K. Irmscher, R. Schewski, Z. Galazka, M. Albrecht, R. Fornari, *J. Cryst. Growth* **2014**, *401*, 665–669.

[120] M. Baldini, M. Albrecht, D. Gogova, R. Schewski, G. Wagner, *Semicond. Sci. Technol.* **2015**, *30*, 24013.

[121] D. J. Comstock, J. W. Elam, *Chem. Mater.* **2012**, *24*, 4011.

[122] R. K. Ramachandran, J. Dendooven, J. Botterman, S. Pulinthanathu Sree, D. Poelman, J. A. Martens, H. Poelman, C. Detavernier, *J. Mater. Chem. A* **2014**, *2*, 19232–19238.

[123] D. Choi, K.-B. Chung, J.-S. Park, *Thin Solid Films* **2013**, *546*, 31–34.

[124] H. Lee, K. Kim, J. J. Woo, D. J. Jun, Y. Park, Y. Kim, H. W. Lee, Y. J. Cho, H. M. Cho, *Chem. Vap. Depos.* **2011**, *17*, 191–197.

[125] M. Nieminen, L. Niinistö, E. Rauhala, *J. Mater. Chem.* **1996**, *6*, 27.

[126] E. G. Víllora, K. Shimamura, K. Kitamura, K. Aoki, *Appl. Phys. Lett.* **2006**, *88*, 31105.

[127] H. Okumura, M. Kita, K. Sasaki, A. Kuramata, M. Higashiwaki, J. S. Speck, *Appl. Phys. Express* **2014**, *7*, 95501.

[128] K. Sasaki, M. Higashiwaki, A. Kuramata, T. Masui, S. Yamakoshi, *IEEE Electron Device Lett.* **2013**, *34*, 493–495.

[129] T. Oishi, Y. Koga, K. Harada, M. Kasu, *Appl. Phys. Express* **2015**, *8*, 31101.

[130] M. Higashiwaki, K. Sasaki, T. Kamimura, M. Hoi Wong, D. Krishnamurthy, A. Kuramata, T. Masui, S. Yamakoshi, *Appl. Phys. Lett.* **2013**, *103*, 123511.

[131] M. H. Wong, K. Sasaki, A. Kuramata, S. Yamakoshi, M. Higashiwaki, *IEEE Electron Device Lett.* **2016**, *37*, 212–215.

[132] Z.-L. Xie, R. Zhang, C.-T. Xia, X.-Q. Xiu, P. Han, B. Liu, H. Zhao, R.-L. Jiang, Y. Shi, Y.-D. Zheng, *Chinese Phys. Lett.* **2008**, *25*, 2185–2186.

[133] V. I. Nikolaev, A. I. Pechnikov, V. N. Maslov, A. A. Golovatenko, V. M. Krymov, S. I. Stepanov, N. K. Zhumashev, V. E. Bougrov, A. E. Romanov, *Mater. Phys. Mech.* **2015**, *22*, 59–63.

[134] K. Kachel, M. Korytov, D. Gogova, Z. Galazka, M. Albrecht, R. Zwierz, D. Siche, S. Golka, A. Kwasniewski, M. Schmidbauer, et al., *CrystEngComm* **2012**, *14*, 8536–8540.

[135] E. G. Víllora, K. Shimamura, K. Aoki, K. Kitamura, *Thin Solid Films* **2006**, *500*, 209–213.

[136] E. G. Víllora, K. Shimamura, K. Kitamura, K. Aoki, T. Ujiie, *Appl. Phys. Lett.* **2007**, *90*, 234102.

[137] M. M. Muhammed, M. Peres, Y. Yamashita, Y. Morishima, S. Sato, N. Franco, K. Lorenz, A. Kuramata, I. S. Roqan, *Appl. Phys. Lett.* **2014**, *105*, 42112.

[138] E. G. Víllora, S. Arjoca, K. Shimamura, D. Inomata, K. Aoki, in *Proc. SPIE* (Eds.: F.H. Teherani, D.C. Look, D.J. Rogers), International Society For Optics And Photonics, **2014**, p. 89871U.

[139] W. H. Zachariasen, *Nor. Vid. Akad.* **1928**, *41*, 1–65.

[140] J. Böhm, *Angew. Chemie* **1940**, *53*, 131.

[141] C. Otero Areán, A. L. Bellan, M. P. Mentruit, M. R. Delgado, G. T. Palomino, *Microporous Mesoporous Mater.* **2000**, *40*, 35–42.

[142] H. Hayashi, R. Huang, H. Ikeno, F. Oba, S. Yoshioka, I. Tanaka, S. Sonoda, *Appl. Phys. Lett.* **2006**, *89*, 181903.

[143] H. Hayashi, R. Huang, F. Oba, T. Hirayama, I. Tanaka, T. Minami, N. Ueda, H. Hosono, R.

Waseda, H. Kawazoe, et al., *J. Mater. Res.* **2011**, *26*, 578–583.

[144] S. Penner, C. Zhuo, R. Thalinger, M. Grünbacher, C. Hejny, S. Vanicek, M. Noisternig, *Monatshefte für Chemie - Chem. Mon.* **2016**, *147*, 289–300.

[145] E. Tronc, C. Chaneác, J. P. Jolivet, *J. Solid State Chem.* **1998**, *139*, 93–104.

[146] M. Orita, H. Hiramatsu, H. Ohta, M. Hirano, H. Hosono, *Thin Solid Films* **2002**, *411*, 134–139.

[147] S. Ge, Z. Zheng, *Solid State Sci.* **2009**, *11*, 1592–1596.

[148] F. Boschi, M. Bosi, T. Berzina, E. Buffagni, C. Ferrari, R. Fornari, *J. Cryst. Growth* **2016**, *443*, 25–30.

[149] X. Xia, Y. Chen, Q. Feng, H. Liang, P. Tao, M. Xu, G. Du, *Appl. Phys. Lett.* **2016**, *108*, 202103.

[150] H. O. Pierson, *Handbook of Chemical Vapor Deposition (CVD) - Principles, Technology, and Applications*, Noyes Publications / William Andrew Publishing, LLC, Norwich, New York, USA, **1999**.

[151] J.-O. Carlsson, P. M. Martin, in *Handb. Depos. Technol. Film. Coatings (Third Ed.*, Elsevier Ltd., **2010**, pp. 314–363.

[152] N. Lovergine, in *Theor. Technol. Asp. Cryst. Growth* (Eds.: R. Fornari, C. Paorici), Transtech Publ., Zurich, **1998**, pp. 153–174.

[153] T. Suntola, M. J. Antson, *U.S. Patent*, **1977**, 4,058,430.

[154] T. Suntola, *Mater. Sci. Reports* **1989**, *4*, 261–312.

[155] T. Suntola, in *Handb. Cryst. Growth* (Ed.: D.T.J. Hurle), North-Holland Publ., Amsterdam, **1994**, pp. 601–663.

[156] S. M. George, *Chem. Rev.* **2010**, *110*, 111–31.

[157] T. Kääriäinen, D. Cameron, M.-L. Kääriäinen, A. Sherman, *Atomic Layer Deposition: Principles, Characteristics, and Nanotechnology Applications*, Scrivener Publishing LLC., John Wiley & Sons Inc., **2013**.

[158] Ensure Scientific Group, "The Principle of Atomic Layer Deposition," can be found under http://www.ennano.com/, **2016**.

[159] D. B. Chrisey, G. K. Hubler, Eds. , *Pulsed Laser Deposition of Thin Films*, Wiley, New York, **1994**.

[160] M. Lorenz, in *Transparent Conduct. Zinc Oxide*, Springer Berlin Heidelberg, **2008**, pp. 303–357.

[161] H. Krebs, M. Weisheit, S. Erik, T. Scharf, C. Fuhse, M. St, K. Sturm, M. Seibt, H. Kijewski, D. Nelke, et al., *Adv. Solid State Phys.* **2003**, *43*, 505–518.

[162] A. Alyamani, O. M. Lemine, in *Scan. Electron Microsc.*, InTech, **2012**, p. 466.

[163] M. Tachiki, M. Noda, K. Yamada, T. Kobayashi, *J. Appl. Phys.* **1998**, *83*, 5351.

[164] M. Siegert, W. Zander, J. Lisoni, J. Schubert, C. Buchal, *Appl. Phys. A Mater. Sci. Process.* **1999**, *69*, S779–S781.

[165] K. Kinoshita, H. Ishibashi, T. Kobayashi, *Jpn. J. Appl. Phys.* **1994**, *33*, L417–L420.

[166] Z. Trajanovic, L. Senapati, R. P. Sharma, T. Venkatesan, *Appl. Phys. Lett.* **1997**, *70*, 3461–3463.

[167] M. Iwabuchi, K. Kinoshita, H. Ishibashi, T. Kobayashi, *Jpn. J. Appl. Phys.* **1994**, *33*, L610–L612.

[168] E. Morita, K. Yamamuro, M. Tachiki, T. Kobayashi, *Nucl. Instruments Methods Phys. Res.* **1997**, *121*, 412–414.

[169] A. Kühle, J. L. Skov, S. Hjorth, I. Rasmussen, J. B. Hansen, *Appl. Phys. Lett.* **1994**, *64*, 3178–3180.

[170] B. Holzapfel, B. Roas, L. Schultz, P. Bauer, G. Saemann-Ischenko, *Appl. Phys. Lett.* **1992**, *61*, 3178–3180.

[171] Z. Trajanovic, L. Senapati, R. P. Sharma, T. Venkatesan, *Appl. Phys. Lett.* **1995**, *66*, 2418–2420.

[172] Sigma-Aldrich catalog, "Product J100015 - Trimethylgallium," can be found under http://www.sigmaaldrich.com/catalog/product/aldrich/j100015?lang=it&region=IT, **2016**.

[173] L. K. Wang, C. T. Yang, M. H. S. Wang, in *Adv. Water Resour. Manag.* (Eds.: L.K. Wang, C.T. Yang, M.-H.S. Wang), Springer International Publishing, **2015**, p. 558.

[174] M. G. Jacko, S. J. W. Price, *Can. J. Chem.* **1963**, *41*, 1560–1567.

[175] P. W. Lee, T. R. Omstead, D. R. Mckenna, K. F. Jensen, *J. Cryst. Growth* **1987**, *85*, 165–174.

[176] S. H. Li, C. A. Larsen, G. B. Stringfellow, *J. Cryst. Growth* **1990**, *102*, 103–116.

[177] E. Dobrovinskaya, L. Lytvynov, V. Pishchik, in *Sapphire Mater. Manuf. Appl.*, Springer, **2009**, p. 61.

[178] D. Shinohara, S. Fujita, *Jpn. J. Appl. Phys.* **2008**, *47*, 7311–7313.

[179] T. Oshima, T. Nakazono, A. Mukai, A. Ohtomo, *J. Cryst. Growth* **2012**, *359*, 60–63.

[180] Y. Oshima, E. G. Víllora, K. Shimamura, *Appl. Phys. Express* **2015**, *8*, 55501.

[181] M. Leszczynski, H. Teisseyre, T. Suski, I. Grzegory, M. Bockowski, J. Jun, S. Porowski, K. Pakula, J. M. Baranowski, C. T. Foxon, et al., *Appl. Phys. Lett.* **1996**, *69*, 73.

[182] A. Taylor, R. M. Jones, in *Silicon Carbide - A High Temp. Semicond.* (Eds.: J.R. O'Connor, J. Smiltens), Pergamon Press, New York, **1960**, p. 147.

[183] F. Mezzadri, G. Calestani, F. Boschi, D. Delmonte, M. Bosi, R. Fornari, *Inorg. Chem.* **2016**, *55*, 12079–12084.

[184] B. E. Warren, in *X-Ray Diffr.*, Addison-Wesley Publishing Company, **1969**, p. 21.

[185] M. C. Burla, R. Caliandro, M. Camalli, B. Carrozzini, G. L. Cascarano, C. Giacovazzo, M. Mallamo, A. Mazzone, G. Polidori, R. Spagna, *J. Appl. Crystallogr.* **2012**, *45*, 357–361.

[186] G. M. Sheldrick, *Acta Crystallogr. Sect. C Struct. Chem.* **2015**, *71*, 3–8.

[187] M. Nespolo, G. Ferraris, H. Ohashi, *Acta Crystallogr. Sect. B Struct. Sci.* **1999**, *55*, 902–916.

[188] S. Hovmöller, *Ultramicroscopy* **1992**, *41*, 121–135.

[189] E. Dobrovinskaya, L. Lytvynov, V. Pishchik, in *Sapphire Mater. Manuf. Appl.*, Springer, **2009**, pp. 116–117.

[190] M. Rebien, W. Henrion, M. Hong, J. P. Mannaerts, M. Fleischer, *Appl. Phys. Lett.* **2002**, *81*, 250.

[191] F. Fabbri, M. J. Smith, D. Recht, M. J. Aziz, S. Gradečak, G. Salviati, *Appl. Phys. Lett.* **2013**, *102*, 31909.

[192] G. Bellocchi, F. Fabbri, M. Miritello, F. Iacona, G. Franzò, *ACS Appl. Mater. Interfaces* **2015**, *7*, 18201–18205.

[193] Z. Liu, X. Jing, L. Wang, *J. Electrochem. Soc.* **2007**, *154*, H440.

[194] Z. Zhang, E. Farzana, A. R. Arehart, S. A. Ringel, *Appl. Phys. Lett.* **2016**, *108*, 52105.

[195] G. Pezzotti, *J. Appl. Phys.* **2013**, *113*, 211301.

[196] H. C. Lin, Z. C. Feng, M. S. Chen, Z. X. Shen, I. T. Ferguson, W. Lu, *J. Appl. Phys.* **2009**, *105*, 36102.

[197] N. Djiedeu, B. Mohamadou, P. Bourson, M. Aillerie, *J. Phys. Condens. Matter* **2009**, *21*, 15905.

[198] T. Sander, S. Eisermann, B. K. Meyer, P. J. Klar, *Phys. Rev. B - Condens. Matter Mater. Phys.* **2012**, *85*, 165208.

[199] A. Filippetti, V. Fiorentini, *Eur. Phys. J. B* **2009**, *71*, 139–183.

[200] A. Filippetti, C. D. Pemmaraju, S. Sanvito, P. Delugas, D. Puggioni, V. Fiorentini, *Phys. Rev. B - Condens. Matter Mater. Phys.* **2011**, *84*, 195127.

[201] V. Petříček, M. Dušek, L. Palatinus, *Zeitschrift für Krist. - Cryst. Mater.* **2014**, *229*, 345–352.

Acknowledgements

A thesis work never comes from the efforts of a single person alone. Of course, giving the proper thanks to all people who helped, taught and supported me in this endeavour is not an easy task, and I will try not to forget anyone within this short space.

First of all I would like to express my deepest gratitude to my supervisor, Prof. Roberto Fornari, for his expert guidance and constant support during these three years. It is mainly thanks to him and to his widespread knowledge of the semiconductor physics world that I was able to experience first-hand so many different aspects of the research in this field.

Thanks to Dr. Matteo Bosi, for the valuable training he provided me and for his constant collaboration in setting up the CVD reactor and developing the deposition process. Many thanks also to Dr. Giovanni Attolini and to Dr. Marco Negri, always ready to help and to share their knowledge.

I would like to thank Professors Andrea Baraldi and Pier Paolo Lottici, for introducing me to the world of spectroscopy and for sharing their deep expertise with me. Their support and kindness were not simply limited to laboratory issues.

My deepest thanks and gratitude go to Prof. Marius Grundmann and Dr. Holger von Wenckstern, who kindly hosted me in Leipzig and gave me the opportunity to extend my expertise, including new deposition and characterisation methods.

Many thanks to Holger Hochmuth, for his patient training and helpfulness in getting me acquainted to the PLD apparatus and process-related issues.

A very special thank goes to Daniel Splith and Stefan Müller, who not only helped planning my research activity in Leipzig and introduced me to all the characterisation/processing techniques I needed for my studies there, but they also really made me feel welcome, always being there whenever I knocked at their door. Without their support, it would have been impossible to achieve so much from the three months spent in Germany, both in terms of learning and of experimental activity.

Thanks to Dr. Tatiana Berzina, for the long hours spent together observing the samples by SEM, and to Dr. Enos Gombia, for his kindness and helpfulness in teaching me the bases of metal contacts deposition and electrical testing.

Thanks to Drs. Elisa Buffagni and Claudio Ferrari, who provided, through XRD measurements and scientific discussion, a constant and insightful feedback to the structural quality of the films grown at IMEM-CNR, and let me take part to some of the measurements.

Many thanks to Professors Maura Pavesi and Antonella Parisini, central figures of the electrical characterisation. The discussions about optical, electrical and transport properties were always pleasant and enlightening.

With Dr. Bernard Watts I shared a couple of weeks working on sol-gel deposition of aluminium oxide. His practical approach towards experimental issues was most inspiring, as were his intuitions.

Many thanks to Dr. Francesco Mezzadri, Prof. Gianluca Calestani and Dr. Fabio Orlandi, whose XRD measurements and experience in the field of crystallography were crucial in understanding the real crystal structure of ε-Ga_2O_3 and in studying the thermal expansion of the β phase.

The contribution of Dr. Davide Delmonte goes well beyond the fruitful collaboration that led to the experimental assessment of ferroelectricity in ε-Ga_2O_3. Being office-neighbours also means every-day discussion (and cheerful times). He puts a contagious passion in everything he does.

Thanks to Drs. Filippo Fabbri and Giancarlo Salviati for their support, never lacking since I graduated under their supervision, and for kindly providing the CL measurements.

I would like to thank Drs. Ildikó Cora and Bela Pécz for performing TEM analysis on our films, unveiling the domain structure of ε-Ga_2O_3, and for hosting me at MFA Institute in Budapest. Many thanks also to Dr. Péter Petrik, who kindly provided the ellipsometry measurements.

Thanks to Dr. Detlef Klimm, for kindly providing the preliminary results of DSC analysis performed at IKZ Institute in Berlin.

Many thanks to Prof. Vincenzo Fiorentini and to his group at Cagliari University, for the important theoretical feedback to the experimental assessments of anisotropic properties in β-Ga_2O_3.

Among those who collaborated and helped me in many ways during these years, I would like to mention Dr. Paola Lagonegro, Salvatore Vantaggio, Drs. Marco Gorni and Giovanni Piacentini, Prof. Laura Romanò, Manuele Bettelli, Dr. Andrea Zappettini, Drs. Masataka Higashiwaki and Akito Kuramata, Patrizia Ferro, Drs. Cesare Frigeri and Francesca Rossi, the "PEDforPV" group of IMEM-CNR, Michael Bonholzer, Jörg Lenzner, Gabriele Ramm, Dr. Zsolt Zolnai.

I would finally like to thank Fondazione Cariparma, for sponsoring my Ph.D. scholarship, and the coordinator of the course, Prof. Cristiano Viappiani, for his constant availability.

Outside the sphere strictly related to the Ph.D. activity, my most heartfelt thanks go to my friends and colleagues who stood by me also in everyday-life: Pietro, Giulio, Simone, Maurizio, Angela, Marco, Paola, Filippo, Greta, Silvio, Nicola, Lucia, Federico, Daniele, Matteo, Davide, Manuele, Giulia, Davide, Martina, Benedetta, Nicola, Michela, Mirco, Elena, Daniele.

To Chiara, for being indeed so "clear", so bright, even after having endured two of my theses.

To my beloved family, to Mauro, Aurelio, Lina, Tina, and Rosaria.

Thank you